Adiabatic Simulated Moving Bed Reactor – Principle, Nonlinear Analysis and Experimental Demonstration

Dissertation

zur Erlangung des akademischen Grades

Doktoringenieur
(Dr.-Ing.)

von

Dipl.-Ing. Volker Michael Zahn

geb. am 10.09.1979 in
Querfurt

genehmigt durch die Fakultät für Verfahrens- und Systemtechnik
der Otto-von-Guericke-Universität Magdeburg

Promotionskommission:
Prof. Dr.-Ing. Kay Sundmacher (Vorsitz)
Prof. Dr.-Ing. Andreas Seidel-Morgenstern (Gutachter)
Prof. Ph.D. Moshe Sheintuch (Gutachter)
Prof. Dr.-Ing. Ulrich Nieken (Gutachter)

eingereicht am: 13. März 2012
Promotionskolloquium am: 30. Juli 2012

Danksagung

Diese Arbeit entstand während meiner Tätigkeit als wissenschaftlicher Mitarbeit in der Arbeitsgruppe Physikalisch-Chemische Grundlagen der Prozesstechnik am Max-Planck-Institut Magdeburg. Ich danke an dieser Stelle allen, die zum Gelingen der Arbeit durch fachliche und persönliche Unterstützung beigetragen haben.

Mein Dank gilt besonders meinem Doktorvater Professor Seidel-Morgenstern für die Anregung zu diesem Thema, die hervorragende Betreuung und das große Interesse an meiner Arbeit. Über die exzellenten Rahmenbedingungen hinaus bot er den Freiraum, auch zahlreiche eigene Ideen zu verwirklichen. Für das entgegen gebrachte Vertrauen bedanke ich mich ausdrücklich.

Darüber hinaus danke ich Professor Sheintuch für die Übernahme des Gutachtens und die wertvollen Diskussionen zu Regelungskonzepten und experimentellen Methoden. Professor Nieken danke ich für die konstruktive Diskussion in Stuttgart und für die Begutachtung dieser Arbeit. Mein Dank gilt Professor Flockerzi für die erhellenden Diskussionen zur Singularitätstheorie, die Literaturhinweise und die kritischen Anregungen zu meiner Arbeit. Für die wertvollen Ratschläge zu instationären Reaktorkonzepten bedanke ich mich bei Professor Eigenberger. Gregor Kolios danke ich für die Ratschläge zur Konstruktion von Versuchsreaktoren, für die sehr gute Zusammenarbeit im Rahmen der studentischen Betreuung und für die kollegiale Atmosphäre in der BASF. Professor Mangold und Michael Krasnyk danke ich für die Zusammenarbeit bei der numerischen Analyse der Reaktormodelle. Besonderer Dank gilt Knut Gedicke für die kritischen Anregungen zu dieser Arbeit. Für die vielen Ideen und die Unterstützung bei dem Aufbau des Versuchsreaktors bedanke ich mich bei Reiner Könning, Detlef Franz und Jan Protzmann. Bedanken möchte mich auch bei den studentischen Hilfskräften für ihren engagierten Einsatz. Für die freundschaftliche und produktive Zusammenarbeit danke ich insbesondere Tanja Wolff, Henning Haida, Jutta Wilke und Christof Hamel. Und nicht zuletzt danke ich allen Freunden und meiner Familie für ihre Geduld, Motivation und Unterstützung während des Studiums und der Promotionsphase.

Abstract

This work investigates a heat integrated reactor concept based on unsteady state operation of several adiabatic catalytic fixed-bed reactors. Exothermic reaction fronts are guided through such a cascade in the gas flow direction, while cold reactor segments are switched to the end for efficient thermal regeneration. This inherently periodic operation attempts to trap a self-sustained exothermic front allowing an autothermal operation. As such, the switching policy simulates a countercurrent of the solid compared to the fluid phase and is therefore denoted as a simulated moving bed reactor (SMBR). Potential applications are seen in catalytic total oxidation of volatile organic compounds (VOC) in diluted off-gases or in performing equilibrium limited exothermic reactions. This work contains a comprehensive theoretical analysis and an experimental proof-of-concept of the adiabatic simulated moving bed reactor.

Thermal and reaction fronts occurring in a SMBR were characterized regarding their constant pattern behavior, required ignition temperatures, dynamics and spatio-temporal patterns. Stable ignited operation can be maintained, when switching times are adjusted to the velocity of the fronts. Within a specific windows of switching times complete conversion without slip of unconverted reactants can be achieved.

In order to avoid expensive dynamic simulations, a true moving bed reactor model was derived, which retains all relevant properties of the periodic reactor needed for reactor analysis and design. This does not only allow a direct approximation of temperature and concentration profiles, but provides an efficient numerical nonlinear analysis essential to understand and control ignition-extinction phenomena. Diverse reactor multiple steady states were encountered and structured with the help of higher order singularities. In this way, reactor control and the identification of feasible reactions are available. Three discrete-time control concepts were investigated to maintain the reactor in the limited range of switchting times. Already a simple temperature control was shown to be appropriate.

The model-system experimentally investigated is the total oxidation of propene and ethene on a $CuCrO_x/Al_2O_3$ catalyst in air. Systematic experiments confirmed the applicable range of switching times as well as the control characteristic. Step experiments altering flow rates and concentrations demonstrated the proper disturbance rejection.

As long as rates of the oxidation reactions are similar, mixtures can be well processed. Otherwise, incomplete conversion of the less oxidizable component can occur. Due to sufficiently high start-up temperatures and an excess of this component the total oxidation of such mixtures can be assured.

Kurzfassung

In der vorliegenden Arbeit wird ein wärmeintegriertes Reaktorkonzept untersucht, dass auf einer instationären Prozessführung mit mehreren adiabaten Festbettreaktoren beruht. Dabei werden exotherme Reaktionsfronten in Strömungsrichtung durch die Reaktorkaskade geführt und erkaltete Segmente zur thermischen Regeneration wieder an das Ende geschaltet. Der periodische Betrieb stabilisiert die exothermen selbsterhaltenden Fronten und gestattet einen effizienten autothermen Betrieb. Mit der periodischen Betriebsweise wird ein Gegenstrom der festen Phase im Vergleich zur fluiden Phase technisch simuliert, weshalb vom simulierten Gegenstromprozess (*simulated moving bed*, SMB) gesprochen wird. Vorzugsweise wird der Einsatz im Bereich von katalytischen Totaloxidationen von VOC (volatile organic compounds) belasteten industriellen Abluftströmen gesehen. In dieser Arbeit wird der adiabate *Simulated Moving Bed* Reaktor (SMBR) zunächst durch eine detaillierte theoretische Analyse charakterisiert und anschließend das Prinzip mit experimentellen Arbeiten überprüft.

Zunächst wurden die Fronten hinsichtlich ihres formstabilen Verhaltens (engl., *constant pattern*), der erforderlichen Zündtemperaturen, der Dynamik sowie Raum-zeitlicher Muster untersucht. Ein stabil gezündeter Reaktorbetrieb ist möglich, wenn die Schaltzeiten auf die Geschwindigkeiten der Reaktionsfronten abgestimmt werden. Innerhalb eines bestimmten Schaltzeitbereichs lässt sich dann nahezu Vollumsatz bei minimalem Schlupf erzielen.

Ein reduziertes stationäres Reaktormodell, das so genannte TMBR (*true moving bed reactor*) Modell hergeleitet, das alle wesentlichen Aussagen eine komplexeren dynamischen Simulationsmodells bewahrt. Neben der direkten Approximation von Temperatur- und Konzentrationsprofilen gestattet das Modell eine effiziente nichtlineare Analyse des Reaktors. Über die Quantifizierung einfacher Zünd-Lösch Phänomene hinausgehend wurde durch die Analyse von Singularitäten höherer Ordnung eine strukturiere Beschreibung des nichtlinearen Verhalten bezüglich mehrerer Parameter untersucht. Die Ergebnisse gestatten sowohl die Bewertung von Systemparametern auf das Zündverhalten als auch eine Auswahl möglicher Reaktionen für den SMBR. Um den gezündeten Reaktorbetrieb sicherzustellen, wurden drei Regelungskonzepte charakterisiert. Bereits eine einfache Temperaturregelung kann erfolgreich eingesetzt werden.

Die Totaloxidationen von Propen und Ethen an einem $CuCrO_x/Al_2O_3$ Katalysator wurde experimentell untersucht. Durch systematische Versuche wurde der Schaltzeitbereich verifiziert und die Reglerkennlinie experimentell bestätigt. Antworten auf aufgeprägte Sprünge in Flussraten und Eingangskonzentrationen zeigten ein gutes Störverhalten.

Solange die Reaktionsraten von Totaloxidationen in ähnlichen Größenordnung liegen, können Gemische zuverlässig umgesetzt werden. Andernfalls kann es zu einer unvollständigen Umsetzung der schwer oxidierbaren Komponente kommen. Durch ausreichend hohe Anfahrtemperaturen in Verbindung mit einem Überschuss dieser Komponente kann die Totaloxidation von Gemischen sichergestellt werden.

Contents

1. Introduction

1.1. Developments in Chemical Reaction Engineering

Advances in Chemical Industries Conventional processes in the chemical industries are based on interconnected unit operations to fulfill the task of reactant pretreatment, chemical conversion and separation of the desired products. A careful design and control of material and energy streams is required to synthesize products with well defined properties [1, 2]. Significant improvements for chemical manufacturing sites can be achieved by coupling process units in an integrative manner. A properly designed *process integration* allows for significant enhancements in e.g. productivity, selectivities, energy efficiency, safety and consumption of auxiliary chemicals [3]. Process integration can also lead to increased complexity regarding apparatuses, design and control. Consequently, research is required to gain sufficient understanding of new concepts which is also a prerequisite for acceptance in the industry.

Process integration can be considered as a subclass of *process intensification*, which contains equipments and methods replacing the classical unit operations to bring a substantial increase in the processes efficiency. In particularly, such improvements address equipment size, energy consumption and waste production, which should further lead to cheaper and more eco-friendly process technologies [4].

Several examples for integrated processes can be found in the recent history of chemical reaction engineering. One of the first work dealt with improvements of heat exchange in chemical reactors, which is the so called reverse-flow reactor. Heat exchange and reaction are carried out in a single fixed-bed imposing periodic flow reversal to trap the reaction zone [5]. Agar et al. [6] exploited selective reactant adsorption in a fixed-bed to improve stack gas denitrification and suggested the terminology "multifunctional reactors", which generalized the integrated concepts to various phenomenological features [7, 8]. Since that time, research activities focused for instance on reactor-separator family designed to overcome chemical equilibrium limitations e.g. by removing products from the reaction volume. Reactive distillation is a prominent example, which is being applied in industry today [8, 9].

Adsorption equilibria were exploited in different ways. In chromatographic reactors, either a multi-bed cyclic operation or periodic operation of a single fixed-bed can be applied to enhance selectivities of equilibrium limited reactions. One of the oldest and most prominent example is the glucose isomerization performed in a simulated moving bed countercurrent process [10, 11]. An example for batch operation, a single fixed-bed process, is the hydrolysis of methyl formate in methanol and formic acid via acid ion exchange resins. Thereby the resin simultaneously acts as a solid catalyst and a selective adsorbent [12].

Another example for of process integration is the application of membrane reactors [13]. Membranes can be used either for (selective/non-selective) extraction of products or for

dosing of reactants, which can improve the selectivities of equilibrium limited reactions or complex parallel reaction networks. Examples are oxidative dehydrogenation of alkanes to alkenes, oxidative coupling of methane, oxidation of butane, hydrogenation of acrolein [14, 15].

Other examples evolved within the research communities, however, with a limited acceptance in the industry so far. Although benefits compared to the conventional unit operations have been achieved, cost factors decide in the end and might prohibit the application of integrated processes [11].

Heat Integrated Concepts An active area of process integration is concerned with improvements in the energy efficiency, so called heat integrated reactor concepts [16]. Comprehensive reviews on conventional technologies, phenomenological aspects and recent trends can be found in Eigenberger et al. [17] and Kolios et al. [18]. In principle, the heat released by exothermic reactions carried out at a certain high reaction temperature should be recovered most efficiently. The recovered thermal energy is spend for heat sinks, either for preheating of reactants or for endothermic reactions. Coupling heat exchange and reaction in a clever way allows for improved heat recovery, thermal efficiency and hence for a more compact process design possibly being more cost effective. Often an adiabatic operation is realized to achieve an autothermal process. In most of the cases it is meant a self sustained reaction at temperatures above ambient without additional external heat supply, whereby inlet and outlet temperatures are almost at ambient conditions [19].

Among the various concepts investigated, the periodically operated reversed-flow reactor has received much attention in the history of chemical engineering. As mention before, the idea is based flow reversal employed to a single catalytic fixed-bed reactor stabilizing a moving high temperature front which has formed due to an exothermic reaction. The fixed-bed serves as a regenerative heat exchanger. Although the first realization is attributed to Cottrell [20] dating back to 1938, Matros and coworkers are responsible for spreading the idea [5, 21].

The concept was widely studied for various exothermic reactions, such as total catalytic oxidation of volatile organic compounds (VOC), the sulfur dioxide oxidation [22–24] and catalytic NO_x reduction by NH_3 [25]. According to Matros [26] these applications have gained commercial realization. Research efforts concentrated on several potential reactions, such as the methanol synthesis [27] and for also on coupling of exothermic and endothermic reaction. Kulkarni et al. [28] [29] investigated a bidirectional fixed-bed reactor process coupling endothermic steam reforming and the exothermic partial combustion of methane. Another example is the styrene synthesis via dehydrogenation of ethylbenzene [30]. Styrene is generated in an endothermic production cycle, and hydrogen, as a byproduct, is oxidized for sufficient heat supply in the regeneration cycle. Improved reverse-flow operation was investigated for the non-oxidative propane dehydrogenation to propene on platinum catalyst combined with coke combustion [31]. The challenges identified are the differences in the velocities of exothermic and endothermic reaction fronts, thus semi-cycles, and unwanted backward reactions due to thermodynamic limitations. The larger velocities of endothermic reaction fronts is well described in Glöckler et al. [32]. Solutions are seen for instance in

asymmetric operation combined with additional heat supply [33, 34].

Another interesting application for reverse-flow operation is the realizing of reduction-oxidation cycles based on the iron ore process [35]. First, the iron is reduced by a lean gas or reformat gas (CO, H_2) in the reduction cycle and in a subsequent regeneration step, the oxidation via water yields highly purified hydrogen, which might be of use for applying in fuel cells [36]. Such a chemical looping is also used for efficient fuel combustion for power generation which becomes attractive due to its intrinsic CO_2 capture [37].

One of the main challenges are instruments for a reasonable fast assessment of such novel reactors for implementation in industry. Exploiting the newly created degrees of freedom efficiently requires research on appropriate tools for reactor design and control. Moreover, experiments with periodic reactors often require nonstandard equipment and time-consuming operation in order to assess periodic settled states. Therefore, to evaluate the potentials of periodic reactors many aspects remain to be investigated, thereby exploiting modern theoretical concepts as well as conducting experiments for proof of concept and validation of appropriate models.

Periodic Operation and Wave Phenomena Unsteady operation is inherently connected with altering reactor states [11, 26, 38], which intuitively makes periodic operation a reasonable process mode. Periodicity is the consequence, if one employs unsteady conditions to the same equipment. It is instructive to classify periodic operation in two instances, periodic input modulation and periodic operation of single or multiple fixed-beds.

Periodic modulation of reactor inputs has shown to improve the conversion and selectivity. Renken [39] and Silveston et al. [40] explored this field considering typical inputs, such as concentration, pressure and temperature. Typically, the inputs are either continuous periodic or employed by so call bang-bang switches between constant values. Recently, a fast method for efficient evaluation of continuous periodic input modulation for ideal reactors was published [41].

Otherwise, periodic operation of fixed-beds exhibits different properties, particularly in multi-bed configurations. Discrete-time switching operations can be seen as immediate changes imposed to the boundaries of the distributed parameter system representing the fixed-beds. Periodicity applies, because the original configuration is always recovered after a certain switching policy. An inherent property are wave phenomena responsible for spatio-temporal transport of heat and mass [42]. Such front phenomena can become considerably complex due to nonlinear coupling introduced by reactions and/or phase equilibria.

Traveling concentration fronts are typically exploited in chromatographic processes, in which components travel with different velocities due to the underlying adsorption equilibria. A multi-bed variant is the simulated moving bed process exploiting a countercurrent switching policy. In this way, accumulation of certain species at withdrawal ports offers an efficient continuous separation process. Applications are found in the petrochemical [43, 44], in the food, and in the pharmaceutical industries [45, 46]. A comprehensive theory for transport in these adsorbers is available [47–49]. It exploits equilibrium theory which allows a simplified description of the nonlinear transport [50].

Concerning heat integration concepts, nonlinear temperature fronts in catalytic fixed-

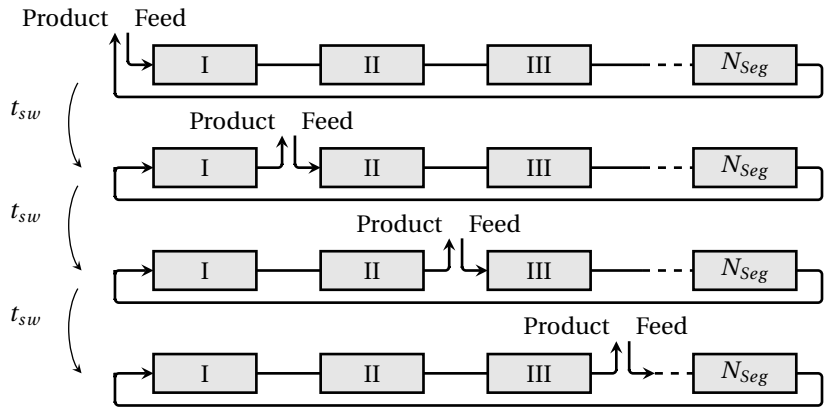

Figure 1.1.: Principle of a periodically operated cascade of N_{Seg} catalytic fixed-bed reactors connected in series, whereby feed and product ports are periodically switched by one segment in the flow direction after the switching time t_{sw}. The operation is based on the principle of a simulated moving bed countercurrent process. In this work it is denoted as SMBR (simulated moving bed reactor).

bed reactors were widely studied [51–53]. In particularly, exothermic reaction fronts can show temperature excursions under transient conditions. This is also well known as the wrong-way behavior [42, 54]. To pick up the reversed-flow principle mentioned above, these accumulation effects in unsteady operation bring an important advantage, as they offer larger temperatures in the same fixed-bed volume compared to steady state operation. The reverse-flow reactor has shown to be an efficient accumulator, however, the slip of unconverted reactants at switching events is a drawback which requires additional measures. An alternative is the circulation loop reactor, which is based on coupling heat exchanger and fixed-bed reactor. It attempts to stabilize autonomously traveling temperature fronts to establish an autothermal process [55]. However, the heat transfer in such heat exchanges is often poor which limits the overall efficiency and may require external energy supply.

In this work it is suggested to exploit the simulated moving bed principle to efficiently accumulate thermal energy for as a heat integration reactor concept. Therefore, in the next section the formation of exothermic reaction fronts and nonlinear accumulation effects in an adiabatic simulated moving bed reactor (SMBR) are considered.

1.2. Adiabatic Simulated Moving Bed Reactor

1.2.1. Reactor Principle

The reactor principle was introduced in theoretical works of Haynes et al. [56], Brinkmann et al. [57] and Sheintuch et al. [58]. Again, the catalytic VOC destruction of larger amounts of diluted waste gases was seen as a possible field of application. Also equilibrium limited reactions, such as the SO_2 oxidation, or the methanol synthesis are seen as potential targets [59–63].

The concept of a periodically operated reactor cascade can be explained supported by figure 1.1. Initially a certain small number of catalytic fixed-beds is assumed (e.g. 2–4), preheated above the ignition temperature. After introducing cold feed a reaction front travels

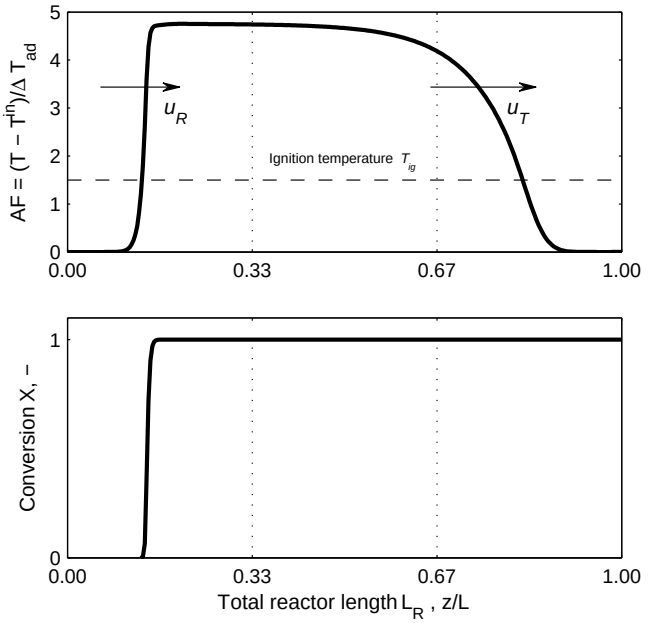

Figure 1.2.: Temperature and conversion profiles in a three bed SMBR unit. The snapshot corresponds to the feed position in front of the first fixed-bed segment at half of the switching period. A fast leading thermal front with a velocity u_T precedes the reaction front traveling with a velocity u_R. The ignition temperature, T_{ig}, indicates the temperatures required for start-up of the reactor.

through the first reactor segment with a characteristic velocity cooling down this segment. After a specific time t_{sw}, a switching shifts feed and product ports by one segment in the gas flow direction. Thereby the cold bed is shifted to the end of the cascade and where it is regenerated.

To maintain successful operation it needs to be assured that the specific ignition temperature is reached again. After several switching events two characteristic fronts have formed, the slower reaction front and a leading thermal front. The periodic switching of ports between the fixed-beds corresponds to the well-known simulated moving bed (SMB) operation [43], because this switching mimics the discrete-time countercurrent movement of the two phases involved. Thus, such an arrangement of several segments resembles a characteristic zone of a chromatographic SMB process, as frequently studied in separation science [45].

The reactor concept will be denoted in this work as an adiabatic simulated moving bed reactor, or in short SMBR, following the notation usually used for simulated moving bed processes [11]. Other research groups use the term "network of reactors" [57] or "loop reactor" [58], which will not be applied in this thesis.

1.2.2. Traveling Fronts and Accumulation of Thermal Energy

A typical snapshot of the temperature and conversion profiles occurring in an adiabatic SMBR are illustrated in figure 1.2.

Typically, two distinct fronts propagate along the fixed-beds in a SMBR, a leading thermal front with a velocity u_T and trailing reaction front with a velocity u_R. Due to the heat accumu-

lation effect, a much larger temperature can be achieved compared to a steady state fixed-bed operation. As a measure of this possible temperature increase the following amplification factor AF can be defined:

$$AF = \frac{T - T^{\text{in}}}{\Delta T_{\text{ad}}} \quad = \quad \frac{\text{unsteady state adiabatic temperature rise}}{\text{steady state adiabatic temperature rise}} \tag{1.1}$$

This factor relates the observed temperature increase under unsteady conditions to the corresponding adiabatic temperature rise ΔT_{ad} valid for steady state operation, which is usually defined as [64, 65]:

$$\Delta T_{\text{ad}} = \frac{(-\Delta H_R) c^{\text{in}}}{(\rho c_p)_g} \tag{1.2}$$

Equation (1.2) describes the temperature rise in an adiabatic system in which a single reactant is completely converted. ΔH_R is the heat of reaction, $(\rho c_p)_g$ the gas phase volumetric heat capacity and c^{in} the inlet or feed concentration of the reactant.

An amplification factor AF of one corresponds to the temperature rise in a steady state fixed-bed reactor. By contrast, periodic reactor operation offers a thermal energy accumulation with amplification factors much larger than one.

1.2.3. Autothermal Operation and Reactor Multiplicities

Autothermal reactor operation is characterized by low, best to say ambient inlet temperatures and a self sustained reaction maintained at much higher temperatures. The conventional solution to this problem is the coupling between the hot effluent stream of an adiabatic fixed-bed reactor and the cold inlet stream via a heat exchanger [66].

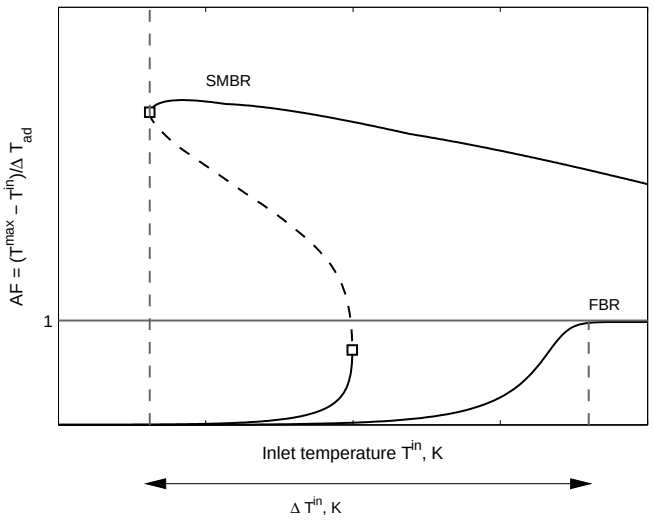

Figure 1.3.: Temperature amplification in steady-state FBR and SMBR. An ignition-extinction hysteresis is generated in the SMBR. The left limit point determines potential for heat integration, as it allows to reduce the inlet temperature T^{in} far below one required to operate the fixed-bed reactor(FBR). The limit points (squares) indicate the domain of multiple reactor states.

It is well known that such a thermal coupling leads to significant parameter sensitivities and reactor multiplicities [67]. Less surprising is the fact, that these phenomena appear in adiabatic simulated moving bed reactors as well. Figure 1.3 explains these reactor multiplicities with a typical ignition-extinction hysteresis, comparing steady state fixed-bed reactor (FBR) with simulated moving bed reactor (SMBR).

The temperature amplification of both reactors is given with respect to the inlet temperature T^{in}. A typical result of the conventional adiabatic FBR is the increase of the maximum reactor temperature according to the adiabatic temperature rise possible ($AF = 1$); in case of an ideal adiabatic FBR the temperature increase is in one-to-one correspondence to the conversion.

In contrast, an ignition-extinction hysteresis appears for the SMBR. Such a hysteresis is an S-shape parameterized solution curve with two turning points framing the region of multiple reactor states (fig. 1.3). High temperature states correspond to *ignited* reactor operation and complete conversion, low temperature (*extinguished*) states show typically no conversion. Thereby an unstable intermediate state separates the stable ones. Consequently, the distance between the limit points determines the range of the multiplicities with respect to the inlet temperature. Regarding the potential for heat integration, the left limit point represents the boundary for a decrease of the inlet temperature to achieve energy savings and to establish an autothermal operation.

Evaluation and process design of an SMBR require a detailed understanding of the multiplicities, as they are key information about achievable heat integration efficiency, design and control of the reactor.

1.3. Motivation and Outline

This work examines the principle of periodic operation using several thermally coupled fixed-bed reactors. Based on the conceptual description above, several problems were identified and investigated. This includes the detailed description of the reactor principle, the development of methods for analysis, reactor control and finally the experimental demonstration. The main part of this work presents results of a theoretical and experimental study for a single irreversible exothermic reaction. As an example the oxidation of a VOC is considered. In addition, the reactor behavior for a mixture of two reactants which are oxidized simultaneously is investigated.

The work is organized as follows. The main properties of the periodic reactor operation are introduced in chapter 2. The individual fronts occurring in SMBR are characterized making use of constant pattern solutions and dynamic simulations. An explicit approximation of the ignition temperature is derived from a simplified isothermal balance. Internal profiles and spatio-temporal pattern are used to explain the SMBR operation. In addition, a comparisons with the competing reverse-flow concept regarding heat integration efficiency and reduction of slip is addressed.

A reduced model to describe the SMBR is derived in chapter 3, namely the hypothetical true moving bed reactor (TMBR) model. This model provides a direct approximation of SMBR reactor states. Convergence of the approximate model is investigated and first parametric

studies are discussed.

Reactor multiplicities are treated in chapter 4. An introduction to nonlinear analysis with basics of the singularity theory are given. It is shown that SMBR and TMBR models describe comparable bifurcation diagrams. A detailed analysis of ignition-extinction phenomena with respect to several parameters is presented and parametric maps for faster assessment of the reactor concept are discussed.

Suitable switching times for the SMBR are limited to a specific range. Therefore, reactor control is required to permanently adjust this control parameter and to maintain ignited states reactor states. In chapter 5 simulation studies for three control concepts are compared and finally evaluated with selected step input experiments. A suitable discrete-time set-point controller is identified and guidelines for its successful parametrization are presented.

The experimental part of this work covers reaction system, SMBR– setup and operation, and control (chapter 6). First, the reaction system is characterized regarding kinetics of the model reactions, i.e. propene/ethene total oxidation in air on a metal oxide catalyst. Thereafter, systematic experiments with a two-bed SMBR unit are presented. The results of the periodic reactor operation are compared with predictions of the parameterized model. Operation in open-loop (prescribing the switching times) as well as in closed-loop control are investigated. The control concept identified in chapter 5 is studied in systematic experiments. Disturbance rejection is evaluated and the oxidation of mixtures present in the SMBR feed is experimentally studied.

Chapter 7 generalizes the reactor operation for cases if feed mixtures of two different VOC with different oxidation rates are applied. The analysis makes particularly use of nonlinear analysis which offers insight into conversion and temperature regimes. These can significantly differ from the single component system. Essential measures for the reactor operation are deduced.

Several appendices provide detailed information regarding important aspects not discussed in depth in the main part of this thesis.

2. Traveling Fronts in Single Fixed-Beds and Simulated Moving Bed Reactors

A phenomenological description of front propagating in catalytic fixed-bed reactors is required to understand control of patterns in simulated moving bed reactors. For this reason, this chapter starts with the characterization of exothermic fronts and corresponding sensitivity towards selected process parameters. The simultaneous movement of two fronts, an exothermic and a thermal front is examined as an introduction to the SMBR concept. This is followed by a detailed characterization of the reactor principle regarding profiles, reactor outlets and spatio-temporal pattern. Finally the SMBR and is compared with the classical reverse-flow reactor based on dynamic simulations. Documentation of the models introduced and the numerical solution methods applied is given in appendix B.

2.1. Characterization of Fronts

2.1.1. Simple Thermal Fronts

The propagation of a temperature disturbance in a fixed-bed can be approximated by a pseudo-homogeneous energy balance (2.1) (see appendix D.1 for the derivation of a one-dimensional pseudo-homogeneous continuum models):

$$\left(\varepsilon(\rho c_p)_g + (1-\varepsilon)(\rho c_p)_s\right)\frac{\partial T}{\partial t} = -\varepsilon(\rho c_p)_g u_g^* \frac{\partial T}{\partial z} \tag{2.1}$$

$$\text{or} \qquad (\rho c_p)_m \frac{\partial T}{\partial t} = -\varepsilon(\rho c_p)_g u_g^* \frac{\partial T}{\partial z} \tag{2.2}$$

In equation (2.2) the individual heat capacities of solid and fluid phase are collected in a mixed capacity $(\rho c_p)_m$. Thereby ε denotes the void fraction as the ratio between fluid to total volume $\varepsilon = V_g/(V_g+V_s)$ and u_g^* an interstitial gas phase velocity assumed to be constant. The hyperbolic transport problem can be solved for given initial condition (IC) and boundary condition (BC) [68, 69]:

$$IC: \qquad T(z,0) = T^{\text{init}} \qquad BC: \qquad T(0,t) = T^{\text{in}} \tag{2.3}$$

$$T(z,t) = T^{\text{init}}(z - u_T t) \qquad \text{with } u_T = \frac{\varepsilon(\rho c_p)_g}{(\rho c_p)_m} u_g^* \tag{2.4}$$

This means, that temperature disturbances are propagating with the constant front velocity u_T. A comprehensive theory of such hyperbolic problems is available [47]. Another illustrative

way to derive the thermal front velocity, u_T, is given with the following manipulations,

$$-\frac{\partial T/\partial t}{\partial T/\partial z} = \frac{\varepsilon(\rho c_p)_g}{(\rho c_p)_m} u_g \qquad \text{yielding: } -\left.\frac{\partial z}{\partial t}\right|_T = u_T = \frac{\varepsilon(\rho c_p)_g}{(\rho c_p)_m} u_g^* \tag{2.5}$$

which is the same as (2.3) just derived from the energy balance. In this work a Lewis-number, Le_1, relating the heat capacity of the solid phase to that of the gas phase according to equation (2.6) is suggested. Since $(\rho c_p)_g \ll (\rho c_p)_m$, it holds that:

$$Le_1 = \frac{(\rho c_p)_m}{\varepsilon(\rho c_p)_g} \approx \frac{(1-\varepsilon)(\rho c_p)_s}{\varepsilon(\rho c_p)_g} \tag{2.6}$$

Consequently, the thermal front velocity u_T can be defined as:

$$u_T = \frac{1}{Le_1} u_g^* \tag{2.7}$$

A thermal non-reactive front propagates with a reduced velocity compared to the gas velocity with the proportionality of $1/Le_1$. Generally, the volumetric heat capacity of the gas phase is by orders of magnitude smaller than that of the solid catalyst phase, thus Lewis numbers of 500 to above 1000 are common values for catalytic fixed-beds. As a consequence, thermal fronts are remarkably slow compared to the transport of concentration disturbances, which are carried along with the gas phase velocity if adsorption can be neglected. This picture changes in liquid-solid fixed-beds significantly, in which a much larger density of the liquid phase leads to similar velocities of the concentration fronts compared to thermal fronts.

Dispersive Thermal Fronts Additional consideration of the fixed-bed heat conduction, λ, in the energy balances yields a dispersive model for the energy transport:

$$(\rho c_p)_m \frac{\partial T}{\partial t} = -\varepsilon(\rho c_p)_g u_g^* \frac{\partial T}{\partial z} + \lambda \frac{\partial^2 T}{\partial z^2} \tag{2.8}$$

Such dispersive fronts are characterized by a permanent reduction of the maximum temperature due to the smearing of temperature profiles, albeit the mean velocity corresponds to that of the thermal front (eq. (2.7)) presuming typical values of fixed-bed heat conduction. An analytical solution is available for an open-open system analogous to the axial dispersion model [65].

2.1.2. Exothermic Reaction Fronts

The problem becomes more complex in case of exothermic reaction fronts traveling under adiabatic conditions. This is due to the strong coupling between the mass and energy balances via the exponential Arrhenius temperature dependence of the reaction rate. Fundamental work on heat transfer and traveling reaction fronts was done by several Russian researchers [53, 70] , and at the same time in Germany by Wicke et al. [51].

Here, two approaches are presented for the derivation of the relation between maximum temperature and front velocity. The starting point is the energy balance in temperature

form and a pseudo-homogeneous mass balance thereby neglecting mass accumulation. The presence of an exothermic reaction with the reaction rate $r(c_i, T)$ and a stoichiometric coefficients of $\nu_i = -1$ is assumed.

$$(\rho c_p)_m \frac{\partial T}{\partial t} + \varepsilon (\rho c_p)_g u_g^* \frac{\partial T}{\partial z} = (-\Delta H_R) r(c_i, T) \tag{2.9}$$

$$\varepsilon u_g^* \frac{\partial c_i}{\partial z} = \nu_i r(c_i, T) \tag{2.10}$$

In equation (2.10) the accumulation of mass is omitted, which is justified due to the dominant capacity term of the thermal energy balance. The mass hold-up is small due to the gas phase density.

Elimination of the reaction rate via substitution yields the following balance:

$$(\rho c_p)_m \frac{\partial T}{\partial t} + \varepsilon (\rho c_p)_g u_g^* \frac{\partial T}{\partial z} = \frac{(-\Delta H_R)}{\nu_i} \varepsilon u_g^* \frac{\partial c_i}{\partial z} \tag{2.11}$$

By expansion with $\partial z / \partial T$ it is possible to derive an equation describing wave phenomena with a characteristic velocity of the reaction front u_R:

$$-\frac{\partial T / \partial t}{\partial T / \partial z} = -\frac{\mathrm{d}z}{\mathrm{d}t}\Big|_T = u_R \tag{2.12}$$

Which yields:

$$-(\rho c_p)_m \frac{\mathrm{d}z}{\mathrm{d}t}\Big|_T + \varepsilon (\rho c_p)_g u_g^* = \frac{(-\Delta H_R)}{\nu_i} \varepsilon u_g^* \frac{\mathrm{d}c_i}{\mathrm{d}T} \tag{2.13}$$

Integration along the reaction front assuming total conversion, thus between $c^{\mathrm{in}} \dots c^{\mathrm{out}} = 0$ and $T^{\mathrm{in}} \dots T^{\max}$, gives:

$$-Le_1 \cdot u_R + u_g^* = u_g^* \frac{\Delta T_{\mathrm{ad}}}{\Delta T} \tag{2.14}$$

and for the reaction front velocity u_R:

$$u_R = \left(1 - \frac{\Delta T_{\mathrm{ad}}}{\Delta T}\right) u_T \tag{2.15}$$

ΔT_{ad} is the adiabatic temperature rise and ΔT is the temperature difference between the base point, the inlet temperature, and the maximum temperature of the front ($\Delta T = T^{\max} - T^{\mathrm{in}}$).

An alternative derivation can be based on a transformation into coordinates moving with the reaction front velocity u_R. The new variables are:

$$t = \acute{t} \qquad \text{and} \qquad \zeta = z - u_R t \tag{2.16}$$

with the following coordinate transformations applied [47]:

$$\frac{\partial T}{\partial t} = \frac{\partial T}{\partial t}\frac{\partial t}{\partial t} + \frac{\partial T}{\partial \zeta}\frac{\partial \zeta}{\partial t} = -u_R \frac{\partial T}{\partial \zeta} \tag{2.17}$$

$$\frac{\partial T}{\partial z} = \frac{\partial T}{\partial t}\frac{\partial t}{\partial z} + \frac{\partial T}{\partial \zeta}\frac{\partial \zeta}{\partial z} = \frac{\partial T}{\partial \zeta} \tag{2.18}$$

one obtains the following system of ordinary differential equations:

$$-u_R(\rho c_p)_m \frac{\mathrm{d}T}{\mathrm{d}\zeta} + \varepsilon(\rho c_p)_g u_g^* \frac{\mathrm{d}T}{\mathrm{d}\zeta} = (-\Delta H_R) r(c_i, T) \tag{2.19}$$

$$\varepsilon u_g^* \frac{\mathrm{d}c_i}{\mathrm{d}\zeta} = \nu_i r(c_i, T) \tag{2.20}$$

Again, by substitution one arrives at an equation describing energy transport on the left hand side and the source of thermal energy on the right hand side:

$$\left(u_g^* \varepsilon(\rho c_p)_g - u_R(\rho c_p)_m\right)\frac{\mathrm{d}T}{\mathrm{d}\zeta} = \frac{(-\Delta H_R)\varepsilon u_g^*}{\nu_i}\frac{\mathrm{d}c_i}{\mathrm{d}\zeta} \tag{2.21}$$

By integration over the front in the limits between T^{in} and T^{max}, and c^{in} and c^{out}, one obtains:

$$\left(\varepsilon u_g^*(\rho c_p)_g - u_R(\rho c_p)_m\right)\Delta T = (-\Delta H_R)\varepsilon u_g^* c^{\mathrm{in}} \tag{2.22}$$

$$\left(\varepsilon u_g^* - u_R Le_1\right)\Delta T = \Delta T_{\mathrm{ad}} \varepsilon u_g^* \tag{2.23}$$

$$(u_T - u_R)\,\Delta T = \Delta T_{\mathrm{ad}} u_T \tag{2.24}$$

Hence equation (2.15) is recovered and the front velocity depends on the maximum temperature and vice versa according to [17]:

$$u_R = \left(1 - \frac{\Delta T_{\mathrm{ad}}}{\Delta T}\right) u_T \qquad \text{or} \qquad \Delta T = \Delta T_{\mathrm{ad}} \frac{u_T}{u_T - u_R} \tag{2.25}$$

Equation (2.25) is valid for an ideal moving exothermic reaction front. Any disturbance at the reactor inlet, for instance in the inlet temperature, the inlet concentration or total flow rate, can result in transient response of the reaction front in accordance with (2.25).

Figure 2.1 illustrates equation (2.25) for the range of interest in this work by relating the temperature amplification AF to the velocity ratio u_R/u_T.

In steady state, $u_R = 0$, the temperature equals that of the adiabatic temperature rise ($AF = 1$). The reaction front is pushed for instance towards the reactor outlet with a positive velocity $u_R > 0$, when the flow rate is increased (gas velocity u_g^*). As a result, the front temperature rises above the adiabatic temperature rise ($AF > 1$). Note, that the front does not necessarily leave the reactor, but can reach a new steady state still located inside the adiabatic fixed-bed. In case of such an downstream moving front, the temporal increase of the temperature can be explained with the larger amounts of reactants transported to the front, while convective energy transport is not yet adjusted to the increased amount of heat liberated. For that reason, the heat liberated can only accumulate within a smaller portion of

the fixed bed resulting in larger maximum temperatures.

Conversely, lower transient front temperatures are possible as well. For instance, after lowering the inlet flow rate the reaction front moves to the reactor entrance ($u_R < 0$). This time, the heat liberated is distributed over a larger portion of the fixed bed resulting in lower transient maximum temperatures ($AF < 1$).

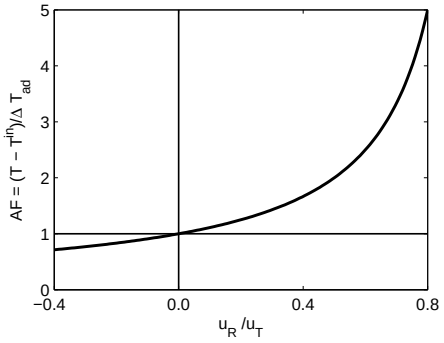

Figure 2.1.: Temperature amplification of an ideal exothermic reaction front.

A singular solution of equation (2.25) exists for $u_R = u_T$. In this situation convective energy transport equals that of the reaction front velocity, which ultimately leads to an infinite increase of the maximum temperature ($u_R/u_T = 1$). However, other factors not considered in the idealized picture, such as heat conduction and heat losses, will become prevalent and limit the maximum temperature to realistic values.

A similar analysis is available for gas-solid reaction being relevant for e.g. coke combustion [17]. Typically, these approximate solution are a good starting point for the evaluation of process condition regarding safety and the magnitude of temperature excursions.

2.1.3. The Constant Pattern of an Exothermic Reaction Front

The problem with the estimation of the maximum temperature with equation (2.25) is the implicit form – either one observes a temperature peak and derive the front velocity, or conversely, the front velocity is known and the temperature maximum can be predicted. Typically u_R is not available directly and one has to solve the dynamic reactor model, i.e. equations (2.9) and (2.10). An alternative description is the constant pattern solution of a reaction front.

A constant pattern state of a front can emerge in a sufficiently long spatial domain, in which the front travels self-preserving without loosing shape. With this assumption, a dispersive front alone (eq. (2.8)) cannot exhibit a constant pattern state, unless a self-sharpening behavior is introduced. In the present case, the heat liberated by the exothermic reaction represents such an effect, which counteracts heat dispersion in the catalytic fixed-bed. The self-sharpening of fronts is also well known phenomena in fixed-bed adsorber [48, 71].

Table 2.1.: Parameter for the constant pattern example representing a typical total oxidation system.

E_a	$1.3 \cdot 10^5$ J/mol	k_0	$1.4 \cdot 10^{10}$ s^{-1}
ΔH_R	−2000 kJ/mol	$(\rho c_p)_g$	1 kJ/kg K
u_g	1 m/s	$(\rho c_p)_m$	1400 kJ/kg K
T^{in}	300 K		

The description of the constant pattern solution presumes a reaction front propagating with a constant velocity u_R on an infinitely large spatial domain. As a starting point the

pseudo-homogeneous reactor model incorporating axial heat conduction is considered.

$$(\rho c_p)_m \frac{\partial T}{\partial t} + \varepsilon (\rho c_p)_g u_g^* \frac{\partial T}{\partial z} = \lambda \frac{\partial^2 T}{\partial z^2} + (-\Delta H_R) r(c_i, T) \tag{2.26}$$

$$\varepsilon u_g^* \frac{\partial c_i}{\partial z} = \nu_i r(c_i, T) \tag{2.27}$$

With following boundary (BC) and initial conditions (IC):

$$BC: \qquad z = 0: \qquad 0 = \varepsilon (\rho c_p)_g u_g^* (T^0 - T^{\text{in}}) - \lambda \frac{\partial T}{\partial z}|_{z=0} \qquad c_i^0 = c_i^{\text{in}} \tag{2.28}$$

$$z = L: \qquad 0 = \frac{\partial T}{\partial z} \tag{2.29}$$

$$IC: \qquad c_i(z, t=0) = c_i^{\text{init}}(z) \qquad T(z, t=0) = T^{\text{init}}(z) \tag{2.30}$$

A single first order reaction and the Arrhenius temperature dependence is assumed [66].

$$r(c_i, T) = k_0 \exp\left(\frac{E_a}{\mathrm{R_g} T}\right) c_i \qquad \nu = -1 \tag{2.31}$$

By transformation into a moving coordinate system propagating with the velocity of the reaction front, the system of partial differential equations is reduced to a system of ordinary equations of second order [72, 73]:

$$0 = -\left(\varepsilon (\rho c_p)_g u_g^* - u_R (\rho c_p)_m\right) \frac{\mathrm{d}T}{\mathrm{d}\zeta} + \lambda \frac{\mathrm{d}^2 T}{\mathrm{d}\zeta^2} + (-\Delta H_R) r(c_i, T) \tag{2.32}$$

$$0 = -\varepsilon u_g^* \frac{\mathrm{d}c_i}{\mathrm{d}\zeta} + \nu_i r(c_i, T) \tag{2.33}$$

$$\zeta \to -\infty \qquad T \to T^{\text{in}} \qquad c_i \to c_i^{\text{in}}; \qquad \zeta \to +\infty \qquad \frac{\mathrm{d}T}{\mathrm{d}\zeta} = 0 \tag{2.34}$$

The front velocity, u_R, is still unknown and the problem can be solved using the shooting method [74]. Another approach is used in this work in accordance to the suggestion made by Mangold [72]: u_R is treated as a variable and therefore implemented in the equation system using an additional equation, $c(\zeta = 0) = 0.5c^{\text{in}}$, fixing the front in the origin. Additionally, a large but finite spatial domain, ζ, must be provided to find a numerical solution. After discretization of the spatial coordinate the large nonlinear system of equation can be solved with standard Newton-type solvers [75–77]. Still the problem is lacking an easy numerical treatment due to the large sensitivity towards the initial values, in particular to the unknown front velocity u_R. A good approach is to generate initial values based on the solution of the corresponding dynamic problem. Then, by starting from a single constant pattern solution it is strait forward to study ranges of the parameters of interest.

This includes the gas velocity u_g^*, the inlet temperature T^{in}, the fixed-bed heat conduction, λ, pre-exponential factor, k_0, and the inlet concentration c^{in}. Below, the impact on the reaction front is illustrated with the help of the temperature front along ξ, the maximum temperature $T^{\max}$ and the front velocity u_R along the respective parameter. Table 2.1 summarizes the standard parameters used. Unless otherwise noted, a constant low inlet temperature of

300 K was assumed.

Gas Phase Velocity The influence of the gas velocity is illustrated in figure 2.2. Maximum temperature and shape of the front are largely affected. With increasing flow rates the front becomes much steeper and faster. Pushing forward the front results in a substantial increase in the temperature, thereby velocities of gas and reaction front are in almost linear relation.

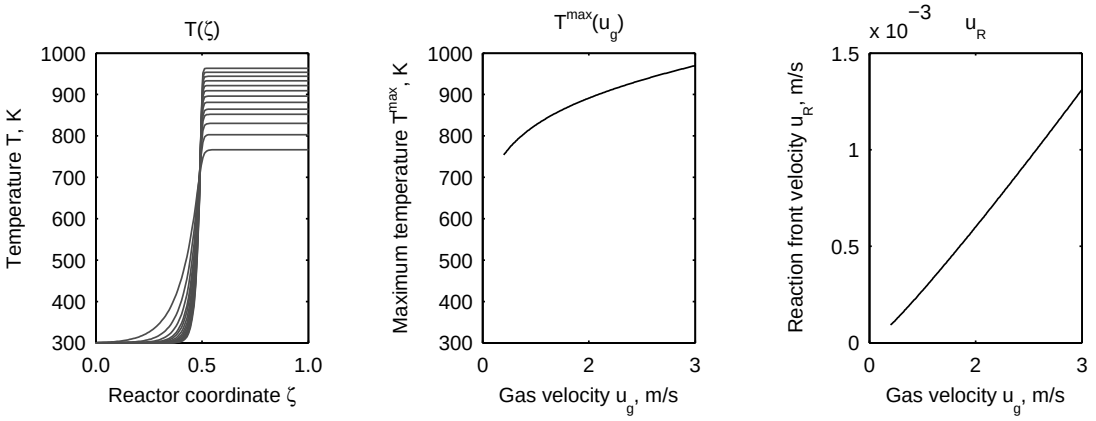

Figure 2.2.: Influence of the gas velocity u_g on the exothermic reaction front. Temperature and front velocity increase with u_g (Constant pattern model with parameters listed in table 2.1).

The maximum temperature is not limited to a certain high value, because transporting larger amounts of the reactant to the front can only result in a further temperature increase. However, the pressure drop would be a limiting factor in real fixed-beds, neglected in the present analysis though. Very small flow rates do not provide a constant pattern solution at all.

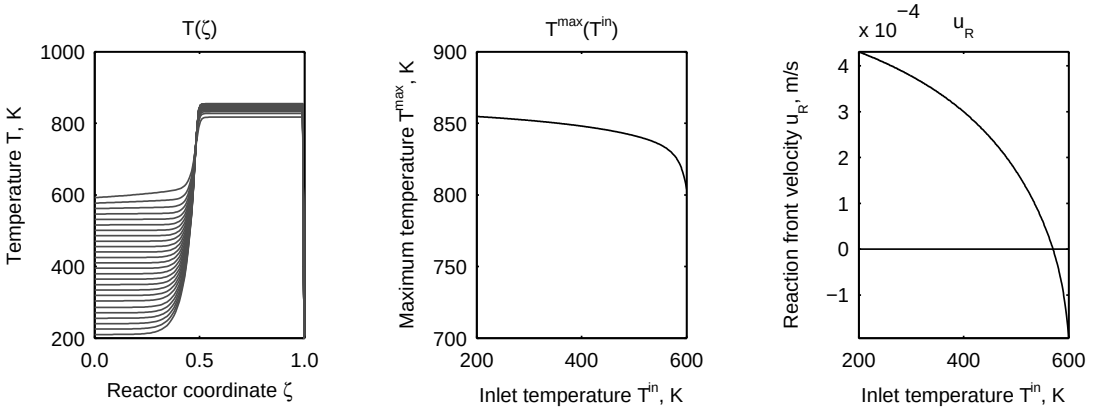

Figure 2.3.: Influence of the inlet temperature T^{in} on the exothermic reaction front. Temperature and velocity decrease with T^{in} (Constant pattern model with parameters listed in table 2.1).

Inlet Temperature Increasing the inlet temperature has no significant effect on the maximum front temperature, until the difference between maximum temperature and inlet temperature equals that of the adiabatic temperature rise (fig. 2.3). This result is important to understand, because it explains the low sensitivity of the reaction fronts w.r.t the inlet temperature over a wide range.

As shown in the figure right, the reaction front velocity decreases even below unity, which means a backward movement of the reaction front. However, the constant pattern solution does not exists any longer for larger inlet temperatures. In fact, the boundary conditions of the constant pattern implemented in the finite domain is violated in this case.

Heat Conduction In figure 2.4 is presented the influence of the bed heat conductivity on the constant pattern solution. Lowering the bed heat conductivity significantly increases

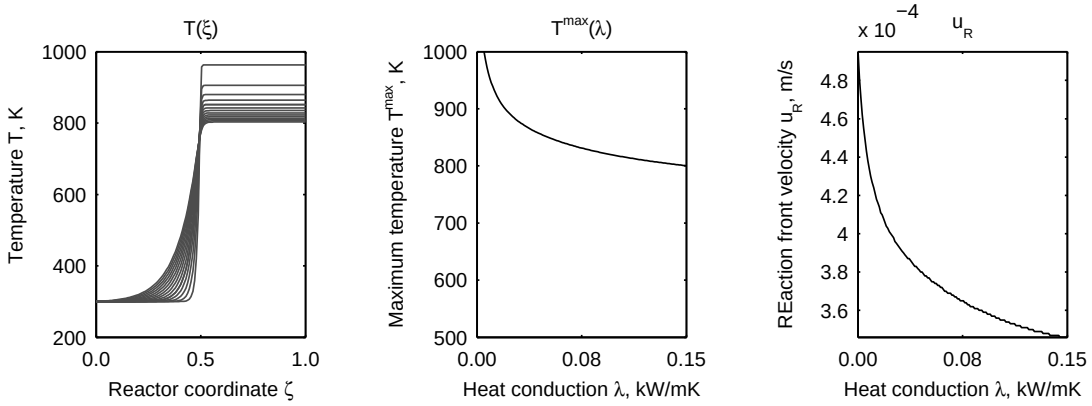

Figure 2.4.: Influence of the fixed-bed heat conductivity on the exothermic reaction front. Temperature and velocity decrease with λ (Constant pattern model with parameters listed in table 2.1).

the front maximum temperature, the steepness and the reaction front velocity. The ideal situation of a dispersive free constant pattern front cannot be represented by the numerical scheme used and very low, as well as lager value cause numerical problems, which can be attributed to the violation of the inlet boundary condition.

Reaction Rate The next example deals with the reaction rate constant, which was studied by changing the pre-exponential factor k_0 at a constant activation energy (fig. 2.5). As the rate increases, the reaction front slows down and the reactor temperature decrease. The sensitivity with respect to the maximum temperature decreases significantly. However, a minimal reactor temperature could not be determined and front velocity as well as maximum temperature decrease in a logarithmic manner.

By contrast, the front temperature increases if the pre-exponential factor is lowered and at a specific limit the exothermic front collapses. This fact will be explained thoroughly as part of reactor multiplicity in chapter 4.

Inlet Concentration Increasing the inlet concentration sharpens the front and leads to a moderate increase in the maximum temperature (fig. 2.6). At larger feed concentrations, the

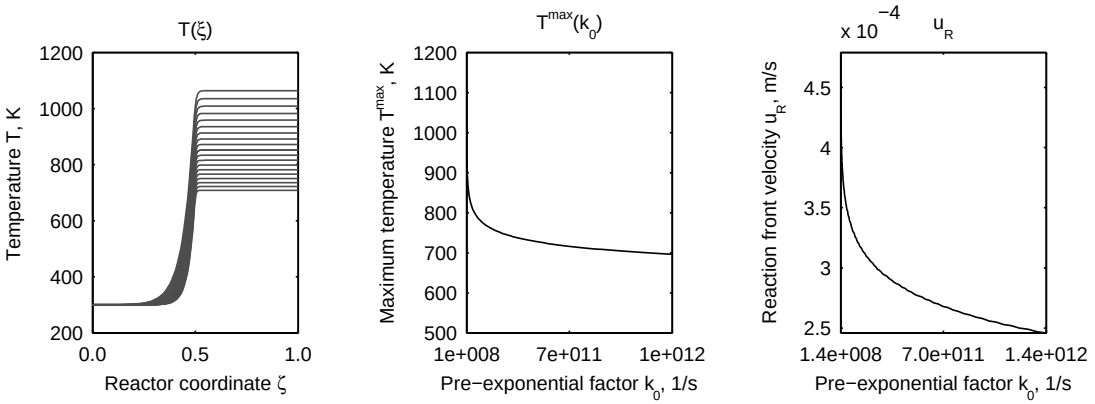

Figure 2.5.: Influence of the pre-exponential factor on the exothermic reaction front. Temperature and velocity decrease with k_0 (Constant pattern model with parameters listed in table 2.1)

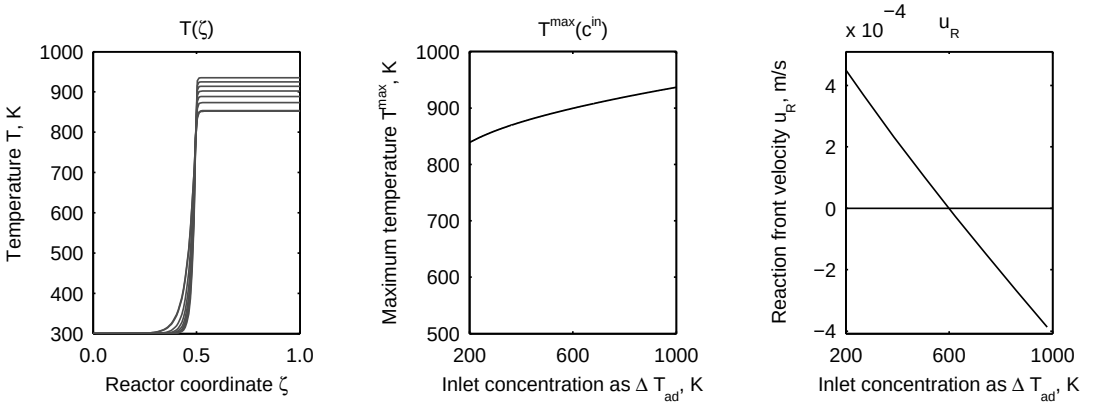

Figure 2.6.: Influence of the inlet concentration on the exothermic reaction front. Temperature increase with c^{in} and front velocity decreases. Even negative velocities are possible meaning backward moving reaction fronts (Constant pattern model with parameters listed in table 2.1).

front velocity decreases below zero. This is why a standing reaction front or even backward moving fronts can form. Remind the relation of the ideal front velocity in figure 2.1, for the case $u_R/u_T < 0$, then $AF < 1$. This is achieved for very large inlet concentrations, at which the adiabatic temperature rise (ΔT_{ad}) exceeds the maximum temperature difference (ΔT) for a specific inlet temperature. Thus, the backward movement sets in for concentrations corresponding to temperature rises above 600 K in the present example.

The analysis of the constant pattern solution has shown the self-sharpening character of the exothermic reaction front. Shape, maximum temperature and front velocity differ significantly as parameters are altered. Though existence of the constant pattern is not guaranteed for all parameter sets. The representation of the front properties is also restricted to isolated fronts without interaction with boundaries. As such, the approach can only be applied for qualitative analysis of reaction fronts, but alternatives are needed to describe all features of the SMBR process. This can be achieved with the representation of the front dynamics offering of comprehensive picture of the switched SMBR.

2.2. Ignition Conditions and Dynamics of Fronts

This section deals with the dynamics of the two fronts involved, namely the reaction and the thermal front. A special focus is set on the temperature level which is required to initiate exothermic reaction fronts. In particular, this level should exceed a specific ignition temperature. An estimation for this ignition temperature is derived, which will be picked up in the following chapters. The dynamics of the reaction and thermal fronts are introduced with illustrative examples, the wrong-way behavior and the transport of temperature pulses.

2.2.1. Estimation of Ignition Temperatures

The ignition temperature is often discussed in connection with autoignition of chemicals, which above a certain temperature ignite and decompose without external heat supply. These aspects are treated in comprehensive works on combustion [78–80] and on process safety the work by Stoessel [81] can be recommended. The fundamentals of the problem were grounded by Semenov and later extended by Frank-Kamenetzki [70]. They developed the explosion theory which can be applied to assess safety criteria in batch reactors and chemical storage systems.

In this work it is shown that an estimate for the ignition temperature in fixed-bed reactors can be derived from a simplified isothermal reactor balance. In addition, an alternative non-isothermal approach based on the explosion theory is discussed in the appendix A.

Isothermal Approach with Zeroth Order Reaction In contrast to the classical approach for a first approximation isothermal behavior is assumed. The reactor balance reads for a zeroth order reaction:

$$u_g \frac{\mathrm{d}c}{\mathrm{d}z} = -k^{(0)}(T) \tag{2.35}$$

with $k^{(0)}(T)$ the reaction rate constant of the zeroth order reaction in $\mathrm{mol/m^3 s}$. Integration over the reactor length L and in the concentration limits between the inlet and a specific outlet concentration c^{out} yields:

$$\frac{L_R}{u_g} = -\frac{1}{k^{(0)}(T)} \left(c^{\mathrm{out}} - c^{\mathrm{in}} \right) \tag{2.36}$$

To derive an explicit expression for the ignition temperature, the following modifications are considered. The reaction rate constant $k^{(0)}(T)$ is replaced by an initial reaction rate of a first order reaction by including the inlet concentration c^{in}:

$$k^{(0)}(T) = k(T) c^{\mathrm{in}} = k_0 \exp\left(-\frac{E_a}{\mathrm{R_g} T} \right) c^{\mathrm{in}} \tag{2.37}$$

The first order rate is defined in $1/\mathrm{s}$ and k_0 is the corresponding pre-exponential factor of the Arrhenius equation. If complete conversion for a specific ignition temperature is presumed,

the concentration c^{out} can be eliminated and one arrives at the following expression:

$$\frac{L_R}{u_g} = \frac{1}{k_0 \exp\left(-\frac{E_a}{\mathrm{R_g} T_{\mathrm{ig}}}\right)} \tag{2.38}$$

In this way, two characteristic time scales have been obtained, a residence time of the gas phase, τ_g, and a characteristic reaction time, τ_R:

$$\tau_g = \frac{L_R}{u_g} \qquad \tau_R = \frac{1}{k(T)} \tag{2.39}$$

Matching these characteristic times, $\tau_g = \tau_R$, provides an explicit equation to estimate the ignition temperature:

$$T_{\mathrm{ig}} = \frac{E_a}{\mathrm{R_g} \ln\left(\frac{L_R k_0}{u_g}\right)} \tag{2.40}$$

Figure 2.7 left illustrates the relation between the ignition temperature and the pre-exponential factor. A decrease in the rate constant leads to much larger ignition temperatures presuming a constant activation energy.

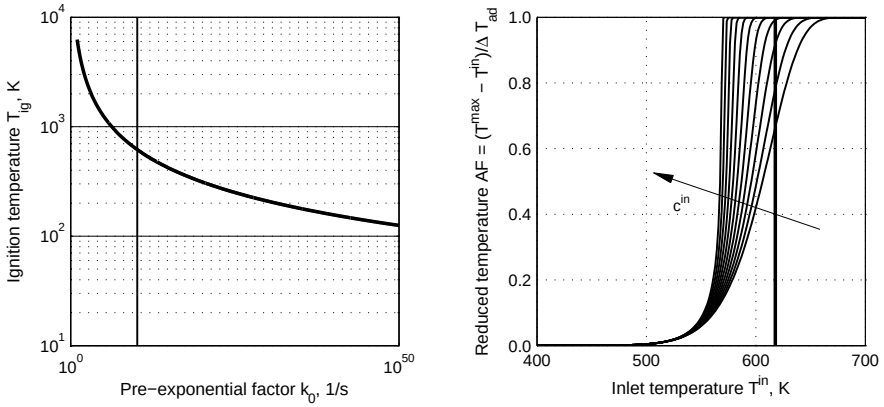

Figure 2.7.: Left: Ignition temperature proportionality to $1/\log(k_0)$, and the case investigated (vertical line). Right: A family of curves relating maximum temperatures to the inlet temperature in a steady state FBR for increasing feed concentrations in the range ΔT_{ad} =1, 20, 40...220 K.

Figure 2.7 right illustrates the reduced maximum temperatures (conversion, respectively) of a steady state non-isothermal adiabatic fixed-bed reactor with a first order kinetic for a range of inlet temperatures (eq. (A.32), (A.32)). Such a curve has already been introduced in figure 1.3 and is given in terms of the amplification factor (eq. (1.1)). Several curves for different feed concentrations are presented. A typical effect of steady state adiabatic fixed-bed reactors is, that larger sensitivities with respect to inlet temperature occur with increasing feed concentrations. As a consequence, complete conversion is already achieved at significantly lower inlet temperatures than estimated with the ignition temperature (T_{ig} – vertical line, fig. 2.7).

In case that for the isothermal system the inlet temperature equals the ignition temperature, the conversion can also be given explicitly for the isothermal reactor. The analytical solution reads:

$$\frac{c}{c^{\text{in}}} = \exp\left(-\frac{z}{u_g}k(T)\right) \tag{2.41}$$

In (2.41), z is the reactor coordinate and $k(T)$ the rate constant for a first order reaction. At $z = L$ the argument of the exponential becomes one and the conversion, defined as:

$$X = 1 - \frac{c^{\text{in}}}{c} \tag{2.42}$$

, assumes a specific value of 0.6322:

$$X = 1 - \frac{1}{\exp\left(\tau_g/\tau_R\right)} = 1 - \frac{1}{\exp(1)} = \frac{\exp - 1}{\exp} = e^* = 0.63212 \tag{2.43}$$

This result means, that in case of a first order reaction an ideal adiabatic fixed-bed reactor has a at least a conversion of 0.6322, if the inlet temperature is set to the ignition temperature defined by equation (2.40). This statement is more applicable for diluted feed, $c^{\text{in}} \to 0$, because the reactor performs isothermal with minimal liberation of thermal energy of the exothermic reaction. With increasing inlet concentrations, the conversion increases as well in the adiabatic system. This means, that the ignition temperature estimated with the isothermal approach gives a lower limit required to start the reaction. It should be noted that the minimal conversion, e^*, corresponds to the first moment of the concentration profile. This results can be obtained when applying the method of moments [65].

In order to take into account non-isothermal effects another approach is investigated in appendix A. The analysis is based on the energy balance and simplifications originating from explosion theory. It is shown that a similar estimate for the ignition temperature applies, though augmented to include the sensitivity with respect to the inlet concentration.

2.2.2. Wrong-Way Behavior

One of the most prominent dynamic phenomena is the so called *wrong-way* behavior in adiabatic catalytic fixed-bed reactors [54, 82]. An example is presented in figure 2.8. After a sudden reduction in the inlet temperature a reaction front may form propagating downstream with a temperature peak larger than that in steady state. This certainly led to the name. Unfortunately, such high temperatures can cause catalyst deactivation, which as a result can lead to even higher temperatures and thermal runaway situations. This can be effectively counteracted by switching to inert gas, although the main problem seems to be the lack of enough sensors distributed in the fixed-bed detecting such temperature fronts.

The initial steady state in figure 2.8 right shows complete conversion which is typically found for inlet temperatures close to the ignition temperature. As a response to a small reduction in the inlet temperature, a traveling front characterized by much larger maximum temperatures forms. The high temperature front leaves the reactor and a new steady state

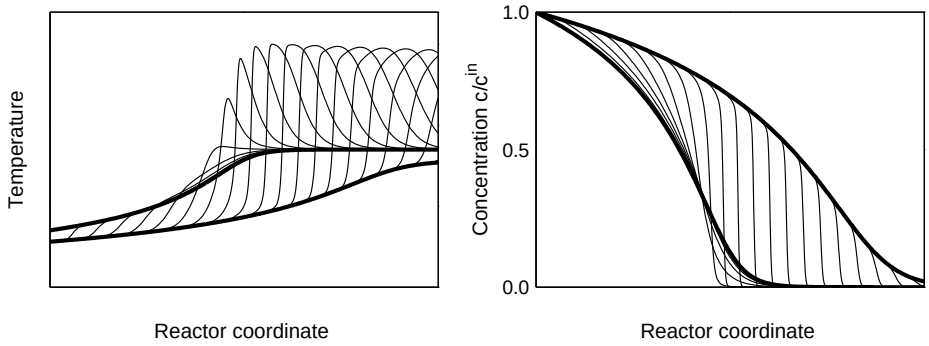

Figure 2.8.: Wrong-Way behavior after immediate reduction of the inlet temperature in the vicinity of the ignition temperature. Left shows the temperature fronts evolving from a high temperature steady-state profile with significant temperature excursions to a state at a lower temperature. Right figure shows the corresponding concentration profiles (parameters in table 2.1).

at still high conversion is attained. Of course, if the inlet temperature is set to much smaller values, the reaction front would leave the reactor which as a consequence extinguishes. Such transient temperature responses with moving hot spots are nowadays well understood and described in the literature [54, 82–87].

2.2.3. The Propagating Temperature Pulse

The ideas closely related to the SMBR concept can be illustrated by assuming a small portion of the catalytic fixed-bed heated up to a certain initial temperature. This situation can be approximated by a rectangular temperature pulse. In figure 2.9 the propagation of such a pulse is investigated for three examples:

- an initial temperature below the ignition temperature $T^{\text{init}} < T_{\text{ig}}$,
- an initial temperature above the ignition temperature $T^{\text{init}} > T_{\text{ig}}$,
- an initial temperature above the maximum temperature under transient conditions $T^{\text{init}} > T^{\max}$.

The figure shows snapshots of the temperature and concentration profiles. In the first case the initial temperature is not high enough to initiate the reaction and the pulse is dispersed away with a significant decline in the maximum temperature and a velocities according to a thermal front (u_T, eq. (2.7)).

If the initial temperature pulse has a sufficient height to generate conversion and heat release, case (2), a slow moving reaction front emerges with a velocity u_R and the leading thermal front with u_T, thereby $u_R < u_T$. Note, that total conversion is not achieved in the initial time step, but when the reaction front has gained height and constant pattern behavior.

The last example shows the relaxation of the pulse into the moving ignited pulse in case of an even higher initial temperature, which shows maximum temperature similar to case (2).

It must be stressed, that the width of the initial pulse has an effect on the formation and existence of the exothermic reaction front. For a certain small width of the rectangular initial

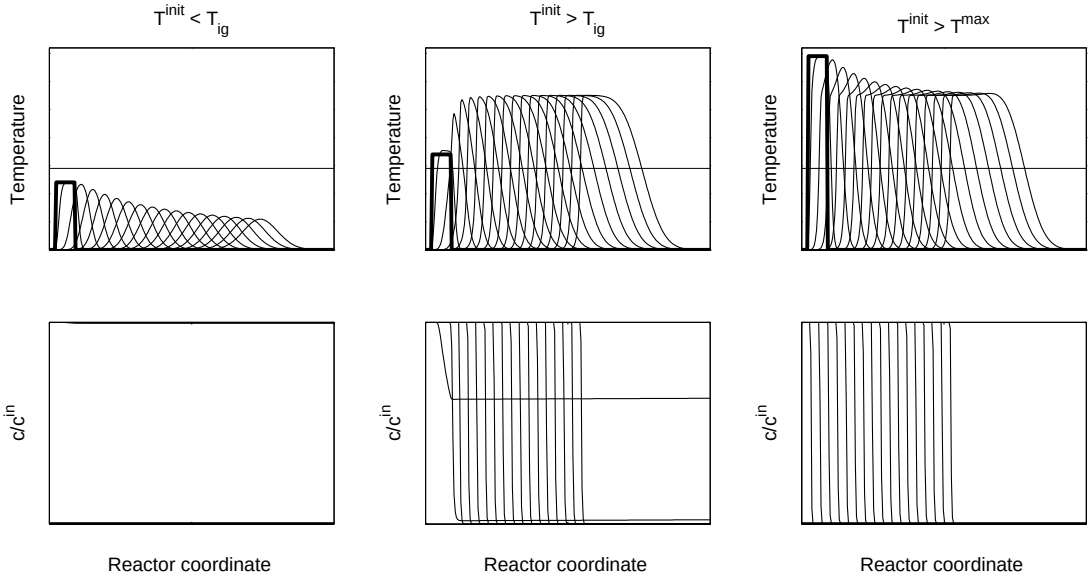

Figure 2.9.: Propagation of a temperature pulse with different initial temperatures. Left, below the ignition temperature the pulse disperses away at zero conversion. Middle, above the ignition temperature a developing reaction front with complete conversion evolves and right, above the maximum temperature complete conversion is achieved from the start on (The horizontal lines correspond to the ignition temperature T_{ig}). Stabilizing such a pulse in an SMBR is illustrated in figures 1.2 and 2.10.

pulse it becomes increasingly difficult to ignite the front and the pulse disperses away. To a certain extend this can be compensated by selecting higher initial temperatures. One reason for this dependency is the dispersive transport, which is scale dependent and thus increasingly important for small pulse widths.

In the example above, the moving hot zone shows a leading thermal front and a trailing reaction front. On an unbounded domain a permanent broadening of the pulse would be observed, which is certainly an unrealistic scenario. Trapping such a pulse in a real cascade of fixed-bed is investigated in the next section.

2.3. Fronts in Simulated Moving Bed Reactors (SMBR)

2.3.1. A Classification

The concept of an SMBR attempts to trap the temperature pulse by an adaption of feed and product port to the position of the moving fronts of pulse. Turning this idea into practice requires a finite domain or reactor length, a certain number of segments and discrete-time shifts of the ports in the direction of the moving pulse. Hence, feed and product ports are periodically switched in the flow direction enclosing the temperature pulse.

From the preceding analysis, three possible dynamic regimes are conceivable:

Constant-pattern regime: The first regime resembles a switching of the feed port to positions in the cold section right in front of the traveling hot zone. Consequently, the

reaction front remains undisturbed and a constant pattern regime of the reaction front would prevail.

Relaxation: Shifting the feed port in the front or directly in the moving pulse can also be considered. This leads to a disturbance of the constant pattern of the reaction front. After a certain time, the front should relax on a constant pattern state again.

Permanent disturbance: As a third regime, a periodic switching, e.g. fast with short segments, relaxation on the constant pattern of an exothermic front may not be achieved. Thus, the profiles in a switched reactor undergo permanent adjustments.

It can be thought of different classifications, though in this work the present form is used. In this way, the results obtained from experiments and simulations can be classified and compared.

2.3.2. Definition of Switching Times

In order to trap the temperature pulse in a switched SMBR it is required to determine switching times which can be aligned to the front velocities. This section introduces a relation which is also suitable for comparison with the TMBR model, which is introduced later in chapter 3.

In order to derive reasonable switching times it is advisable to choose a specific basis. This will be the thermal front velocity u_T defined by eq. (2.7). The switching velocity, u_{sw}, is defined with the length of a segment, L_{Seg}, and the switching time t_{sw}:

$$u_{\mathrm{sw}} = \frac{L_{\mathrm{Seg}}}{t_{\mathrm{sw}}} = \frac{L_R}{t_{\mathrm{sw}} N_{\mathrm{Seg}}} \tag{2.44}$$

In (2.44) is also given the number of segments N_{Seg} and the total reactor length L_R. Next, a reduced switching time, γ, relates the thermal front velocity to the switching velocity:

$$\gamma = \frac{u_T}{u_{\mathrm{sw}}} \tag{2.45}$$

Expansion of equation (2.45) with the thermal front velocity (eq. (2.7)) yields:

$$\gamma = \frac{N_{\mathrm{Seg}} t_{\mathrm{sw}}}{L_R} \frac{u_g^*}{Le_1} \tag{2.46}$$

In (2.46) is used the Lewis number defined previously by equation (2.6). Now, a second Lewis-number, Le_2, based on the pure heat capacity ratio is introduced. It can be derived by a correction of the first Lewis-number, Le_1, with the phase ratio F, which describes the void fraction of the packing:

$$Le_2 = \frac{Le_1}{F} \qquad \text{with} \quad F = \frac{1-\varepsilon}{\varepsilon} \tag{2.47}$$

Replacing (2.47) in (2.46) the form used for the SMBR throughout this work is obtained:

$$\gamma = \frac{t_{\mathrm{sw}} N_{\mathrm{Seg}}}{(1-\varepsilon) L_R} \frac{u_g}{Le_2} \tag{2.48}$$

In equation (2.48), u_g is the superficial gas phase velocity ($u_g = \varepsilon u_g^*$). If $\gamma = 1$, the switching time is adjusted to the thermal front velocity. In case $\gamma > 1$, the switching time increases or the corresponding switching velocities, u_{sw}, becomes smaller. Otherwise, if $\gamma < 1$, a fast switching regime at decreased switching times is selected.

Throughout this work, two characteristic times scales of the periodic process are distinguished. A *switching period* refers to the timespan of the switching time, while the *cycle time* means the timespan, after which the initial reactor configuration, regardless of the number of segments, is restored. Thus, after three switching periods of a three bed unit a cycle is completed.

2.3.3. Characterization of Reactor Operation

In this section the front dynamics in the SMBR are examined assuming a cyclic steady state has been attained. This means, that the reactor has settled and the initial reactor state repeats after a switching cycle. A detailed discussion on this aspect is given in the appendix B.4.2 and the SMBR model used is given in section B.1 together with the parameters in table B.1.

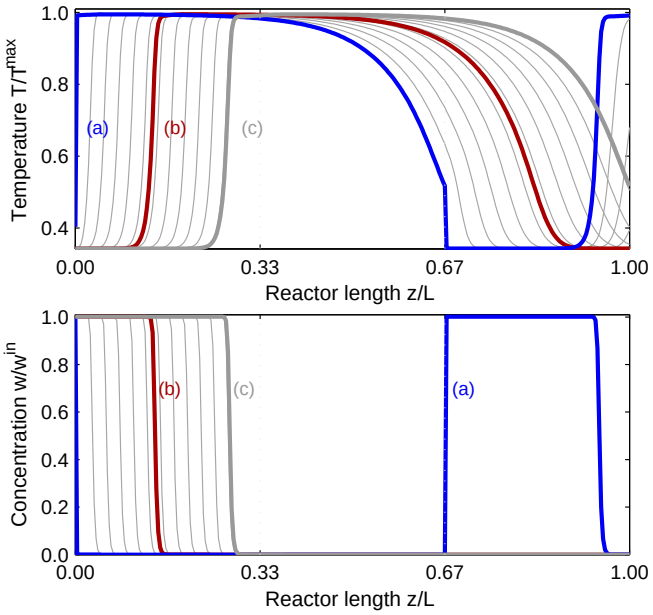

Figure 2.10.: Temperature and conversions profiles of a SMBR, highlighting the profiles at (a) the initial, (b) the middle and (c) the end of a switching period ($\gamma = 1.0$, $\Delta T_{\mathrm{ad}} = 120$ K). The reactor model is documented in section B.1 with parameters from table B.1.

Profiles of Temperature and Conversion Figure 2.10 illustrates the snapshots of the temperature and conversion profiles within one period in cyclic steady state, which was

needed in the introduction before (fig. 1.2). A reduced switching time of $\gamma = 1$ was selected and the situation corresponds to a feed position in front of the first segment, while product withdrawal is located after the third segment. In addition to figure 1.2, snapshots of several intermediate profiles are shown, initial (a), final (c) and half-period (b) profiles are highlighted.

The initial profile (a) is disrupted at the outlet position of the second segment. A hot portion at the end of the third segment is a leftover from the previous switching period, in which the feed position was right before the third segment (the first segment of in the preceding switching period). Initially a plug of unconverted reactant is present in the last segment (profiles (a), lower figure 2.10).

The temperature profiles at half of a switching period shows a typical bell shape explained already in figure 1.2, the reaction front is located in the first and the leading thermal front in the last segment.

Before subsequent switching period, in the last profile part of the leading thermal front has already left the reactor, while the reaction front is still in the first segment. In the following switching period, the feed position would be in front of the second segment dosing the cold feed directly on top of the high temperature pulse – this corresponds to the second (relaxed) regime suggested in 2.3.1.

Temperature and Conversion Pattern Another perspective on the reactor dynamics are spatio-temporal patterns providing an overview on the cyclic process and the front formation (fig. 2.11). The temperature pattern is characterized by band like structured high temperature

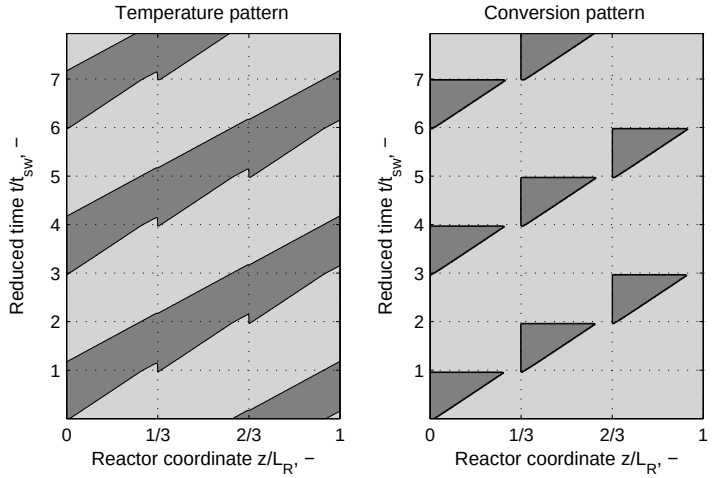

Figure 2.11.: Spatio-temporal pattern for temperature and conversion, with dark areas indicating low values ($\gamma = 1.0$, $\Delta T_{ad} = 120\,K$). Temperature pattern shows a band-like structure and conversion staircase-like patterns. Model given in section B.1, parameters in table B.1.

waves. It should be noted that the spatial coordinate is fixed, but left and right boundaries are coupled in case the feed position is in front of the second and the third segment. According to this, the profiles in figure 2.10 correspond to the pattern in the reduced times between 0 to 1, 3 and 4, 6 to 7 and so forth, thus only in case the feed position is in front of the first segment.

The conversion pattern shows stair case like structures due to the concentration fronts which are in accord to the reaction front position. In downstream sections complete conversion is achieved.

Reactor Outlets The periodic operation of the SMBR generates sawtooth-like temperature outlet signals as illustrated in figure 2.12. Furthermore, the plug of unconverted reactants will be flushed in the beginning of a switching period leading to a sudden increase in the outlet concentration.

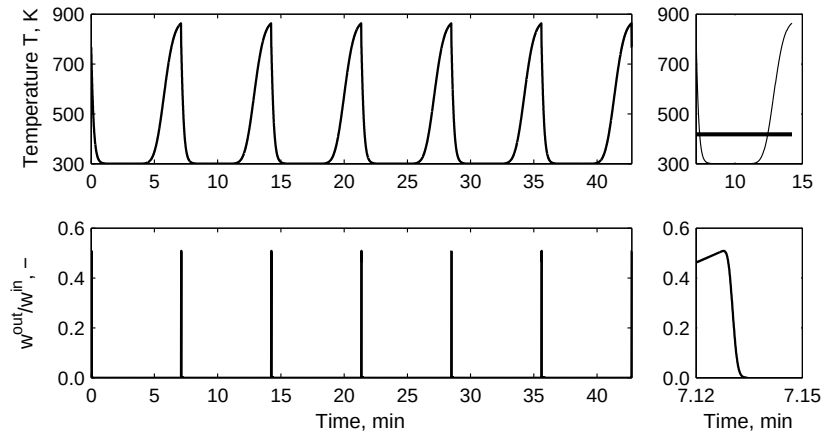

Figure 2.12.: Reactor outlets, temperature and reduced mass fraction. Top right for the temperature in a single period, below the zoom of unconverted slip ($\gamma = 1.0$, $\Delta T_{\mathrm{ad}} = 120\,\mathrm{K}$). Model given in section B.1, parameters in table B.1.

It is also interesting to investigated the integral energy balance of the reactor, which should show that conservation law applies regardless of the unsteady operation. The energy liberated by the reaction leads to an increase of the temperature of the adiabatic system beyond in- and outlet temperatures. Because it is an open system, a certain amount of energy gets lost with the effluent, which explains the sawtooth like temperature signals in the reactor outlet.

As a starting point, first the adiabatic temperature rise (ΔT_{ad}) is considered, which results from the temperature increase due to exothermic reactions in a closed system with a volume V_R. The heat released by the reaction, Q_R, is defined with the extent of reaction ξ_j and the heat of reaction ΔH_{Rj} assuming N_R participating reactions.

$$Q_R = \sum_{j=1}^{N_R} \left(-\Delta H_{Rj}\right) \xi_j \tag{2.49}$$

The heat responsible for the temperature change of the volume, Q_V, is defined by:

$$Q_V = V_R (\rho c_p)_g \Delta T \tag{2.50}$$

Thereby the extent of the reaction can be specified with the change of the mole number of a

species i in a reaction volume, V_R, in which N_R participating reactions occur [65]:

$$\sum_{j=1}^{N_R} \nu_{ij} r_j = \frac{1}{V_R} \frac{\mathrm{d}n_i}{\mathrm{d}t} = \sum_{j=1}^{N_R} \nu_{ij} \frac{1}{V_R} \frac{\mathrm{d}\xi_j}{\mathrm{d}t} \tag{2.51}$$

Thus, for a single reaction a single species needs to be observed to obtain $\xi = \Delta n_i / \nu_i$. Presuming a constant volume reaction, $\xi = \Delta c_i V_R / \nu_i$, thereby $\Delta c_i = c_i^{\mathrm{out}} - c_i^{\mathrm{in}}$ and $\nu = -1$, one arrives at the adiabatic temperature rise already given by equation (1.2).

The analysis is now applied to an open system to analyze the product temperature $T^{\mathrm{out}}(t)$ of the SMB reactor. The integral constant pressure energy balance reads:

$$V_R (\rho c_p)_g \frac{\mathrm{d}T}{\mathrm{d}t} = \dot{M}_g c_{p,g} \left(T^{\mathrm{in}} - T^{\mathrm{out}} \right) + V_R \sum_{j=1}^{N_R} (-\Delta H_{Rj}) r_j \tag{2.52}$$

with $T^{\mathrm{out}} = T$. Since the reaction rate can be defined as $r_j = \frac{1}{V_R} \frac{\mathrm{d}\xi_j}{\mathrm{d}t}$, the expansion by $\mathrm{d}t$ yields.

$$V_R (\rho c_p)_g \mathrm{d}T = \dot{M}_g c_{p,g} \left(T^{\mathrm{in}} - T^{\mathrm{out}}(t) \right) \mathrm{d}t + \sum_j (-\Delta H_{R,j}) \mathrm{d}\xi_j \tag{2.53}$$

After division by the capacity term one obtains:

$$\mathrm{d}T = \frac{\dot{M}_g c_{p,g}}{V_R (\rho c_p)_g} \left(T^{\mathrm{in}} - T^{\mathrm{out}}(t) \right) \mathrm{d}t + \frac{\sum_j (-\Delta H_{Rj}) \mathrm{d}\xi_j}{V_R (\rho c_p)_g} \tag{2.54}$$

By integration assuming a single reaction running to completion it is possible to calculate the integral energy balance within a switching period $(t, t + t_{\mathrm{sw}})$.

$$\Delta T_{\mathrm{acc}} = \frac{1}{t_{\mathrm{sw}}} \int_t^{t+t_{\mathrm{sw}}} \left(T^{\mathrm{in}} - T^{\mathrm{out}}(t) \right) \mathrm{d}t + \frac{(-\Delta H_R) c^{\mathrm{in}}}{(\rho c_p)_g} \tag{2.55}$$

In equation (2.55) the first term on the right hand side represents the difference between inlet and mean outlet temperature and the second term is the adiabatic temperature rise (eq. (1.2)). The temperature difference on the left hand side stems from the accumulation term and represents an integral value, which should assume zero in cyclic steady state. In such a case the temperature difference between in and outlet of the reactor matches the adiabatic temperature rise according to:

$$\Delta T_{\mathrm{ad}} = \frac{1}{t_{\mathrm{sw}}} \int_t^{t+t_{\mathrm{sw}}} T^{\mathrm{out}}(t) \mathrm{d}t - T^{\mathrm{in}} \tag{2.56}$$

Thereby the window of analysis should cover a characteristic timespan of the reactor, e.g. a single switching period.

In figure 2.12 right a single period is shown together with the mean outlet temperature. The mean temperature value is 120 K which satisfies equation (2.56). Thus, the temperature rise between inlet and time averaged outlet of an SMBR corresponds to the adiabatic temperature

rise of the steady state system (eq. (1.2)).

2.3.4. Influence of the Switching Time

The aim of this section is to elucidate the influence of the switching time on the fronts. This is illustrated with temperature profiles and spatio-temporal pattern. Further, limitations for the switching times to maintain an ignited state are addressed.

Cyclic Steady State Profiles Figure 2.13 illustrates different temperature profiles based on half-period snapshots for several switching times.

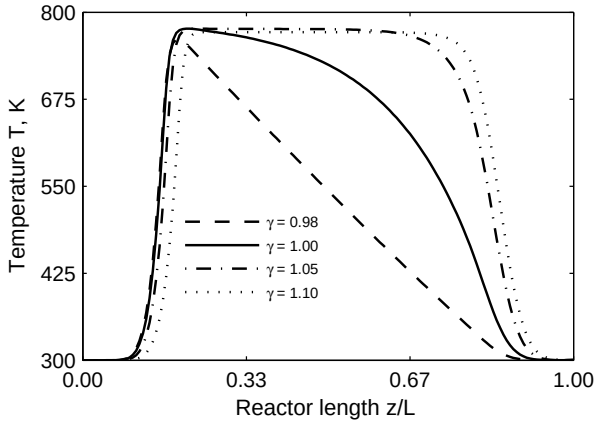

Figure 2.13.: Influence of the switching time on the profiles compare at half of the switching period in cyclic steady state. Model given in section B.1, parameters in table B.1.

Different effects regarding the thermal or the reaction front can be observed. The reaction front is slightly shifted to the entrance of the reactor in case of smaller switching times, but steepness is preserved. On the other hand, the switching time has a much larger impact on the leading thermal front. Smaller switching times flatten out the fronts and larger values provide steeper thermal fronts. In such a case the temperature base point is shifted to the reactor outlet and the high temperature zone is broadened.

Spatio-Temporal Pattern Two examples, $\gamma = 0.98$ and 1.10, are considered to illustrate the influence on spatio-temporal pattern (fig. 2.14).

In case of a fast switching regime, $\gamma = 0.98$, the temperature band is narrow as expected from the previous analysis (fig. 2.13). Also comparison with the $\gamma = 1.0$ in figure 2.11 is recommended. The conversion patter indicate a disruption, thus the zones of incomplete conversion are isolated. This is due to the fact, that the reaction front does not leave the active first segment of the cascade in the event of switching. Concerning the classification suggested in section 2.3.1, this regime corresponds to the second case, where the feed position is switched in the temperature pulse.

The second example, $\gamma = 1.10$, represents a slower switching regime. Now a larger portion of leading thermal front has left the reactor product causing the serration in the spatio-temporal fronts. The reaction front has almost left the active segment at the switching event,

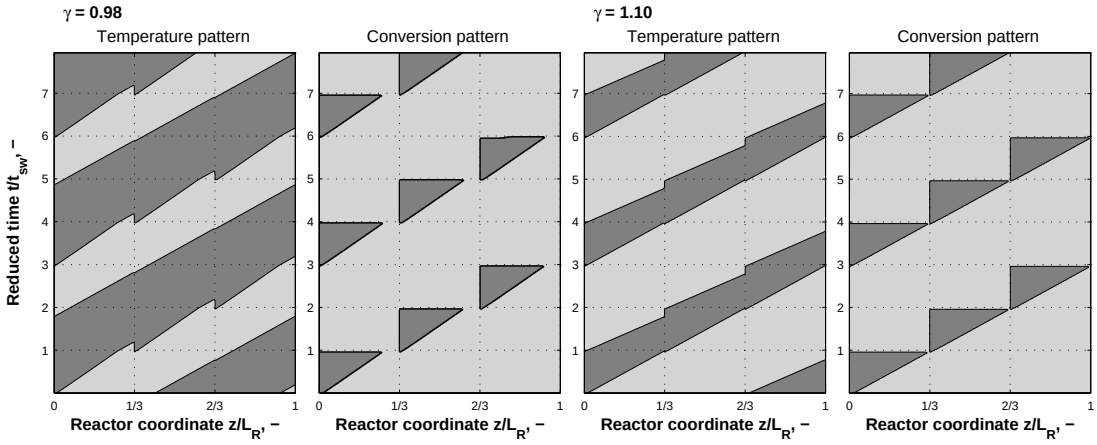

Figure 2.14.: Spatio-temporal pattern for temperature and conversion, with dark areas indicating low values for two different reduced switching times γ of 0.98 (left) and 1.10 (right). Model given in section B.1, parameters in table B.1.

thereby only minor serration is obtained. The conversion pattern shows almost contact of areas with conversion of nil.

Comparison of Reactor Outlets The reactor outlets are significantly affected by the choice for a certain switching time. The result for the faster switching with $\gamma = 0.98$ is shown in 2.15. In the initial phase directly after the switch, the outlet temperature remains high and falls to the inlet temperature. This corresponds to the reaction front which is shifted to the end on the reactor cascade and being flushed out slowly. Concerning the slip of the reactant, meaning the portion being flushed, only a very small fraction at the scales of the numerical precision is released. Thus, no slip would occur and complete conversion can be achieved.

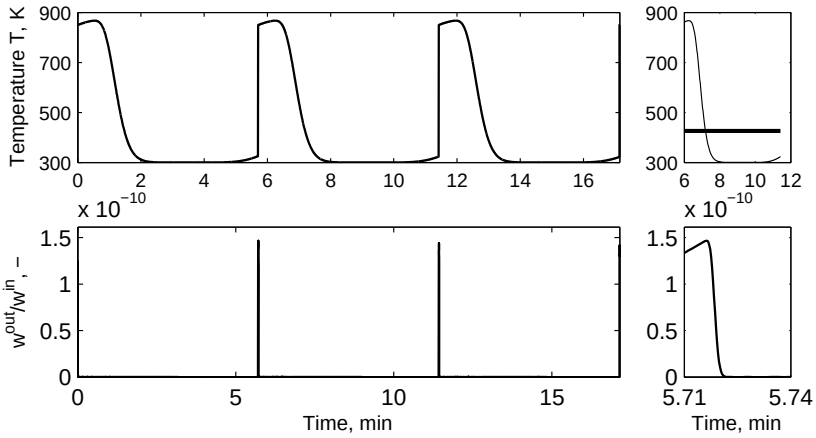

Figure 2.15.: Reactor outlets, temperature and reduced mass fraction, for $\gamma = 0.98$. Model given in section B.1, parameters in table B.1.

The slip is much larger in case of the slower switching regime (figure 2.16). Initially the outlet concentration attains values of the inlet, being flushed out in a very small time frame

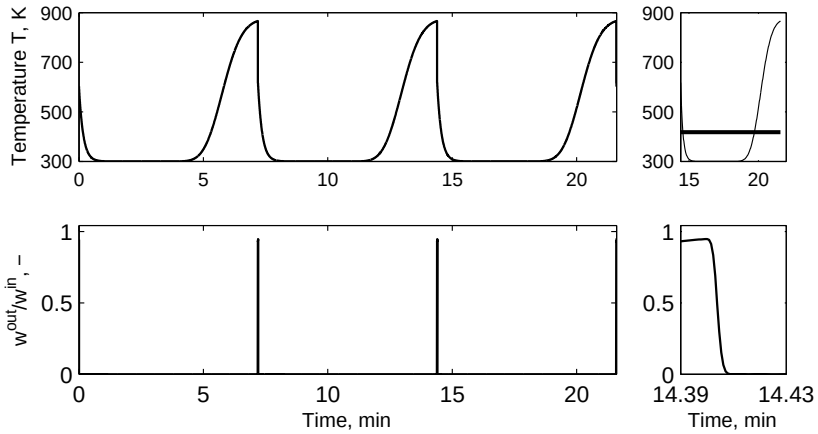

Figure 2.16.: Reactor outlets, temperature and reduced mass fraction, for $\gamma = 1.1$. Model given in section B.1, parameters in table B.1.

however. Also the outlet temperatures signals are different. In the beginning of the switching period the outlet remains cold. The increase later stems from the leading thermal front reaching the reactor outlet, or to pick up the previous analysis, heating up the last segment. Despite the differences in the temperatures outlet, either parts of the former reaction front, or the leading thermal front leaving the reactor, the integral energy balance (eq. (2.56)) is valid. Conversion pattern differ and are responsible for the slip of the reactant, which will be detailed in section 2.4.2.

Ignition Limits of the SMBR Ignited reactor operation is restricted to a certain range of switching times. As a first approach the ignited states available were systematically investigated with dynamic simulations to obtain the cyclic steady states in this range. In addition, the number of cycles needed to reach the cyclic steady states were recorded. An error bound of 10^{-6} was selected and compared with the norm of the reactor states to make this decision. The result is shown in the left figure 2.17.

Two maxima in respect to the number of cycles, N_{cyc}, appear, which bound the region of ignited periodic reactor operation ($0.93 \lessapprox \gamma \lessapprox 1.25$). Outside this range reactor extinction sets in. A maximum number of 102 cycles, right maximum, and a minimal number of 17 cycles have been found for this example. The relaxation on the cyclic steady state significantly changes inside the domain of ignited states. An dip is observed at $\gamma \approx 1$, which was verified by multiple simulation runs. If one considers the cyclic relaxation time as an indicator for the underlying dynamic reactor operation, it can be assumed that a change in the reactor behavior occurs below the reduced switching time of one.

Another important result obtained from this analysis is the problem to identify the exact limits for ignition based on such time consuming direct dynamic calculations. Even if the tolerance for identification is reduced further, this would only result in even larger calculation times. In addition, numerical problems arise, an issue which was also found for other cyclic processes [88, 89]. As depicted in the right side of figure 2.17, slightly different switching times can decide whether an ignited or extinguished state is attained. Unfortunately, a very

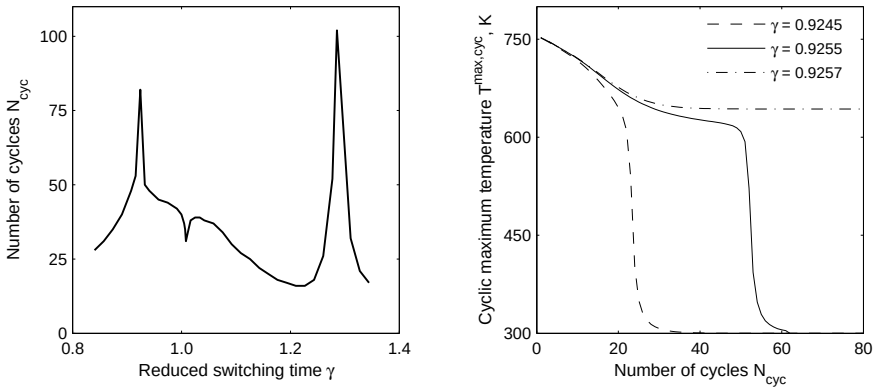

Figure 2.17.: Left: Influence of the switching time on the number of cycles needed to reach a cyclic steady state of the SMBR. Right: Maximum cyclic temperatures from start-up along the cycles for reduced switching times at the left ignition bound at $\gamma \approx 0.925$. Model given in section B.1, parameters in table B.1.

high number of cycles can be required to make this decision (see e.g. the example $\gamma = 0.9255$ represented by the solid line). The reason for this slow asymptotic behavior is known as the occurrence of creeping fronts, which means, that marginal differences in the energy accumulation within subsequent periods strongly prolongs the time to finally reach the cyclic steady state.

It appears questionable, if parametric studies based on the direct dynamic simulation provide valid information near critical parameters, in particular if a maximum number of cycles or course tolerances are set as a default truncation criterion. For this reason, in this work also alternative approaches are applied to determine the critical parameters, which may cause an unexpected and rather late extinction of the reactor. This is treated in section 4 making use of nonlinear analysis tools.

2.4. Comparison Between SMBR and Reverse-Flow Reactor Concepts

In this section a comparison between SMBR and reverse-flow reactor is discussed with a focus on fronts and the slip phenomena. Reverse-flow operation is considered for a single catalytic fixed-bed with compatible properties to the SMBR. This means, that an identical one dimensional pseudo-homogeneous models, but different boundary conditions were applied as detailed in appendix B.2.

2.4.1. Reactor Dynamics

Analysis of Process Pattern Reverse-flow reactor operation have been well explored by many researchers, e.g. Matros [26], Nieken et al. [74] to name important works. As a foreword, it should be stressed that the reverse-flow reactor has a much larger range of set-points to sustain ignited states. Even very fast switching would trap the temperature inside the bed, which is however not attractive as it means excessive valve operation. At a certain larger

switching time a limit is found at which the reactor goes to extinction.

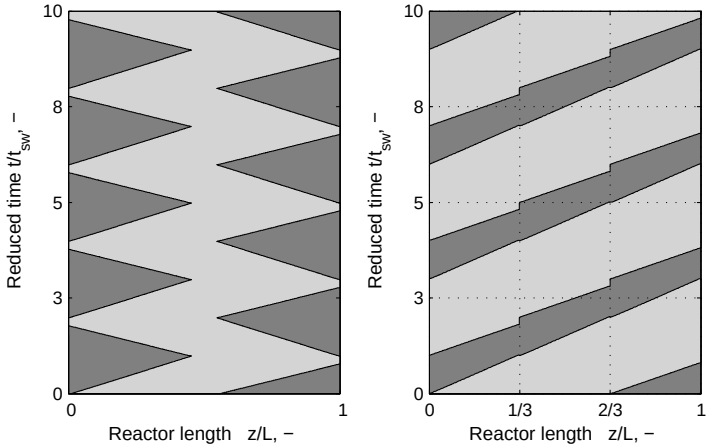

Figure 2.18.: Spatio-temporal temperature pattern of reverse-flow reactor (left) and SMBR (right), explained in section 2.4. Models are given in sections B.1 and B.2, parameters are listed in table B.1.

Figure 2.18 compares spatio-temporal temperature pattern, reverse-flow left and SMBR right. Typical staggered temperature fronts evolve for the former type of operation. Reaction front and thermal front are pushed in one direction and interchange their properties after flow reversal, this means, that the previous reaction front becomes a thermal front and vice versa. Thus, the dynamics are different to SMBR operation regarding front propagation. The SMBR is always based on an unidirectional propagation leading to band structures of high temperatures (fig. 2.18 right).

The in- and outlet section of the reverse-flow seem to be less used and remain cooler compared to the center. This temperature distribution strongly depends on the switching time of the reverse-flow operation. As the switching time is increased, the reaction front travels a longer distance cooling the boundary section. Faster switching, on the other hand, should yield a better exploitation of the section at the boundaries. In addition to this qualitative analysis several temperature profiles and process limits were studied as detailed below.

Analysis of Temperature Profiles In figure 2.19 are compared the temperature profiles of the reverse-flow reactor with the cyclic steady state profiles of the SMBR. Different feed concentration corresponding to adiabatic temperature rises of $30, 60, 90$ K have been investigated. The fronts of the reverse-flow are shown in the middle of the first semi-cycle for a positive gas flow direction. For the cases investigated, the maximum temperature of the reverse-flow exceeds those of the SMBR. The difference becomes less, as the feed concentration is reduced and in the limit of lean feed concentration, the reverse-flow reactor performs better. This was checked with systematic simulations. An explanation is the more effective heat regeneration due to the reshaping of the thermal fronts.[1] This means, that the fast and dispersive thermal front is exposed to self sharpening effects when applying cold feed after flow reversal. For this reason, less thermal energy is lost in reverse-flow operation compared to the SMBR concept.

[1] Communication with Prof. Eigenberger

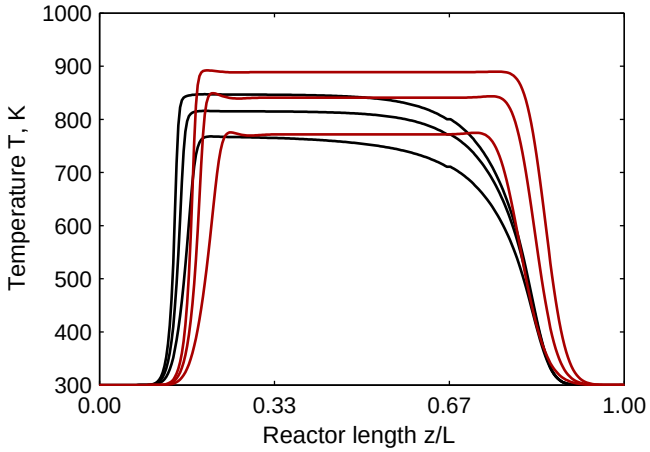

Figure 2.19.: SMBR (black) and reverse-flow reactor (red) temperature profiles at half of the switching period for different feed concentrations corresponding to $\Delta T_{ad} = 30, 60, 90$ K. Models are given in sections B.1 and B.2, parameters are listed in table B.1.

Therefore, the SMBR is less efficient for very lean feeds, though, differences are in the range of $\Delta T_{ad} \approx 5 - 10$ K. If a lower reactor temperature is desired, e.g. to avoid thermal catalyst degradation, then the SMBR should be considered offering lower reactor temperatures for larger feed concentrations.

2.4.2. Analysis of the Slip of Unconverted Reactants

The undesired release of unconverted reactant, which can immediately occur after switching events, is called slip. This effect can hardly be minimized in a reverse-flow reactor unless special strategies, e.g. guard beds or recycle streams are considered [90]. This section is dedicated to evaluate the potential of the simulated moving bed reactor to reduce the slip of unconverted species. A quantitative comparison with the reverse-flow reactor will be also presented.

A calculation of the amount of unconverted reactant in the outlet has to be conveyed with care for the convergence problems mentioned in the previous section. Because of the fact that the slip takes place within a relative short period of time, a switching period has to be resolved with a high time resolution in the cyclic steady state. The average outlet concentration of the reactant which should be converted can be calculated with the following equation:

$$c_i^{\text{out}} = \frac{\rho_g}{t_{\text{sw}} \widetilde{M}_i} \int_{t_k}^{t_{k+1}} w_i(t) dt \tag{2.57}$$

This expression, valid for any component was applied for the reactant propane. For a direct comparison with the reverse-flow reactor the dynamic model was applied to study a large region of relevant switching times (10 s ... 1300 s, other parameters according to table B.1) and to calculate the corresponding average propane outlet concentration. Typically the ignited states of the SMBR are located within a narrower region of switching times. The following

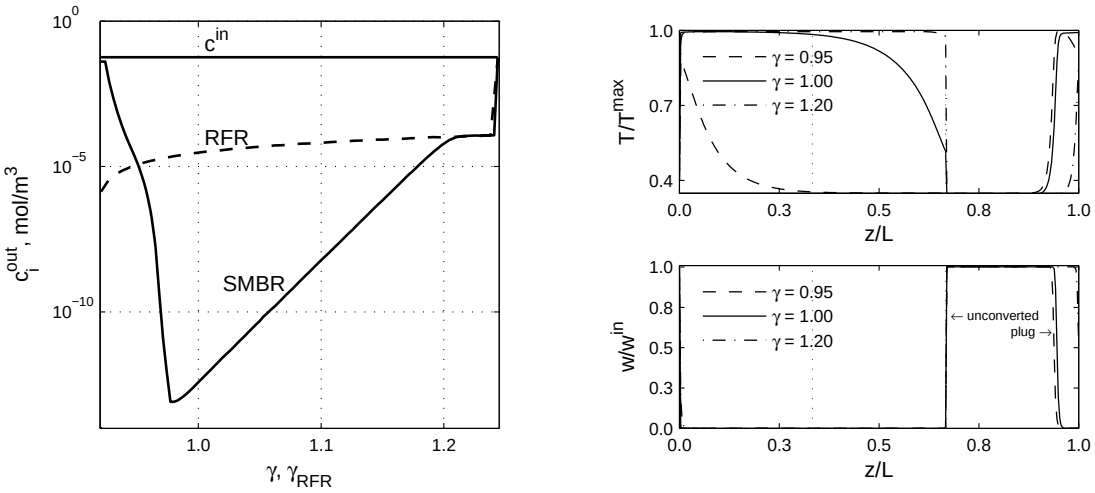

Figure 2.20.: Comparison of the slip of unconverted reactants in reverse-flow and SMB reactors (left), and respective fronts of the SMBR right. Models are given in sections B.1 and B.2, parameters are listed in table B.1.

scaling helps to illustrate the differences of these concepts using the covered range of flow rate ratios of an SMBR:

$$\gamma_{\mathrm{RFR}}\left(t_{\mathrm{sw,RFR}}\right) = \gamma_{\mathrm{SMBR}}^{\mathrm{min}} + \left(\gamma_{\mathrm{SMBR}}^{\mathrm{max}} - \gamma_{\mathrm{SMBR}}^{\mathrm{min}}\right) \frac{t_{\mathrm{sw,RFR}} - t_{\mathrm{sw,RFR}}^{\mathrm{min}}}{t_{\mathrm{sw,RFR}}^{\mathrm{max}} - t_{\mathrm{sw,RFR}}^{\mathrm{min}}} \tag{2.58}$$

Selected results obtained are shown in figure 2.20 (left). The average outlet concentrations of the SMBR reactor cascade shows a sharp decline and a minimum at γ approximately 0.98 and a further increase for $\gamma > 1$. The reverse-flow reactor outlet concentrations show a slight increase with rising the switching times (higher γ_{RFR} values) until values resulting in an extinguished state are reached (γ-RFR > 1.24). In this case the average outlet concentration equals the inlet concentration. Obviously the SMBR system has the potential to reach an enhanced average conversion. An explanation for this observation is based on the specific propagation of the characteristic temperature fronts.

The reverse-flow reactor causes a slip of unconverted species which can be explained with the position of the temperature fronts at the switching events. Depending on the switching time, smaller or larger sections of the fixed-bed are filled at this moment with unconverted reactant, which will leak after flow reversal. Hereby the portion of unconverted reactant released is increasing for higher switching times and fast switching would lower the slip.

Due to the multi-bed operation of the SMBR a slip reduction can be achieved, which is due to the positioning of the temperature fronts as indicated in figure 2.20, right. At the beginning of one switching period, the profiles reveal a temperature front at the end of segment III, which remains from the previous period where the feed position was active at this segment. A plug of unconverted reactant is located right before the reaction front. Obviously, this plug will overtake the slow moving temperature front and is partially or completely converted, thus lowering the slip. This property of the simulated moving bed reactor depends on the

switching time in the following manner: for γ smaller than one, the fronts are shifted towards the feed position. The maximum temperature is also lowered, which is accompanied by increased outlet concentration. A too fast switching is consequently not a desired strategy to minimize the slip of an SMBR.

Characteristic flow rate ratios γ above one will cause an increase of the average outlet concentration, though still below the reverse-flow reactor. Since for a late switching (higher switching times, e.g. for $\gamma = 1.1$ and 1.2) the temperature front almost leaves the active feed segment, there is only a little part of the front left to convert the plug of unconverted material. This influence is rather of continuous nature and vanishes when the switching time becomes to slow to maintain an autothermal operation. The minimal slip is obtained for the example for flow rate ratios of approximately 1.0. It should be noted that for different feed conditions, e.g. very low inlet concentrations, it will be more difficult to exploit the narrow temperature front responsible for the slip reduction. However, the potential is an attractive property of the SMBR, providing advantages compared to the reverse-flow reactor.

2.5. Summary

This chapter introduced the SMBR concept and provided a characterization of the underlying phenomenas determining the reactor principle. A special focus was set on analyzing front dynamics and on a comparison with the reverse-flow concept.

Basically two types of fronts have to be considered in fixed-bed reactors. A non-reactive thermal front and an exothermic reaction front, which exhibits a self-sharpening behavior. The constant pattern solution of the reaction front was investigated for various process parameters. Maximum temperatures and front velocities are largely affected by the changing these parameters. Backward moving reaction fronts can also occur at increased inlet concentrations.

Front dynamics were illustrated based on extensive numerical simulations, first for the example of the wrong-way behavior and then for a moving temperature pulse. Together with an estimate for the ignition temperature, a reasonable picture of stabilized fronts has been developed forming the basis for the simulated moving bed reactor concept studied later.

The reactor principle was characterized regarding internal temperature and conversion profiles, spatio-temporal pattern and outlet signals. Only a limited range of switching times is available to ensure ignited reactor states. The timespan for relaxation on a cyclic steady state revealed significant parameter sensitivities of the reactor.

The comparison of the SMBR with the reverse-flow reactor revealed a slightly better heat integration for very lean feeds for the conventional reverse-flow. On the other hand, a much better reduction of the slip of reactants can be achieved with the SMBR.

The need for very time consuming calculations for solving the periodic dynamic models exceeds acceptable values for systematic parametric studies. Efficient design and analysis of the SMBR concept requires much faster solutions. Therefore a reduced model was developed which is introduced in the next chapter.

3. Model Reduction

The time consuming simulation of the switched SMBR, even for the simple pseudo-homogeneous case, cannot be conceived as the optimal model depth to perform systematic parameter studies. Model reduction is needed and should allow for a fast approximation of the steady state of the reactor, while preserving essential information and significance required for reactor design and scale-up.

Among the model reduction techniques available for periodic systems, an efficient approach is the transformation in the frequency domain [91]. Recently Markovic et al. [41] reported that for reactors with periodic input modulation only the second order frequency response function needs to be calculated in order to decide whether periodic operation is attractive or not.

Periodic operation of multi-bed processes on the other hand is represented by hybrid models incorporating discrete jumps, which cannot be treated that easily by a transformation into the frequency domain. Nevertheless, several concepts for an efficient reduction have appeared. Often it is desired to at least approximate mean values as representatives of the cyclic periodic process, such as mean internal concentration and temperature profiles. A suitable approximation for a periodically operated fixed-bed can be based on fast switching asymptotes, which may result in a so called frozen solution. This was demonstrated for the reverse-flow reactor by Nieken et al. [74], where the fast switching asymptote is represented by a true countercurrent process. Gorbach et al. [89] considered model reduction for pressure swing adsorption process exploited analogy to membrane processes. Also an approximate solution of the SMBR was suggested by Sheintuch et al. [58]. Transformation of the port switching into a moving coordinate system was suggested and a convergence into an increased number of ports demonstrated.

In this work an approach originating from separation science is developed. The periodic switching of ports between the fixed-beds corresponds to the well-known simulated moving bed (SMB) operation [43, 45]. Hereby the port switching mimics the time-discrete countercurrent movement of the two phases involved. The simulated moving bed process was mainly applied for the adsorption from gaseous phase, sugar separation and later, in the 90th, established in the pharmaceutical industries. Since the underlying separation principle, the adsorption equilibrium, is often a nonlinear, steep concentration fronts evolve whose precise calculation becomes numerically demanding. Even though special numerical algorithms have been developed [92], the direct dynamic simulation of a cyclic multi-bed process remains to be a challenge. Approximate solutions of the periodic process are highly demanded, in particular when it comes to the conceptual process design phase.

A suitable approximation is the true moving bed countercurrent process [44, 47, 49]. This so call true moving bed process (TMB) has found widespread acceptance particularly in the chromatography community [49, 93–95], however, the origins are found in the classical

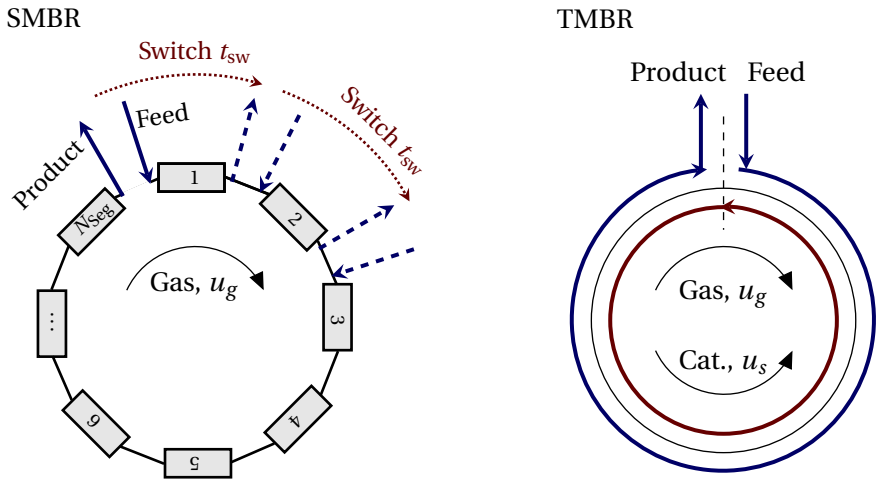

Figure 3.1.: Left: original SMBR scheme based on switching of feed and product ports in the flow direction. Right: the limiting case of a true moving bed reactor (TMBR) for infinite number of fixed-beds employed.

equilibrium stage models for distillation and countercurrent extraction.

The principle is explained with the help of figure 3.1. In the left figure is shown the simulated moving bed process drafting two switching operation in the gas flow direction. In the limit case of an infinite segmented reactor, the discrete switching operation is transformed to a continuous movement of the solid phase ("Cat. u_S") in countercurrent to the gas phase (3.1 right) – the true moving bed reactor (TMBR).

This chapter explains in detail the derivation of the TMBR model, the boundary conditions and discusses numerical features. The approximated profiles are compared with the SMBR model and finally the influence of process parameters using the TMBR model is illustrated.

3.1. The True Moving Bed Reactor Model (TMBR)

In this section two modeling approaches are presented. At first, a simple stage model is discussed briefly and then a general continuum model is introduced.

3.1.1. Stage Model

In adsorption processes the coupling between solid and fluid phase is typically established by adsorption equilibria. These equilibria relate the concentration in the fluid phase to the loading in the solid phase, typically in a nonlinear manner. Often a stage model is used to calculate the concentration fronts emerging in a fixed-bed adsorber. The stages can be related to a space position along the adsorber bed and the total number of stages of theoretical plates, NTP, is adjusted to represent a specific apparent dispersion of the species. In order to simulate a true moving bed adsorption process, an additional solid phase flux is included in the model. Stage models are also common for fixed-bed reactors (fixed-bed dispersive model [65, 96]).

In contrast to adsorption processes, below an additional reaction term is included in the mass and energy balances, while the adsorption equilibrium is omitted. At first it is instructive to consider a heterogeneous material balance and to introduce the solid phase countercurrent flux in a mole balance for the solid phase. Coupling of the phases is implemented by a linear driving force term (conventional mass transfer resistance). The energy balance is written in it's pseudo-homogeneous form, equipped with an additional solid phase flux:

$$\varepsilon \frac{\mathrm{d}c_{i,g}^{k}}{\mathrm{d}t} = \frac{1}{\tau_g}\left(c_{i,g}^{k-1} - c_{i,g}^{k}\right) + \beta a_V \left(c_{i,g}^{k} - c_{i,s}^{k}\right) \tag{3.1}$$

$$(1-\varepsilon)\frac{\mathrm{d}c_{i,s}^{k}}{\mathrm{d}t} = \frac{1}{\tau_s}\left(c_{i,s}^{k+1} - c_{i,s}^{k}\right) - \beta a_V \left(c_{i,g}^{k} - c_{i,s}^{k}\right) + \sum_j \nu_{ij} r_j(c_{i,s}^{k}, T^k) \tag{3.2}$$

$$(\rho c_p)_m \frac{\mathrm{d}T^k}{\mathrm{d}t} = \frac{(\rho c_p)_g}{\tau_g}\left(T^{k-1} - T^k\right) + \frac{(\rho c_p)_s}{\tau_s}\left(T^{k+1} - T^k\right) + \sum_j (-\Delta H_{R,j}) r_j(c_{i,s}^{k}, T^k) \tag{3.3}$$

$$\text{stage index:} \qquad k = 1, \ldots, N \tag{3.4}$$

$$\text{IC:} \qquad c_{i,g}^{k}(t=0) = c_{i,g}^{\text{init}}(k) \qquad c_{i,s}^{k}(t=0) = c_{i,s}^{\text{init}}(k) \qquad T^k(t=0) = T^{\text{init}}(k) \tag{3.5}$$
$$\forall k \quad i = 1, \ldots, N_c$$

In the balances (3.1)-(3.3), the transport of the phases is determined by residence times of the gas and the solid phase, τ_g and τ_s, which relate the respective flow rates to the stage volume, $\dot{V}/V^k$. k is the stage index (eq. (3.4)) and a solid phase heat capacity $(\rho c_p)_s$ is introduced in energy balance (3.3).

As illustrated in figure 3.1, the solid phase circulates in a closed loop. For that reason, coupling between the first and the last stage needs to be considered:

$$c_{i,s}^{N+1} = c_{i,s}^{1} \qquad i = 1, \ldots, N_c \qquad \text{and} \qquad T^{N+1} = T^1 \tag{3.6}$$

Two important simplifications for the scheme are suggested in the following. At first, the countercurrent flux in the mole balance (eq. (3.2)) is disregarded, which is justified since $\tau_s \gg \tau_g$. Hence, the countercurrent is considered only in the energy balance (eq. (3.3)) and the coefficients of the difference terms have the same order of magnitude assuming a high volumetric heat capacity of the solid phase, $(\rho c_p)_s$, and a large residence time of the solid, τ_s. Note, that if this simplification is not considered, the coupling of feed and product stage molar balances would automatically lead to a permanent discharge of a small portion of unconverted reactants via the short bypass, feed to product. This can be regarded as an analogy to the slip phenomena in the SMBR as discussed in section 2.3.3.

If the mass transfer resistance between the gas and the catalyst phase is neglected, one obtains a pseudo-homogeneous mole balance (eq. (3.1)+ eq. (3.2)):

$$\varepsilon \frac{\mathrm{d}c_{i,g}^{k}}{\mathrm{d}t} + (1-\varepsilon)\frac{\mathrm{d}c_{i,s}^{k}}{\mathrm{d}t} = \frac{1}{\tau_g}\left(c_{i,g}^{k-1} - c_{i,g}^{k}\right) + \sum_j \nu_{ij} r_j(c_{i,g}^{k}, T^k) \qquad i = 1, \ldots, N_c \tag{3.7}$$

The mass accumulation in the solid phase on left hand side of equation (3.7) is neglected,

which is justified for a first principle approach and typically assumed for catalytic fixed-bed reactor models. The stage model of the TMBR finally reads:

$$\varepsilon \frac{\mathrm{d}c_i^k}{\mathrm{d}t} = \frac{1}{\tau_g}\left(c_i^{k-1} - c_i^k\right) + \sum_j \nu_{ij} r_j(c_i^k, T^k) \tag{3.8}$$

$$(\rho c_p)_m \frac{\mathrm{d}T^k}{\mathrm{d}t} = \frac{(\rho c_p)_g}{\tau_g}\left(T^{k-1} - T^k\right) + \frac{(\rho c_p)_s}{\tau_s}\left(T^{k+1} - T^k\right) + \sum_j (-\Delta H_{R,j}) r_j(c_i^k, T^k) \tag{3.9}$$

$$\text{stage index:} \qquad k = 1, \ldots, N \tag{3.10}$$

$$\text{IC:} \qquad c_i^k(t=0) = c_i^{\text{init}} \qquad T^k(t=0) = T^{\text{init}} \quad \forall k \quad i = 1, N_c \tag{3.11}$$

This model represents a system of ordinary differential equations which can be solved with the corresponding initial conditions. Another option is the direct calculation of the steady state profiles solving the resulting system of nonlinear equations (setting left hand side to zero and solve right hand side (3.8)-(3.10)).

Since the difference approximation is also employed to the countercurrent solid phase flow, the solid phase transport appears to be convective and an dispersive simultaneously. However, this *additional dispersion or backmixing of the solid* is not physically meaningful. The objective of the model reduction was to transfer only the simulated discrete-time transport into a true countercurrent convective transport of the solid phase. Dispersive solid phase transport was not part of the transformation, but seems to be part of the solution of the stage model. For this reason, special requirements have to be considered for the numerical solution of the stage model (examined in section 3.2).

3.1.2. Continuous Model

The stage model above has also the disadvantage that the dispersion is determined by a certain large stage number. Thus, representation of small dispersion effects requires the solution of very large system of equations. To avoid scaling of the equation system with physical dispersion, a continuous model is suggested accounting for convective and dispersive transport separately:

$$\varepsilon\rho \frac{\partial w_i}{\partial t} = -u_g \rho_g \frac{\partial w_i}{\partial z} + D \frac{\partial^2 w_i}{\partial z^2} + \sum_j \nu_i r_j(c_i, T) \tag{3.12}$$

$$\begin{aligned}\left(\rho c_p\right)_m \frac{\partial T}{\partial t} = &-u_g (\rho c_p)_g \frac{\partial T}{\partial z} + u_s (\rho c_p)_s \frac{\partial T}{\partial z} \\ &+ \lambda \frac{\partial^2 T}{\partial z^2} + \sum_j (-\Delta H_R) r_j(c_i, T) - 2h_w/R_w (T - T_u)\end{aligned} \tag{3.13}$$

$$\text{IC:} \quad w_i(t=0,z) = w_i^{\text{init}}(z) \qquad T(t=0,z) = T^{\text{init}}(z) \tag{3.14}$$

(boundary conditions given in sec. 3.1.3)

Equation (3.13) also accounts for the heat transfer through the wall using a linear driving force with respect to an ambient temperature T_u. It is important to understand that dispersive and convective transport are represented by different terms in energy balance ((3.13)).

When investigating the limiting case for a large number of segments in the SMBR with the stage model (eq. (3.8)- (3.10)), discrepancies to the SMBR will occur due to the artificial solid phase dispersion. However, also in the continuous model the solid convection can be subject to dispersion, which is usually introduced by numerical approximation errors. Therefore it is suggested to investigate a rather simple numerical scheme for the continuous model and to derive rules for the evaluation of such numerical errors. These rules will then apply to the stage model as well as to the discretized form of the continuous model.

Before turning to a further analysis of the boundary conditions and to the details of dispersion effects, the features of the TMBR model are summarized:

- The countercurrent solid flow was omitted in the molar (and material) balance, since $u_g \gg u_s$, and is only implemented in the energy balance.
- Mass accumulation in the solid phase is assumed to be negligible as well as transport limitations between gas and catalyst phases.
- In the TMBR continuous model the solid countercurrent is a true convective flux, in the stage model this solid flux is inherently subject to backmixing.

3.1.3. Boundary Conditions of the Continuous TMBR Model

For the partial differential equations, eq. (3.12) and (3.13), appropriate boundary conditions need to be specified. An arbitrary true moving bed models may contain several zones with different velocities as typically found in separation technology [11, 97]. For that reason, node balances with boundary conditions (BC)[1] of the third kind are sometimes suggested [11]. However, they can be replaced by BC of first kind in many cases. In particularly, it was shown for mass dispersion that differences between the first and third kind are marginal [99].

The significance of third kind version is restricted to processes with larger dispersion effects. For the sake of completeness the derivation with mixed BC of third kind are first introduced and simplifications suggested to end up with a simpler form. The notion „mixed BC“ is generally used for problems with different kinds of BC's of a specific domain. Since the left and the right boundary conditions differ, this terminology is also used here [98].

In figure 3.2 are illustrated the fluxes connected to the boundaries of an TMBR. The scheme on top represents the case of a balance of a heterogeneous model, below is shown the corresponding schema for a pseudo-homogeneous model. The boundaries are denoted as $0^-/0^+$ and L^-/L^+ for the left and right sides, and the signs discriminate between inner and outer values of the solution domain. This illustration helps to derive accurate BCs step by step as being derived for the energy balance in the following.

For a heterogeneous case backmixing is assumed to be present for the gas phase balance

[1] Boundary conditions BC: a constant value corresponds to a BC of first kind (Dirichlet), for constant flux of second kind (Neumann) and in case of a linear combination of these here a BC of third kind (Cauchy) is considered [98].

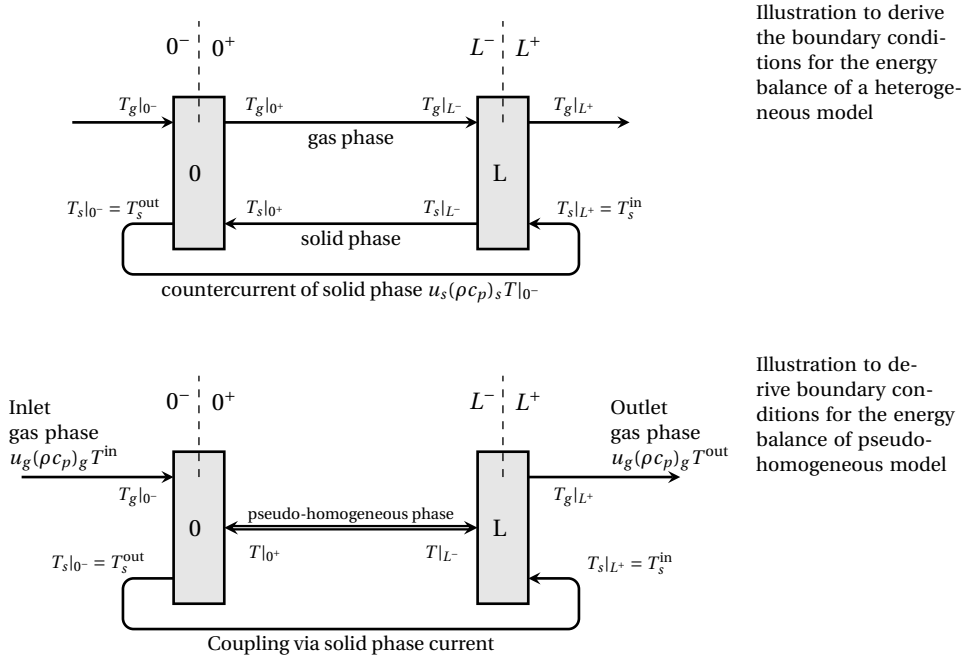

Figure 3.2.: Domain boundaries and flux relations in TMBR models, in the scheme on top for a heterogeneous model and below for the reduced pseudo-homogeneous model used in this work.

at the left BC (0^+):

$$\left(u_g(\rho c_p)_g T_g\right)_{0^-} = \left(u_g(\rho c_p)_g T_g - \lambda \frac{\partial T_g}{\partial z}\right)_{0^+} \tag{3.15}$$

$$\left(-u_s(\rho c_p)_s T_s\right)_{0^-} = \left(-u_s(\rho c_p)_s T_s\right)_{0^+} \tag{3.16}$$

Eq. (3.15) correspond the known BC according to Danckwerts [100], Wehner et al. [101]. By eq. (3.16) a constant flux of the solid phase without backmixing is assumed. Adding (3.15) and (3.16) yields for the corresponding pseudo-homogeneous case:

$$\lambda \frac{\partial T_g}{\partial z}\Big|_{0^+} = u_g(\rho c_p)_g \left(T_g|_{0^+} - T_g|_{0^-}\right) - u_s(\rho c_p)_s \left(T_s|_{0^+} - T_s|_{0^-}\right) \tag{3.17}$$

Furthermore, in the pseudo-homogeneous model are assumed identical temperatures of the distinct phases for the variables within the domain $\left(0^+, L^-\right)$. Additionally, a separate notation for the variables connecting from outside of the domain (in, out) is introduced. This helps to distinguish solid and gas specific variables and allows a comparison with the conventions of the standard fixed-bed reactor model. Equation (3.17) is now given by:

$$\lambda \frac{\partial T}{\partial z}\Big|_{0^+} = u_g(\rho c_p)_g \left(T|_{0^+} - T_g^{\text{in}}\right) - u_s(\rho c_p)_s \left(T|_{0^+} - T_s^{\text{out}}\right) \tag{3.18}$$

At the right boundary ($z = L$) the following balance can be defined:

$$\lambda \frac{\partial T}{\partial z}\Big|_{L^-} = u_g(\rho c_p)_g \left(T|_{L^-} - T_g^{\text{out}}\right) - u_s(\rho c_p)_s \left(T|_{L^-} - T_s^{\text{in}}\right) \tag{3.19}$$

To describe the coupling of the circulating solid flow outside the solution domain it holds that:

$$\left(u_s(\rho c_p)_s T_s^{\text{in}}\right)_{L^-} = \left(u_s(\rho c_p)_s T_s^{\text{out}}\right)_{0^-} \tag{3.20}$$

These equations, (3.18) and (3.19), represent the general case of the boundary conditions for the energy balance of the pseudo-homogeneous model and they can also be applied to arrangements with several different zones similar to the common TMB models in separation science. Finally, the closed loop of the TMBR is established by equation (3.20). Further simplifications for the one-zone TMBR are suggested:

1. At the outlet backmixing can be omitted and it holds:

$$\frac{\partial T}{\partial z}\Big|_{L^-} = 0 \tag{3.21}$$

   This is an appropriate assumption similar to classical fixed-bed, where backmixing from the pipe outlet is neglected [65].

2. The solid phase flux at $z = 0$ adopts to the temperature inside the domain: $T_s^{\text{out}} = T|_{0^+}$

3. The outlet temperature is equal to the conditions inside of the domain: $T_g^{\text{out}} = T|_{L^-}$

4. The BC of third kind is negligible for the entrance section, so that the gradient is assumed to be zero: $\frac{\partial T}{\partial z}\Big|_{0^+} = 0$. This is justified for small fixed-bed heat conduction.

Applying assumption (1) and (2), the following boundary conditions are obtained:

$$\lambda \frac{\partial T}{\partial z}\Big|_{0^+} = u_g(\rho c_p)_g \left(T|_{0^+} - T_g^{\text{in}}\right) \tag{3.22}$$

$$0 = u_g(\rho c_p)_g \left(T|_{L^-} - T_g^{\text{out}}\right) - u_s(\rho c_p)_s \left(T|_{L^-} - T_s^{\text{in}}\right) \tag{3.23}$$

The left boundary condition is of third kind and that for the outlet is a simple algebraic expression. Using the coupling condition eq. (3.20) and assumption (2) yields $T_s^{\text{in}} = T_s^{\text{out}} = T|_{0^+}$ and instead of eq. (3.23) the following condition holds:

$$0 = u_g(\rho c_p)_g \left(T|_{L^-} - T_g^{\text{out}}\right) - u_s(\rho c_p)_s \left(T|_{L^-} - T|_0^+\right) \tag{3.24}$$

Considering assumption (3), eq. (3.24) reduces to $T|_L^- = T|_0^+$, which means that the temperatures at the inner domain boundaries are identical.

But as long as equation (3.22) is valid, it should be noted that still $T_g^{\text{in}} \neq \left(T_s^{\text{out}} = T|_0^+\right)$. This means, that only under the assumption of a boundary condition of first kind for the reactor entrance, as it is required by assumption (4), the following conditions apply:

$$T_g^{\text{in}} = T_s^{\text{out}} = T_s^{\text{in}} = T|_{L^-} = T|_{0^+} \tag{3.25}$$

This is the trivial coupling, because the temperature of the solid entering at $z = L$ is identical to the inlet temperature of the gas at $z = 0$.

Summary of Possible Boundary Conditions Concerning a general TMBR, possibly using several zones of different velocities, the following relations can be used:

$$z = 0: \qquad \lambda \frac{\partial T}{\partial z}\Big|_{0^+} = u_g (\rho c_p)_g \left(T|_{0^+} - T_g^{\text{in}} \right) - u_s (\rho c_p)_s \left(T|_{0^+} - T_s^{\text{out}} \right) \tag{3.26}$$

$$z = L: \qquad \lambda \frac{\partial T}{\partial z}\Big|_{L^-} = u_g (\rho c_p)_g \left(T|_{L^-} - T_g^{\text{out}} \right) - u_s (\rho c_p)_s \left(T|_{L^-} - T_s^{\text{in}} \right) \tag{3.27}$$

A further simplification for the one zone TMBR investigated in this work yields:

$$z = 0: \qquad \lambda \frac{\partial T}{\partial z}\Big|_{0^+} = u_g (\rho c_p)_g \left(T|_{0^+} - T_g^{\text{in}} \right) \tag{3.28}$$

$$z = L: \qquad 0 = u_g (\rho c_p)_g \left(T|_{L^-} - T_g^{\text{out}} \right) - u_s (\rho c_p)_s \left(T|_{L^-} - T|_{0^+} \right) \tag{3.29}$$

Only when neglecting mixed boundary conditions, the trivial solution in equation (3.25) is obtained. Notice that for the material balance the BC are used:

$$z = 0: \qquad u_g \rho_g w_i^{\text{in}} = u_g \rho_g w_i|_{0^+} - D \frac{\partial w_i}{\partial z}\Big|_{0^+} \tag{3.30}$$

$$z = L: \qquad 0 = \frac{\partial w_i}{\partial z}\Big|_{L^-} \tag{3.31}$$

The analysis above offers meaningful simplifications of the boundary conditions for the energy balance. Because the model is an approximation solution, the trivial version ((3.25)) can be considered as a reasonable approach.

3.1.4. Equivalence to SMBR Switching Times

In this section an equivalence relationship between SMBR and TMBR is derived in order to transform switching times into solid flow rates.

Solid Flow Rate A solid flow rate $\dot{V}_s$ can be considered, either based on an interstitial velocity, u_s^*, or on a superficial solid phase velocity, $u_s = (1-\varepsilon) u_s^*$. With A_q being the cross section of the reactor, one obtains:

$$\dot{V}_s = (1-\varepsilon) u_s^* A_q \quad \text{or} \quad \dot{V}_s = u_s A_q \tag{3.32}$$

Assuming that this solid phase flow rate corresponds to the solid volume of a single segment $\left((1-\varepsilon) V_{\text{Seg}}\right)$ transported within a switching period in the SMBR, the following relation holds:

$$\dot{V}_s = \frac{(1-\varepsilon) V_{\text{Seg}}}{t_{\text{sw}}} \tag{3.33}$$

Considering $V_{\text{Seg}} = A_q L_{\text{Seg}}$, the solid phase velocity is defined as:

$$u_s = \frac{(1-\varepsilon) L_{\text{Seg}}}{t_{\text{sw}}} \tag{3.34}$$

or with the total reactor length, $L_R = L_{\text{Seg}} N_{\text{Seg}}$, as:

$$u_s = \frac{(1-\varepsilon) L_R}{t_{\text{sw}} N_{\text{Seg}}} \tag{3.35}$$

Hence, the solid phase velocity can be related to the switching time of an equivalent SMBR unit.

Gas Flow Rate Regarding the gas flow rate in the SMBR, a correction is considered, which is due to the gas volume transported in the segment at the switching event:

$$\dot{V}_g^{\text{SMBR}} = \dot{V}_g^{\text{TMBR}} + \frac{V_g}{t_{\text{sw}}} \tag{3.36}$$

Since $V_g = \varepsilon V_{\text{Seg}}$, this yield with the definitions above:

$$u_g^{\text{SMBR}} = u_g^{\text{TMBR}} + \frac{\varepsilon}{1-\varepsilon} u_s \tag{3.37}$$

However, in the present work the solid phase velocity is much smaller than that of the gas phase, $u_s \ll u_g$, and the last term in (3.37) can be omitted.

Scaling Solid Velocity by Matching Countercurrent Heat Fluxes If the heat capacities fluxes of the two phases involved are balanced, the accumulation of thermal energy should also be maximized. Then it holds:

$$u_g (\rho c_p)_g = \dot{m}_s c_{p,s} \quad \text{or} \quad u_g (\rho c_p)_g = u_s (\rho c_p)_s \tag{3.38}$$

In this work, a *flow rate ratio*, γ, relating gas heat capacity flux to the solid heat capacity flux is defined by:

$$\gamma = \frac{(\rho c_p)_g}{(\rho c_p)_s} \frac{u_g}{u_s} = \frac{u_g (\rho c_p)_g}{u_s (\rho c_p)_s} = \frac{u_g}{u_s} \frac{1}{Le_2} \tag{3.39}$$

Regarding the transformation into the SMBR, one may also use equation (3.35) to show that:

$$\gamma = \frac{t_{\text{sw}} N_{\text{Seg}}}{(1-\varepsilon) L_R} \frac{u_g}{Le_2} \tag{3.40}$$

Assuming parity of the capacity fluxes, $\gamma = 1$, and with (3.34) the following relationships appear:

$$(1-\varepsilon) L_R Le_2 = t_{\mathrm{sw}} N_{\mathrm{Seg}} u_g \tag{3.41}$$

$$u_s Le_2 = u_g \tag{3.42}$$

Considering the thermal front velocity $u_T = u_g^* / Le_1$, it can be found for the case of $\gamma = 1$:

$$u_s = \frac{\varepsilon Le_1}{Le_2} u_T = (1-\varepsilon) u_T \tag{3.43}$$

Again, one arrives at a switching velocity $u_{\mathrm{sw}} = L_{\mathrm{Seg}} / t_{\mathrm{sw}}$, after substitution of (3.34) in (3.43):

$$(1-\varepsilon) u_T = \frac{(1-\varepsilon) L_{\mathrm{Seg}}}{t_{\mathrm{sw}}} \qquad \text{such that:} \quad u_T = u_{\mathrm{sw}} \tag{3.44}$$

Equation (3.44) is similar to the switching velocity defined by equation (2.45). It can be concluded, that the flow rate ratio and reduced switching times represent the accurate transformation equations to relate both models:

$$\text{TMBR:} \quad \gamma = \frac{u_g}{u_s} \frac{1}{Le_2} \qquad \text{SMBR:} \quad \gamma = \frac{t_{\mathrm{sw}} N_{\mathrm{Seg}}}{(1-\varepsilon) L_R} \frac{u_g}{Le_2} \tag{3.45}$$

Moreover, for both reactor models it holds that for $\gamma = 1$ the energy accumulation should be maximized and the countercurrent transport, either simulated (SMBR) or true (TMBR), is adjusted to the velocity of a thermal front, u_T.

3.2. Evaluation of Numerically Induced Dispersion in SMBR and TMBR Models

Similar to the SMBR model described in the appendix B.4, the solution of the TMBR continuous model can be based on approximating the spatial gradients by finite differences. If the boundary conditions are implemented by algebraic equations, the solution via integration of the resulting differential algebraic equation system allows to calculate the steady-state profiles.

In order to compare the TMBR with the SMBR it is essential to quantify numerical errors of both schemes. Therefore, negligible errors of the integrator schemes are assumed and methods to evaluate the numerical error of the spatial discretization scheme are derived.

At first, the energy balance of a dispersive model as used in the SMBR is evaluated followed by the countercurrent model. Relations to quantify numerical dispersion for the transformation from SMBR to TMBR are finally derived. Since only errors induced by the transport terms are of interest, the reaction term, heat losses and possible errors introduced by the boundary conditions are not considered in the analysis below. It is noteworthy to mention that boundary conditions can have a large influence on the solution of dispersive models, in

particularly when dispersion becomes dominating.[2]

3.2.1. The Fixed-Bed Dispersive Model

The analysis is performed for the balance (3.46) using simple up-wind approximation for the first order spatial gradients and central scheme for the dispersive transport. First, the spatial domain is discretized in N_p nodes with finite increments $\Delta z = \frac{L_R}{N_p - 1}$ yielding (3.47).

$$(\rho c_p)_m \frac{\partial T}{\partial t} = -u_g (\rho c_p)_g \frac{\partial T}{\partial z} + \lambda \frac{\partial^2 T}{\partial z^2} \tag{3.46}$$

$$(\rho c_p)_m \frac{\partial T}{\partial t} \approx -u_g (\rho c_p)_g \frac{T_n - T_{n-1}}{\Delta z} + \lambda \frac{T_{n+1} - 2T_n + T_{n-1}}{\Delta z^2} \tag{3.47}$$

It is instructive to define a numerical or grid Peclet number $\mathrm{Pe_n}$ as:

$$\mathrm{Pe_n} = \frac{u_g (\rho c_p)_g \Delta z}{\lambda} \tag{3.48}$$

and expansion of (3.46) with $\frac{\Delta z^2}{\lambda}$ yields a differential equation, in which the left hand side is abbreviated by f_D in equation (3.49):

$$f_D = -\mathrm{Pe_n} \Delta z \frac{\partial T}{\partial z} + \Delta z^2 \frac{\partial^2 T}{\partial z^2} \tag{3.49}$$

And from difference equation (3.47) one obtains the difference equation (3.50) of the numerical scheme, abbreviated by f_n:

$$f_n = T_{n+1} + (-2 - \mathrm{Pe_n}) T_n + (\mathrm{Pe_n} + 1) T_{n-1} \tag{3.50}$$

In the next step, the temperatures of the grid, T_{n+1} and T_{n-1}, are replaced by the corresponding Taylor series defined as:

$$T_{n+1} \approx T_n + \frac{\partial T}{\partial z}\Big|_n \frac{\Delta z}{1!} + \frac{\partial^2 T}{\partial z^2}\Big|_n \frac{\Delta z^2}{2!} + \frac{\partial^3 T}{\partial z^3}\Big|_n \frac{\Delta z^3}{3!} + \ldots + \mathcal{O}(\Delta z^4) \tag{3.51}$$

$$T_{n-1} \approx T_n - \frac{\partial T}{\partial z}\Big|_n \frac{\Delta z}{1!} + \frac{\partial^2 T}{\partial z^2}\Big|_n \frac{\Delta z^2}{2!} - \frac{\partial^3 T}{\partial z^3}\Big|_n \frac{\Delta z^3}{3!} + \ldots + \mathcal{O}(\Delta z^4) \tag{3.52}$$

Below, a simplified notation is used, in which ∇ represents the first order derivative in the space, and ∇^n for the n-th order derivatives with respect to the spatial coordinate.[3]

Replacing in the difference formula (3.50) the variables T_{n+1} and T_{n-1} by the corresponding

[2] Consult Westerterp et al. [65] regarding types of BCs and effects in the dispersion model.

[3] Notation used here:

$$\nabla = \frac{\partial}{\partial z} \qquad \nabla^n = \frac{\partial^n}{\partial z^n}$$

Taylor series (3.51, 3.52) yields the following expression (3.53):

$$f_n = -\mathrm{Pe_n}\nabla T\Delta z + (2+\mathrm{Pe_n})\nabla^2 T\frac{\Delta z^2}{2} - \mathrm{Pe_n}\nabla^3 T\frac{\Delta z^3}{6} + (2+\mathrm{Pe_n})\nabla^4 T\frac{\Delta z^4}{24} + \ldots + \mathcal{O}(\Delta z^5) \quad (3.53)$$

The higher order terms ($\mathcal{O}\left(\Delta z^5\right)$) have been skipped. Subtraction of the original differential equation (3.49) from the expanded difference equation (3.53) leads to the following expression, in which the first order derivative has dropped out.

$$f_n - f_D = \frac{\mathrm{Pe_n}\Delta z^2}{2}\nabla^2 T - \mathrm{Pe_n}\frac{\Delta z^3}{6}\nabla^3 T + (2+\mathrm{Pe_n})\frac{\Delta z^4}{24}\nabla^4 T + \ldots + \mathcal{O}(\Delta z^5) \quad (3.54)$$

The numerical truncation error Θ_n can be specified in the original dimension, thus after expansion by $\left(\frac{\lambda}{\Delta z^2}\right)$ and truncation of terms of the order of 4:

$$\Theta_n = u_g(\rho c_p)_g\frac{\Delta z}{2}\nabla T^2 - \frac{\Delta z^2}{6}\left(u_g(\rho c_p)_g\nabla^3 T - \frac{\lambda}{2}\nabla^4 T\right) + u_g(\rho c_p)_g\frac{\Delta z^3}{24}\nabla T^4 + \ldots + \mathcal{O}(\Delta z^4) \quad (3.55)$$

Apparently, the truncation error of up-winding combined with central difference scheme is proportional to Δz in the first instance, while higher order terms are of order 2 $\left(\mathcal{O}\left(\Delta z^2\right)\right)$, or in short:

$$\Theta_n = \frac{u_g(\rho c_p)_g\Delta z}{2}\nabla^2 T + \ldots + \mathcal{O}\left(\Delta z^2\right) \quad (3.56)$$

Finally the numerical error can be implemented in the original differential equation (3.46) to obtain:

$$(\rho c_p)_m\frac{\partial T}{\partial t} = -u_g(\rho c_p)_g\frac{\partial T}{\partial z} + \left(\lambda + \frac{u_g(\rho c_p)_g\Delta z}{2}\right)\frac{\partial^2 T}{\partial z^2} + \ldots + \mathcal{O}(\Delta z^2) \quad (3.57)$$

This analysis reveals that the *simulated heat conduction* , λ_{sim}, is proportional to the space increment Δz and the physical convection of the gas phase with the velocity u_g. Assuming a uniform grid for the reactor domain, $\Delta z = \frac{L_R}{N_p-1}$, the simulated heat conduction can be expressed in the following way:

$$\lambda_{\mathrm{sim}} = \lambda + u_g(\rho c_p)_g\frac{\Delta z}{2} = \lambda + u_g(\rho c_p)_g\frac{L_R}{2(N_p-1)} \quad (3.58)$$

Thereby a fraction of the *numerical heat conduction* defined by $\lambda_n = u_g(\rho c_p)_g\frac{\Delta z}{2}$ can be considered. With the Peclet number for heat transport defined as:

$$\mathrm{Pe_h} = \frac{u_g\rho_g c_{p,g}L_R}{\lambda} \quad (3.59)$$

a relation between numerical Peclet number and physical Peclet number can be specified

according to:

$$\mathrm{Pe_h} = (N_p - 1)\mathrm{Pe_n} = \frac{L_R}{\Delta z}\mathrm{Pe_n} \tag{3.60}$$

It is further instructive to relate the simulated heat conduction (3.58) to the real *physical heat conduction* λ.

$$\frac{\lambda_{\mathrm{sim}}}{\lambda} = 1 + \frac{\mathrm{Pe_n}}{2} = 1 + \frac{\mathrm{Pe_h}}{2(N_p - 1)} = 1 + \frac{\mathrm{Pe_h}}{2}\frac{\Delta z}{L_R} \tag{3.61}$$

Physical and simulated heat conduction are identical if Δz tends to zero. And, what is more important, for a rather convective transport (large $\mathrm{Pe_h}$), it becomes increasingly difficult to represent realistic heat conduction with the uniform scheme used. For that reason, it is known that convective dominated systems can only be well approximated with very small Δz.

However, partial differential equations with a parabolic character on the other hand can be efficiently and precisely calculated, if the numerical dispersion is adjusted to the physical dispersion. As a first approximation, it is possible to define a maximum space increment Δz_m or a minimum number of nodes N_m, respectively, for exactly the case where these two sources of dispersion match. According to (3.61) assuming $\lambda_n = \lambda$ one obtains[4]:

$$\mathrm{Pe_n} = 2 \qquad \Delta z_m = \frac{2L_R}{\mathrm{Pe_h}} \qquad \text{or} \qquad N_m = \frac{\mathrm{Pe_h}}{2} + 1 \tag{3.62}$$

For this specific case, the numerical Peclet number $\mathrm{Pe_n}$ is 2, which corresponds to the stage or cascade model for larger stage numbers. In the literature it is given for the stage model $\frac{Pe}{2} = N_m - 1$, see e.g. Westerterp et al. [65], which immediately results from equation (3.62). Figure 3.3 illustrates these relationships.

Below the Peclet number $\mathrm{Pe_n}$ of 2, it is possible to exactly simulate any physical dispersion. Thereby the physical dispersion λ needs a correction by a portion λ^* yielding a modified value λ_{mod} to be implemented in the model. It holds for the correction $\lambda_{\mathrm{sim}} - \lambda^* = \lambda$ and for the modified value $\lambda_{\mathrm{mod}} = \lambda - \lambda^*$:

$$\frac{\lambda^*}{\lambda} = \frac{\mathrm{Pe_n}}{2} \qquad \text{or} \qquad \frac{\lambda_{\mathrm{mod}}}{\lambda} = 1 - \frac{\mathrm{Pe_n}}{2} \tag{3.63}$$

As long as $\mathrm{Pe_n} < 2$ is ensured. The main results of this approach are:

- The suggested scheme is first order accurate and the numerical dispersion is proportional to the grid Peclet number $\mathrm{Pe_n}$.
- There exists a critical Peclet number $\mathrm{Pe_n} = 2$, which corresponds to the conventional cascade model (eq. (3.62)).
- Above $\mathrm{Pe_n} = 2$ the simulated dispersion is always composed of physical and numerical dispersion.
- Below $\mathrm{Pe_n} = 2$ it is possible to accurately simulate the physical dispersion using (3.63).

[4] $\lambda_{\mathrm{sim}} = \lambda + \lambda_n = 2\lambda$ thus $2 = 1 + 1/2\mathrm{Pe_n}$ yielding $4 = 2 + \mathrm{Pe_n}$ which is $\mathrm{Pe_n} = 2$.

3.2.2. The Countercurrent Model

The preceding method is applied to the transport term in the TMBR countercurrent model. Differential equation (3.64) and the difference equation (3.65) of the TMBR are given below. The solid flow is approximated by downwind scheme and one obtains (3.65):

$$(\rho c_p)_m \frac{\partial T}{\partial t} = -u_g(\rho c_p)_g \frac{\partial T}{\partial z} + u_s(\rho c_p)_g \frac{\partial T}{\partial z} + \lambda \frac{\partial^2 T}{\partial z^2} \tag{3.64}$$

$$\approx -u_g(\rho c_p)_g \frac{T_n - T_{n-1}}{\Delta z} + u_s(\rho c_p)_g \frac{T_{n+1} - T_n}{\Delta z} + \lambda \frac{T_{n+1} - 2T_n + T_{n-1}}{\Delta z^2} \tag{3.65}$$

Two numerical Peclet number, $\mathrm{Pe_n}$ and $\mathrm{Pe_{ns}}$, are defined to account for gas and solid phases separately:

$$\mathrm{Pe_n} = \frac{u_g(\rho c_p)_g \Delta z}{\lambda} \qquad \mathrm{Pe_{ns}} = \frac{u_s(\rho c_p)_g \Delta z}{\lambda} \tag{3.66}$$

Expansion by $\frac{\Delta z^2}{\lambda}$ yields for the differential equation (3.64):

$$f_D = -\mathrm{Pe_n} \nabla T \Delta z + \mathrm{Pe_{ns}} \nabla T \Delta z + \Delta z^2 \nabla^2 T \tag{3.67}$$

and for the difference equation (3.65)

$$f_n = (\mathrm{Pe_{ns}} + 1)\, T_{n+1} + (-2 - \mathrm{Pe_n} - \mathrm{Pe_{ns}})\, T_n + (\mathrm{Pe_n} + 1)\, T_{n-1} \tag{3.68}$$

After implementation of the Taylor series and some rearrangement the truncation error in its compact form reads:

$$\Theta_{ns} = \left(u_s(\rho c_p)_g + u_g(\rho c_p)_g\right) \frac{\Delta z}{2} \nabla^2 T + \ldots + \mathcal{O}(\Delta z^2) \tag{3.69}$$

The scheme is first order accurate, whereby the numerical dispersion is determined by the velocity of both phases. For the simulated heat conduction λ_{sim} it is defined:

$$\frac{\lambda_{\mathrm{sim}}}{\lambda} = 1 + \frac{\mathrm{Pe_n} + \mathrm{Pe_{ns}}}{2} = 1 + \frac{\mathrm{Pe_h} + \mathrm{Pe_{hs}}}{2(N_p - 1)} = 1 + \frac{\mathrm{Pe_h} + \mathrm{Pe_{hs}}}{2} \frac{\Delta z}{L_R} \tag{3.70}$$

In equation (3.70) the heat Peclet number of the solid phase $\mathrm{Pe_{hs}}$ relates the convective solid transport to the apparent physical dispersion.

$$\mathrm{Pe_{hs}} = \frac{u_s(\rho c_p)_s L_R}{\lambda} = \mathrm{Pe_{ns}} \frac{L_R}{\Delta z} \tag{3.71}$$

This is an artificial number only constructed for the analysis of numerical errors.

Again, one can identify a criterion which yields a dispersion corresponding to a stage or cascade model:

$$\mathrm{Pe_n} + \mathrm{Pe_{ns}} = 2 \qquad \Delta z_m = \frac{2L_R}{\mathrm{Pe_h} + \mathrm{Pe_{hs}}} \qquad \text{or} \qquad N_m = \frac{\mathrm{Pe_h} + \mathrm{Pe_{hs}}}{2} + 1 \tag{3.72}$$

Similar to (3.63), a modified dispersion can be defined in order to simulate the physical dispersion exactly.

$$\frac{\lambda^*}{\lambda} = \frac{\mathrm{Pe_n} + \mathrm{Pe_{ns}}}{2} \qquad \frac{\lambda_{\mathrm{mod}}}{\lambda} = 1 - \frac{\mathrm{Pe_n} + \mathrm{Pe_{ns}}}{2} \tag{3.73}$$

This is restricted to the situation $\mathrm{Pe_{ns}} + \mathrm{Pe_n} < 2$. Above this limit the simulated dispersion is given by (3.70). Finally, the numerical induced dispersion of both models TMBR and SMBR

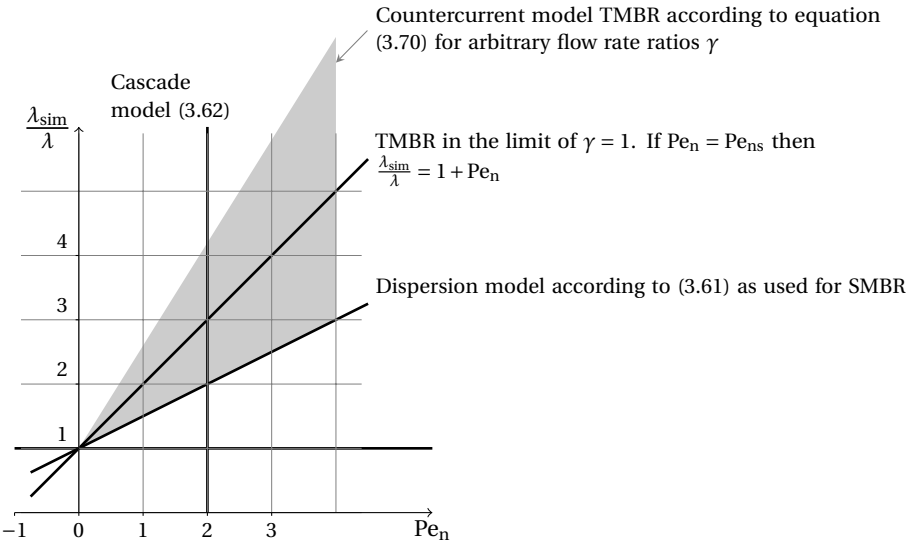

Figure 3.3.: Evaluation of the numerical dispersion generated during solving the energy balance for SMBR and TMBR models based on a finite difference schemes of first order accuracy. The reduced simulated dispersion $\lambda_{\mathrm{sim}}/\lambda$ is given as a function of the numerical Peclet number $\mathrm{Pe_n}$ with respect to the fluid phase velocity. The cascade model represents a limiting case, below physical dispersion can be simulated exactly, above the simulated dispersion is composed of a physical and a numerical part.

can be related by inspection of (3.72) and (3.62), respectively. In terms of space increments, Δz, or a total grid number, N_p, one obtains:

$$\Delta z_{\mathrm{TMBR}} = \frac{\mathrm{Pe_h}}{\mathrm{Pe_h} + \mathrm{Pe_{hs}}} \Delta z_{\mathrm{SMBR}} \tag{3.74}$$

$$N_{p,\mathrm{TMBR}} = \frac{\mathrm{Pe_h} + \mathrm{Pe_{hs}} + 2}{\mathrm{Pe_h} + 2} N_{p,\mathrm{SMBR}} \tag{3.75}$$

These relations between the dispersive model as the basis of SMBR dynamic calculations and the countercurrent model of the TMBR model are valid for arbitrary solid phase velocities. Note, that only if the Peclet number $\mathrm{Pe_{hs}}$ is nil, the numerical schemes match exactly.

It is important to understand that the solid phase dispersion stems only from the numerical error of the finite difference approximation and is completely unphysical. But with (3.74) or (3.75) it is possible to match the numerical dispersion of both models. In principle, the TMBR needs a finer numerical mesh in order to represent compatible dispersion effects of the SMBR.

For simplification it is suggested to assume a flow rate ratio of one, in which the convective

transport of gas and solid balance (eq. (3.38)).

$$\gamma = 1 \qquad \rightarrow \qquad u_s(\rho c_p)_s = u_g(\rho c_p)_g \qquad \rightarrow \qquad \mathrm{Pe_h} = \mathrm{Pe_{hs}} \tag{3.76}$$

In this case the Peclet numbers match and it can be defined for the space incrementation:

$$\Delta z_{\mathrm{TMBR}} = \frac{1}{2}\Delta z_{\mathrm{SMBR}} \qquad \text{or} \qquad N_{p,\mathrm{TMBR}} = 2N_{p,\mathrm{SMBR}} \tag{3.77}$$

Thus, a factor of two between the space increment or the grid number, respectively, is an appropriate value in order to establish compatible numerical dispersion in both models. This result applies also for the stage model [102]. The main results obtained are:

- The continuous model of the countercurrent TMBR does not include a solid phase dispersion – the transport is solely convective. The numerical approximation introduces an additional dispersion.
- Mesh refinement for the TMBR model is required to match the numerical dispersion of both models. A factor of two between the uniform meshes is a reasonable value based on the condition of a flow rate ratio of $\gamma = 1$.

3.2.3. Evaluation of the Numerical Method

As long as the character of the equation remains parabolic, the suggested finite difference scheme is appropriate for the representation of the physical dispersion. For convection dominated problems either a very fine spatial grid resolution is required, or alternatives numerical techniques need to be considered. E.g. adaptive grids, flux limiter finite volume methods, essentially non-oscillating schemes and so forth [103–105].

The advantage of the simple scheme chosen is the good convergence and stability due to the up-winding for arbitrary Peclet numbers $\mathrm{Pe_h}$, but on the cost of precision. With the derived equations it is possible to calculate the apparent simulated dispersion correctly. Concerning calculation times, the simple scheme often outperforms the various high resolution methods, which operate with substantial numerical overhead in order to meet those high precisions. Thus, the stability and speed of up-winding are essential advantages in respect to the simulation of cyclic processes. Moreover, the numerical error is acceptable, since other sources of errors can have a much larger impact on the solution, for instance:

- Errors in the model, because the radial resolution, the discrimination in different phases and detailed chemistry are omitted (model depth).
- Errors in parameters, because of the uncertainties in correlations and in the estimated parameters (parameter uncertainties).

In this work numerical errors of the simple scheme are accepted in order to speed up the simulation of the SMBR, and with transformation equations, a comparison with the TMBR is readily available. Finally, the calculation of the steady state using the TMBR model is by a factors of 100 – 150 faster than the dynamic simulations to obtain the cyclic steady state of

the SMBR model. This renders the TMBR model well suited to perform systematic parameter studies.

3.3. Steady State Profiles of the TMBR Model

Figure 3.4 illustrates the steady state profiles for the TMBR model for different grid numbers, N_p, ranging from 75 to 2400 nodes. The temperature profiles of the TMBR model shows an asymmetric bell shape. The maximum temperature increases rapidly to the maximum value at the reactor entrance and then declines towards the reactor outlet. Complete conversion is already achieved close to the inlet.

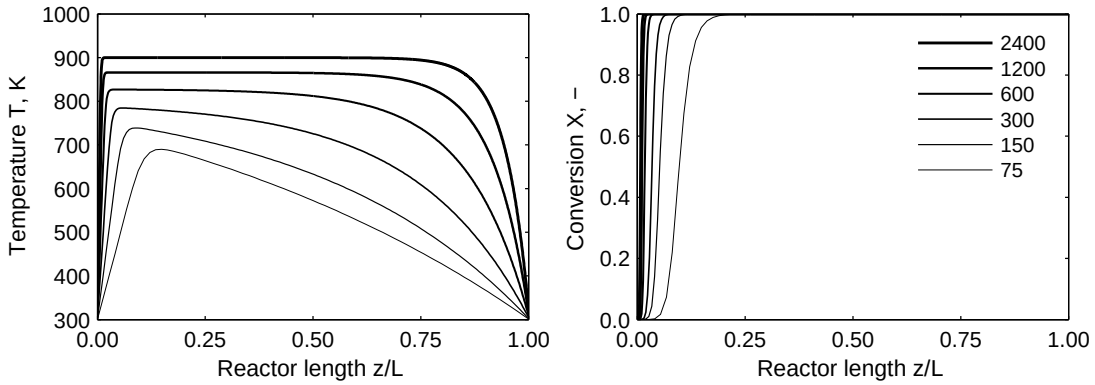

Figure 3.4.: Steady State profiles of the TMBR model for a series of grid nodes N_p, left temperature profiles and right conversion profiles (model B.3 for $\gamma = 1$ according to eq. (3.77)).

The number of nodes adjusting the additional dispersion in the model has a large influence on the temperature and conversion. Less nodes result in a significantly lower maximum temperature and the maximum is shifted towards the center of the reactor domain, the concentration front is shifted accordingly.

Figure 3.5 presents the relation between the number of nodes as a function of the numerical Peclet number. For typical cases in this work, a numerical Peclet number $\mathrm{Pe_n}$ of 2 would require 1200 nodes for the SMBR. With eq. (3.77) it is possible to reach the cascade criterion (eq. (3.72)) at 2400 nodes for the TMBR. However, this large number is numerically to expensive. Therefore a number of 300 was typically used for the TMBR and 150 for the SMBR, respectively.

Another interesting situation arises in case of a flow rate ratio of one (eq. (3.77)). The convective terms in the energy balance drop out and the remaining energy transport is determined by heat conduction only (eq. (3.13)). From a theoretical point of view, it could be thought of a complete absence of heat conduction. Then only the source term would remain and the energy transport would be nil. As a result, one would observe an infinitely large temperature increase, which is of course not a realistic picture, but indicates the main parameters to adjust temperatures in the reactor (convection, conduction and heat release by reaction).

Another difference to the SMBR model has to be addressed. The energy balance of the

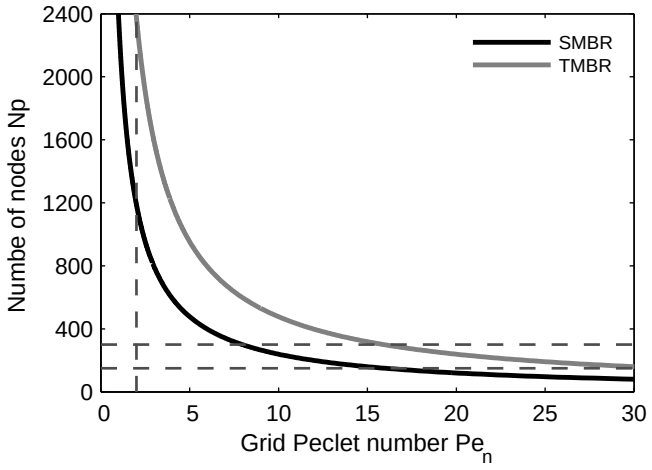

Figure 3.5.: Example for the required number of nodes as a function of the numerical Peclet number, based on $\gamma = 1$ according to eq. (3.77).

TMBR (eq. (3.13)) is somewhat artificial in that the outlet temperature is assumed to coincide with the inlet temperature. This, however, violates the integral energy balance, which has already been applied to evaluate the outlet temperatures of the SMBR model (equation (2.52)). It was shown in section 2.3.3, that time averaged temperatures are in accordance with the adiabatic temperature rise valid for the corresponding steady state system, thus satisfying energy conservation. This condition is not fulfilled in the TMBR model when assuming identical temperatures, which leads to an overestimation of the energy accumulation. As a correction, the outlet boundary condition should account for the additional energy flux. A temperature rise depending on the achieved conversion, e.g. $\left(T(z = L_R) = T^{\text{in}} + \Delta T_{\text{ad}} \cdot X(z = L_R)\right)$, could be implemented.

3.4. Evaluation of the TMBR Limit Case

In the limit of large number of segments in the SMBR the temperature and concentration profiles should be represented by the TMBR model. This was investigated for an increased number of segments of N_{Seg} of 3, 5 and 10 for the SMBR as shown in figures 3.6 and 3.7. The comparisons are based on the profiles at half of the switching period and when the feed position is in front of the first segment.

With increased number of segments convergence in the TMBR limiting case is achieved. For smaller number of segments, the switching time is larger and the fronts move along larger distances until switching occurs. This means on the other hand, that for larger number of segments the fronts move only short distances, and in the limiting case a standing wave would have been established. This limit is represented by the TMBR accordingly.

This holds also for the second example with a larger switching time in figure 3.7. This time, the leading thermal front is much steeper, which is also well represented by the TMBR model. Deviations of about $5 - 10\,^{\circ}\text{C}$ between SMBR and TMBR differing according to process conditions have been found throughout these investigations.

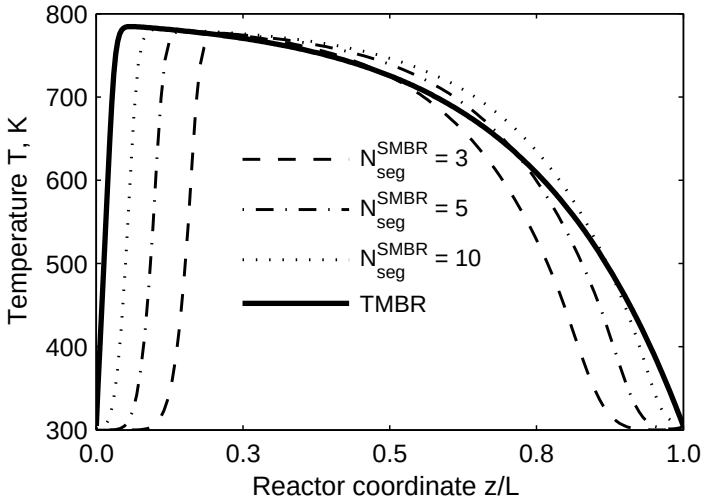

Figure 3.6.: Comparison between TMBR limiting case (continuous line) and SMBR for different segmentations of 3, 5 and 10 segments ($\gamma = 1.0$, with a feed concentration of $\Delta T_{ad} = 60$ K, SMBR model section B.1, TMBR section B.3).

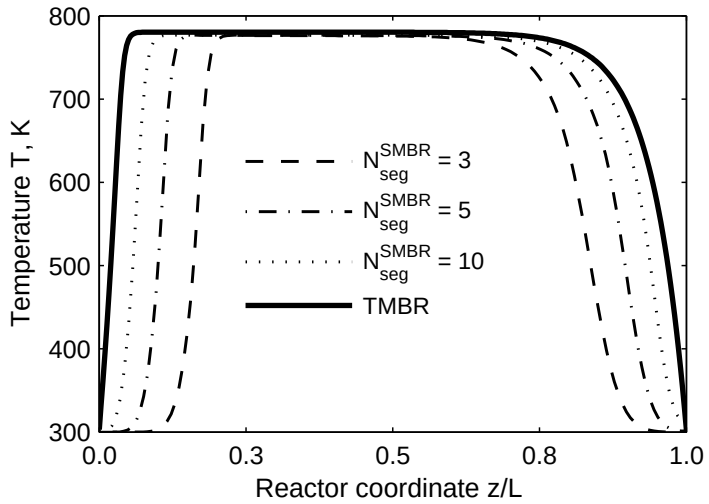

Figure 3.7.: Comparison between TMBR limiting case and SMBR model for different segmentations ($\gamma = 1.05$, with a feed concentration of $\Delta T_{ad} = 60$ K, SMBR model section B.1, TMBR section B.3).

3.5. Effect of Flow Rate Ratio and Heat Losses

3.5.1. Flow Rate Ratio

According to equation (3.45) the impact of the countercurrent solid flow can be compared to SMBR switching times. In figure 3.8 are presented temperature and conversion profiles for different flow rates of the solid phase given in terms of flow rate ratios.

As explained already in section 2.3.3, only a certain window of switching times is accessible to achieve ignited states. For the example considered, the window is between approximately $0.93 < \gamma < 1.13$, outside only extinguished solutions can be obtained. In this range, the solid flow has a significant influence on the internal temperature and conversion profiles. With increasing the solid flow rate, meaning a decrease in γ, the temperature profiles lean to the left towards the inlet boundary. This is accompanied with a decrease in the maximum reactor temperature and a breakdown of the dispersive thermal front.

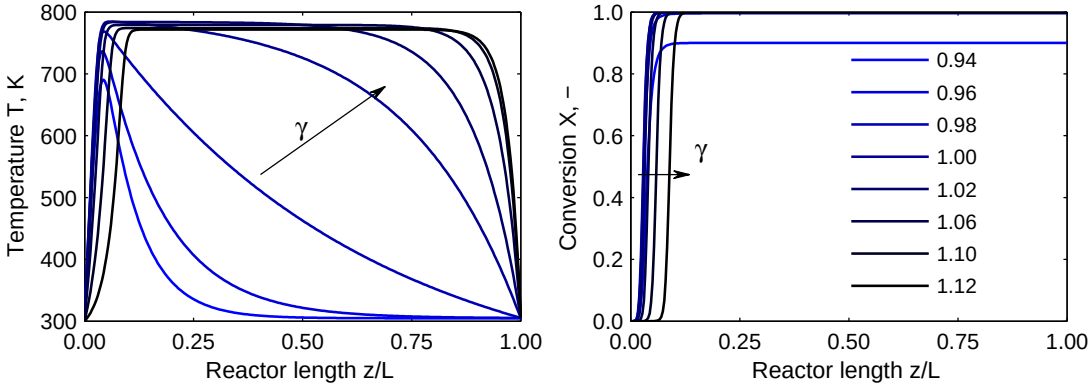

Figure 3.8.: Influence of the solid flow rate in terms of γ on the temperature and conversion profiles using the TMBR model ($\Delta T_{ad} = 60$ K, TMBR model in section B.3).

Contrary, if the solid phase velocity is reduced, the reaction and the dispersive thermal front are shifted to the reactor outlet and complete conversion can be achieved even close to the ignition limit.

Is is also important to stress that for $\gamma = 0.94$ a stable ignited state of the reactor exists, which is characterized by significantly lower conversion. This fact will be treated in the next chapter in detail.

3.5.2. Heat Losses

Heat losses are interesting to analyze because of two reasons. First, in lab scale reactors they often can not be avoided, and secondly, it is important to consider the option to cool down the reactor for safety reason, e.g. to prevent catalyst deactivation and thermal runaway. Another interesting option can be seen in heat generation.

The influence of distributed heat losses was studied by a systematic increase of the wall heat transfer coefficient in the range of $0 < h_w < 4$ W/m^{2}K. A constant wall temperature at ambient conditions was assumed and two different flow ratios, $\gamma = 1$ and $\gamma = 1.05$, were

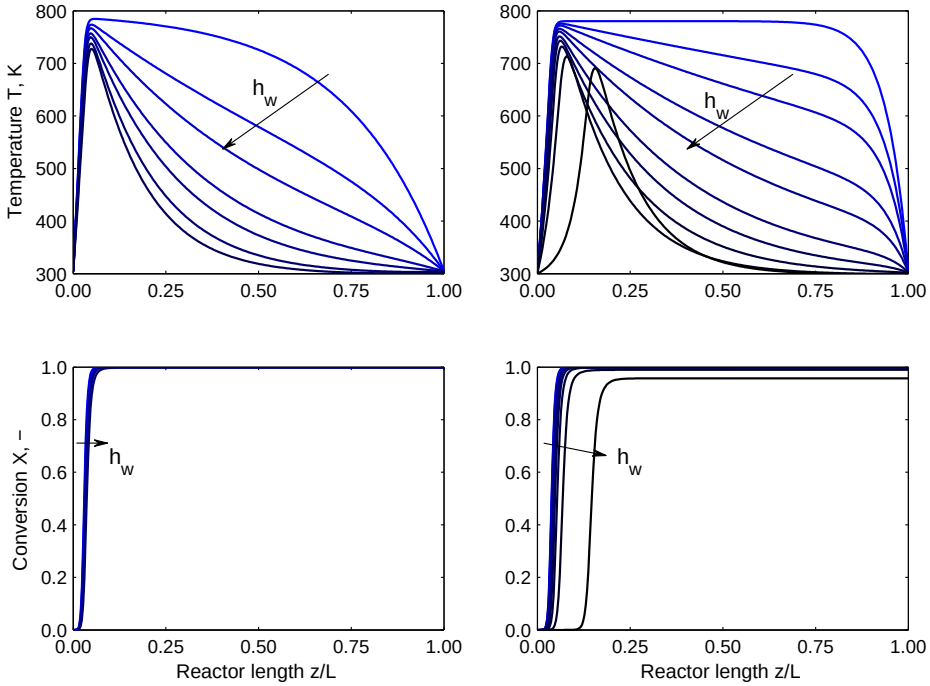

Figure 3.9.: Influence of the heat transfer coefficient on the internal temperature and conversion profiles of the TMBR model. In case of $\gamma = 1.0$ (left) the range $h_w = (0,1,2,3,4,6,10,14) \cdot 10^{-4}$ kW/m^{2}K and in case of $\gamma = 1.05$ (right) the range $h_w = (0,1,2,3,4,6,10,14,20,30,40) \cdot 10^{-4}$ kW/m^{2}K is considered.

compared (figure 3.9).

Clearly, heat losses have a significant influence on the temperature and conversion profiles. Particularly the dispersive thermal fronts are flattened out and, beyond a certain heat transfer coefficient, reactor extinction sets in. For the larger flow rate ratios ($\gamma = 1.05$) higher heat losses are allowed up to 4 W/m^{2}K, while in case of $\gamma = 1.0$ and already 0.14 W/m^{2}K the reactor extinguishes. Another important observation is, that close to the ignition limit the peak temperature is shifted towards the center, the temperature profile shows another inflection point and the corresponding conversion falls significantly below unity.

A deeper understanding of these effects is possible with the help of nonlinear analysis, which is treated in the next chapter.

3.6. Summary

The advantage of the reduced TMBR model developed in this work is a much faster calculation than for the periodic SMBR model, while losing some information about the process. The idea of the model reduction is to approximate the simulated counter current process of the SMBR by a hypothetical true counter current between the gas and the solid phase.

At first, the TMBR was developed as a stage model, which revealed that the solid phase is inherently subject to unphysical backmixing. This aspect required a detailed evaluation, since the artificial dispersion largely affects the result of the TMBR approximation when comparing to the periodic SMBR model.

Therefore, in order to study convective and dispersive transport separately, a continuous TMBR model was derived. Either boundary conditions of third kind or the trivial boundary conditions with equal inlet temperatures at both domain boundaries can be applied. Appropriate transformation equation for switching time into the solid phase velocity were derived as well.

Even though this continuous TMBR model is equipped with a pure convective flux, additional numerical dispersion due to the spatial discretization also leads to an artificial numerical dispersion. Quantification of numerical errors of both discretized continuous models, SMBR and TMBR, were considered to improve the precision of the approximation. The truncation errors of the discretized models were analyzed and relations to match the numerical dispersion in both models given. In principle, grid refinement of the TMBR model is required to achieve compatibility to the SMBR model.

Larger number of segments in an SMBR were investigated with dynamical simulations and the results compared with the TMBR model. Maximum temperatures and the qualitative shape of the internal profiles are well represented by the TMBR model. This was demonstrated for different flow rates.

Finally, parametric studies regarding to the effects of the solid phase velocity and heat losses were presented. The TMBR model shows ignited states for a certain window of flow rate ratios but also a decline of the conversion close to ignition limits. In particular, these results motivated to carry out a thorough analysis of reactor multiplicities in order to reveal parametric sensitivities and to identify suitable process conditions. The results obtained are summarized in the next chapter.

4. Nonlinear Analysis of Single Reaction Systems

The identification of the ignition limits of the SMB reactor, specifically ignition-extinction phenomena, is an essential step for understanding parameter sensitivity and the development of suitable control concepts for a SMBR. The corresponding theoretical framework is treated in the field of nonlinear analysis of dynamical systems making use of bifurcation and singularity analysis tools. These methods help to reveal the complexity of dynamical systems, which may exhibit multiple steady states, oscillations and also chaotic behavior.

In chemical systems divers complex behavior on different scales has been observed for long time. For instance, the *Belousov-Zhabotinsky* reaction taking place in homogeneous solution represents a famous example exhibiting chaotic oscillations [106]. Ertl [107] showed remarkable results for the CO oxidation on platinum facets and many other works have evolved in this field adding new insight into nonlinear phenomena, recently with a focus on spatio-temporal patterns arising in distributed reactive systems [108, 109].

It is also well known that multiple steady states can occur at reactor scale with a significant impact on conversion and temperatures attained, documented for instance by Bilous et al. [110], Padberg et al. [111], Uppal et al. [112] and Schmitz [113]. Further interesting contributions are Gilles et al. [114], Subramanian et al. [115] and others [116, 117] on coupled systems. It is often desired to control and stabilize the reactor in specific states. Several studies in this field also deal with controller tuning for chemical processes with multiplicities [118–120] allowing operation near unstable states [121].

The reverse-flow reactor has been widely characterized regarding multiplicities [122, 123]. Ignited states are characterized mainly by complete conversion at high temperatures, while in extinguished states there is no significant reactant conversion. Also several studies have been carried out for SMBR like reactors, e.g. by Barresi's group [61, 124–127] and by the group of Sheintuch [58, 128]. Similar to the reverse-flow ignited and extinguished states occur, but the effect of the switching time seems to be more complex.

This work will especially make use of the analysis of local bifurcations and higher order singularity using numerical parameter continuation techniques exploiting mainly the TMBR model. The investigation attempts to construct parameter windows framing regions of similar qualitative reactor operation. While many studies are often concerned with only one or two parameter maps, this work will go beyond these dimensions adding new insights to the reactor operating limits.

As a prerequisite, the first part of this chapter is concerned with the description of the methods and definitions. Then, multiplicities arising with respect to different process parameters are introduced. It is also shown that SMBR and TMBR exhibit similar bifurcation phenomena. This motivated the examination of higher order singularities exploiting the

TMBR model, which helps to identify process limits required for reactor design and control.

4.1. Introduction to Complex Systems and Numerical Nonlinear Analysis

4.1.1. Preliminaries

Concerning the notion of a "system", it may represent a variety of observations in biological, physical, chemical or even ecological and behavioral context. Such real world systems have shown complex behavior, for instance, sudden changes in the states, periodic and even chaotic motions of the systems states. See for introductory books e.g. Epstein et al. [106], Hilborn [129] and Aris [130]. The reason for the complex behavior can be attributed to the nonlinearity of the systems. Two important phenomena are typically associated with the behavior observed:

- A large sensitivity with respect to the initial state of the system[1], meaning a strong dependence on the system's history, where small incidents in the beginning can lead to very different outcomes.
- A large sensitivity with respect to control parameters, which may lead to sudden changes in the qualitative and quantitative behavior of the system as the result of small changes in these parameters.

Since nature provides us with an inherent nonlinearity, simple linear analysis often fails and a deeper understanding of the underlying phenomena should be acquired using nonlinear analysis tools. Some important names building the fundamentals are Thom [132] and Arnold [133]. A vast literature is available with a predominantly mathematical treatment of this topic, e.g. Golubitsky et al. [134], Kuznetsov [135], Seydel [136] and other [137–139].

The bifurcation phenomena is concerned with changes of the solution structure of the nonlinear system as a result of changing a parameter. Of particular interest is the transition behavior for specific control parameters. Typically the calculation of the solution is based on parameter continuation, which is a numerical method for a measure of a variable along a bifurcation parameter. As a result, one obtains bifurcation diagrams graphing a system state, e.g. concentration or temperature, over the bifurcation parameter. A certain number of solution branches may be found, which can show crossings or multiple solution, but even no solution at all.

The stability of the solution branches is an important property which allows for an interpretation of the system's behavior in the neighborhood of the branches. If the branch is stable, the system is mainly[2] attracted to the solution, otherwise for unstable branches the system is

[1] which is often pictured as the "butterfly effect" going back to Lorenz, "*Predictability: Does the flap of a butterfly's wings in Brazil set off a tornado in Texas?*". Lorenz was actually referring to the unpredictable effect of unknowns and errors in the calculation of weather dynamics. This fact reveals the limitations of model predictability and numerical accuracy in (unstable) complex systems ("... errors in finer structure, having attained appreciable size, tend to induce errors in the coarser structure..." [131]). After popularity peaked in the 80th and early 90th accompanied by equivocal overstraining of the theory in various, more or less scientific fields, the methods are now well incorporated in natural science and engineering coping with complex systems.

[2] Stability deserves a broader discussion, but here it is meant Lyapunov stability of a solution branch.

repelled.

Remarks About the Bifurcation of Periodic Systems Many systems can be described by a set of ordinary differential equations, e.g. the TMBR model, where the fixed points represent unique temperature and conversion profiles. Even though this model is unforced – autonomous due to the absence of an explicit time dependency, periodicity can also be observed. An interesting example is the heat integrated circulation loop reactor [72, 140], where the system exhibits periodic modes without external forcing. In such system the transition from a stationary to periodic solution is characterized by *Hopf*-bifurcations.

In contrast, the forced SMBR is a non-autonomous periodic (discrete-time) system and the fixed point can be associated with a point of a Poincaré section. See appendix B.4.2 for details. The time dependence is explicitly introduced in the equations and the bifurcation analysis can be regarded as on the one parameter continuation of a fixed point of an appropriate *Poincaré* section. Such a numerical method is available in DIVA and allows for the calculation of stable and unstable solution branches via a shooting technique. For details of the method the work of Mangold [72] is recommended. This shooting method was used to compare the bifurcation diagram for both models, SMBR and TMBR investigated in section 4.2.2.

The next section deals with autonomous systems corresponding to the steady state of discretized form of the TMBR model (sec. B.3).

4.1.2. Concepts of Bifurcation and Singularity Theory

This section will briefly sketch the ideas of singularity analysis with the help of some introductory examples.

The first example explains the most simple type of bifurcation, the saddle or limit point, as illustrated in figure 4.1. Along the bifurcation parameter λ there exist either no solution or two solutions of the state x simultaneously. The point at which the transition occurs and the number of solution changes is the limit point. Stable solutions are found for the continuous line and unstable solutions on the intercepted line. This property originates from the analysis of the linearized system and provides a local information, whether a system tends to or away from a solution branch [136]. Arrows indicate the systems tendency. Such a qualitative picture allows for predicting the systems behavior in the neighborhood of the solution branches.

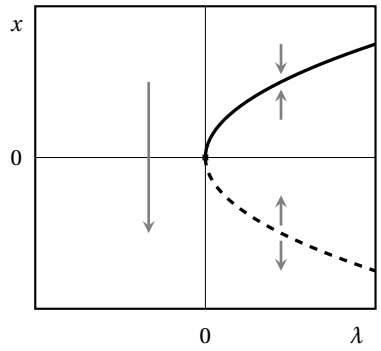

Figure 4.1.: Solution branches of the limit point.

A useful element of the analysis are *normal forms*, which are the simplest representatives of bifurcations. The normal form of the limit point is given by $\dot{x} = -x^2 + \lambda$ with the fixed points defined by a quadratic equation $0 = -x^2 + \lambda$ with respect to x. Solving for $\lambda = 0$ gives the limit point in the origin. Generally, normal forms can be used for description and classification of bifurcation phenomena.

Since physical models are typically equipped with more than one parameter, it appears to be interesting to extend the analysis to additional model parameters of interest. The system may now be described by a scalar function (f, x scalar) in a general form [136]:

$$\dot{x} = f(x, \lambda, \alpha_1 \ldots \alpha_k) \qquad \alpha \in \mathbb{R}^k \tag{4.1}$$

with a distinguished or characteristic bifurcation parameter, λ, and k additional parameters α. The fixed points of eq. (4.1) are defined by:

$$f(x, \lambda, \alpha_k) = 0, \tag{4.2}$$

which is satisfied for the solution branches in figure 4.1. For a singular solution, e.g. the limit point, the gradient is zero:

$$\frac{\partial f(x, \lambda, \alpha_k)}{\partial x} = 0 \tag{4.3}$$

Both equations, (4.2) and (4.3), represent the singular set and their projection in the (λ, α_k)-parameter space is associated with the bifurcation or catastrophe set [136]. For higher order singularities it is necessary to consider higher order derivatives, which is part of the software used in this work [141, 142]. Here, the one-parameter bifurcation is associated with the solution $x = x(\lambda)$. The singularity analysis on the other hand deals with description of a particular singular point, in the first instance the limit point, in an enlarged parameter space (λ, α_k). This means that the limit point is continued, e.g. in the plane (λ, α_1), which results in parameterized curve. If in the course of continuation a singularity of higher order is encountered, this particular point can be solved in $(\lambda, \alpha_1, \alpha_2)$ and so forth. In this work, often families of such curves are illustrated as they provide a better understanding of the interplay between parameters and the transition between qualitatively different solutions.

In what follows is a short survey of the approach described by Golubitsky et al. [134] using the methods provided by Krasnyk [142] to deal in a systematic manner with the question of identification and classification of singularities.

4.1.2.1. Reduction and Identification of Singularities

An important concept of the singularity analysis is the reduction of the a dynamical system of equations to a scalar equation, say $g(x, \lambda, \alpha)$, which possesses an equivalent bifurcation set to the original system. The technique is the *Lyapunov-Schmidt* reduction described e.g. in Golubitsky et al. [134, page 25][142]. It basically assumes a rank loss of Jacobian of the original system which appears in case of a limit point. This condition is exploited to state that under certain restrictions it is valid to analyze only the reduced scalar function g with respect to the set of parameters (λ, α) in order to describe singularities. Derivatives of g with respect to x and the model parameters are required for the analysis. A sufficient precision for the numerical approximation of these derivatives is essential for the method. This is provided by the software DIANA making use of symbolic differentiation. Moreover, it is possible to link those derivatives to normal forms representing certain types of bifurcations.

Normal forms are the simplest representatives of a class of equivalent bifurcation problems.

Table 4.1 lists the normal forms encountered in this work: the fold or limit point, the simple bifurcation, the isola center, the hysteresis and the pitchfork bifurcation. These normal forms are polynomials of a certain low order consisting of two monomials.

Table 4.1.: Classification of singularities, their normal forms and definitions.

Nomenclature	Codimension	Normal form	Recognition
Limit point (LP)	0	$\pm(x^2 \pm \lambda) = 0$	$g = g_x = 0$
Simple bifurcation (S_b)	1	$\pm(x^2 \pm \lambda^2) = 0$	$g = g_x = g_\lambda = 0$
Isola center (I_c)	1	$\pm(x^2 \pm \lambda^2) = 0$	$g = g_x = g_\lambda = 0$
Hysteresis (H)	1	$\pm(x^3 \pm \lambda) = 0$	$g = g_x = g_{xx} = 0$
Pitchfork (P)	2	$\pm(x^3 \pm \lambda x) = 0$	$g = g_x = g_{xx} = g_\lambda = 0$

The bifurcation problem is solved by recognizing the vanishing of low order derivatives, g_x, g_λ and g_{xx}, while maintaining non-zeros of (the known) intermediate order derivatives.

The normal forms are given in accordance to the numerical implementation [142], which differs slightly from the definitions documented in Golubitsky et al. [134, page 196] considering the signs of the monomials. This is the reason why it cannot be distinguished between the simple bifurcation and the isola center with this software. Solving this problem requires the analysis of the local environment of the singular point.

4.1.2.2. Unfolding and Classification of Singularities

The identification of a singularity based on derivatives is not always sufficient for its unique classification. For that purpose the *codimension* of a bifurcation as noted in table 4.1 is defined. This work follows the idea, in which the codimension corresponds to minimal number of so called unfolding parameters of the perturbed form of a specific singularity based on the reduced equation g, so called *imperfect bifurcations*.

Here it is considered a function G with a characteristic bifurcation parameter λ and a set of unfolding parameters α:

$$G(x, \lambda, \alpha) \tag{4.4}$$

The analysis is restricted to *versal unfolding* and following relation is assumed:

$$G(x, \lambda, 0) = g(x, \lambda) \tag{4.5}$$

In other words, a family of perturbations or deformations of the normal form of a bifurcation is considered, and by equation (4.5) only perturbations by adding parameters in form of monomials are assumed. A precise definition of the "*versal*" character can be found in Arnold [143]. Moreover, g may be perturbed, e.g. it holds that

$$g(x, \lambda) + p(x, \lambda) = 0 \tag{4.6}$$

and p is small, yielding qualitatively different bifurcation diagrams. Further it is assumed that there exist some unfolding parameters α, such that the family of functions (eq. (4.4)) is

equivalent to a perturbed form of g (eq. (4.6)). The minimal number of unfolding parameters required to describe all qualitatively different perturbations is equivalent to the codimension of a particular singularity. In this case G is a *universal unfolding*.

4.1.2.3. Universal Unfolding and Perturbed Normal Forms

Preliminary Example In order to illustrate what is meant with universal unfolding, the deformation of a normal form is investigated for the example of the hysteresis bifurcation. The corresponding normal form is given in table 4.1 as a third order polynomial ($x^3 - \lambda = 0$). A versal unfolding can be generated by introducing lower order monomials, as for example in equation (4.7):

$$x^3 + \alpha_2 x^2 + \alpha_1 x - \lambda = 0 \tag{4.7}$$

It is instructive to examine the qualitative solutions, the roots of the polynomial with respect to λ, as the α_k differ. The results are illustrated in figure 4.2 below. Left and right figure show

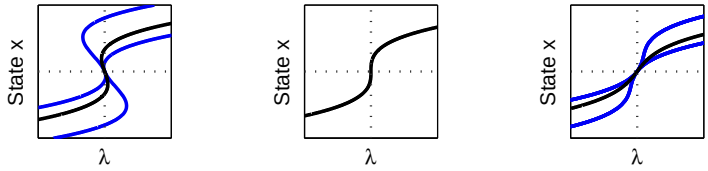

Figure 4.2.: Perturbations of the hysteresis. Left for $\alpha_1 < 0$ and $\alpha_2 \neq 0$ (blue lines) and $\alpha_2 = 0$ (black line). Right figure $\alpha_1 > 0$ and $\alpha_2 \neq 0$ (blue lines) and $\alpha_2 = 0$ (black line). The middle figure presents the normal form for $\alpha_2 = \alpha_1 = 0$.

the cases with $\alpha_k \neq 0$, the figure in the middle the normal form ($\alpha_k = 0$). The hysteresis is characterized by two turning points and the typical S-shape, as shown left. On the other hand, stretched solutions are possible as presented in the figure right.

Both perturbations, either by α_1 or α_2, would independently result in a hysteresis. Since the perturbation with α_2 does not add any new qualitative features to the solution, the universal unfolding requires perturbation using only the monomial $\alpha_1 x$.

$$x^3 + \alpha_1 x - \lambda = 0 \tag{4.8}$$

Hence, the universal unfolding in the form (4.8) is of codimension one. This short example should illustrate the problem of universal unfolding in contrast to a versal unfolding. Notice that such perturbed forms are also referred to as *persistent bifurcations*, while the associated unperturbed form is sometimes termed a *transition variety*. Further details on perturbations of normal forms are discussed by Golubitsky et al. [134, page 203] and, for definitions, Arnold [133] is recommended.

Codimension 1 – Elementary Bifurcations In figure 4.3 the three elementary bifurcations of codimension one are shown with the unperturbed bifurcation diagrams in the middle column. The bifurcation diagrams are constructed for a certain value of the single

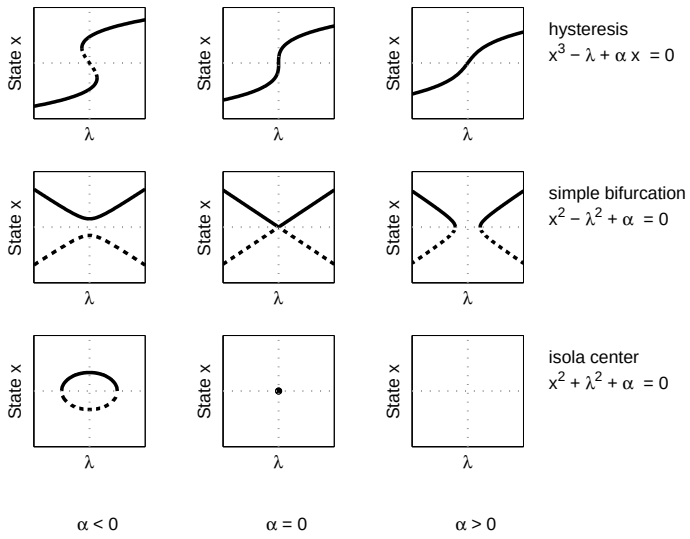

Figure 4.3.: Universal unfolding of the singularities of codimension one according to Golubitsky et al. [134]. Transition varieties are given in the middle figures.

unfolding parameter α. The assignment of the stability already corresponds to the results obtained for the reactor in this work, but could generally be interchanged by reversing the sign of monomials.

The first type of bifurcation is the hysteresis similar to figure 4.2, which is characterized by a typical S-shape for $\alpha < 0$, providing two distinct turning points and an unstable solution in the origin. A stretched solution without multiplicities is obtained for $\alpha > 0$. In case $\alpha = 0$ the unique form of the transition between the qualitatively different perturbed forms is shown. Put simply, the unperturbed form represents the special case where a hysteresis is born or dies out.

The simple bifurcation, S_b, represents the melting and dissolution of branches. For $\alpha < 0$ a single stable and a single unstable branch below has formed. A sign change of α leads to the configuration with two distinct limit points. The stability and the number of two branches are maintained, only the connections have switched. Contact of the branches in the origin is obtained for $\alpha = 0$, the unperturbed simple bifurcation.

The isola center, I_c, describes the formation of a ringlike solution branch, which exists for $\alpha < 0$ characterized by two turning points dividing the branch into a stable and an unstable region. If $\alpha > 0$, no real solution is possible. The transition between those forms is a point solution.

These codimension one singularities share the fact, that their unfoldings are completely described by a single perturbation parameter α.

Codimension 2 – Pitchfork The next example illustrates the unfolding of the pitchfork which requires two parameter for its unique characterization. Figure 4.4 illustrates four persistent bifurcation diagrams with α_1 and α_2 as perturbation parameters and the distinguished bifurcation parameter λ.

Four qualitatively different diagrams are obtained. Note the number of turning points is either one, as shown in the top row, or three, for the cases in the lower row. The form in the left and in the right are mirror images – thus one obtains four perturbed forms of this particular bifurcation.

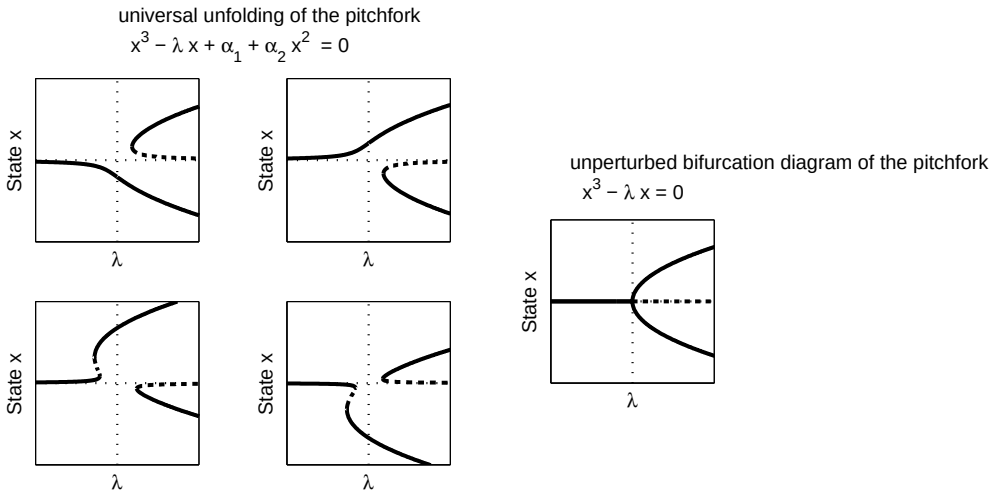

Figure 4.4.: Universal unfolding of the pitchfork bifurcation of codimension two according to Golubitsky et al. [134]. A detailed graphical representation is available elsewhere [144].

The transition variety of the pitchfork, right figure, explains the origin of the name of this particular bifurcation. The interested reader is referred for instance to Golubitsky et al. [134] and Gilmore [145] to study other complex scenarios with even higher order singularities.

4.1.3. Methodology

Typically the analysis of the system proceeds via the step by step recognition of singularities with increasing codimension starting from the identification of a single limit point. Determination of the locus of limit points in a two parameter plane is possible by solving the defining condition, see table 4.1. The resulting curve is also referred to as a limit point curve (LPC). In case a point of codimension one is identified by zeros of intermediate derivatives, this point can also be solved as a continuation in a three dimensional parameter space, and so forth (see [142]). This may finally result in a certain point in the parameter space, which possesses the most singular behavior. If all, or at least many of the possible bifurcation diagrams of the system are found in the neighborhood of this point, the so called *organizing center* has been identified. In other words, the singularities are structured by the one with the highest order [136]. The step back from higher order singularities to the ones with lower order is essential for the description of the neighborhood of a particular singularities. For this approach an unfolding in the next lower codimension is suitable or, what is often performed, a one-parameter bifurcation of the investigated parameter set is calculated.

However, the analysis is still a matter of tedious work. Projections in different parameter planes are required in order to reveal complex structures.

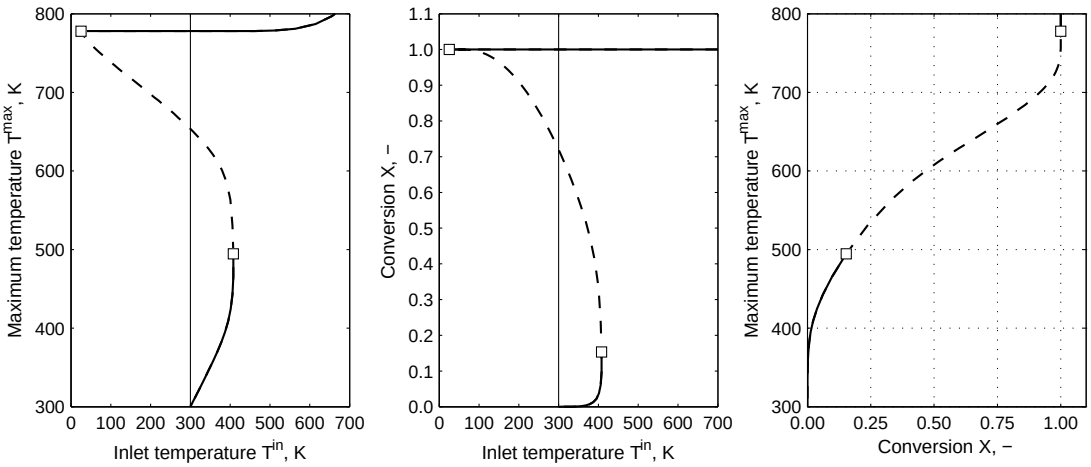

Figure 4.5.: Bifurcation diagrams for the maximum temperature (left) and the conversion (middle) with respect to the inlet temperature T^{in}. Right, state space in terms of the maximum temperature $T^{\max}$ and conversion at the outlet of the reactor, $X(z = L_R)$. Symbols for limit point, stable branches as continuous lines and unstable as dashed lines. Example for $\Delta T_{\text{ad}} = 60$ K, $\gamma = 1.07$, TMBR model in sec. B.3, discussed in sec. 4.2.1.

4.2. Ignition and Extinction Phenomena in TMBR and SMBR

4.2.1. One-parameter Bifurcation Diagrams

Inlet Temperature T^{in} Typical bifurcation diagrams in this work are discussed, at first for the example of the inlet temperature. Figure 4.5 provides different views on the same bifurcation diagram. The maximum temperature over the bifurcation parameter is presented in the left figure, conversion at the reactor outlet in the middle and the corresponding state space in terms of $\left(T^{\max}, X(z = L)\right)$ relates the reactor temperature to the outlet conversion. The lines for constant inlet temperature represents the desired low value of 300 K. The bifurcation diagram shows a typical ignition-extinction hysteresis with multiple solutions for a certain range of the inlet temperature. Two turning points indicate the change of the stability. The solution branch at high reactor temperatures and low inlet temperatures is characterized by complete conversion. The range available for the inlet temperature is determined by the left limit point located far below ambient conditions. This particular feature is exploited in this work and guarantees ignited reactor states to achieve an autothermal operation at ambient inlet temperatures. The state space shows that the desired stable operation regime to achieve complete conversion is obtained only at sufficiently high reactor temperatures.

Solid Phase Velocity in Terms of γ as a Function of the Solid Phase Velocity u_s Another important process design parameter is the flow rate ratio, which was investigated by continuation of the solid flow rate u_s at a constant inlet temperature of 300 K. An isola with two turning points framing unstable and a stable ignited branch are obtained (fig. 4.6). Another branch exists representing stable extinguished states at reactor temperature corresponding to the inlet temperature. Complete conversion can be achieved for a certain range of solid phase velocities (middle fig. 4.6), however, for smaller γ, the conversion falls to 80 %.

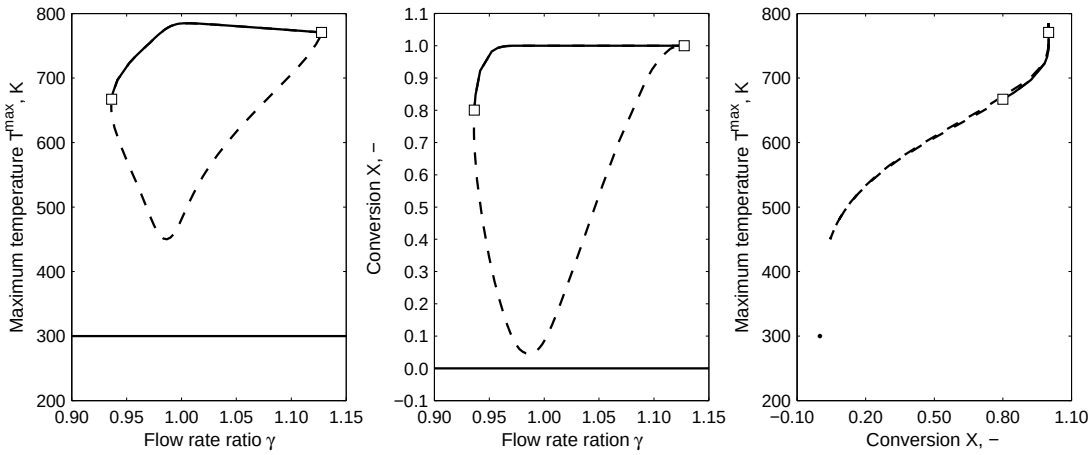

Figure 4.6.: Bifurcation diagrams for the maximum temperature (left) and the conversion (middle) with respect to the flow rate ratio ($\gamma(u_s)$) as bifurcation parameter. Right, state space as $T^{\max}$ and conversion at the reactor outlet, $X(z = L_R)$. Symbols for limit points, stable solutions as continuous lines, unstable as dashed lines. Example based on $\Delta T_{\text{ad}} = 60$ K, $T^{\text{in}} = 300$ K, TMBR model in sec. B.3.

For the example considered, the conversion starts to decrease below $\gamma = 0.96$ down to limit point at $\gamma = 0.936$. Corresponding state space indicates unstable and stable solutions at high reactor temperatures and a point solution representing the extinguished state at an inlet temperature of 300 K and zero conversion.

The bifurcation diagrams, hysteresis and isola, are two important ignition-extinction phenomena. It should be stressed that other bifurcation parameters can also produce similar bifurcation diagrams. For example, the feed flow rate shows an isola similar to the solid phase velocity. Therefore, when referring to γ as a bifurcation parameter, it is actually meant the solid phase velocity.

Additional Parameters To illustrate the variety of bifurcation diagrams and their qualitative interpretation, three more examples are considered: Serving as bifurcation parameters are the feed concentration given in terms of ΔT_{ad}, the reactor length L_R and the wall heat transfer coefficient h_w. The bifurcation diagrams are presented in figure 4.7 graphing the reactor states in terms of maximum temperature and conversion along with the respective parameter. For these investigations, γ was set to 1.0 and ignited states were selected as a starting points of the calculations.

At first the feed concentration (as ΔT_{ad}) was studied showing an extinction for a certain low concentration (left limit point). The unstable branch reaches up to unrealistic high feed values beyond 6000 K yielding a second turning point and finally an extinguished, but stable branch at very low reactor temperatures. On the other hand, an increase leads to higher reactor temperatures, while the conversion remains complete. For the sake of clarity, temperature values above 1000 K are omitted. Again, the bifurcation diagram resembles that of an ignition-extinction hysteresis.

The reactor length L_R is considered in the middle column of figure 4.7. Decreasing this parameter initially increases the reactor temperature until a critical value has been reached.

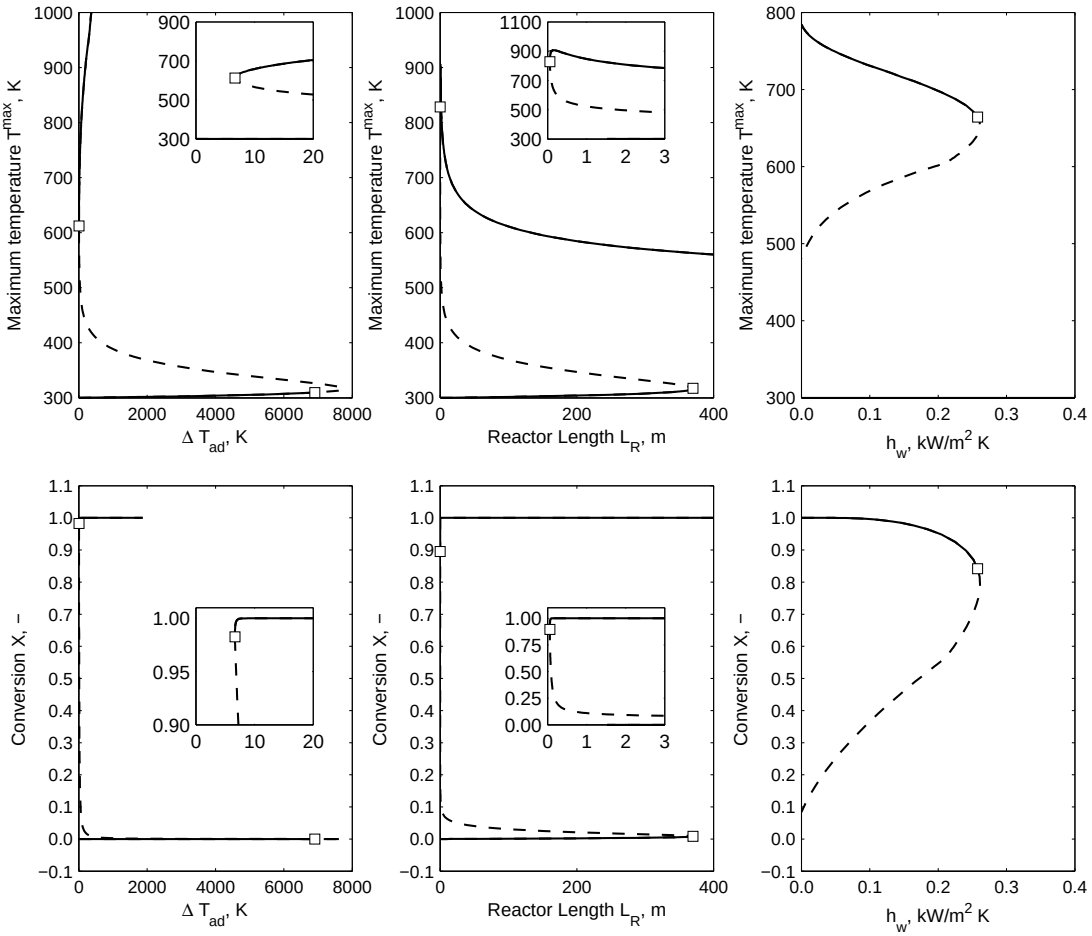

Figure 4.7.: Bifurcation diagrams for the maximum temperature (top row) and conversion (bottom row) with respect to the feed concentration in terms of ΔT_{ad} (left), the reactor length (middle) and the wall heat transfer coefficient (right). (TMBR model sec. B.3).

Close to the limit point the conversion falls below unity (see the inset). To show that there exist a second turning point and a stable extinguished branch, also unrealistic valued up to 600 m are illustrated. Note that a similar result can be obtained, when the pre-exponential factor is used as the bifurcation parameter. Reactor length and the pre-exponential factor show the same quality, though not identical bifurcation branches. This can be explained with characteristic relation between residence time and reaction rate encountered in chemical reactors and often described by *Damköhler* number [64]. Such limitations will be addressed later in this chapter.

The last example is concerned with the wall heat transfer coefficient. Heat losses lead to a reduced reactor temperatures until a critical value has been attained and an unstable solution emerges. Extinguished reactor states exists at low inlet temperatures, which are not shown in the figure. Note that a qualitatively similar result can be obtained in the case of the bed heat conduction which leads to reactor extinction in case of large values as well.

4.2.2. Comparison Between SMBR and TMBR

In this section the two reactor models are compared based on bifurcation diagrams. The analysis for the SMBR was performed with the package DIVA, while the TMBR was analyzed with DIANA software. Continuation of the periodic state of the SMBR was computationally more demanding than the continuation of steady states of the TMBR model.

Three configurations of the SMBR, $N_{\mathrm{Seg}} = 3$, 5 and 10, and two different bifurcation parameters were examined: the inlet temperature T^{in} and the for the flow rate ratio γ, the switching time t_{sw} in the SMBR model and the solid phase velocity u_s in case of the TMBR model is used, respectively. The results are presented in figure 4.8, where, for the better comparison, the stability of the solution branches is omitted.

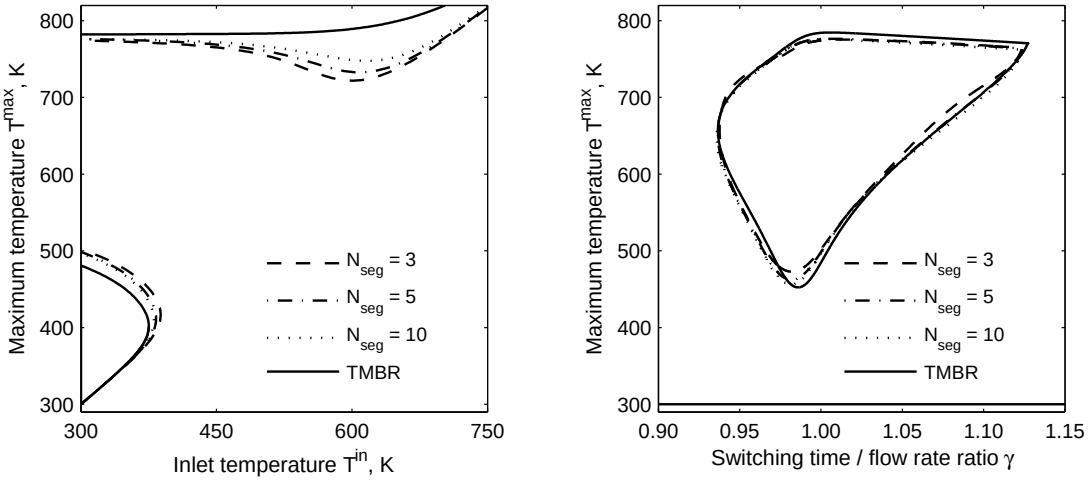

Figure 4.8.: Comparison between the SMBR and the TMBR for the example of the ignition-extinction hysteresis (left) and the isola (right). Intercepted lines indicate the branches of the SMBR for different segments, N_{Seg} of 3, 5 and 10. The solid line represents the TMBR model (the stability is omitted here). The SMBR model (sec. B.1) was solved via shooting (DIVA) and the TMBR model (sec. B.3) in DIANA.

In the left figure 4.8 is given a part of the hysteresis (values below 300 K are skipped). The hysteresis shows the existence of an upper solution branch over a wide range of inlet temperatures which can be attained when preheating the beds and initiating the switching operation facilitating the desired autothermal operation with cold feeds. An increased segmentation obviously shifts the solution branches towards the solution of the TMBR model. Deviations of the SMBR model appear particularly for higher inlet temperatures (600 K), but the qualitative behavior is already very well described by the TMBR model.

The continuation of the switching time (SMBR) and the solid phase velocity (TMBR) shows the isola (fig. 4.8, right). The segmentation does not change the qualitative behavior, which means that the flow rate ratio γ (eq. (3.45)) provides an accurate basis for the analysis of the SMBR, independent of its segmentation. The good agreement with the TMBR model is of great value to identify suitable switching times instead of the computationally more expensive SMBR model.

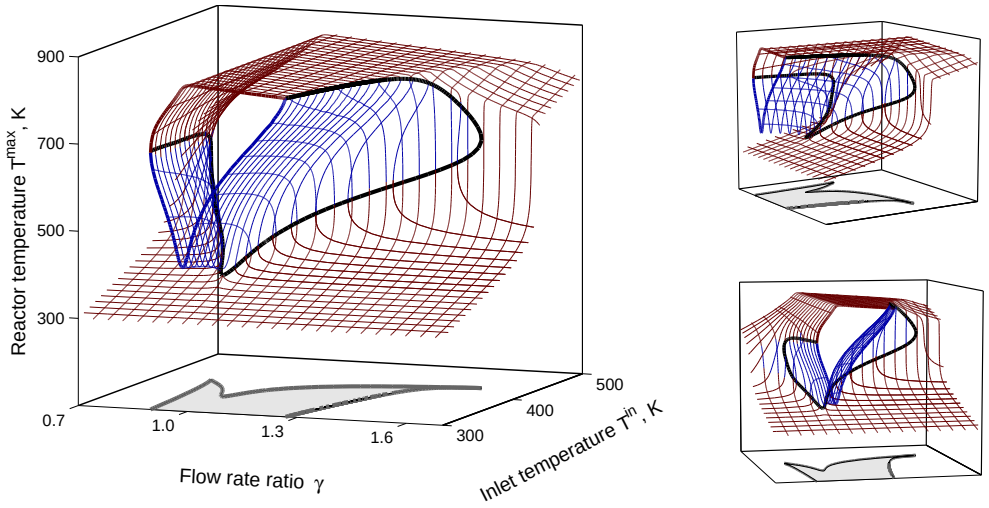

Figure 4.9.: Solution shell illustrating the region of multiplicities in terms of the maximum reactor temperature in the parameter plane of the flow rate ratio and the inlet temperature (T^{in}, γ). Stable high temperature states and extinguished stable states are possible at low inlet temperatures (red lines). Unstable solution branches (blue lines) separate the stable solutions in the finger like multiplicity region, whereby stability exchange is located with the curve of limit points (black line). The projection (gray scaled) in the parameter plane at γ, T^{in}, $T^{\max}$ = const, indicates the region for multiple steady states. Discussion in sec. 4.3.1.

4.3. Operation Window and Process Limits Based on Higher Order Singularities

This section shows the results of a step by step analysis of higher order singularities to provide a deeper understanding of the interplay of parameters. The parameters investigated are the aforementioned inlet temperature, the flow rate ratio, the feed concentration and finally several secondary parameters (heat transfer coefficient, heat conduction, heat of reaction, reactor length, pre-exponential factor).

4.3.1. Operation Window for the Inlet Temperature T^{in} and Flow Rate Ratio γ

The existence of limit points for two parameters, as explained in the previous section (fig. 4.5 and 4.6), raise the question of their interrelation in the parameter plane $\left(T^{\text{in}}, \gamma\right)$. This was studied by calculating families of one-parameter continuations illustrated in figure 4.9. Typically, stable reactor states can be found at low and high reactor temperatures separated by unstable solutions, whereby stability exchange is given by the curve of limit points ($LPC\left(\gamma, T^{\text{in}}\right)$ thick line). The locus of the limit points in the parameter plane is also illustrated by a projection to constant low reactor temperatures.

Multiple solutions are possible for a specific parameter combination. In brief, the region of multiplicities resembles the shape of a finger. At a fixed low inlet temperature, the „chopped finger“ provides an isola solution of a certain dimension with respect to the switching time, characterized by high reactor temperatures and high conversions. At larger inlet temperature

unique ignited states can be achieved, similar to a conventional FBR in steady state.

Figure 4.10 provides a detailed perspective on the region of multiplicities (left part). This limit point curve, $LPC = LPC\left(\gamma, T^{\text{in}}\right)$, encloses the region of three possible steady states (gray area), two stable and one unstable. Values below $T^{\text{in}} = 300$ K are omitted.

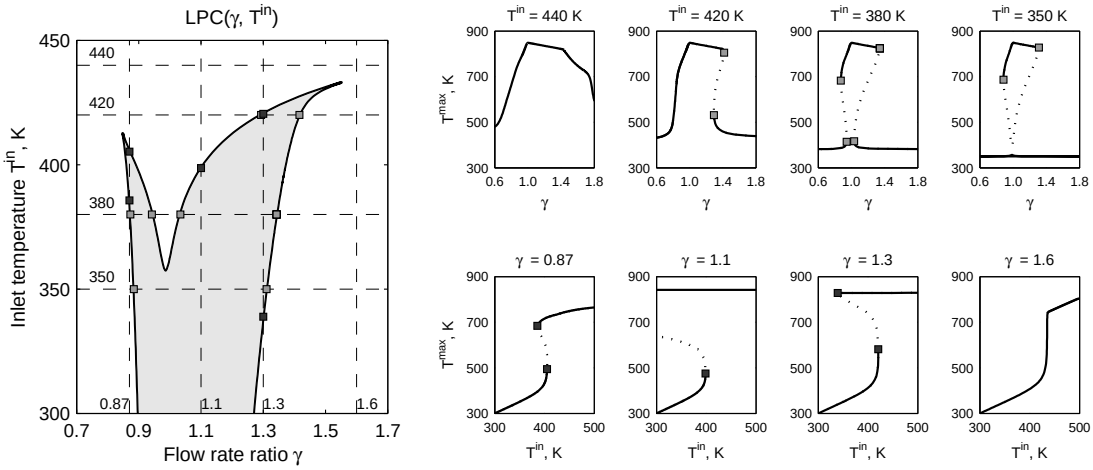

Figure 4.10.: Region of multiple steady states for high reactant conversion enclosed by the limit point curve (LPC left figure) and selected bifurcation diagrams for the maximum reactor temperature with respect to the parameter γ (top row) and the inlet temperature T^{in} (bottom row). The feed concentration was set to a corresponding adiabatic temperature rise of 120 K. Symbols represent limit points. Calculations based on the TMBR model B.3.

Additional intercepted lines highlight the solution branches of several one parameter bifurcation diagrams displayed in figures right (fig. 4.10). Four qualitatively different diagrams according to specific constant inlet temperatures are shown in the top row. At an inlet temperature of 440 K a unique solution is possible, below (420 K), a hysteresis appears. At 380 K a so called *mushroom* is detected, see Aris [130] for an illustrative example, and finally the completely isolated solution appears.

Otherwise, if γ is held constant, the bifurcation diagrams of the ignition-extinction hysteresis with respect to T^{in} are obtained (fig. 4.10, lower row). The case of $\gamma = 1.1$ is representative for an autothermal operation, since the left turning point is located far below the inlet temperature at ambient condition.

The limit point curve represents the operation window in terms of the parameters T^{in} and γ. From the size of this window, in particular for the range of γ at low inlet temperature (cold feeds), one can deduce switching times required to maintain an ignited state for a specific adiabatic temperature rise. One would expect this operation window to shrink for lower feed concentrations. This behavior was studied by analyzing singularities of the next higher codimension in the enlarged parameter space $\left(T^{\text{in}}, \gamma, \Delta T_{\text{ad}}\right)$.

4.3.2. Influence of Feed Concentration

Three examples for reduced feed concentrations, corresponding to $\Delta T_{\text{ad}} = 11.9$, 5.7 and 3.2 K are presented in figure 4.11 together with codimension one singularities as lines and the

codimension two pitchfork with a square. Since three parameters are used for the analysis, the left figure shows the results in the plane (T^{in}, γ) and the right figure in the plane $(T^{\text{in}}, \Delta T_{\text{ad}})$.

The solution branch connecting the cusps represents the codimension one hysteresis (red line), which can be regarded as a parameterized curve $H = H\left(\gamma, T^{\text{in}}, \Delta T_{\text{ad}}\right)$. For the sake of a clearer assignment, the branch is further distinguished into H_{left} and H_{right}.

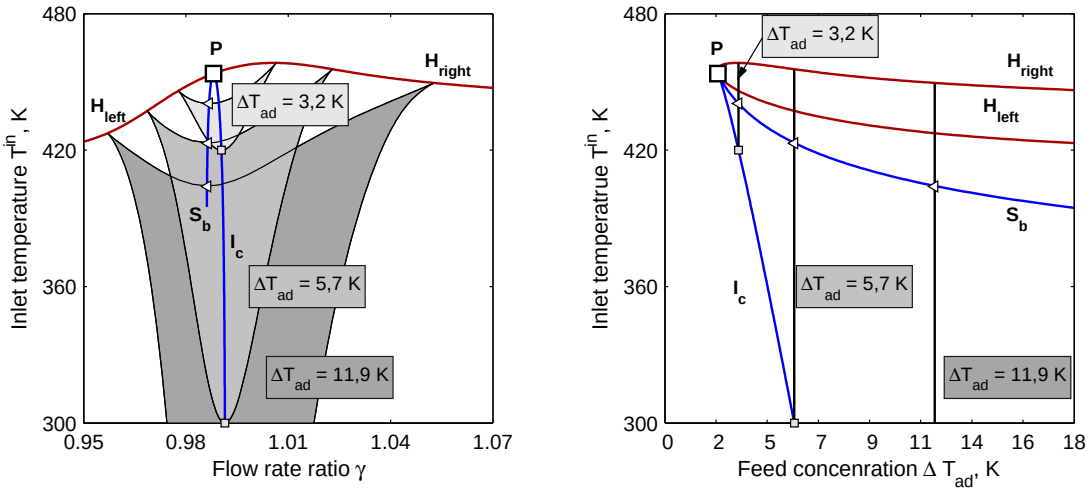

Figure 4.11.: Shrinking of operation window due to decreasing the feed concentration in terms of ΔT_{ad} for three examples and higher order singularities. Hysteresis as red lines (H_{left} and H_{right}), the isola center, I_c, the simple bifurcation, S_b, (blue lines) and the pitchfork point, P (square). Calculations based on the TMBR model B.3.

Apparently, these cusps cumulate in a single point (P) when reducing ΔT_{ad} further and the limit point curve seems to vanish. This point can be classified as a pitchfork of codimension two[3], which will be considered in detail in the next section.

From that point on, the codimension one isola center, I_c, and a curve of simple bifurcations, S_b, evolve, which connect the minima of the limit point curves LPC in terms of $T^{\text{in}}(\gamma)$. The minima intersecting the curve S_b are highlighted with a triangle and the minimum intersecting I_c with a square. They can be regarded as parameterized curves[4] $S_b = S_b\left(\gamma, T^{\text{in}}, \Delta T_{\text{ad}}\right)$ and $I_c = I_c\left(\gamma, T^{\text{in}}, \Delta T_{\text{ad}}\right)$.

For this particular example, two minima exists for a certain limit point curve and two characteristic inlet temperatures are associated with these codimension-one varieties. The one at higher inlet temperature is related to the locus of the simple bifurcation and the one at lower inlet temperatures to the isola center. The latter, the curve connecting the isola center singularities, I_c, is responsible for the long tongue like shape of the operating window and the expansion towards very low inlet temperatures, which finally allows an ignited autothermal reactor operation.

From this observation it can be deduced, that the isola center I_c represents a *theoretical operation limit of the reactor*. The solution curve I_c is almost independent of the flow rate

[3] The pitchfork P is defined as a point in the parameter set $P = P\left(\gamma, T^{\text{in}}, \Delta T_{\text{ad}}\right)$

[4] H, I_c and S_b are singular points of codimension 1 in the parameter plane $\left(\gamma, T^{\text{in}}\right)$, which are solved in a third parameter ΔT_{ad} yielding a curve or *variety* of the respective singularity.

ratio γ. This result is important, because it means that the switching time should always be adjusted to $\gamma \approx 1$ when processing very lean feeds.

Another important result can be obtained from this analysis regarding the minimum feed concentration. This is best explained with the projection in the parameter plane (T^{in}, ΔT_{ad}) in figure 4.11 right. At a constant low inlet temperature of 300 K, a feed concentration corresponding to an adiabatic temperature rise of 5.7 K is required for the birth of an isolated solution ensuring an reactor state at high temperatures and complete conversion. This limit, however, represents only a single set of parameter required to fulfill this condition, which means that even minor deviations, i.e. due to parameter uncertainties in real systems, will lead to extinction. Therefore, larger feed concentrations are required providing a sufficient range of possible flow rate ratios and respective switching times. After all, if the isola center is compared for different reactions or compared within analogous processes, it provides a valuable information about the process limits in a very condensed form.

It is also interesting to discuss the locus of the isola center I_c at higher inlet temperatures up to the pitchfork point P, which is the organizing center (see details later). The gradient of the center $I_c\left(T^{\text{in}}\right)$ with respect to ΔT_{ad} is quite large, such that the concentration effect is small and only slightly lower concentrations down to 2.5 K are sufficient for an ignited state. This result clearly shows that the sensitivity of the stability domain with respect to the feed concentration is much larger than with respect to the inlet temperature.

On the other hand, the limit for a unique reactor state at higher feed concentrations is defined by the simple bifurcation S_b. Above that curve the reactor attains automatically an ignited, which implies of course a specific flow rate ratio. This limit is much more sensitive regarding the inlet temperature compared to the feed concentration. And finally, to add an interpretation concerning the curves of the hysteresis varieties: selecting inlet temperatures above those limits, above H_{right}, will drive the reactor in an ignited state regardless of the flow rate ratios γ. Altogether:

- There exists an important operation limit, the isola center $I_c\left(\gamma, \Delta T_{\text{ad}}\right)$ originating from a pitchfork point at high inlet temperatures.
- The locus of the isola center I_c with respect to T^{in} shows that the process is more sensitive regarding the feed concentration than the inlet temperature.

Consequently, autothermal operation at low inlet temperatures depends mainly on the parameters $(\gamma, \Delta T_{\text{ad}})$ defining the isola center bifurcation.

4.3.3. Identification of the Organizing Center

In the previous section it was stated that the organizing center is a pitchfork bifurcation, the point denoted as P. This is explained in more detail with the help of figure 4.12.

When reducing the feed concentration, the operation window or window of multiple steady states shrinks with respect to the inlet temperature and γ. However, a total vanishing cannot be observed, but a finite tiny region of the limit point curve (LPC) remains. Note the small scales of the parameters and the reactor temperature. The LPC is shown together with the codimension one curves, the hysteresis (H_{left}, H_{right} red line) and the isola center, I_c,

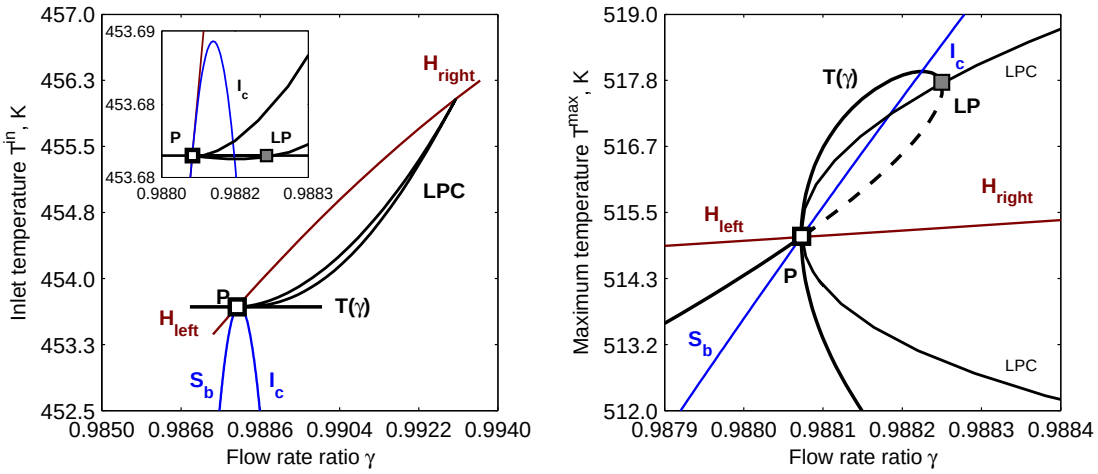

Figure 4.12.: Characterization of the organizing center, a pitchfork in point P, from which all lower order singularities originate: the limit point curve, LPC, the hysteresis, H, isola center, I_c, and simple bifurcation, S_b (left). Right figure illustrates the results in the bifurcation diagram for the maximum temperature with respect to flow rate ratio, γ.

together with simple bifurcation, S_b, as blue curves in left figure of 4.12, and in the right figure, the corresponding functions are given in terms of $T(\gamma)$ (state variable over characteristic bifurcation parameter).

From the pitchfork point P originate the hysteresis variety, H, the isola center, I_c, and the simple bifurcation curves, S_b. The point P also coincides with the left cusp of the limit point curve, LPC. When performing a parameter continuation in γ, see $T(\gamma)$ right, meeting this cusp, the pitchfork bifurcation is finally detected. Actually a loop with an additional limit point (LP - gray square) located on the limit point curve LPC is observed. This second limit point appears due to minimum of the limit point curve in terms of $T^{\text{in}}(\gamma)$[5]. Thus, the pitchfork is found when directly approaching the tip of the cuspoid, while the second limit point is rather a byproduct of the limit point curve.

Following remarks should elucidate the classification problem in the vicinity of the cusp. Depending on the path of the bifurcation parameter (with γ as the distinguished parameter) approaching the cuspoid, different singularities can be identified [134]:

1. The simplest case is the codimension one hysteresis (fig. 4.3), which results if the cusp is approached from one side (orthogonal). Here the inlet temperature was used as the bifurcation parameter as shown in figure 4.10. In this case only one additional parameter, for instance γ, is required for a unique characterization of the corresponding singularity (perturbation of hysteresis).

2. The pitchfork bifurcation appears only, if the tip of the cuspoid is approached upfront or in a small angle, as shown in figure 4.12. Note also the normal form illustrated in

[5] The inset in figure 4.12 zooms in the organizing center. The lower branch of the LPC crosses the line at constant inlet temperature (T^{in}), such that the gray marked limit point appears. The white square marks the origin of the pitchfork.

figure 4.4. The difference is, that two additional parameters are required for its unique characterization. In the reactor model the bifurcation parameter λ is determined by the flow rate ratio γ and the perturbations α_k correspond to the feed concentration and the inlet temperature, respectively.

For a detailed discussion on path formulations in the vicinity of the cuspoid consult Golubitsky et al. [134, page 167]. In this work it should be noted, that by continuing the pitchfork in an additional parameter, thus in a set of four parameters, no higher order singularity could be detected. Therefore it is assumed, that the pitchfork represents the organizing center under the restriction of the specific parameter ranges investigated.

In Zahn et al. [146] it is shown how to make use of a continuation of the pitchfork in a fourth parameter with subsequent calculation of isola center curves to determine new process limits. This is an interesting approach to investigate the influence of secondary effects on the reactor performance. Below, a similar approach is considered with a simplified analysis considering only the isola center.

4.3.4. Assessment of Process Limits Based on the Isola Center

If the information about the dependence of process limits, e.g. hysteresis, on the inlet temperature is not required, the isola center can be investigated with regard to additional parameters.

A constant inlet temperature of 300 K was assumed and the isola center calculated in the prescribed way. Then, this point can also be investigated by continuation in a third parameter fixing the defining condition $g = g_x = g_\lambda = 0$ (see table 4.1 for the isola center). Pictorially speaking, only the finger tip of the solution shell at 300 K moving in a two dimensional parameter space defined by $(\gamma, \Delta T_{\mathrm{ad}})$ is of interest. The results are shown in figure 4.13 together with several other process parameters explained below.

The first example is concerned with the heat transfer coefficient, h_w. In case of larger heat losses, the flow rate ratio and the feed concentration need to be increased for compensation. Note that the transfer coefficients are small for the example of an inner diameter of only 0.05 m.

The next example is the heat conduction, λ, of the fixed-bed. In order to avoid a collapse of the reaction front, also compensation with higher feed concentrations is required. This is accompanied with adjustments in the flow rate ratio. First, an increase is required and then the ratio decreases significantly. In section 4.2.1 it was stated that secondary effects, such as heat losses and heat conduction show qualitatively similar bifurcation phenomena for the TMBR model. This is, according to the analysis of the isola center, not true and the underlying phenomena is more complex.

Third, the heat of reaction, ΔH_R, was studied showing no effect regarding the flow rate ratio. But of course, reactions with smaller reaction enthalpies have to be compensated by increased feed concentration. This relation is exponential, meaning also, that reactions with smaller exothermicity would require very high inlet concentration in order to realize an autothermal operation.

The reactor length, L_R, was investigated as the forth example in figure 4.13. This parameter was already examined by means of one-parameter continuation in figure 4.7, in which a

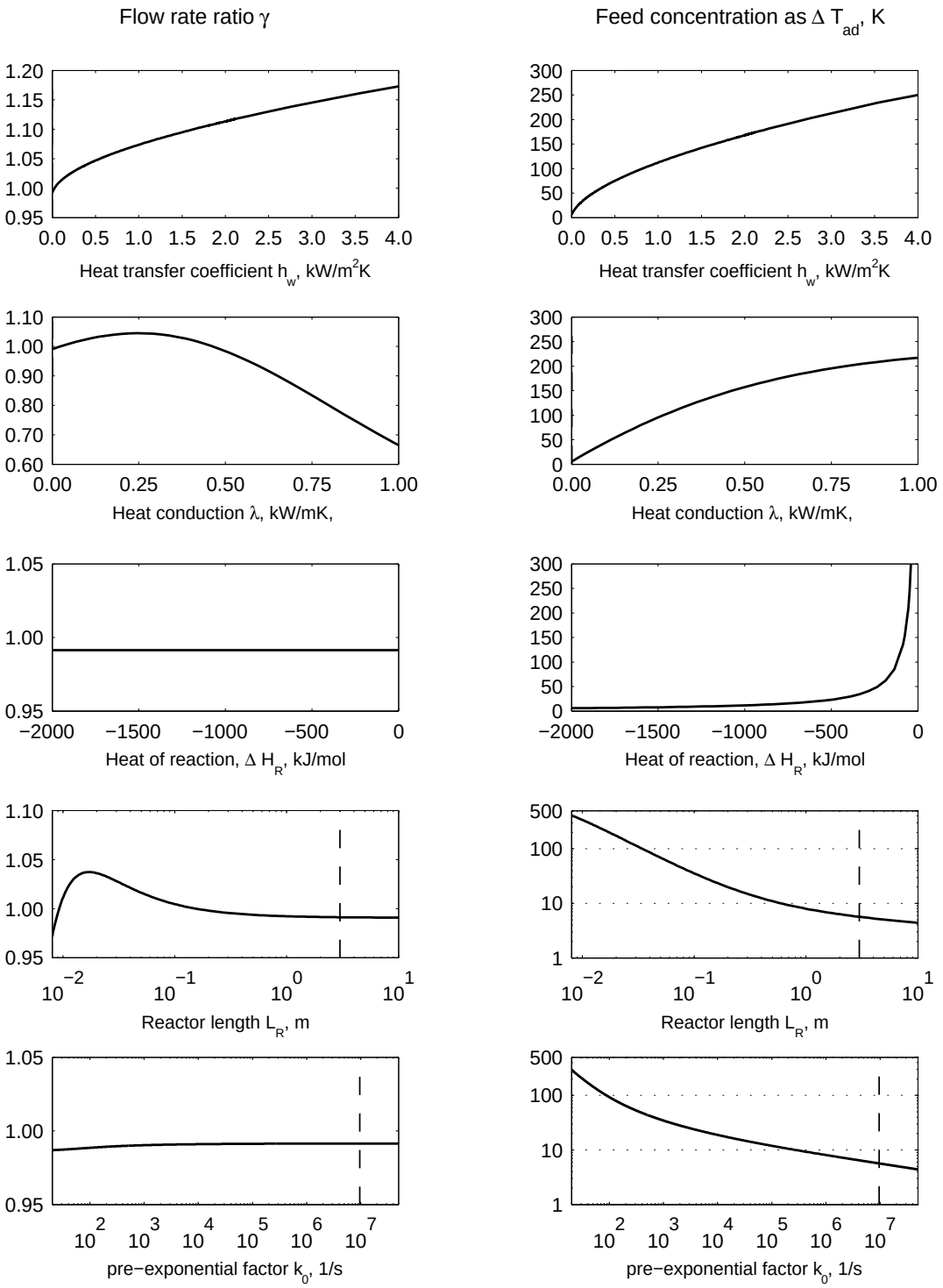

Figure 4.13.: Isola center $I_c = I_c\left(\gamma, \Delta T_{\mathrm{ad}}\right)$ at a constant inlet temperature of $T^{\mathrm{in}} = 300\,\mathrm{K}$ as a function of secondary process parameter. From the top, heat transfer coefficient, heat conduction, heat of reaction, reactor length and pre-exponential factor. Vertical dashed lines highlight the example for L_R and k_0. Calculations based on the TMBR model sec. B.3.

certain low reactor length limited the ignited solution branch. The analysis reveals that shorter reactor length can also be compensated by increased feed concentration. The relation is almost exponential above 1 m, below however, the situation changes to an even stronger increase when approaching unphysical small reactor scales. Below 0.5 m the required feed concentration increases rigorously. The flow rate ratio γ is almost constant, only at very small length scales an increase followed by a drop below one is observed. Of course, an engineering perspective demands reasonable parameter values, which would exclude very short length scales[6]. On the other hand, if one considers much greater reactor length, the feed concentration could even be reduced.

The last parameter is the pre-exponential factor, k_0. Similar to the reactor length, a decrease requires compensation by larger feed concentrations (ΔT_{ad}). The flow rate ratio, however, remains to be almost constant.

The results based on the continuation of the isola center have demonstrated the flexibility of this particular stability limit, if compensation in γ and ΔT_{ad} is allowed.

- Heat losses should not only be compensated by increased feed concentrations, but require larger switching times.
- In most cases, compensation by increased feed concentration is always possible to maintain an autothermal operation.

It is convenient to apply the suggested strategies to study other parameters. However, these procedures do not always provide a complete picture of the behavior in intermediate or extrapolated parameter ranges. In addition, the analysis presented deals only with steady state solutions, but also dynamic phenomena like autonomous oscillations can occur. This was found to happen at higher inlet temperature in the vicinity of the cusp at $\gamma < 1$. However, those parameter combinations are not considered for reactor operation. This work therefore intends to identify the interplay of most reasonable parameters rather than to reveal all possible complex features of the reactor. Concerning other phenomena, several works have appeared [126, 147] and an interesting work dealing with the conventional reverse-flow reactors is Khinast et al. [148].

4.4. Kinetic Limitations

Reactor design is basically concerned with the specification of the optimal reactor dimension (i.e. length and diameter) for a particular set of reactions. Their kinetics determine the reactor scale. In order to identify possible candidates, this section investigates parameter maps which reveal kinetic limitations – thus offering a fast assessment of possible fields of application for the SMBR reactor.

At first it is treated the Arrhenius term with activation energy E_a and pre-exponential factor k_0 as parameters, then the parameter set k_0 and the reactor length L_R.

In order to generate these parameter maps, a constant flow rate ratio of one and an inlet temperature of 300 K were assumed. The limit point curves were calculated based on the

[6] Models accounting for radial coordinate would be required for a precise description at small length scales.

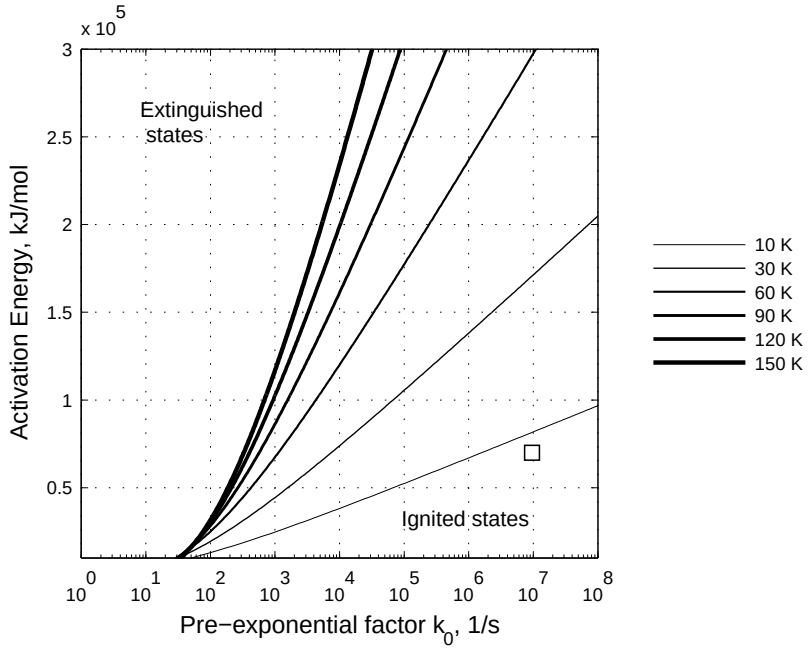

Figure 4.14.: Ignition limits for the parameters of the Arrhenius equation in plane (k_0, E_a) for several feed concentrations (as ΔT_{ad}). (Parameters $\gamma = 1.0$, $T^{in} = 300$ K, TMBR model sec. B.3). The square marks the standard case used in previous investigations. Calculations based on the TMBR model (sec. B.3).

continuation of the limit point appearing for certain small reactor length or a small pre-exponential factor, respectively, while demanding a conversion of 99.95 %. Note that this limit is not identical to the isola center discussed previously, because it neglects the existence of an optimally adjusted flow rate ratio. However, this method represents an meaningful approach, since γ was shown to be almost constant and close to unity, and the sensitivity with respect to the inlet temperature is low as well. The loci for different feed concentrations corresponding to adiabatic temperature rises in the range of $10 - 150$ K were investigated.

4.4.1. Limitations due to the Arrhenius Temperature Dependence

The parameters, activation energy and pre-exponential factor, are highly correlated and a certain combination decides about a sufficient reaction rate allowing ignited reactor states.

Limiting curves for several feed concentrations are illustrated in figure 4.14 together with the standard case used throughout the analysis (square corresponds to standard case used in previous investigations). The limits divide the parameter plane in an upper left corner characterized by extinguished states and the lower right corner for ignited states.

The activatin energy can be perceived as barrier to be surmounted in oder to initiate the reaction. This explains, that for a given pre-exponential factor, a certain large activation energy represents an ignition limit, beyond which only extinguished reactor states exist. Conversely, for a fixed activation energy also a sufficient high pre-exponential factor is required. As such, the ignition limit depends on both parameter in an logarithmic manner with respect to k_0.

Another important result is connected with the inlet concentration and the corresponding

release of thermal energy. For lean feeds, only fast reactions (large k_0, small E_a) can be processed, but with increased inlet concentrations also slower reactions are allowed. Two major contributions to the shift in the ignition limits can be considered. First, the reaction rate is increased with the concentration and secondly, larger amounts of heat are being released thus increasing domains of ignition. Although the ignition limits can be shifted by increased concentrations, a finite limit exits preventing reactions with arbitrary small pre-exponential factors.

Despite the fact, that different length scales and Lewis numbers would change the given stability map, the qualitative picture will remain similar and is therefore still meaningful for a fast assessment of possible candidates for the SMBR.

Some further aspects need to be addressed. Kinetic limitations also affect the available space time yields. About 12 mol/m^{3}s with respect to the VOC loaded air can be achieved with the SMBR, which fits well to the numbers of 0.1…10 mol/m^{3}s typically reported for heterogeneously catalyzed reactors [64, 149]. This means, that the SMBR reactor concepts fits well in the conventional family of fixed-bed reactors. However, pre-exponential factors in the given parameter map are valid for the diluted hydrocarbons being oxidized. Therefore a generalization to arbitrary reactions is not permitted with this results. Comparisons with reaction rates in conventional processes need to account for this aspect.

In principle, the SMBR requires fast enough reaction rates to guarantee the formation of the exothermic reaction fronts for an autothermal operation. Only in this way, the concepts enables the low feed temperatures and self sustained operation. When comparing the reaction rates, it consequently needs to be considered a specific temperature level for the operation. The maximum temperature or an ignition temperature could serve as a basis.

Altogether, the limitations of the SMBR depend on the inlet concentrations and a sufficiently fast reaction rate. An insurmountable boundary due to slow reactions decides about successful autothermal SMBR operation.

4.4.2. Limitations in Rate and Reactor Dimension

Reaction rate and the residence time are important design reactor parameter. A constant gas flow rate was assumed and the reactor length L_R investigated. In figure 4.15 are presented the limits for different feed concentration (ΔT_{ad}) together with the standard case of this study (square).

The limits divide the plane in the upper right corner and lower left. Above these limits, a sufficient rate allows for an ignited state, below only extinguished states are possible. The figure is in double logarithmic scale, which reveals the log-log – relation beyond 0.5 m. The ignition limit significantly increases with smaller reactor length. This result indicates two mechanisms. The region at larger length scales is mainly affected by convective energy transport and residence time effects rule; reaction rate and residence time balance. At smaller scales however, conductive transport becomes increasingly important, which can be regarded as the main factor for the increase in the k_0 values required.

Small feed concentrations shift the curves to larger pre-exponential factors. This can be explained with the less heat released and also with the smaller reaction rates due to the concentration dependence in the rate law. On the other hand, the limiting curves approach

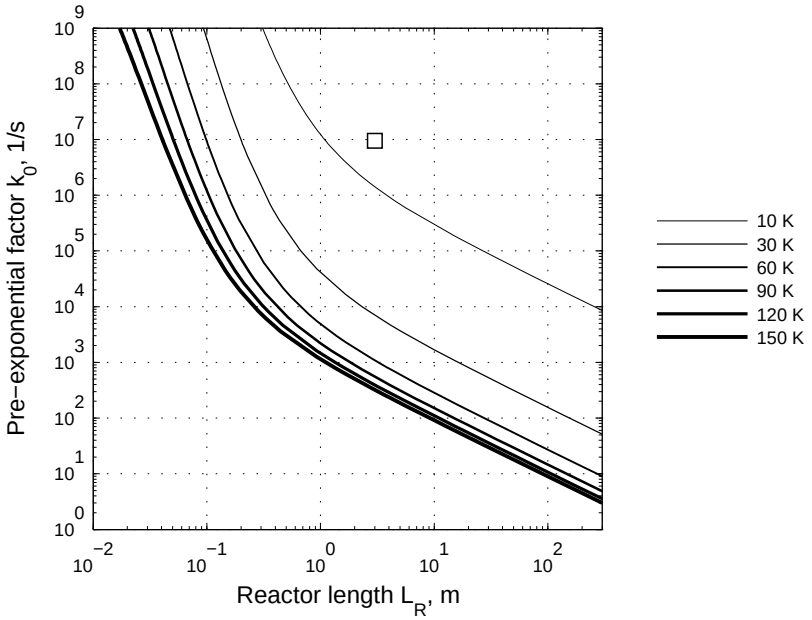

Figure 4.15.: Ignition limits in the parameter plane spanned by the pre-exponential factor k_0 and the reactor length L_R for several feed concentrations given in terms of adiabatic temperature rises. Constant flow rate ratio of $\gamma = 1.0$ and a low inlet temperature $T^{\text{in}} = 300$ K are presumed. The square indicated the standard case according to parameter obtain from [74]. Calculations based on the TMBR model (sec. B.3).

a boundary as the inlet concentrations are increased. A further increase would provide additional thermal energy, which however, cannot be utilized due to the kinetic limitation. This result is important for design purposes with respect to reactor dimensions and catalytic properties. An insurmountable ignition limit exits according to this analysis.

Consequently, two different limitations can be considered. The first one corresponds to the required thermal energy provided by the feed, and the second one is mainly driven by kinetic limitations for the specific catalytic system.

4.5. Summary

Nonlinear analysis is important to consider whenever multiple solutions occur and reactor states abruptly switch when a parameter is only slightly changed.

The methods used for the SMBR were briefly examined while this section predominantly exploited the reduced TMBR model. This was justified because both models showed a good agreement regarding most important bifurcation phenomena, the ignition-extinction hysteresis and the isola.

The singularity analysis revealed the formation of multiplicities in respect to the parameters, such as the inlet temperature, the flow rate ratio, the feed concentration or the heat transfer coefficient.

An ignition limit with respect to a minimum feed concentration was identified as an isola center (sec. 4.3). This limit is defined by the flow rate ratio and the inlet temperature. At

ambient inlet temperature a concentration corresponding to $\Delta T_{ad} = 5.7$ K for the example studied, is required to maintain an autothermal operation valid for specific flow rate ratio close to one.

A step by step analysis of higher order singularities was performed, revealing also hysteresis and simple bifurcations. Considering the relevant parameter set for the reactor, the organizing center could be identified as a pitchfork bifurcation.

It was suggested to exploit the continuation of the isola center to obtain new process limits with respect to several parameters. This method was demonstrated for the heat transfer coefficient, heat of reaction, heat conduction and reactor length. It was found, that compensation by increased feed concentrations and also by an adjusted flow rate ratio is required to maintain ignited states.

A further study dealt with kinetic limitations to provide a faster assessment of applicable candidates to be processed in the reactor. For the parameters of the Arrhenius equation, activation energy and pre-exponential factor, the ignition limits revealed that sufficiently fast reactions are required. Increased feed concentration would make it possible to process slower reactions, however, this is also restricted to a specific kinetic boundary.

Regarding the reactor design, reaction rate and reactor length were considered. A log-log – relation was obtained for realistic length scale, which turns into an increasingly nonlinear relation at small scales being attributed to fixed-bed heat conduction. In principle, the requirements concerning a minimum reactor length can be reduced, if larger amount of heat is liberated via an increased inlet concentration. However, in the end, kinetic limitations will decide about the reactor dimension.

Since the nonlinear analysis revealed that only specific flow rate ratios or switching times are appropriate, it was important to consider a control concepts to maintain ignited reactor operation. The next chapter examines several options to control the SMBR.

5. Analysis of Control Concepts

In the previous chapter multiplicities regarding of various process parameters were examined. It was shown that the flow rate ratio is limited to a certain ignition domain, which applies to the corresponding switching times in a SMBR as well. Such an attainable operation window also depends on the heat capacity ratio, the Lewis number and the bed void fraction. These figures are often not precisely known, and, as will be shown later in the experimental section, the reactor jacket and the valves may also contribute to deviations of reactor operation from ideal conditions. To handle these uncertainties a proper control concept is required. In addition it is important to adjust the switching time in case of fluctuations in the feed conditions, such as in the gas flow rate and the feed concentration. This chapter therefor deals with the identification of an appropriate controller based on dynamic simulations of the SMBR. Hereinafter the notion *open-loop* applies to the reactor operation with predefined switching times, thus without feedback, and the term *closed-loop* will be used in case of a feedback of a specific temperature signal.

The first theoretical study on control of autothermal SMBR type reactors was published by Barresi et al. [150]. One approach investigated theoretically is based on triggering the switch when the local temperature at the beginning of the active fixed-bed segment falls below a threshold value. However, the results obtained were poor. A second approach suggested by the same authors included a comparison with the local temperature at the beginning of the subsequent reactor segment. If in addition, the temperature at this second sensor exceeded a typically higher threshold value, the feed and product positions were switched. Using this concept, the second sensor was mainly active and the leading thermal front was monitored for control. Methods for the identification of suitable set-points have not been reported.

Additional research was carried out on advanced control concepts. For instance, an observer design for the catalytic reduction was suggested by Fissore et al. [151]. Also a stability analysis for a specific control concept was investigated by Smagina et al. [152] based on an approximate model of the rotating pulse solution reported earlier [58]. The same group presented also a theoretical study dealing with equilibrium limited reactions [58] suggesting a control concept based on several sensors. Reconstruction of the pulse using a parabola and estimation of the pulse velocity was exploited within a proportional and PI controller. However, an optimal number of sensors has not been reported, yet.

The present work compares three control concepts and discusses several obstacles one has to overcome when dealing with controller parameterization. As a first concept it is suggested to place only a single sensor at the end of the first reactor segment and to monitor the reaction front at the sensor location. If a certain temperature set-point has been reached, the switch is triggered and the corresponding switching time is used for the subsequent segments until an update is available in the next cycle. This concept is denoted as *controller 1*.

The next control concept is based on monitoring the leading thermal front. This concept

can be compared to the second method reported by Barresi et al. [150]. In this work, however, it is suggested to simplify the controller hereinafter denoted as *controller 2*. Only two sensors are needed for an arbitrary large number of units installed. One sensor is again located in the first segment to monitor the reaction front in the startup phase. The second sensor is placed at the end of the last segment to monitor the leading thermal front. Similar to *controller 1*, the recorded switching times are used for the intermediate switching periods until an update after a cycle completed.

A third controller *controller 3* is suggested in this work. It exploits one thermocouple installed at the end of each reactor segment to trigger the switching events. This approach should improve controller robustness considerably. In this work a reliably heuristic for the parameterization of the *controller 3* is presented dealing with the determination of the boundaries of the temperature set-point. For that reason, such a controller will be suitable for reactors of an arbitrary number of segments subject to important uncertainties, e.g. in the values of the heat capacities. The three concepts considered are characterized in this chapter and corresponding experimental results given in the next chapter.

5.1. Characterization of Control Concepts

This section is dedicated to introduce the properties of the three controller investigated. Specifications of the controller are summarized in appendix C. At first the startup from a high initial temperature is considered and then the proposed *controller 3* is characterized in more detail. To illustrate results of the analysis performed the period maximum temperatures ($T^{\max}$) are presented as a function of the switching times as well as the cyclic profiles.

5.1.1. Single Sensor Control (*controller 1*)

The approach of *controller 1* is monitoring the reaction in the first segment and applying the measured switching time for subsequent periods until the update after a completed cycle. In figure 5.1 is presented the startup situation with a preheating temperature of 700 K and a set-point of T_A= 460 K. The profiles are shown after a completed cycle, when the feed is in front of the first segment just before the switch to segment two. The reactor settles on the cyclic periodic state after approximately 50 cycles. Typically the trailing reaction front is steep and the dispersive thermal front shows a smooth temperature decline. In terms of the switching times, larger oscillations appear at startup with a subsequent decline to the cyclic steady-state switching time. Oscillation takes place between two different switching times in every cycle. This is due to the fact, that keeping the switching time constant over period two and three, this switching time is either to large or too small to match the updated switching time in the first segment of the subsequent cycle.

In figure 5.1 right are shown the cyclic maximum temperatures over the transients of the specific switching time together with the typical isola solution. The bifurcation diagram of the isola was calculated by parameter continuation of the TMBR in the solid phase velocity u_s. The intercepted line represents the unstable branch and the thick line indicates the stable ignited solution, whereas the stable extinguished branch is not shown for the sake of clarity. It was found in the previous chapter that such isola branch is in good agreement with

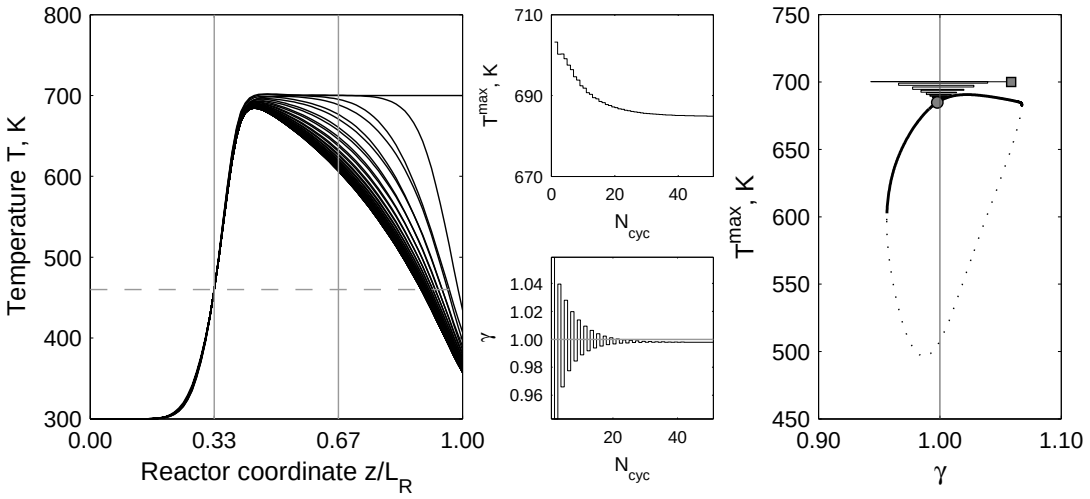

Figure 5.1.: Single sensor *controller 1* with a set-point of $T_A = 460\,\mathrm{K}$. Left, cyclic temperature profiles. Middle, the periodic transients of the maximum temperature and the specific switching time. Right, isola solution branch and temperature transients. Model, parameters and definitions of the controller are given in the appendices B.1, table B.1 and section C.3.

the maximum temperature calculated with the periodic SMBR model, though a deviation between these rector models by several degrees is present. The reactor transients start at the initial temperature of 700 K and then oscillations occur before settling on the stable solution branch at a certain reduced switching time. Basically, the selection of an appropriate set-point of the controller is the main challenge.

Following examples reveal the problems encountered with such a simple controller. At first, the lower range of the set-points was investigated. Reducing the set-point towards the feed temperature is accompanied with increased oscillations at startup and it takes longer for the relaxation on the single switching time. Interestingly, sustained oscillations occurred in the range of $T_{A,\mathrm{sp}} = 317 - 425\,\mathrm{K}$ with typical oscillating profiles as shown in figure 5.2 left. A slight decrease of the set-point below 317 K causes extinction of the reactor.

There are two findings concerning the upper bound of the set-point. First of all, there is a certain high set-point value where extinction will occur and secondly, the type of controller transitions becomes important. With regard to the first issue, extinction was found to occur later when selecting parameters closer to ignition bounds. In the case considered, it took about 120 cycles to finally show light off.

For the second aspect it should be stressed that transitions of the Petri net, which is used as a an element to specify the discrete part of the dynamic model as defined in the appendix C.1, can be given e.g. in two different ways: In this work termed uni- or bidirectional transitions. This means, that a temperature signal triggers the switch when crossing the set-point either from one (uni) or from both sides (bidirectional). In this way, a decision about the recognition of the type of front passing the sensor is made. Applying the bidirectional transition may lead to a misinterpretation of the correct switching event due to the recognition of either thermal or reaction fronts. Figure 5.2 (middle) illustrates the effect also reported by [150]. In the right figure an unidirectional transition was implemented showing extinction as well.

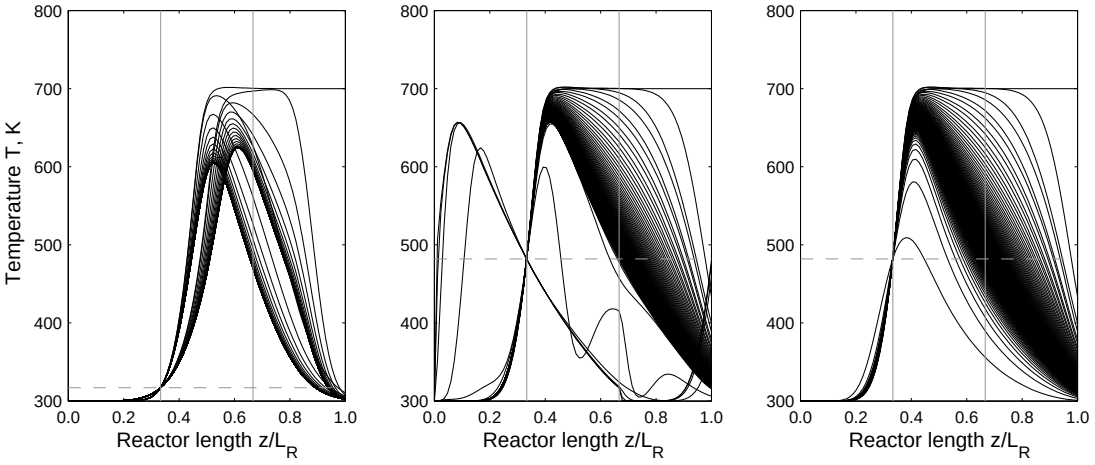

Figure 5.2.: Left oscillations over one cycle for low set-points. Extinction occurs at a high set-point of 481 K, either by bidirectional event handling which causes to trigger the dispersive thermal front (middle) by mistake or by unidirectional events (right). Model, parameters and definitions of the controller are given in the appendices B.1, table B.1 and section C.3.

Thus, a set-point for ignited states has to be identified for both cases. Though concerning a precise identification of a certain front requires the consideration of the type of transition. This will become specifically important when for instance different switching regimes, as suggested by Mancusi et al. [153], are investigated.

Because of the relatively small range of set-points of only 55 K for a stable ignited operation, *controller 1* does not offer optimal properties.

5.1.2. Two Sensor Control (*controller 2*)

The purpose of *controller 2* is to observe the leading thermal front with a second sensor T_B in order to determine the switching times. However, for startup the reaction front has to be observed (with sensor T_A) over a certain number of cycles until the thermal front is steep enough to reach the set-point $T_{B,\mathrm{sp}}$. Figure 5.3 gives a typical example with $T_{A,\mathrm{sp}} = 550$ K and $T_{B,\mathrm{sp}} = 400$ K. After two cycles, the second sensor is active and at startup oscillations are observed. If the first set-point is set to lower values comparable to the *controller 1*, it is likely that only this one remains active. In general, for a sufficiently high value of $T_{A,\mathrm{sp}}$ the second sensor will become ruling.

For lower set-points of sensor B, again sustained oscillations occur below, i.e. $T_{B,\mathrm{sp}} = 320$ K. This is illustrated in figure 5.4. The reactor shows a narrow temperature pulse and oscillations in the switching time. Extinction occurs at 305 K. An upper stability bound can be identified as well. For the particular case a set-point of $T_{B,\mathrm{sp}} = 490$ K causes light off.

Compared to *controller 1*, the range of suitable set-points is significantly larger for the thermal front sensor T_B, however it is required to provide two different set-points. I.e. this first set-point should exceed the upper stability bound in order to make the second becoming active, which is of course limited by the preheating temperature. The second set-point can be selected in a larger range, e.g. from $320 - 490$ K for the particular example. To further simplify

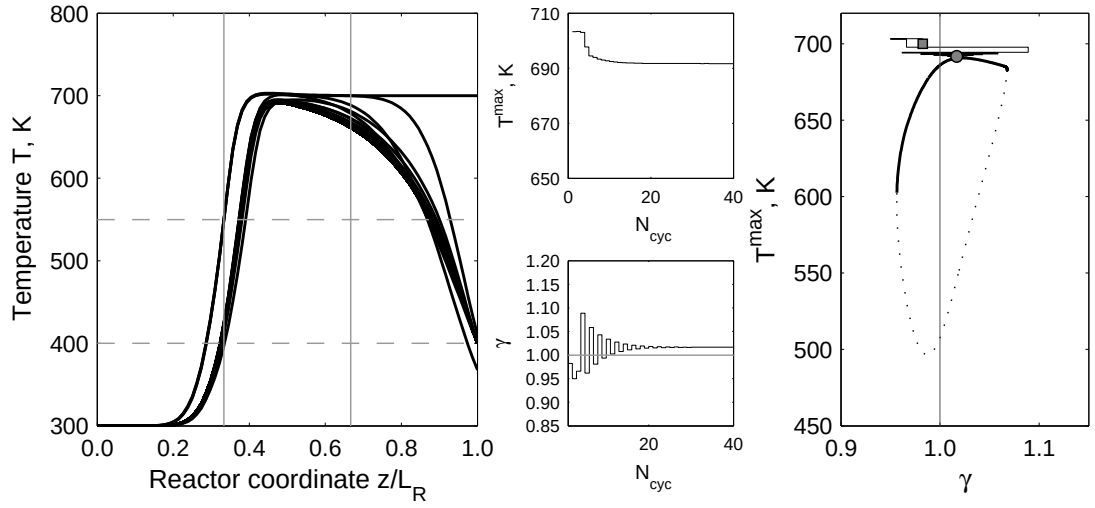

Figure 5.3.: Two sensor control (*controller 2*) with a set-point $T_{A,\mathrm{sp}} = 550$ K and $T_{B,\mathrm{sp}} = 400$ K. Left, cyclic temperature profiles. Middle, periodic maximum temperature and the specific switching time. Right, isola solution branches and temperature transients. The points indicate start and end of observation with a preheating temperature of 700 K. Model, parameters and definitions of the controller are given in the appendices B.1, table B.1 and section C.3.

the controller tuning a new *controller 3* is suggested and explained below.

5.1.3. Multi-Sensor Control (*controller 3*)

In this work it is suggested to use a single sensor in each of the reactor segments installed for monitoring the reaction front leaving the active segment. Hereby the advantage is seen in an easier controller design due to an increased robustness. The more robust a controller can operate the reactor, the less the effort for parameterization (finding appropriate set-points).

Throughout the following investigations a single set-point T_{sp} applies for all three sensors (T_A, T_B, T_C). Displayed in figure 5.5 are temperature profiles, cyclic temperature transients and the stability window. The reactor settles very fast to a final switching time without showing oscillations. Note that the switching times are identical in the first period of *controller 1* and *controller 3*, but deviate in the further course significantly. Since both controllers, *1* and *3*, monitor the reaction front, similar switching times result in the cyclic steady state. The next sections explain in detail the parameterization of the *controller 3* and the preheating temperature required.

5.1.3.1. Analogy Between Open-Loop Control and Window for Ignited States

The set-points for *controller 3* can be selected for the example considered in wide range from slightly above the inlet temperature of 300 K up to 480 K. Figure 5.6 (left) presents the controller characteristic relating the parameter of the controller, the set-point T_{sp}, to the controller output given in terms of the reduced switching time γ. The influence of the mass flow density and the feed concentration is investigated.

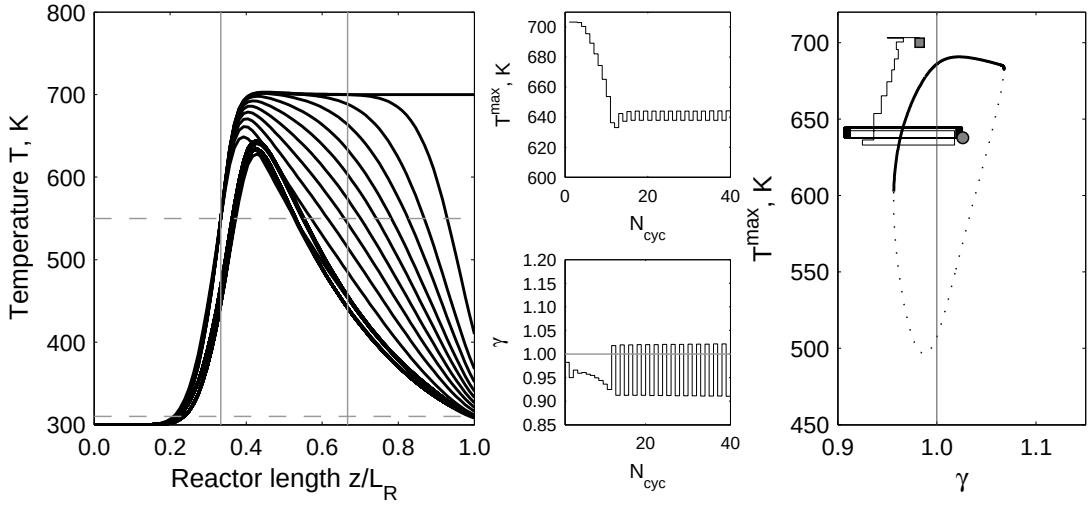

Figure 5.4.: Control of reactor using a two thermocouples monitoring the thermal front (*controller 2*). Oscillations occur at set-points below 320 K - extinction sets in below 305 K. Model, parameters and definitions of the controller are given in the appendices B.1, table B.1 and section C.3.

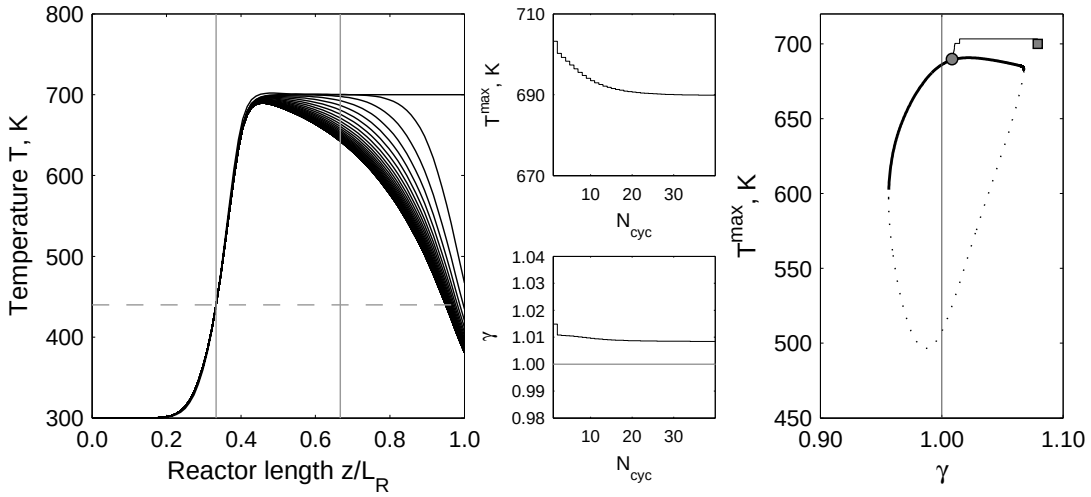

Figure 5.5.: Three sensor control with T_{sp} = 400 K. Left, the cyclic temperature profiles. Middle, the cyclic transients of the maximum temperature and the specific switching time. Right, isola solution branch and temperature transients. Model, parameters and definitions of the controller are given in the appendices B.1, table B.1 and section C.3.

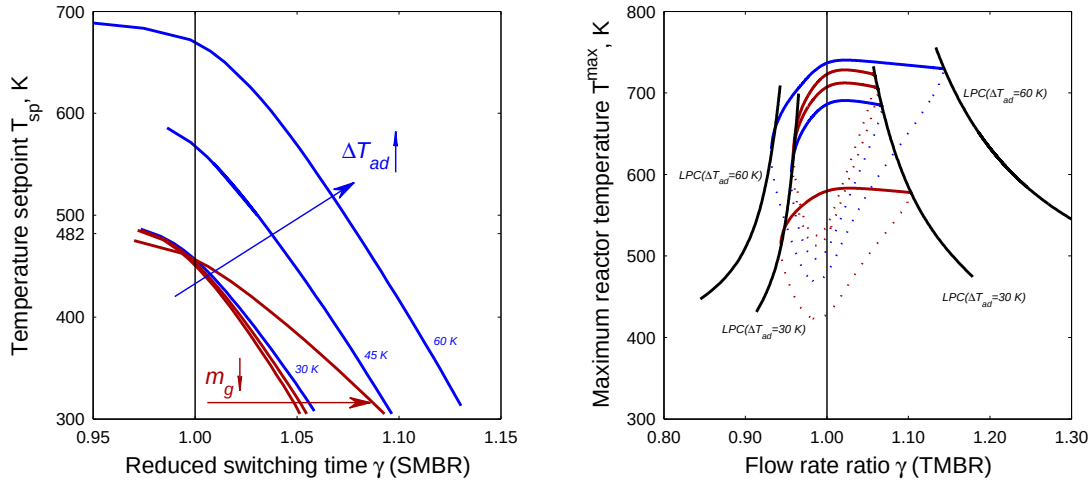

Figure 5.6.: Left: controller characteristic relating temperature set-point (parameter) to reduced switching time (output) for *controller 3*. Examples include different mass flow densities of 0.1, 0.5, 1.0, and 1.5 kg/m^{2}s at constant feed concentration corresponding to ΔT_{ad} = 30 K (red lines) and at different feed concentration corresponding to ΔT_{ad} = 30, 45 and 60 K at 1.0 kg/m^{2}s (blue lines).
Right: isola solutions relating maximum reactor temperature to flow rate ratio γ (TMBR) for two different feed concentrations corresponding to ΔT_{ad} = 30 and 60 K and different mass flow densities (red lines). The loci of the limit points are given as a function of the flow rate ratio γ and the mass flow density $\dot{m}_g$ for a constant feed concentration (black lines).
Models, parameters and definitions of the controller are given in the appendices B.1 (SMBR), B.3 (TMBR) table B.1 and section C.3.

Generally, with increased set-points, smaller switching times are obtained until a stability limit depending on the feed conditions bound has been reached. Each set-point can also be related to a switching time of the corresponding open loop control in cyclic steady state, which in turn can be associated with a steady state of the TMBR model. To clarify this relation several isola are illustrated in figure 5.6 (right). The limit points of the isola can be located with a function for different mass flow densities and flow rate ratios. This function, denoted here as a limit point curve $LPC = LPC\left(\gamma, \Delta T_{ad}\right)$. Thereby, only two examples are given for the sake of clarity, for a constant feed concentration corresponding to ΔT_{ad} = 30 and 60 K.

The feed concentration significantly influences the upper bound of the set-points. As an example, comparing the isola for 30 and 60 K an increase in width is observed, while the maximum temperature is only slightly increased.

The flow rate has only a minor influence on the range of available set-points. An increase of the range of specific switching times γ is observed for lower flow rates. But the main influence is seen in the reactor maximum temperature, which becomes obvious with the limit point curves *LPC* (fig. 5.6 right). A tenfold reduction in the flow rate from 1 down to 0.1 kg/m^{2}s causes only a slightly larger isola, however, at significantly smaller reactor temperatures. In contrast, the feed concentration has a much stronger impact on the isola width than on the maximum temperature.

These results indicate that the range of possible set-points is mainly limited by the feed concentration. In contrast to *controller 1* and *controller 2*, where low set-points cause difficulties,

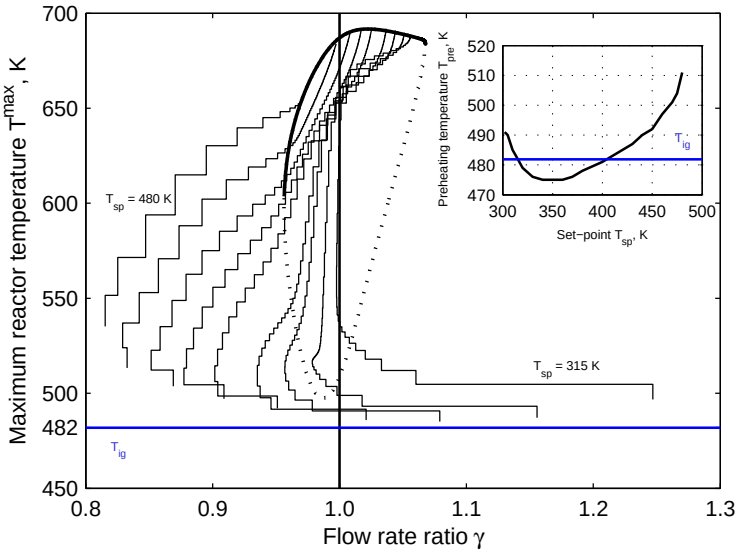

Figure 5.7.: Periodic maximum temperature for a range of set-points starting from a specific minimum preheating temperature (ΔT_{ad} = 30 K, $\dot{m}_g$ = 1.0 kg/m^{2}s). The reactor states settle on the ignited stable solution branch of the isola, for low set-point on larger specific switching and vice versa. Inset: exact preheating temperatures for the range of set-points. The ignition temperature T_{ig} is based on equation 2.40. Models, parameters and definitions of the controller are given in the appendices B.1 (SMBR), B.3 (TMBR) table B.1 and section C.3.

for *controller 3* low temperature set-points provide even for lean feeds stable operation.

5.1.3.2. Ignition and Startup

For startup of the reactor preheating is needed, such that the exothermic reaction is initiated and supplies sufficient heat to assure ongoing ignited operation. A first estimate for the required preheating temperature is the ignition temperature derived in section 2.2.1.

For an open loop control the unstable branch of the approximated isola represents the ignition-extinction limit. This is not the case for the proposed controller. Figure 5.7 shows the transient periodic maximum temperature for several set-points starting always from a minimum preheating temperatures together with the isola branches (for ΔT_{ad} =30 K, $\dot{m}_g$ = 1.0 kg/m^{2}s). The transient reactor temperatures start in a specific point (γ, T^{max}) in period one and approaches in the further course the stable branch of the isola. In case of low set-points the reactor transients do not follow a direct path to the stable solution. Initially larger switching times occur followed by values below $\gamma = 1$. After temperature increases the reactor state finally turns towards larger reduced switching times on the stable isola solution branch.

The preheating temperatures T_{pre} together with the estimated ignition temperature (eq. 2.40) are presented in the inset of figure 5.7.

The preheating temperature is not constant for the attainable range of set-points and resembles a parabola. Compared to the reactor temperatures in the first period, even lower values are possible. This can be explained with transient temperature excursion due to the well known wrong way behavior [83]. The required preheating temperature can even be less

than the ignition temperature. It should be stressed that the estimated ignition temperature given by equation (2.40) does not take into account concentration effects. For example, the isola stability window significantly grows in size for larger feed concentrations, which in turn reduces the required preheating temperature. Hence, the ignition temperature calculated can be regarded as a first estimate of the required preheating temperatures. Startup with much larger feed concentrations would result in lower effective preheating temperatures of the SMBR. A possible estimate including concentration effects is investigated in appendix A.

Moreover, the ignition temperature is also a course estimate for an upper stability limit of the temperature set-points, particularly for *controller 1* and *controller 3*. The estimate of the ignition temperature for the case considered is 482 K. This is in good qualitative agreement with largest set-point applicable for the small feed concentration corresponding to $\Delta T_{\mathrm{ad}} = 30$ K. Thus, the set-point T_{sp} should be selected between the inlet temperature and the estimated ignition temperature, and the preheating temperature should exceed the ignition temperature.

5.2. Controller Performance

In this section the performance of the controller is discussed for the case of introducing step inputs, at first for the example of varying the feed concentration and then for step inputs of the total flow rate.

5.2.1. Perturbation of Feed Concentration

The feed concentration is a typical example for a process input which is subject to perturbations. The effect of steps of concentrations, which are given as corresponding adiabatic temperature rises of $\Delta T_{\mathrm{ad}} = 30 - 90 - 30$ K on the controller performance is presented in figure 5.8. All controllers are capable to adjust properly the switching times, with set-points of 440 K, which was selected to guarantee a stabilization of *controller 1*. The results show decaying oscillation if *controller 1* is applied, which are also present in the startup phase for *controller 2*. *Controller 3* adjusts instantaneously the proper switching time.

Note also that the *controller 1* and *3* monitoring the reaction front are closely related. Typically the switching times in accordance to the controller characteristic explained in section 5.1.3.1 are obtained, resulting in identical switching times in case the cyclic steady state has been reached. *Controller 2* provides also a stable operation when the second sensor becomes active and only slight changes in the switching times are observed compared to the ones used by *controller 1* and *3*. The perturbations in the feed concentration can be handled by all controller types providing proper set-points are available.

5.2.2. Perturbation of Flow Rate

The flow rate has a strong effect on the front velocity as discussed in section 5.1.3.1. Changes have to be compensated by adjusted switching times. A comparison of the controller is shown in figure 5.9 for the example of steps in the flow rate. The observed temperatures of the sensor T_A are shown to illustrate the front velocity, which considerably changes as the flow rate is

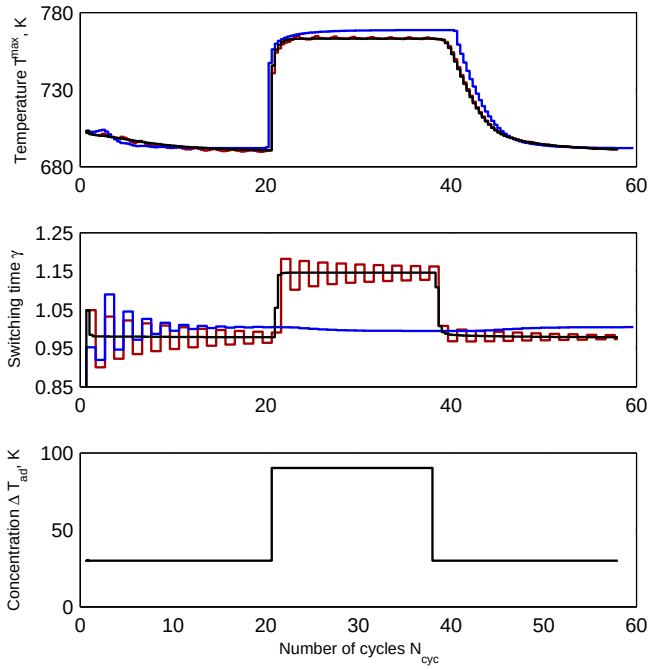

Figure 5.8.: Comparison of the controller based on responses to input steps in the feed concentration according to ΔT_{ad} = 30-90-30 K, the red lines *controller 1* (single sensor), blue lines *controller 2* (two sensors), black lines for the suggested *controller 3*. Model, parameters and definitions of the controller are given in the appendices B.1, table B.1 and section C.3.

switched to a new level. The first input step is downward to almost half the initial flow rate and then a larger step heights were considered.

Controller 1 shows in figure 5.9 light off at the input step to the higher flow rate after 30 cycles. The second controller still keeps the reactor ignited. Thereby adjustment of the set-point $T_{A,\mathrm{sp}}$ up to 680 K was necessary in order to monitor only the leading thermal front. Otherwise, light off would occur much earlier, similar to *controller 1*. *Controller 2* almost lights off for the step 0.55 back to 1 at 60 cycles and finally shows a failure at the last large step. Oscillations in the switching times are also present for *controller 2*.

The set-point of *controller 3* was set to 440 K in order to attain similar switching times compared to *controller 1*. *Controller 3* ensures ignited states for the particular example without oscillations. Also larger perturbations than shown are possible, whereby the other two controllers *1* and *2* do not operate at all. For example, even a large step change in the mass flow density 0.5 up to 14 kg/m^{2}s can be handled by *controller 3*. It was found that the largest acceptable step difference can be identified in the following manner: Given an isola solution with a certain stable high temperature solution branch, then a jump to larger flow rates is restricted to the presence of the unstable solution branch of the new isola with at least the same height. Such cases appear to be hypothetical, but demonstrate the robustness of *controller 3* suggested in this work.

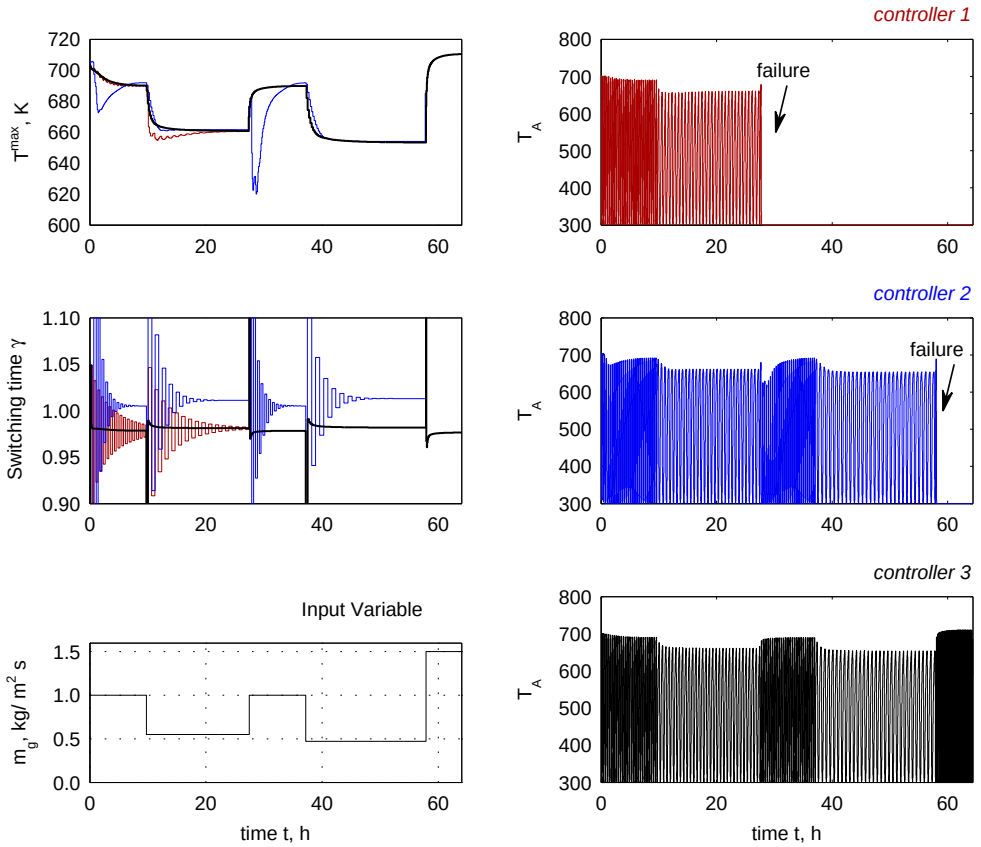

Figure 5.9.: Comparison of the controller based on responses to input steps in the total flow rate. Red lines represent *controller 1* (single sensor), blue lines *controller 2* (two sensors), black lines for the suggested *controller 3*. Model, parameters and definitions of the controller are given in the appendices B.1, table B.1 and section C.3.

5.2.3. Evaluation of Control Concepts

The main features of the controller concepts are compared in table 5.1. The characteristics of the fronts determine in the first instance the properties of the investigated controller. If the dispersive thermal front is monitored (*controller 2*), the velocity depends on the Lewis number and the bed heat dispersion. For a constant set-point also the maximum temperature will have an effect on the switching time, which in turn will be determined by the reaction front.

Triggering the switching events based on the observation of the reaction front increases the number of variables directly involved. Accordingly, the controller output is directly affected by the local reaction front characteristics and the switching times will tend to settle on larger switching times due to the smaller reaction fronts velocities. Thus they are more sensitive towards reaction related variables, e.g. catalyst aging and concentration related disturbances.

In section 5.1 limitations with respect to the set-points were discussed. For *controller 2* at least the range of the second sensor was larger. For *controller 3* it was shown that a low value above the feed temperature is sufficient and the upper bound is mainly determined

by the feed concentration. Furthermore an important factor is the horizon or the window of observation. It was demonstrated that a reduction from a full cycle to only a single period efficiently prevents oscillations. The range of suitable set-point becomes larger comparing *controller 3* and *controller 1*. Concepts with an even greater number of sensors could further improve robustness, but would require a more complex implementation.

Table 5.1.: Comparison of controller characteristics.

	controller 1	*controller 2*	*controller 3*
Dependency	reaction front	thermal front	reaction front
Parameterization	single set-point	two set-points at different temperatures	one identical set-point for all sensors
Set-point range	very narrow	limited	larger, limited by feed concentration
Robustness	low	intermediate	high

A selection of the appropriate controller concepts can be made considering the following aspects: Operating reactors where identical properties of each segment cannot be guaranteed (e.g. in real equipment), in principle the window of observation should cover only a single switching period. Furthermore, in the presence of heat losses or non-idealities resulting from the equipment, also the dispersive thermal front observed with *controller 2* will greatly deviate from the ideal shape, while the reaction front generally preserves its steep shape and a sufficient height due to its ability to exhibit a constant pattern characteristic. It was also found for certain situations that the reaction front has already positioned in the subsequent segment at the switching event using *controller 2*. Unfortunately this fact can be regarded as an obstacle when trying to reduce the slip. This option was explained in section 2.4.2, whereby shifting a portion of the reaction front with a high temperature left over in the active segment to the end of the cascade ensures an almost complete suppression of the slip compared to reversed-flow reactors. Considering this option, the reaction front has to be monitored. Only *controller 3* could solve this task efficiently. Thereby it is also interesting to think of shifting the sensor location from the end of the reaction segment towards inner positions in order to trigger the switches at a low and stable set-point, while ensuring that a predefined hot portion is shifted to the end to achieve total conversion.

Considering the above mentioned aspects, *controller 3* monitoring the reaction front in each segment installed was favored concerning an experimental realization. In the next chapter the experimental implementation of this controller for the example of perturbation of the feed concentration and total flow rate is demonstrated.

5.3. Summary

Due to the narrow window of switching times available, the uncertainties in the heat capacity ratio would make it rather complicated to operate the reactor in open-loop control. In addition, for fluctuations in the reactor input a suitable feedback control to operate the SMBR is required.

Two basically different control strategies were considered; either monitoring the reaction front or the leading dispersive thermal front. Furthermore, the window of observation was distinguished into a complete cycle or only a single switching period.

The first concept, *controller 1*, was based on a single sensor monitoring the reaction front in every cycle. It was found, that the range of set-points was very limited and sustained oscillations are likely to occur prohibiting robust ignited operation. An improved second *controller 2* is based on monitoring the leading thermal front in every cycle. The investigations revealed a better performance compared to *controller 1*, but parameterization can become an elaborate task. This is due to the two different set-points to be specified, a first one is required to monitor the reaction front for start-up, the second one is needed for the leading thermal front.

Controller 3 suggested in this work is based on monitoring the reaction front in each segment. This allows for a robust control due to an observation window of only a single switching period. The controller characteristic can be associated with the TMBR model and a the domain of set-points was identified to be between the inlet temperature and the estimate of the ignition temperature.

Responses to step inputs in the flow rate and the feed concentration confirmed the proper disturbance rejection of *controller 3* compared to *controller 1* and *controller 2*. It was finally discussed in which way the properties of the different fronts influence the controller output.

The next chapter contains the experimental realization of *controller 3* to operate the reactor in case of perturbations in the flow rate and the feed concentration.

6. Experimental Investigations

This chapter presents the experimental results of a SMBR reactor for the example of the model reactions, the total oxidation of propene and ethene on a $CuCrO_x/Al_2O_3$ catalyst in air. A two bed SMBR unit was built and set into operation.

First section gives an overview on the industrial background and then presents the experimental system. The reactions system and the evaluation of kinetic parameters is reported as well as the elements of the SMBR setup. Experiments in open-loop control have been conducted to screen the range of applicable switching times and closed-loop operation was characterized regarding the controller set-points and the performance under step-inputs. The oxidation of propene–ethene mixtures is finally discussed.

6.1. Catalytic Oxidation of VOCs

Reduction of greenhouse gases and the destruction of harmful and toxicological compounds are important areas, where legal acts have been implemented to set strict limits [154]. Among the problems arising in this field, specifically the treatment of volatile organic compounds (VOCs) is a task often appearing at chemical manufacturing sites and abandoned emission sources. VOCs are organic compounds with a specific vapor pressure of at least 0.01 kPa (at 298.15 K) as specified by the European Commission [155]. In other countries different definitions apply. Industrial sources of VOCs are often connected with organic solvents, which are employed in the chemical and pharmaceutical, as well as in coating and printing industries. Removing the VOCs from effluent streams can be achieved by oxidation for the final destruction into the oxidation products, water and CO_2.

However, the problem with flame based oxidation is seen in the NO_x formation due to the reaction of the air constituents at high reaction temperatures. Above 1700 °C thermal NO_x formation occurs, but also at lower temperatures ($\approx$ 1500 °C) a hydrocarbon radical initiated NO_x formation is possible [154]. In case of chlorinated VOCs, high temperatures contribute to the formation of toxic *polychlorinated dibenzo-p-dioxines* (PCDD) [156].

Catalytic oxidation offers much lower reaction temperatures due to the role of catalyst promoting the oxidation reactions. In this way, undesired side reactions are successfully suppressed. Moreover, flame based destruction requires considerable amounts of fuel to achieve for complete destruction sufficiently high temperature in the range of 800 to 1200 °C. However, the catalytic oxidation is not that common, which is due to the danger of poisoning the catalyst in the presence of certain VOCs. Also thermal deactivation can be an issue, but these factors can often be handled by proper catalyst and process design [157].

Typical VOC oxidation catalyst include noble metals like platinum and palladium, which are highly active oxidation catalyst, but too expensive to be applied in industrial off gas treatment and are thus limited to applications in small scale units, i.e. in cars. Moreover, their

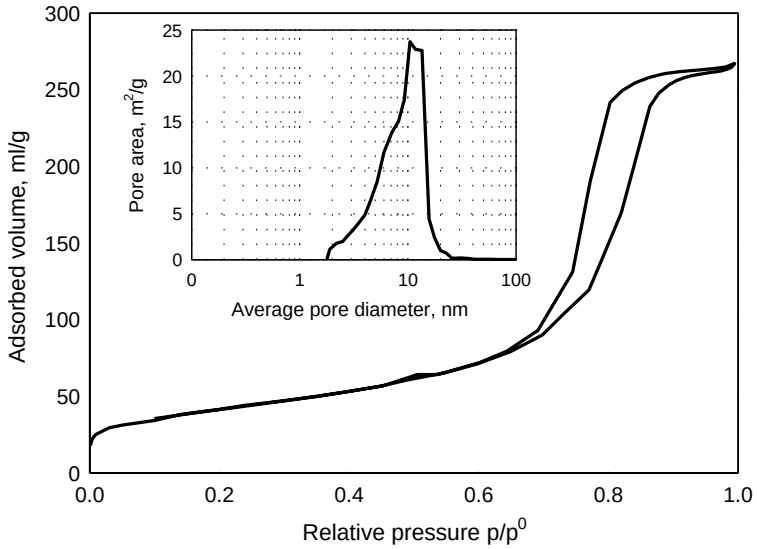

Figure 6.1.: BET measurement with N_2 gives typical type IV isotherm and a rather narrow distribution of the pore area of the $CuCrO_x/Al_2O_3$ catalyst.

low stability in the presence of halogenated contaminants have motivated the research for different catalytic systems. Supported transition metal oxides of chromium, nickel, manganese or copper are identified as possible candidates. Also many mixed metal oxides, supported e.g. by metal oxides such as TiO_2 or Al_2O_3, show the required activity and stability .

6.2. Catalytic System and Identification of Reaction Kinetics

6.2.1. Characterization of Reaction System

In this work, the total oxidation of propene and ethylene on an oxide catalyst was investigated. It is assumed that these reactions are reasonable representatives for the treatment of volatile organic compounds. The hydrocarbons are completely oxidized according to the chemical formula:

$$C_mH_n + \left(m + \frac{n}{4}\right)O_2 \longleftrightarrow mCO_2 + \frac{n}{2}H_2O \tag{6.1}$$

In 6.1 the mole numbers are denoted as m and n. In this total oxidation the reaction products are carbon dioxide and water. Anyway, reaction intermediates such as alcohols, aldehydes and carbon monoxide may occur, but in negligible amounts. Thus, the selectivity towards the total oxidation products is assumed to be very high and thermodynamic limitations are assumed to be absent [157].

The catalyst was prepared by wet impregnation of an γ-aluminum oxide support ($\gamma - Al_2O_3$) with a $Cu(NO_3)_2/Cr(NO_3)_3$ precursor. After drying and calcination the greenish material was further characterized by BET adsorption and atomic absorption spectroscopy (methods described in [158]). The results of the BET measurements (standard N_2) are shown in figure 6.1.

A hysteresis forms due to capillary condensation which is typical for mesoporous adsorbents like many oxides – the isotherm is a classical type IV according to IUPAC. Based on the BET isotherm the average surface was estimated to 138.4 m^2/g and the pore diameter to 11.4 nm according to BJH method. The metal species consisted of 6.6 % copper, 2.4 % chromium and 35.42 % aluminum. The original pellets size was 1.8 mm, after milling and screening the 1 mm fraction of crushed catalyst particles was used throughout the experiments.

6.2.2. Kinetics of the Total Oxidations

Steady-state experiments with fixed-bed reactors were carried out to quantify the reaction kinetics. The scope of this work was to derive parameters of power law kinetics. Although this approach is often applied, it is not considered to yield very accurate results, however, it provides reasonable mathematical descriptions of the reaction rates as a good starting point for reactor design and analysis. Regarding detailed kinetic studies of complex chemical networks a different experimental approach would have been required [159].

The kinetics of the total oxidations have been investigated using a tubular fixed-bed reactor with bed dimensions of 3 cm in length and with an inner diameter of 2.1 cm. Thermocouples where placed in front of the bed, in the center and at the outlet. A more detailed description of the experimental setup and quantification methods, including automation of the reactor setup and *GC* analytic, are described in [160] and in report [161]. To reduce mass transfer resistance a particle fraction of 250 µm was used (6 g).

Typically the temperature was increased step wise in the range of 180 – 420 °C withdrawing samples when steady states had been established. The specific residence time defined with the mass of catalyst:

$$\tau_{K,g} = \frac{m_K}{\dot{V}_g} \tag{6.2}$$

was systematically investigated for 15 , 25 and 40 kgs/m^3. The inlet concentration for each single alkene was studied in the range of 0.15, 0.25, 0.35 and 0.5 %. Additionally, mixtures of propene and ethene were investigated for the ratios 1:3, 1:1 and 3:1 for the total concentrations of 0.15 , 0.25 and 0.35 %.

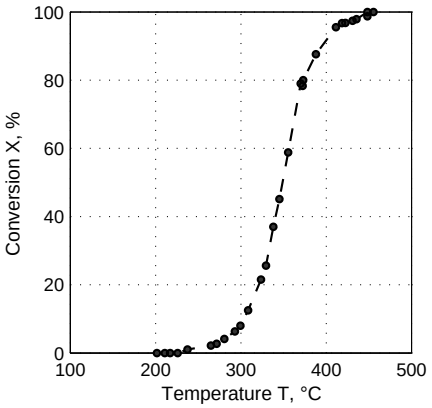

Figure 6.2.: Typical relationship between conversion and catalyst temperature.

Oxidation products were found to be water and carbon dioxide only. Possible intermediates, like carbon monoxide or other hydrocarbons, could not be detected. With 100 % selectivity the hydrocarbon conversion (eq. (2.43)) was therefore sufficient to quantify the reaction progress. In the course of the experiments a typical S-shaped conversion vs. temperature dependency was observed, also denoted as *light-off curve* (fig. 6.2). A moderate increase at lower temperatures is followed by a temperature zone with significantly larger conversions up to 80 %. For total oxidation the temperature has to be raised by approximately 60 °C up to 450 °C. Even though the conversion vs. temperature plots are frequently used in environmental catalysis studies [162], they should be evaluated with care. Due to the exothermicity of the oxidation reaction, deviations from isothermal

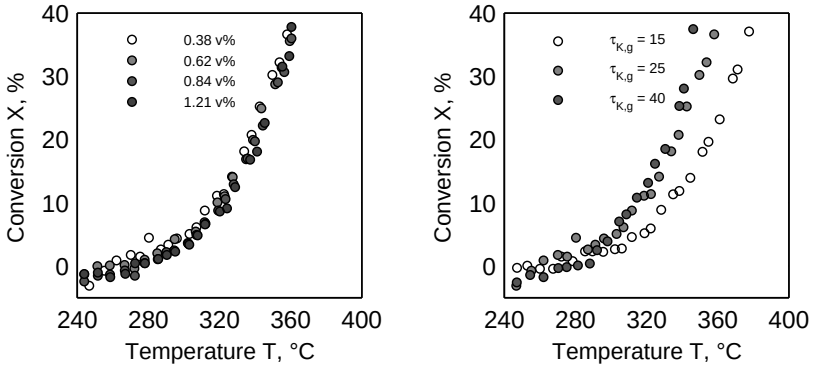

Figure 6.3.: Experimental results for ethylene total oxidation on $CuCrO_x/Al_2O_3$ catalyst for different feed concentrations (left) and the residence time $\tau_{K,g}$(right).

conditions with significant axial and radial temperature gradients are likely to occur which can lead to misinterpretation of the observed reaction rates.

6.2.2.1. Oxidation of Single Hydrocarbons

The feed concentration of the single alkenes has been varied systematically, thereby ensuring excess of oxygen in air. Figures 6.3 and 6.4 illustrate the experimental conversion of ethene and propene. The ethene feed concentration was varied from 0.38 up to 1.2 % with increased conversion at small inlet concentrations. Beyond 340 °C, the differences in the conversion with respect to different inlet concentration decrease. A similar relationship is observed for the propene oxidation (fig. 6.4), whereby higher conversions for lean feeds are obtained. Residence time effects were considered with $\tau_{K,g} = 15, 25, 40$ kgs/m^3. Typically, larger contact times lead to increased conversion.

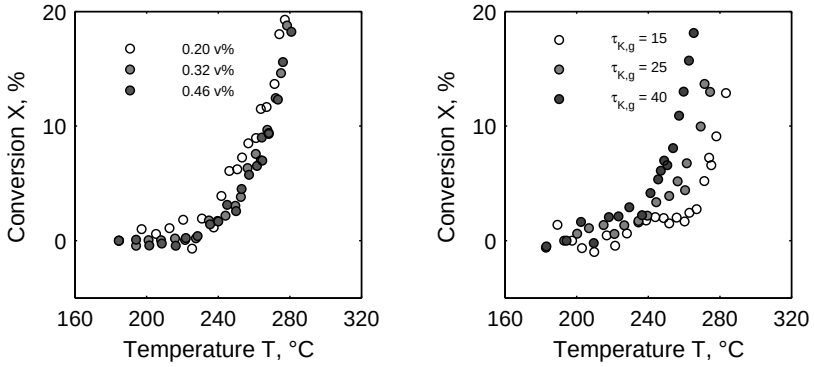

Figure 6.4.: Experimental results for propene total oxidation on $CuCrO_x/Al_2O_3$ catalyst for different feed concentrations (left) and the residence time $\tau_{K,g}$ (right).

The catalyst activity is higher with respect to propene oxidation compared the ethylene. 10% conversion is achieved at 270 °C for propene at 320 °C for ethylene. This gap increases at higher catalyst temperatures. This observation can be explained with the larger sensitivity of propene oxidation with respect to the catalyst temperature. However, non-isothermal

conditions can also be responsible for increased conversions at high temperatures.

6.2.2.2. Oxidation of Mixtures

The oxidation of mixtures of hydrocarbons can deviate from the behavior of the single components. In most cases it is believed that competitive adsorption leads to an inhibition effect and the reaction rate in the mixture is lower compared to that of the corresponding single hydrocarbons [162].

Experiments were performed to check the activity in the mixture (fig. 6.5). Three compositions were investigated at constant hydrocarbon concentration. For comparison the

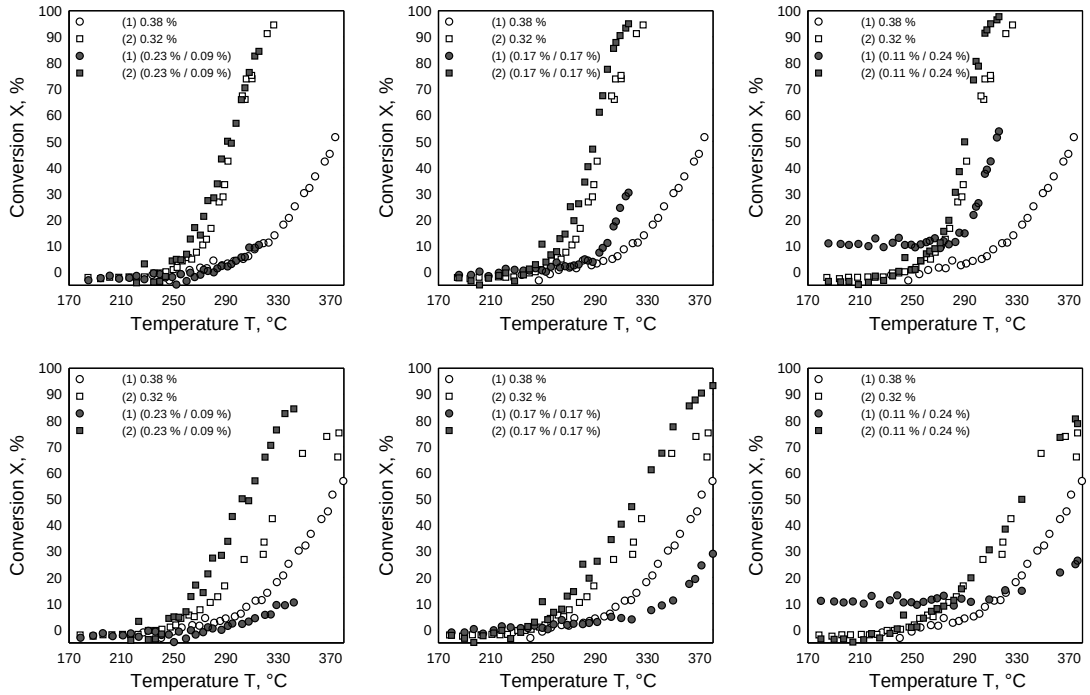

Figure 6.5.: Total oxidation of mixtures of ethylene (1) and propene (2), in the top row for the temperature in the middle section and in the second row for the thermocouple for the outlet of the fixed bed. The fraction of propene increases from left to the right.

experimental results of the pure ethylene (1) or propene (2) (white marks) are shown together with the mixture (gray marks). The top row in figure 6.5 illustrates the conversion with respect to temperature in the catalyst center and the second row for the temperature at the reactor outlet.

Concerning the first ratio of approx 2.6:1 (ethene/propene, left figure), only minor differences to the single hydrocarbon oxidation occur. However, if a 1:1 mixture is applied (middle figures), significant deviations from the oxidation of the respective single components is observed. In this case, the conversion in particular of ethylene is increased. If propene is in excess (1:2.2, right figure), a conversion for ethylene of more than 10 % is even achieved at lower temperatures, at which the catalyst did not exhibit any significant activity for single propene or ethylene oxidation.

This can be partly explained with hot spot formation and a nonuniform temperature profiles, as revealed with results shown for the temperature measured at the outlet of the fixed-bed reactor (second row in fig. 6.5). Now the situation changes for the lean propene mixtures. Conversion of ethylene is lower compared to the pure ethylene considering the 2.6:1 and 1:1 mixtures. This time, the results would indicate inhibition effects in the mixture. However, propene still shows an enhanced rate in the mixture, independent of the thermocouple chosen for data representation. It is noteworthy that a repetition of the experiment showed the similar results of significant ethylene conversion below 200 °C.

Non-isothermal conditions cannot explain the increased activity of ethylene in excess of propene at low temperatures. Inhibition effects are also not systematic, because in excess of ethylene, the oxidation of propene is also enhanced, while that of ethylene is inhibited (at high temperatures). But in excess of propene, the oxidation of ethylene is enhanced at low temperature. Some aspects regarding these contradictions are discussed in more detail below.

Discussion of Mechanisms and Mixture Effects The oxidation on transition metal oxides is sometimes explained with a redox mechanism, with lattice oxygen being the oxidant of the hydrocarbon, which directly reacts from the gas phase or from an neighboring adsorbed site according to *Mars-van Krevelen* (M-vK) mechanism [163], see also [162, 164–167]. The redox cycle start with oxidation of a reduced site of the catalyst. In a subsequent step, the VOC reacts with the lattice oxygen to the products thereby reducing the catalyst again. After re-oxidation of the readily reduceable site, the catalytic cycle is completed [162].

Recent studies with mixed non-noble catalyst are [168–170]. For a cerium, zirconium mixed oxides Gutiérrez-Ortiz et al. [171] found, that introducing ZrO_2 increases the activity, which is explained by a distortion of structure and a possibly higher lattice oxygen mobility. A systematic study by Kim et al. [172] for benzene and toluene oxidation on a series of manganese oxides (Mn_3O_4,Mn_2O_3 and MnO_2) evidenced these finding. Further works on manganese oxides concerning oxidation states can be found in [173, 174].

On noble-metal catalyst the oxidation can proceed via surface reaction of the adsorbed molecules and is often explained by a *Langmuir-Hinshelwood* (L-H) mechanism [162]. One proposed mechanism assumes the dissociative adsorption of oxygen and the adsorption of the VOC on a different site followed by the rate-determine surface reaction. If the VOC adsorbs strongly on the site, the rate approaches zero order with respect to the VOC. Otherwise, if the oxygen is in excess, the rate becomes first order with respect to the VOC. In the mixture of five aromatic hydrocarbons [1] Barresi et al. [175] could ascribe the inhibition effects on the $Pt/\gamma-Al_2O_3$ catalyst to competitive adsorption.

For the deep oxidation of ethylene and propane on Pd/Al_2O_3 Beld et al. [176] investigated the influence of the reaction products CO_2 and H_2O on the activity. They evidenced experimentally that CO_2 has no significant affect, whereas water was supposed to inhibit the oxidation. In the mixture of hydrocarbons, water is already present due to the oxidation of the more activated hydrocarbon, which may inhibit the reaction of the less activated hydrocarbon. However, Beld et al. [176] found no clear evidence for such mechanism. The inhibition

[1] Benzene, toluene, ethylbenzene, o-xylene and styrene.

observed for the hydrocarbon mixture was even higher compared to the case, where the corresponding amount of water was introduced to the feed with the single hydrocarbon. They suggested, that unknown reaction intermediates would explain these findings.

Strong inhibitory effects were reported by Kim et al. [172] for the oxidation of benzene and toluene on a manganese oxide catalyst. Applying pure feed, benzene is preferably oxidized compared to toluene, while in the mixture the order of activity is reversed and activity towards benzene is even lower than that of toluene.

Despite the frequently observed inhibitory effects, either due to competitive adsorption or complex reactions intermediates, it was Harris et al. [177] who reported rate enhancements in mixtures [178]. On an uranium oxide (U_3O_8) catalyst the activity for benzene total oxidation could be increased by applying 2.6 % water in the feed. They speculate, that water in co-feed can increase the rate of the re-oxidation of the uranium oxide, which may explain their findings as this reaction step is rate determining as part of an M-vK mechanism. However, the observation seems to remain an exceptional case.

Most of the studies show rate inhibition in mixtures. However, the experimental results obtained in this work are not appropriate to derive a detailed mechanism. Further experiments with gradient free reactors and a larger set of experimental conditions and co-feeding of reactions products, are required. In addition, the composition of the active metals (copper and chromate) should be considered as well. In this work therefore only a formal kinetic description of the oxidation reaction was performed for the design of an experimental SMBR unit.

6.2.3. Evaluation of Experimental Data

For the kinetic characterization the obtained data clusters where evaluated and selected for parameter estimation based on established criteria. High temperatures cause large rates and therefore significant concentration gradients in the pellet and across the boundary layer. Thus, only a fraction of the catalyst site would contribute to chemical reaction which leads to errors in the estimates of the respective rates laws.

Useful criteria to assess mass transfer limitations are available. For a detailed description Butt [179] is recommended and for a real application Emberger [180] is a good example. The intra-particle mass transfer resistance was estimated based on the *Weiz*-criteria, assuming a 5 % deviation from a flat profile. *Anderson* and *Mears* criteria were considered as well. The numbers were derived with the help of transport correlations for heat and mass given in [181] and based on a maximum concentration of 0.5 %. Kinetic parameters were used according to the power law kinetic explained below. In this way, only experimental data ensuring absence of transfer limitations had been selected. Additionally, a maximal temperature difference between in- and outlet of the reactor of 10 °C was considered to further limit the experimental data set.

Plug flow conditions and the absence of maldistribution due to boundary effects was assumed. Therefore a steady state mass balance of the fixed-bed reactor was considered:

$$u_g \frac{\mathrm{d}c_i}{\mathrm{d}z} = \rho_b \sum_j \nu_{ij} r_j(c_i, T) \qquad c_i(z=0) = c_i^0 \tag{6.3}$$

with u the superficial gas velocity, ν_{ij} the stoichiometric matrix and r_j the rate law. $\rho_b = m_K/V_R$ is catalyst bulk density, which can also be replaced by $\rho_b = (1-\varepsilon)\rho_K$ to introduce the bed void fraction with the density of the solid catalyst, $\rho_K = m_K/V_K$. After some rearrangements, a balance accounting for the desired input variables, the flow rate, $\dot{V}$, and the inlet concentration, c_i^0, is obtained:

$$\frac{\mathrm{d}c_i}{\mathrm{d}z} = \frac{m_K}{L_R \dot{V}} \sum_j \nu_{ij} r_j(c_i, T) \qquad c_i(z=0) = c_i^0 \tag{6.4}$$

The following power law kinetics where considered for both reactions:

$$r_j = k_j(T) c_i^n \qquad \text{with} \qquad k_j(T) = k_{0j} \exp\left(-\frac{E_{aj}}{\mathrm{R_g} T}\right) \tag{6.5}$$

with n, the reaction order, k_{0j} the pre-exponential factor, and E_{aj} the activation energy of the j-th reaction. An analytical solution of equation 6.4 is:

$$c_i = \begin{cases} \exp\left(\frac{m_K}{\dot{V}} k_j(T) + \log\left(c_i^0\right)\right) & \text{if } n = 1 \\ \left(\frac{m_K}{\dot{V}} k_j(T)(1-n) + \left(c_i^0\right)^{(1-n)}\right)^{1/(1-n)} & \text{if } n \neq 1 \end{cases} \tag{6.6}$$

According to Mezaki et al. [182], a transformation of the highly correlated pre-exponential factor and the activation energy is recommended, yielding:

$$k_j(T) = k_{\mathrm{ref},j}(T_{\mathrm{ref}}) \exp\left(-\frac{E_{aj}}{\mathrm{R_g}}\left(\frac{1}{T} - \frac{1}{T_{\mathrm{ref}}}\right)\right) \quad \text{with} \quad k_{\mathrm{ref},j}(T_{\mathrm{ref}}) = k_{0j} \exp\left(-\frac{E_{aj}}{\mathrm{R_g} T_{\mathrm{ref}}}\right) \tag{6.7}$$

The choice for the reference temperature, T_{ref}, is typically the mean of the investigated temperature range.

6.2.4. Parameter Estimation and Statistical Evaluation of Kinetic Parameters

For parameter estimation a simple mathematical description is considered [183], with $i = 1, \ldots, N_{\mathrm{obs}}$ experimental observations of a variable y_i, $k = 1, \ldots, N_{\boldsymbol{\theta}}$ free parameters $\boldsymbol{\theta}$ to be estimated, and the model predictions f_i, which is a function of model inputs $\boldsymbol{u}$ according to:

$$f_i = f_i(\boldsymbol{u}, \boldsymbol{\theta}) \tag{6.8}$$

The model is a nonlinear function of the parameters and given by equation 6.4 in this work, with the outlet concentrations $c_i(z = L_R)$ as the observed variables. The model inputs consist of inlet concentration, flow rate and temperature, i.e. $\boldsymbol{u} = \left[c_i^0, \dot{V}, T\right]^T$, varying according to the i-th experimental observation.

As a measure for the agreement between experimental and model variables, either with

absolute or relative differences, the sum of squares of residuals (SSR) is usually considered:

$$SSR(\boldsymbol{\theta})^{\text{abs}} = \sum_{i}^{N_{\text{obs}}} \left(y_i - f_i\right)^2 \qquad SSR(\boldsymbol{\theta})^{\text{rel}} = \sum_{i}^{N_{\text{obs}}} \left(\frac{y_i - f_i}{y_i}\right)^2 \tag{6.9}$$

The choice for either the ordinary least squares (abs) or the weighted least squares (rel), can significantly affect the outcome of the parameters estimation [183]. More sophisticated approaches would implement error distribution to improve the parameter estimation which, however, requires a detailed knowledge about the errors in the experiment.

Numerical parameter estimation corresponds to the iterative solution of the optimization problem to minimize $SSR(\boldsymbol{\theta})$ in order to obtain the vector of estimated parameters, $\hat{\boldsymbol{\theta}}$. Often, the underlying model is numerically demanding and gradient based numerical optimization are less efficient and alternatives should be considered [184–186]. In the present work, a *Nelder-Mead* simplex algorithm showed reliable performance, which was readily available in *Matlab*®.

The variance based on the ordinary least squares with respect to the residues can used to measure the quality of fit:

$$\sigma^2 = \frac{1}{d_f} \sum_{i=1}^{N_{\text{obs}}} \left(y_i - f_i\right)^2 \tag{6.10}$$

The degree of freedom is defined with the difference between the number of observations and the number of parameters, $d_f = N_{\text{obs}} - N_{\text{par}}$. With $\bar{y}$, the experimental mean and SST, the total sum of squares defined as:

$$\bar{y} = \frac{1}{N_{\text{obs}}} \sum_{i=1}^{N_{\text{obs}}} y_i \qquad SST = \sum_{i=1}^{N_{\text{obs}}} \left(y_i - \bar{y}\right)^2 \tag{6.11}$$

The regression coefficient, R^2, and a corrected coefficient, R_c^2, are defined as:

$$R^2 = 1 - \frac{SSR}{SST} \qquad R_c^2 = R^2 - \frac{N_{\text{par}}\left(1 - R^2\right)}{d_f - 1} \tag{6.12}$$

R^2 is a measure of the fraction of the variability of y based on a linear relation, meaning, that in case of a perfect fit, the residues (SSR) are nil and R^2 would be one. Otherwise, the variation of y shows a linear decline when approaching the total sum of squares (SST), thus the variability becomes larger. To account for the number of parameters a more generalized corrected R_c^2 is suggested. This can help to exclude the fact, that by adding arbitrary free parameters to the model, the fit generally improves, R^2 increases, but thereby neglecting any significance of the parameters [183].

The figure above provides only a measure of the fit in terms of agreement, but not in terms of the quality of the estimated parameters. Therefore confidence intervals are usually calculated for statistically meaningful evaluation of the parameters. The elements required are parameter sensitivities, variances of the fit and the *Student-t* distribution.

The parameter sensitivities are defined by the derivatives of the observed model state, $f_{i,k}$,

with respect to the parameters in the solution vector, $\hat{\boldsymbol{\theta}}$, arranged in a $N_{\text{obs}} \times N_{\boldsymbol{\theta}}$ matrix $\boldsymbol{\omega}$:

$$\omega_{i,k} = \frac{\partial f_{i,k}}{\partial \theta_k}\Big|_{\hat{\boldsymbol{\theta}}} \tag{6.13}$$

The derivatives can be approximated numerically for instance by one sided or the symmetric difference equations [75],

$$\text{one sided} \quad \nabla_\theta f \approx \frac{f(\theta + \Delta\theta) - f(\theta)}{\Delta\theta} \qquad \text{with} \qquad \Delta\theta = \theta\,(\epsilon_m)^{1/2} \tag{6.14}$$

$$\text{symmetric} \quad \nabla_\theta f \approx \frac{f(\theta + \Delta\theta) - f(\theta - \Delta\theta)}{2\Delta\theta} \qquad \text{with} \qquad \Delta\theta = \theta\,(\epsilon_m)^{1/3} \tag{6.15}$$

with ϵ_m the machine precision. The difference $\Delta\theta$ is a trade-off between truncation error of the finite difference approximation of the gradient and the computer round-off error. Reducing $\Delta\theta$ will improve the accuracy until round-off errors predominate and the approximation becomes weaker. Advanced concepts, e.g. complex step, internal numerical and automatic differentiation, can help to improve the reliability and accuracy [187–190]. The finite difference approximations showed reliable performance in this work. However, it was found that the gradient approximations were most sensitive to the numerical errors of the numerical integrator to solve the reactor balance 6.4, when used instead of the analytical solution 6.6.

In the next step, the *Fisher-Information Matrix* of dimension $N_{\boldsymbol{\theta}} \times N_{\boldsymbol{\theta}}$ is calculated according to the following matrix product.

$$\boldsymbol{FIM} = \boldsymbol{\omega}^T \boldsymbol{\sigma}^{-1} \boldsymbol{\omega} \tag{6.16}$$

If experimental variances, $\boldsymbol{\sigma}$, of the individual experimental measurements are not available, a constant value based on the ordinary least squares variance is suitable as well. The confidence interval according to the *Cramer-Rao* lower bound is then defined with the inverse of $\boldsymbol{FIM}$ as:

$$\boldsymbol{\sigma}^2_{\hat{\boldsymbol{\theta}}_k} \geq (\boldsymbol{FIM}_{kk})^{-1} \tag{6.17}$$

With a quantile of the *Student*-t distribution the following inequality applies:

$$\hat{\theta}_k - \sigma_{\hat{\theta}_k} t^{d_f}_{\alpha/2} \leq \theta_k \leq \hat{\theta}_k + \sigma_{\hat{\theta}_k} t^{d_f}_{\alpha/2} \tag{6.18}$$

Often the relative one sided interval for a specific parameter is given:

$$\%\Delta\hat{\theta}_k = \frac{\sigma_{\hat{\theta}_k} t^{d_f}_{\alpha/2}}{\hat{\theta}_k} \cdot 100 \tag{6.19}$$

An indicator, if the parameter estimation problem is well posed is the condition of the $\boldsymbol{FIM}$, which is also a measure for parameter identifiability. The condition κ relates the largest to

the smallest eigenvalues of the square matrix according to:

$$\kappa = \left| \frac{\lambda^{\max}\left(\boldsymbol{FIM}^{-1}\right)}{\lambda^{\min}\left(\boldsymbol{FIM}^{-1}\right)} \right| \tag{6.20}$$

If the κ is small and close to unity, the problem is well posed and up to $\kappa = 50$ the parameters are identifiable. Beyond 1000, serious problems in the parameter estimation concerning identifiability and accuracy can be expected [180, 183].

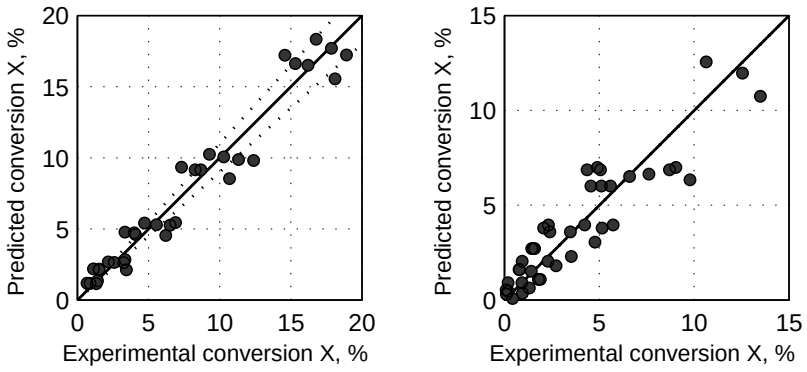

Figure 6.6.: Parity plots for ethene (left) and propene (right) assuming first order reaction rates.

First Order Rate The results for the parameter estimation based on a first order rate with respect to the VOC are given in table 6.1 and the corresponding parity plots are shown in figure 6.6. The pre-exponential factor and the activation energy are larger for propene compared to ethylene.

Table 6.1.: Parameters for the first order reaction rates for ethene and propene.

	k_0	E_a	R_c^2	κ
	$l/(kg\ s)$	kJ/mol		
Ethene	$2.947 \cdot 10^{10}(\pm 7.53\ \%)$	$111.4(\pm 8.14\ \%)$	0.9466	$1.5 \cdot 10^{8}$
Propene	$1.012 \cdot 10^{13}(\pm 26.98\ \%)$	$128.4(\pm 13.39\ \%)$	0.8460	$1.8 \cdot 10^{6}$

Concerning the accuracy of the fit, ethylene yields better regression coefficient with 0.9466 compared to propene with 0.8460 . The conditions κ are in the order of magnitude of 8 and 6 indicating the significant parameter correlation. The confidence intervals reveal that the parameter uncertainty is larger for propene than for ethylene.

N-th Order Rate Table 6.2 reports the estimated parameters, table 6.3 gives the statistical figures and the corresponding parity plots that are shown in figure 6.7.

The smaller reaction orders are typically obtained in heterogeneous catalysis indicating that the underlying kinetic mechanism obeys to more complex mechanism. Propene with 0.29 has the smaller reaction order which is in agreement with higher sensitivity towards the concentration. This means, that a smaller reaction orders shift the light-off curve to lower temperatures as the inlet concentrations are decreased.

Table 6.2.: Parameters for the n-th order rate laws for the oxidation of ethene and propene on $CuCrO_x/Al_2O_3$ catalyst.

	k_0	E_a	n
	$mol^{1-n}/(kg\ s\ l^{1-n})$	kJ/mol	
Ethene	$5.131 \cdot 10^9$	116.5	0.689
Propene	$8.672 \cdot 10^{10}$	135.3	0.292

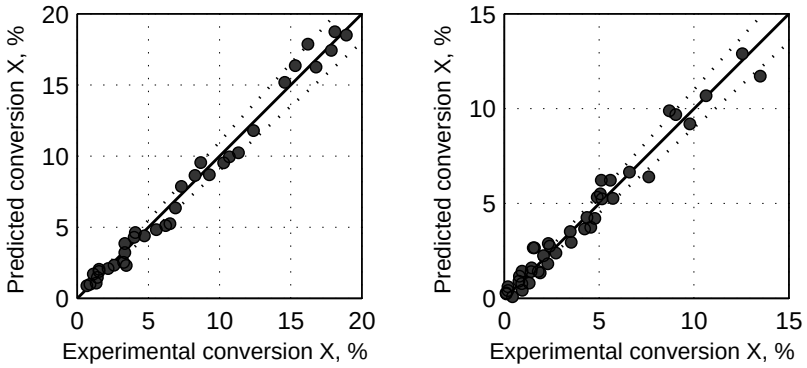

Figure 6.7.: Parity plots for ethene (left) and propene (right) for n-th order rate law.

Concerning the quality of fit, an improvement could be achieved compared to the first order rate. Correlation coefficients of 0.98 and 0.96 for ethene and propene are much better now and the parity plots (c.f. 6.7) reveal a better fit. However, the condition of the fisher information matrix was found to be higher with $6 \cdot 10^{11}$ for propene and $1 \cdot 10^{11}$ for ethene. Those large values indicate that the problem is ill posed, the parameters are highly correlated and identifiability weak. The confidence intervals are larger for the pre-exponential factor

Table 6.3.: Statistical figures for the parameter set in table 6.2 - regression coefficient, confidence bounds and condition number.

	R_c^2	$\%\Delta_{k_0}$	$\%\Delta_{E_a}$	$\%\Delta_n$	κ
Ethene	0.9852	54.81 %	4.49 %	8.66 %	$1.1 \cdot 10^{11}$
Propene	0.9676	88.90 %	5.84 %	34.58 %	$5.8 \cdot 10^{11}$

compared to the activation energy, the reaction order of propene is also uncertain.

Based on the given data set and the kinetic models assumed, the precision of the fitted parameters is acceptable, however, parameter correlation can not be avoided. In other words, it can not be statistically guaranteed that the real (and unknown) parameters have been identified, although the experimental observations can be well described.

The estimation of ignition temperatures (sec. 2.2.1) required to initiate the oxidation reactions can be calculated with the parameters for the first order rates (tab. 6.1). Assuming a typical flow rate of 1.2 m^3/h, the ignition temperature for propene is 253 °C and for the less activated ethene about 297 °C (tab. 6.4). This is in agreement with the experimental findings.

It should be noted that the activation energies estimated with 128.5 kJ/mol and 111.4 kJ/mol for ethene respectively (tab. 6.1), would indicate an opposite trend, i.e. ethylene oxidation can be activated at lower temperatures. However, this is because the activation energies are

Table 6.4.: Ignition temperature for the example of 1.2 m^3/h based on the parameters given in table 6.1.

	propene	ethene
Ignition temperatures, °C	253	297

highly correlated with the pre-exponential factors, which can lead to misinterpretation of the catalytic activities. In this regard, the ignition temperatures estimated with equation (2.40) provide reasonable figures.

6.3. SMBR Design and Equipment

6.3.1. Reactor Design

The experimental setup consists of two reactor segments, RA and RB, arranged according to the process flow diagram in figure 6.8. An additional fixed-bed was used for preheating allowing an appropriate start-up procedure of the SMBR. Seven on-off valves were used to control the line switching for the periodic operation of the reactor segments. The thermal coupling of RA and RB required valves withstanding high temperatures (HT- vales V5 and V6). The other valves operated in cold streams below 120 °C.

Table 6.5.: Valve assignment for the three operation modes, preheating, feed on reactor RA, and feed on reactor RB.

operation mode	V1	V2	V3	V4	V5	V6	V7
preheating	0	0	1	0	1	0	1
feed RA	1	0	1	0	1	0	0
feed RB	0	1	0	1	0	1	0

Three modes of operation were designed, the corresponding valve assignments are summarized in table 6.5. In "*preheating*" mode the gas flows through the preheater and subsequent reactor RA and RB via the high-temperature valve V5. Mode "*feed RA*" assigns the valve, such that the preheater is exempted from operation and the cold feed gas enters the first reactor RA directly. The flow sequence is FEED–RA–RB–PRODUCT. The third mode switches the order to FEED–RB–RA–PRODUCT, while maintaining the flow direction through the fixed-beds.

A typical operation procedure includes a start-up phase followed by a periodic alternation between the two operation modes "*feed RA*" and "*feed RB*". Open-loop and closed-loop control according to *controller 3* was implemented (see section 5.1.3 and appendix C for specifications).

6.3.2. Elements of the Experimental Setup

Fixed-Bed Reactor Segments Heat losses pose the main challenge for adiabatic conditions in small scale laboratory reactor. Several strategies have been investigated to at least approximate adiabatic operation. Often compensation heating in combination with an additional air gap between the reactor tube and the jacket is suggested for steady state

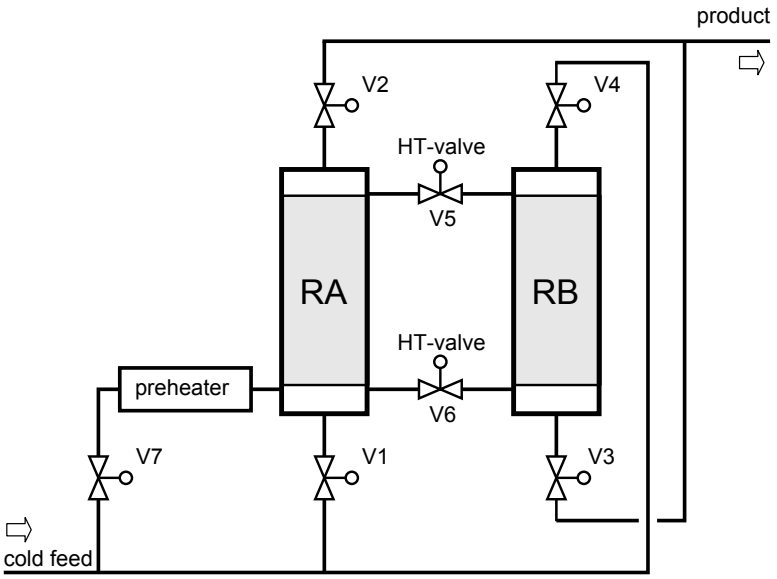

Figure 6.8.: Two-bed SMBR unit with an additional preheater for reactor start-up.

adiabatic reactor operation [191]. Unsteady state operation, however, requires additional efforts in order to dynamically adjust compensation heating. A concept with several segments independently controlled was considered for a reverse-flow reactor by Fissore et al. [192] and [193].

In this work the fixed-bed reactors were designed to reduce the heat losses as far as possible. A double jacket reactor was built accounting for several aspects (fig. 6.9). Evacuation of the jacket volume allowed for minimization of heat conduction. Radiative heat transport dominating at higher temperatures was reduced by a heat shield based on a ceramic canvas. Short distances and compensation heating of the connecting lines was considered to minimize heat losses of the flanges and HT-valves.

The inner diameter is a compromise – a large reactor diameter leads to radial temperature gradients, while flow maldistribution at the reactor wall increases with narrow diameters. Moreover, a sufficient reactor length is required to establish moving reaction fronts, but the pressure drop is limiting. In this work, an inner reactor diameter of 21.5 mm and a particle size of 1 mm were used. With an aspect ratio above 20 flow maldistribution was assumed to be negligible [194]. The length of the fixed-beds was 450 mm and metal sieved for fixation of the catalyst were installed. The connection lines (1/4") between the fixed-beds were placed close to the sieves in order to increase the distance to flanges, which are considered as heat sinks strongly affecting the dynamics of the temperature fronts.

The double jacket reactor was equipped with a steel grid for the fixation of the flexible radiation shield made of *3M*^{TM} *Nextel*^{TM} fiber between the inner reactor tube and the jacket. A line for the suction pump was placed in the void between the insulation and the reactor tube. For additional insulation, the void between the grid and the jacket was filled with stone wool.

In order to observe the temperature fronts along the fixed-bed, thermocouples of 0.5 mm diameter were installed from the top of the reactor unit. Since thermocouples of different

length were inserted, the main distortion of the bed was located at the top section. This procedure caused a disruption of the packing with 0.5 to 3 mm diameter depending on the number and position of the sensors. Radial heat bridges could be avoided with this strategy, however, at the cost of several experimental errors introduced with the thermocouples: axially non-uniform flow maldistribution, fixed-bed heat conduction and activity profile.

Supplementary Parts, Process Media and Process Control Two different types of switching valves were used for the reactor control. Two-way magnetic valves (*Bürkert*) were selected for the switching of cold lines. Higher requirements had to be considered for the switching of gases at high temperatures (V5 and V6). Packed bellows-sealed valves (series U *Swagelok*) were installed together with pneumatic actuator (*SS-4UW-HT-6C*).

Feed gas supply was mastered with mass flow controller type *F-201C-FBC* for hydrocarbons and *F-202AC-FBC* for air (*Bronkhorst*), respectively. Propene was of technical grade 2.5 (purity 99.5 %) and ethylene of grade 3.5 (purity 99.95 %). The air was dried to 5.9 mg/m^3 while traces of oil to 0.003 mg/m^3 were expected . The total pressure drop of the reactor unit and corresponding absolute pressures were monitored by pressure transmitters (series *BTE, TetraTec*).

A fixed-bed reactor equipped with a heating coil filled with $\alpha - Al_2O_3$ was used for preheating of the feed gas. An additional fixed-bed reactor was installed downstream of the product line for the total oxidation of unconverted hydrocarbons. The reactor was filled with platinum based catalyst and operated at 450 °C.

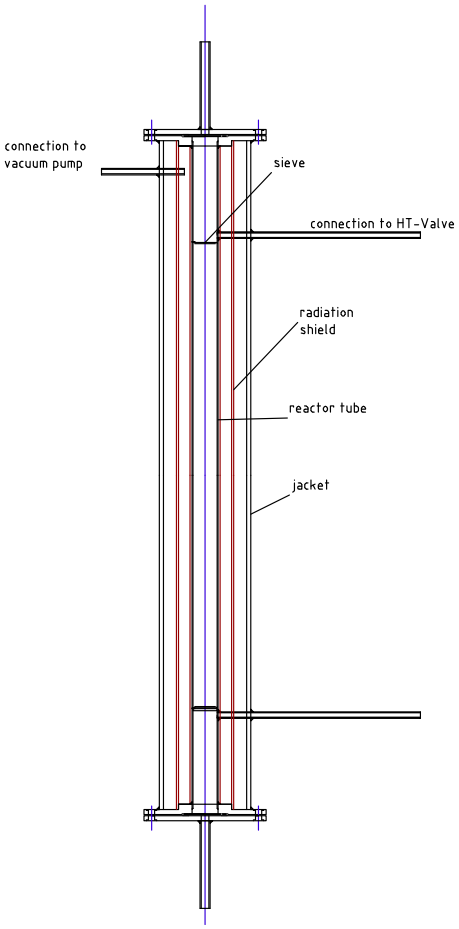

Figure 6.9.: Construction drawing of laboratory fixed-bed reactor.

The SMBR was controlled by a *Siemens SIMATIC PCS7* system, including the temperature control of fixed-bed reactors, control of flow rates and valve positions. Data acquisition and implementation of safety procedures as well as for post processing of measured signals were managed with the system.

A mass spectrometer (*Prolab MS*) was applied for time resolved product analysis. Additionally, the gas composition could be analyzed by a gas chromatograph *Agilent 6890 GC* combined with a mass spectrometer *Agilent 5973 MS*. The setup was equipped with a *HP-PLOT-Q* column for hydrocarbon separation and a *HP-Molsieve 5 A* column for the separation of permanent gases.

Despite the efforts to reduce heat transfer to the surroundings, an ideal adiabatic conditions could not be realized. This was due to the lack of exact experimental boundary conditions, meaning, that the experimental equipment takes part in the energy transport and storage, thus affecting the moving fronts. Hence, the lab scale SMBR was rather designed to provide a proof of concept of open- and closed–loop SMBR operation.

6.4. Periodic Reactor Operation

6.4.1. Characterization of Continuous Periodic Operation

Typical temperature signals of the distributed thermo couples are presented in figure 6.10, left for reactor R A and right figure for both, R A and R B, over two cycles. This particular experiment was carried out in open-loop control. To compensate heat losses, an inlet concentration of 0.41 % was selected providing sufficient amount of thermal energy being released.

In the start up phase, up to the runtime of 3 h, the reactor segments were heated until a steady state had been reached. Then periodic switching was initiated. The cyclic steady state

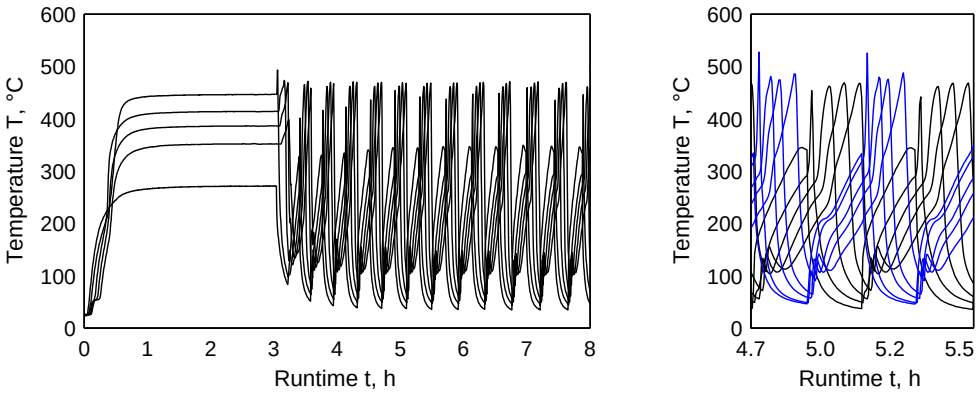

Figure 6.10.: Open-loop reactor operation. Left: Temperature signals of RA for the Start-up phase and periodic operation. Right: Temperature signal of RA (black lines) and RB (blue lines) within two reactor cycles.

had already been attained after approximately six cycles, thereby the maximum temperature remained almost constant at a temperature of about 480 °C. The maximum temperatures differed about 10 °C. Note that the temperature spike observed in R B can be explained with an additional fast reaction front forming due to the differences in the heat capacities between fixed-bed and the valve section. However, the fronts decay fast and do not contribute to the overall dynamics of the reactor.

Here it is instructive to discuss reconstructed spatial temperature profiles. Figure 6.11 illustrates a typical result for an open-loop control – the top row presents the signals in the first switching period and below for the second period with a feed position in front of R B.

In the first period, the reaction front travels through reactor R A with a relatively sharp temperature front reaching to 480 °C, thereby the leading thermal front reheats reactor R B. If the feed is active for reactor R B, thus dosing at the spatial coordinate at 0.5 and withdrawing product right before, the reaction front moves through R B thereby reactor R A is heated up again.

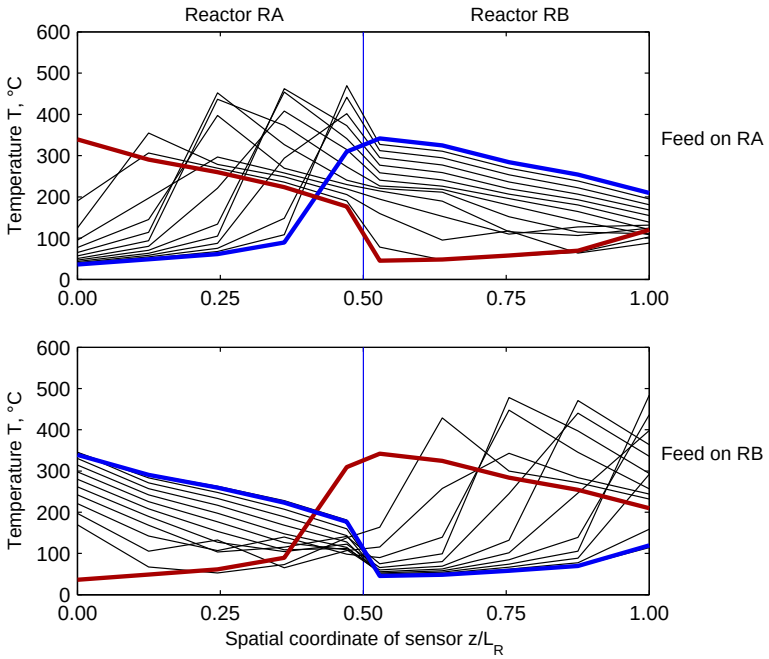

Figure 6.11.: Reconstructed temperature profiles in cyclic steady state open-loop control for two switching periods. Snapshots are shown every 30 s. Start and end profiles are highlighted for the first period (Feed on RA) with red lines, and for the second (Feed on RB) using blue lines.

The fronts show the characteristic properties explained in the first part of this work. The reaction front is self-sharpening, which means a self preserving shape at a certain maximum temperature and a constant velocity. Such a behavior is attained approximately after 1/3 of the length of a reactor segment. The reaction front has a velocity of about 3 cm/min (in the first period). By contrast, the dispersive leading thermal front is considerably faster than the reaction front with a velocity of 5.4 cm/min. In this way, the thermal front allows for a fast thermal regeneration of the cold fixed-bed segment in the upstream section.

In the experimental setup the fronts cannot be transferred from one reactor to the other without heat losses. This means, that high temperatures peaks are usually cleared away by the heat losses in the valve sections. For that reason, the initial profile directly after the switch shows a kink. The heat losses along the reactor are responsible for the decreasing temperature profile. These non-ideal conditions are responsible for the deviation of the initial temperature profiles from the predictions made with the ideal adiabatic reactor model.

Another important observation is, that the front velocities differ in the reactor segments, the reaction front in the segment R_B is faster than that in R_A. This can be explained with different void fractions of 0.43 in R_A and 0.47 in R_B. The larger void fraction in R_B explains the faster reaction fronts.

Although the experimental uncertainties could not be avoided, this offered to study more realistic effects, such as heat losses, fast dispersive fronts, and a significant induction length to attain constant pattern behavior. Below these important findings are investigated in more detail.

6.4.2. Model Based Reconstruction of Temperature Profiles

The model used for the theoretical characterization of the reactor concept is not appropriate for the quantification of the experimental results obtained. For instance, the reaction fronts do not travel with a base point temperature equal to that of the inlet temperature. Smearing or spreading of fronts at lower temperatures can be attributed to additional storage effects, which stem from the reactor jackets, piping and valves. An extended one-dimensional reactor model was therefor investigated including a additional energy balances for the wall and the valves, thus, allowing to represent different heat losses and accumulations in the respective sections. Derivation and parameterization is detailed in the appendix D.

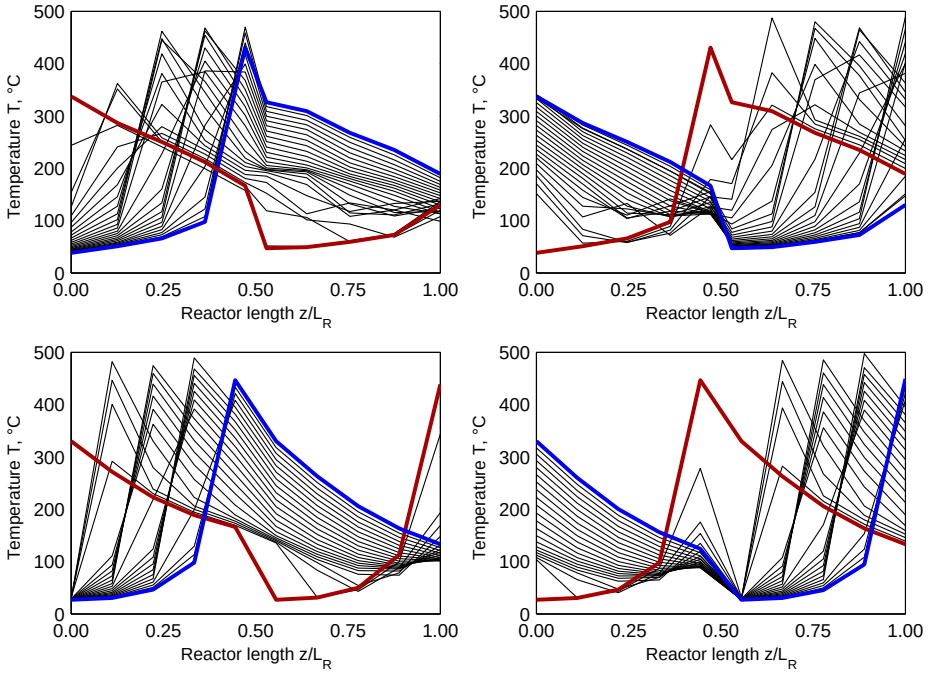

Figure 6.12.: Comparison of temperature profiles in open-loop control, top row experiments and second row simulation (1/4 minutes snapshots of profiles).

Figure 6.12 compares two consecutive switching periods in open-loop control, experiments in the first row and the simulation in the second; time stepping and sensor positions simulated coincide. In both switching periods, the simulations are in good qualitative agreement with the experimental findings, though, heat losses of the valves are underestimated. One should also stress that the base point of the temperature fronts significantly differs from the ideal model used before in section 2.3.3. The is due to the additional wall balance, which introduces a larger heat capacity and an increased overall heat conduction. For that reason, also the thermal fronts exhibit a much stronger spreading which is also seen in the experiments.

Despite the good agreement for the leading dispersive front, the induction section to reach the constant pattern state of the reaction front is underestimated. The simulation shows such a developed state already after one fifth of the segment length, whereas the experimental reactor needs about one third. In this regard, heat losses and local volumetric heat capacities can strongly affect the dynamics of the fronts. Either a higher precision of these parameters or an improved experimental reactor design would yield better agreements between theoretical

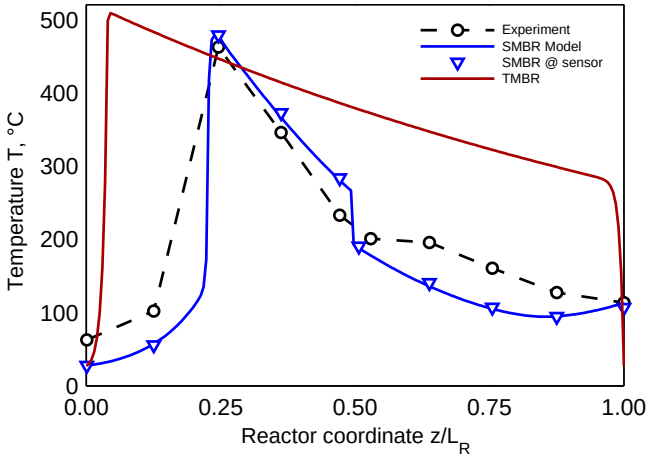

Figure 6.13.: Experimental temperature profile at half of the switching period compared with the SMBR and the TMBR model. Maximum temperatures: experiment at ≈464 °C, SMBR model at 478 °C and TMBR at 507 °C.

predictions and experiments.

In order to discuss the simulation results better, figure 6.13 compares snapshots of temperature profiles at half of the switching period (feed at RA). The simulated profile shows the steep reaction front, a sharp decline of the leading thermal front in RA and a discontinuity at the valve position. The corresponding experimental values are in qualitative agreement, particularly for the maximum temperature.

It is instructive for the analysis of the fronts to revert to the ignition temperatures introduced previously in this work. As an estimate for the experimental system ignition temperature of 253 °C for propene and (297 °C for ethylene) are typical values (tab. 6.4). One may try to align those numbers to the shape of the reaction front, in particular to the point where transition from dispersive to the steep front occurs. However, this happens already at lower temperatures at about 130 °C. As an explanation it should be noted that for the estimate an ideal adiabatic system was assumed, which obviously does not hold for the experimental system. In addition, a much larger feed concentration was selected. Both effects are not considered in the estimate for the ignition temperature. In real adiabatic systems it would be interesting to operate with very lean feeds and to examine the interaction of front dynamics and ignition temperatures, possibly accounting for inlet concentrations as suggested in the appendix A.

For comparison the TMBR temperature profile is shown. The solid phase velocity was calculated with eq. 3.45 using the experimental switching time of 10.8 min and physical properties in accordance to the inlet conditions. The TMBR temperature profile obtained shows a maximum peak temperature of 507 °C exceeding that of the experiment with 464 °C and the SMBR with 478 °C. Of course the TMBR model does not represent the real situation in a two bed SMBR, but offers a reasonable approximation for the maximum temperature and the switching domain for ignited reactor operation.

6.4.3. Open-loop Reactor Control

Ignited reactor states can be maintained within a limited range of switching times. Systematic experiments in open-loop control were carried out to demonstrate the existence of the operation limits predicted earlier. The switching time was investigated by step wise variations between 6 to 25 minutes. Figure 6.14 illustrates the window of ignited states for two different concentrations. The one with the higher concentration (0.41 % propene corresponding to $\Delta T_{ad} = 310$ K) shows a larger window of switching times in the range of 8.75 – 19.3 min. The lean mixture was at 0.37 % corresponding to $\Delta T_{ad} = 290$ K with ignited states between 10.7 – 16.7 min. Maximum temperatures of 470 °C and 505 °C, respectively, have been achieved.

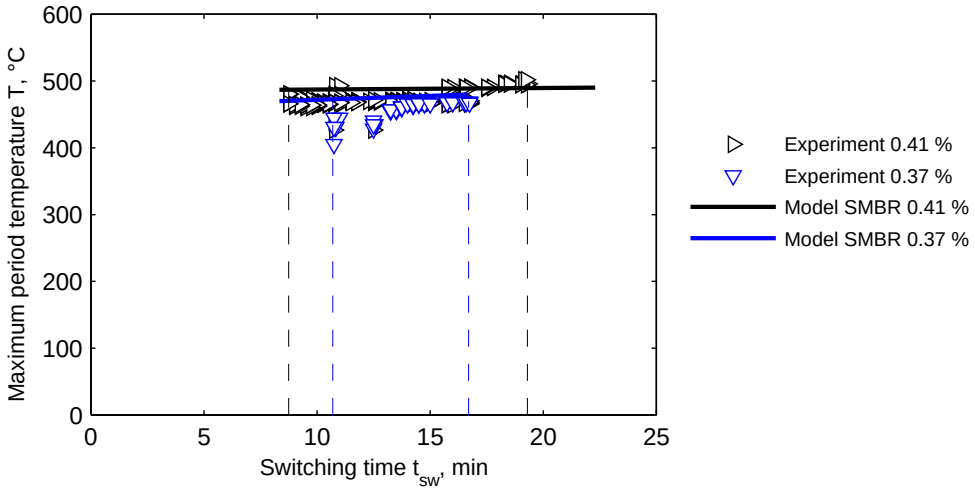

Figure 6.14.: Verification of the domain of switching times for ignites reactors states. Experimental and simulated peak temperatures are compared for propene concentrations of 0.41 % and 0.37 %.

Systematic simulation of the SMBR model was performed to compare the domain of ignited states. The results are given as horizontal lines connecting the peak temperatures of the simulated results. For the case of a high inlet concentration, the model predicts quite accurately the left stability limit for fast switching (8.3 min), the right boundary is overestimated by 3.2 min with 22.5 min. In case of the smaller concentration, the left bound is overestimated, which means that the model predicts ignited states similar to the larger concentration case, which is not correct, though, the right limit is well represented. The SMBR model predicts the domain of ignition and the shrinking due to a decrease in the inlet concentration. However, it fails to meet ignition limits exactly.

The range of switching times was also examined with the TMBR model, which is not shown to avoid confusions with results already presented. The maximum temperatures were not constant in the ignited domain. Such deviations can not be explained with the heat losses alone, rather with a combined effect of large feed concentrations, large heat losses, and the implemented wall balance. Nevertheless, the range of switching times can also be fairly good approximated the TMBR model, although the limits for faster switching is overestimated.

Despite the higher precision of the SMBR model used for the analysis of the systematic experiments, the stability limits regarding the switching time could not be predicted with sufficient accuracy. At this point it becomes obvious that the reactor should be operated in

closed-loop control in order to eliminate the need to specify switching times in advance.

6.5. Closed-Loop Reactor Control

The control concept, *controller 3*, introduced in chapter 5, was implemented in the experimental reactor setup. The idea was to trigger the switch when the reaction front passes a temperature sensor located at the end of each reactor segment.

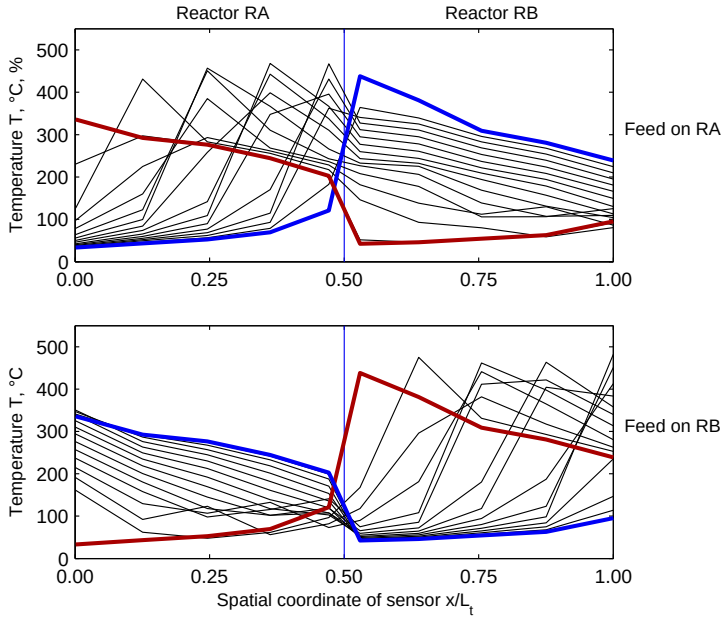

Figure 6.15.: Reconstructed experimental temperature profiles in periodic steady in closed-loop control (*controller 3*) for a temperature set-point of 100 °C. Snapshots are shown every 15 s.

Typical temperature profiles for a set-point at 100 °C are illustrated in figure 6.15. Although the reaction front is faster in segment RB than in RA, the initial situation almost coincide for both segments directly after the switch (compare with open-loop control in figure 6.11). This is due to the fact, that the decision for switching is made at the outlet of the segments and therefore an identical portion of energy has been transferred to the subsequent segment. However, unequal heat losses in the valve sections bring an asymmetry in the heat transport and experimental initial profiles deviate when comparing each segment. Concerning the closed-loop control of the SMBR in cyclic steady-state, the most important advantage of the controller is the decoupling of the individual reaction fronts, which means that every period has its specific switching time. In this way, it is possible to effectively compensate experimental uncertainties, i.e. due to the catalyst packing.

Several experiments were carried out in order to identify the range of set-points applicable. A typical controller characteristic, relating controlled switching time to the set-point, is illustrated in figure 6.16 together with the maximum temperatures. Comparison with the SMBR model in closed-loop control is given as well.

In experiments, the set-point below 100 °C and above 360 °C lead to reactor extinction, controlled ignited states can be achieved within this domain. The data scattering for a specific

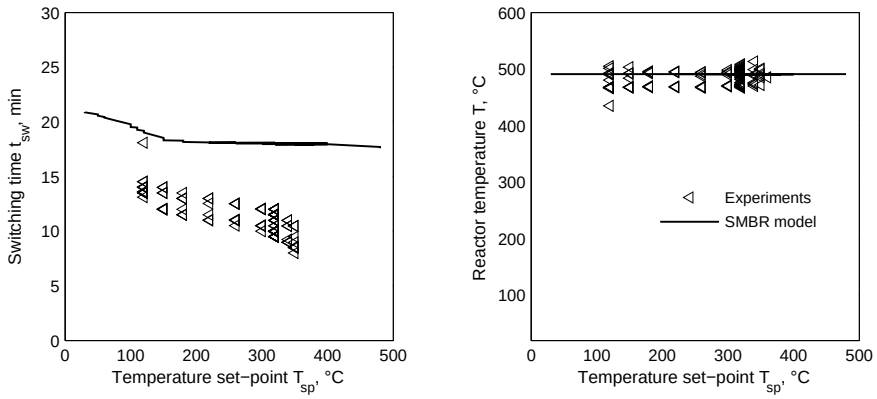

Figure 6.16.: Experimental investigation for a range of applicable set-points based on controller 3 compared with the SMBR model in open-loop control. The SMBR model and parameters are described in section C.3.3 and appendix D.

set-point can be attributed to the differences in the reaction front velocities. The SMBR model overestimates the domain of ignited states with deviations by approximately 5 min in the switching times.

Despite these experimental uncertainties, the trend of a decline in the switching time with increasing the set-point is qualitatively represented by the model, at least in the first part at smaller set-points.

It is interesting to note that the controller output can be associated with the shape of the reaction front: As the sensor indirectly measures the front velocity (finite length of segment by event time), the switching time for a specific set-point corresponds to the velocity of the front at a certain height in the respective segment. In this case, it means an integral front velocity containing the slightly faster front in the induction section, still changing its shape and velocity, and the second larger part in which constant pattern behavior prevails at a constant front velocity. Consequently, one can describe the qualitative shape of the front based on the controller characteristic analyzed.

In the present case the simulated controller characteristic shows two specific properties: First, since ignited states exists for set-point below 100 °C, the lower part of the experimental reaction front less accurate represented by the model. This is due to unrealistic low temperature base point enforced by the boundary condition, which is set to 23 °C. In contrast, base points of only 80 °C are observed in experiments indicating that larger amounts of heat are accumulated in the reactor and that heat transport is more complex than assumed in the model. This includes the heat transfer due to heat conduction in the heterogeneous system (catalyst phase, jacket, valves, piping). Secondly, the simulated switching times do not change much, as the set-point is increased further. In contrast, the experimental values fall significantly, which can be attributed to larger heat conduction. Thus, although the model was augmented by a wall balance increasing the heat conduction, it does not accurately describe the experimental reaction fronts.

The maximum temperatures are well represented as illustrated 6.16 right. Deviations up to 50 °C are observed, which can be attributed the aforementioned effects, such as different properties of the respective segments but also not completely settled cyclic steady states.

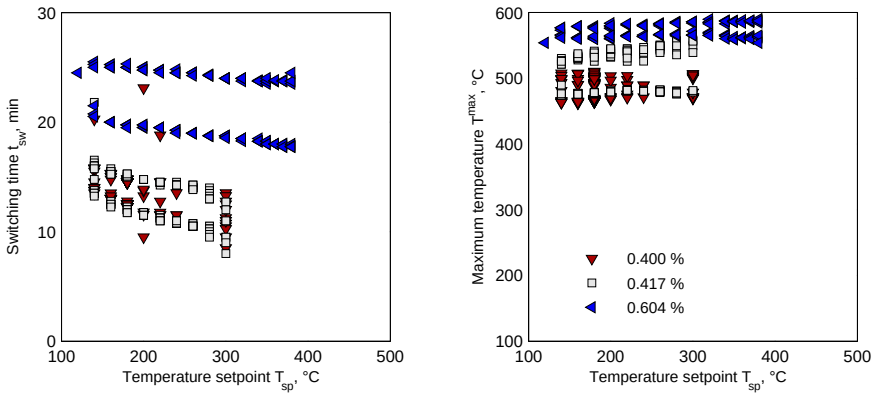

Figure 6.17.: Range of switching times in closed-loop control for three different feed concentration (0.4, 0.417 and 0.604 % propene). Larger concentrations lead to an increase in the range of possible switching times and to higher reactor temperatures.

Similar to the analysis of cyclic-steady state open-loop control, maximum temperatures are well approximated by the model but precision regarding the influence of switching related parameters is still weak. Model uncertainties, specifically in local heat capacities and heat conduction lead to deviations from shape of the reaction fronts. It should be noted, that unless precise experimental boundary conditions are provided, improvements in the model will not per se yield better agreements. Therefore, the controller was developed taking care not only of external disturbances, but in particular of such uncertainties in the experimental equipment.

6.5.1. Influence of the Feed Concentration

Section 5.1.3.1 has shown that the feed concentration is limiting the range of applicable set-points. A series of experiments with 0.4, 0.417 and 0.604 % propene feed was carried out to examine this influence on the reactor in closed-loop control. By a stepwise increase of the set-point beginning with 120 °C, the range of applicable values could be identified.

The results are shown in figure 6.17, the controller output (switching times) left and the corresponding maximum temperature in the right figure. Only minor deviations in switching time and maximum temperature are observed for 0.4 and 0.417 % propene feed. For the 0.604 % feed applied, the maximum temperature increases up to 580 °C. This is accompanied by largely increased switching times ranging from about 17 min up to 26 min for reactor R A. As illustrated in section 2.1.3 (fig. 2.6), the increased concentrations lead to slower reaction fronts, which in turn requires larger switching times. However, R B shows a significantly smaller switching time of about 20 min. Again, this can be explained with different reaction front velocities in R A and R B. The difference becomes larger in case of the slow switching regime being obtained for increased feed concentrations.

6.5.2. Influence of the Flow Rate

According to the theoretical analysis, the total flow rate should not affect the limit of the set-point at constant feed concentrations (see fig. 5.6). Systematic experiments were performed

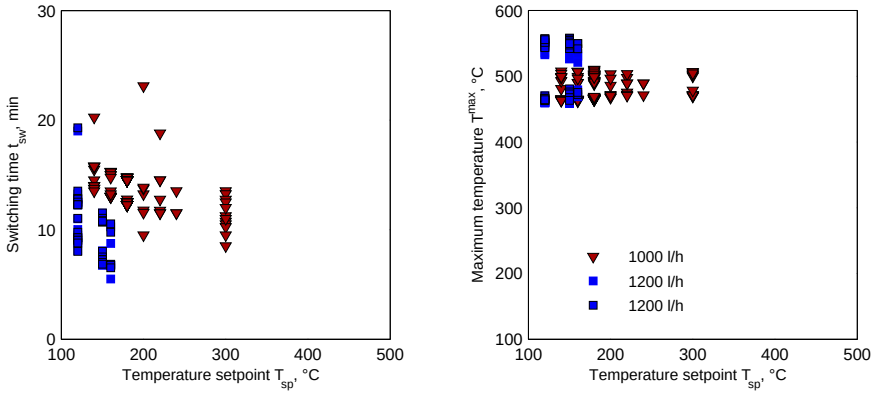

Figure 6.18.: Operation window in closed-loop control investigated by a systematic increase of the switching time until extinction occurred. Concentration was 0.4 % propene.

to investigate this important parameter. The results are shown in figure 6.18. Two flow rates, 1000 and 1200 l/h, respectively, at identical inlet concentrations of 0.4 % were considered. As expected, the controller adjusts to smaller switching times in case of higher flow rates and vice versa. Also the maximum temperature increase with larger flow rates. However, it was found for the larger flow rate, that only a smaller range of set-points is available, which was confirmed by repetition of the experiment.

The reason for the deviations from the theoretical prediction can be explained with two sources of non-ideal reactor behavior. At first, the theoretical analysis of reactor control did not include influences of heat losses on the available range of set-points. Secondly, the concentration of 0.4 % is close to the ignition limit, which makes experimental uncertainties deciding about ignited states. Another uncertainty stems from the fact, that changing the set-point in a running operation can trigger the switching unintentionally, or in worst cases, jump over the front immediately resulting in extinction.

To sum up the experimental findings for the characterization of the controller:

- The predictions made in chapter 5 could be confirmed by systematic experiments. A sufficiently large domain of temperature set-points is available allowing ignited reactor states.
- Predictions of the closed-loop control based on the effective SMBR model is restricted to the maximum temperatures. Discrepancies in the exact front velocities stem from underestimation of apparent heat conduction and uncertainties in volumetric heat capacities of the setup (fixed-bed, jackets, pipings and valves).
- Different feed concentrations and flow rates can be handled by the controller.
- The control concept is basically insensitive to uncertainties as long as the range of set-points is met. Experimental unknowns are well compensated and the controller shows sufficient robustness.

The controller can handle experimental uncertainties, which can be regarded as a proper interference compensation. Below is demonstrated disturbance rejection by responses to specific perturbations introduced to the reactor.

6.6. Demonstration of Controller Performance

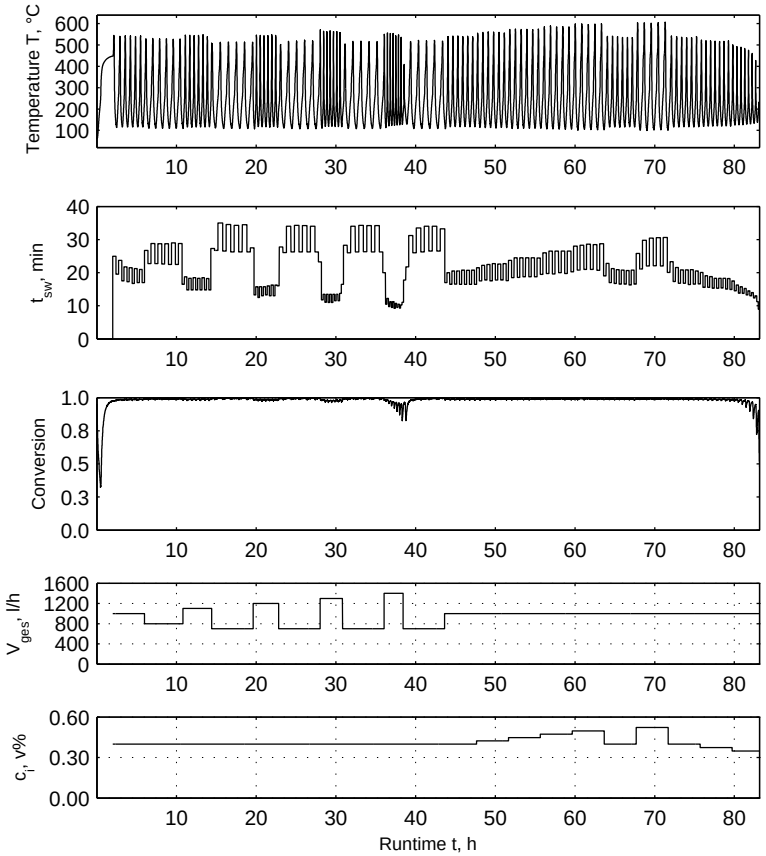

Figure 6.19.: Experimental investigation of controller subject to steps in the flow rate (up to 45 h) and in the feed concentration (after 45 h). Maximum temperature, switching time, conversion and below are given the flow rate and the feed concentration.

The reactor operation subject to step inputs of the flow rate and the feed concentration was considered. Figure 6.19 illustrated the results of an experiment lasting for 3.5 days. The first figure displays the signal of a thermocouple in one of the segments, which can be considered as a good indicator for changes in the front velocity. Below are illustrated the controller output (adjusted switching times), the conversion and the two inputs (flow rate and concentration).

Up to 45 h the total flow rate at a constant feed concentration was stepwise changed with increasing step heights. In the second part, for a constant total flow rate the feed concentration changed, starting with a stepwise increase, then larger steps down an up and finally a stepwise decrease.

Increased flow rates push the heat front faster through the reactor, consequently a faster switching is required and hence the switching times become smaller. Significant deviations in the switching time between the two segments can be observed, particularly at smaller flow rates. This is due to the different reaction front velocity in each segment. In case of the highest flow rate, almost extinction occurs which is being accompanied by decreased conversions at about 39 h runtime.

In the second part, after 45 h, the feed concentration was stepwise increased yielding higher

temperatures and slower reaction fronts. Accordingly, the switching times increased. Finally, steps in the feed concentration to small values caused extinction of the reactor.

The robust controller concept investigated effectively controls the switching time of the reactor unit. Large input steps in the total flow rate and in the feed concentration can be handled offering a good disturbance rejection.

An improved controller concept should account for limitations in the feed concentrations in order to avoid extinction in a running operation. In addition, it seems to be interesting to control the maximum temperature, for instance to prevent catalyst degradation and also for withdrawal of excess energy used elsewhere. Control actions require e.g. the application of co-feeding of an additional fuel and heat release at certain position in or between the fixed-beds. Even implementation of additional heat exchanger systems are options which could be considered. There is much room left to organize proper control loops and to identify advanced control concepts. As an inherent feature of the reactor, the multi-stability of the reactor need to be considered accordingly.

6.7. Investigations of Mixtures

Several experiments were performed to investigate the oxidation of mixture of propene and ethene. A typical run is shown in figure 6.20. After preheating the two fixed-beds, the reactor was started and operated with *controller 3*, and the ethylene fraction was step wise increased while maintaining a constant adiabatic temperature rise. As a result, the maximum reactor temperature increased with the ethylene fraction and the switching times became slightly smaller revealing higher front velocities. This can be explained with reaction kinetics. The ethylene oxidation was found to be less active on $CuCrO_x/Al_2O_3$ as reported in table 6.1. With decreasing rates the reaction fronts become faster and temperatures increase, thus, these relationships also apply for mixtures (see figure 2.5).

After 16 hours the total flow rate was set to 900 l/h and the fraction of ethene stepwise increased again, thereby maintaining a constant adiabatic temperature rise of the mixture. Decreasing the total flow rate, even at higher total feed concentration, lead to a smaller maximum temperature compared to the first part of the experimental run. This time, the maximum temperature increased only by several degrees with the fraction of ethylene. Again, the switching times decreased due to the faster reaction fronts.

Reactor control of such a binary mixture does not seem to be a problem. The reaction system examined, however, does not exhibit large differences in the reaction rates. The next chapter therefore deals with the complexity involved in the reactor operation as the reaction rates become increasingly different.

6.8. Summary

This chapter described the experiments performed in scope of this work and to present a model based analysis of SMBR reactor in open and closed-loop control.

As a model system the total oxidation of propene and ethene in air on a metal oxide supported $\gamma - Al_2O_3$ catalyst ($CuCrO_x/Al_2O_3$) was studied. Kinetic parameters have been

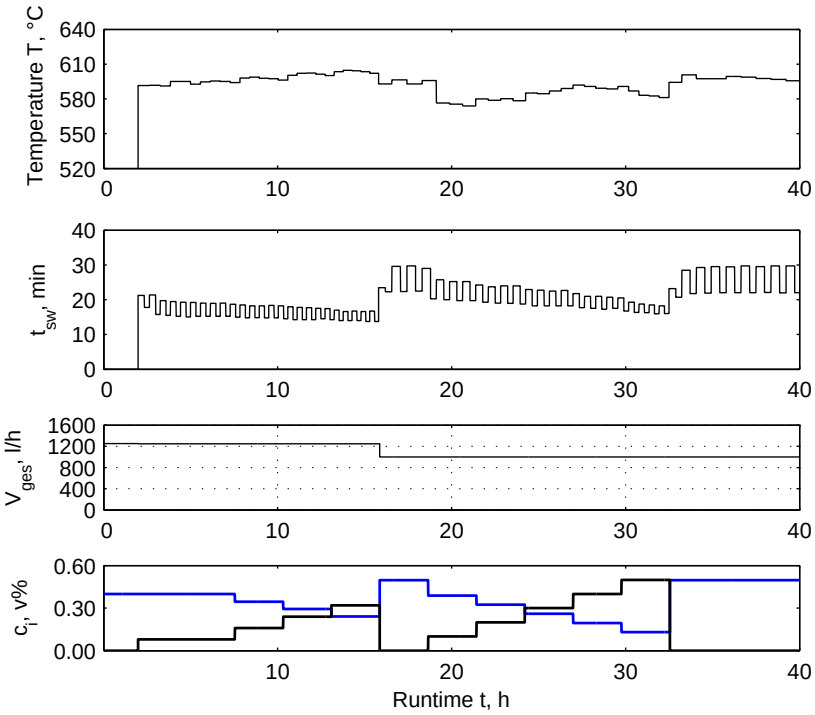

Figure 6.20.: Experimental investigation of reactor by step wise input variation of the composition of the propene/ethene mixture. In the first part a flow rate of 1200 l/h was used, after 16 h switched to 900 l/h. The composition was alter according to the bottom figure (blue line for propene and black for ethene).

determined by analyzing steady-state experimental data. Propene showed a higher activity than ethene. Mixtures of these reactants were investigated but could not be aligned to common kinetic models. Further experiments are needed to fill this gap.

Periodic operation of a two bed SMBR was investigated experimentally. Systematic experiments in open-loop control revealed the domain of ignited reactor states for two different feed concentrations. Simulation with an augmented SMBR model showed a good qualitative agreement with the domains of ignition in the experiments. It was parameterized by kinetic parameters determined experimentally and contains additional balances for the reactor wall and valve section. In this way, a better representation of heat losses, heat conduction and storage effects could be achieved. Maximum temperatures were well represented, though the prediction made regarding switching times close to the stability limits were found to be weak. As an explanation are seen experimental uncertainties, such as differences in the packing of each segment and heat bridges.

Closed-loop control was characterized regarding the range of temperature set-points applicable to maintain ignited states. The relationship predicted in the previous chapter has been confirmed. Feed concentration and flow rate were investigated by systematically altering the set-point in the available range for ignited states. The controller performance was also verified by applying step inputs in the feed with respect to these parameters. Proper disturbance rejection could be achieved with the *controller 3* identified in the theoretical study (chapter 5).

In addition, the oxidation of mixtures of propene and ethene was investigated. It was shown that for larger fractions of ethene, the reaction fronts become faster, which is consequently compensated by adjusting smaller switching times. These observations can be explained with the increased front velocity as the reaction rate increases, which accordingly applies for the mixture. The experiments also revealed, that for mixtures with similar rates for the oxidation of the constituents reactor control does not pose larger problems.

The next chapter deals with mixtures in general, in order to identify special requirements to be considered for cases where large kinetic selectivities prevail.

7. Reactor Operation in the Case of Feed Mixtures

This chapter deals with the reactor operation when mixtures of various compositions are applied. The experimental observations shown in the preceding chapter motivated a thorough analysis of the qualitative reactor behavior considering properties of the important mixture and process parameters. These include the composition, the total feed concentration, the flow rate ratio, and the differences in the reaction rates of two oxidation reactions.

Below, a step by step analysis of the singularities is performed to identify different reactor states for specific parameter combinations. Again, the TMBR model (sec. B.3) provided the adequate basis for the investigation. A two dimensional map finally summarizes the attainable operating regimes in terms of the most important parameters, namely feed concentration and kinetic selectivity, allowing to extract important guidelines for SMBR operation.

7.1. Parameters of the Mixture

In this chapter mixtures of two component oxidized simultaneously are considered. Salinger et al. [122] published a valuable analysis of mixtures in a reverse-flow reactor. For a quantitative characterization of the feed mixture three parameters are considered: first, the total concentration corresponding to a adiabatic temperature rise due to converting the mixture, $\Delta T_{\mathrm{ad}}^{\mathrm{mix}}$:

$$\Delta T_{\mathrm{ad}}^{\mathrm{mix}} = \frac{(-\Delta H_{R,1})\, w_1^{\mathrm{in}}}{c_{p,g}\widetilde{M}_1} + \frac{(-\Delta H_{R,2})\, w_2^{\mathrm{in}}}{c_{p,g}\widetilde{M}_2} \tag{7.1}$$

the fraction α based on mass fraction with respect to the second component (corresponding to ethylene in the experiments):

$$\alpha = \frac{w_2^{\mathrm{in}}}{w_1^{\mathrm{in}} + w_2^{\mathrm{in}}} \tag{7.2}$$

The third parameter, σ, quantifies the ratio between the pre-exponential factors:

$$\sigma = \frac{k_{0,1}}{k_{0,2}} \tag{7.3}$$

In this way a kinetic selectivity for two parallel reactions is considered. The ratio is 343 for the experimental system propene/ethene investigated (compare tab. 6.1). In order to generalize the analysis, the selectivity is treated below as a free parameter by changing the

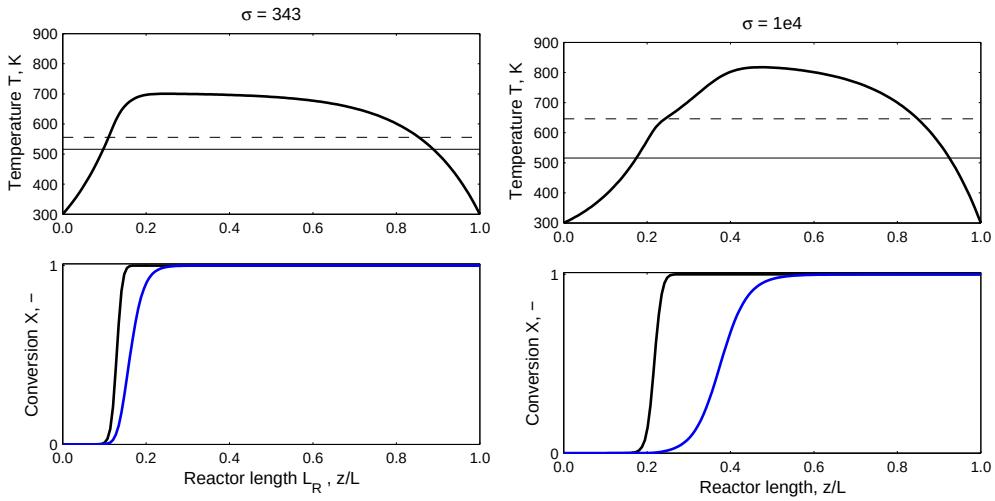

Figure 7.1.: Temperature and conversion profiles in a mixture. Left: for a kinetic selectivity of $\sigma = 343$, and right for $\sigma = 1e4$. Horizontal lines indicate the estimated ignition temperatures, black lines for component (1), blue for component (2) ($\Delta T_{ad}^{mix} = 30$ K, $\gamma = 1.05$, $\alpha = 0.5$, $N_p = 150$, TMBR model according to sec. B.3).

pre-exponential factor $k_{0,2}$ of the second oxidation reaction. At the same time, the activation energies are kept constant at values corresponding to the experimental reaction system (tab. 6.1). In this way, the second reaction is assumed to slow down with increasing kinetic selectivities σ. This corresponds also to an increase in the ignition temperature (eq. (2.40)).

Basically, the system is characterized by an energetic coupling of the participating parallel oxidation reactions: the fraction α together with the total feed concentration ΔT_{ad}^{mix} determines the potential amount of heat being released, the kinetic selectivity σ determines, whether this can be achieved for the second component, and as a process parameter, the flow rate ratio γ used above intensively is an identifier for the domain of ignition.

As a starting point the steady state profiles of the TMBR model are shown for two different selectivities in case of an 1:1 mixture ($\alpha = 0.5$) in figure 7.1. A feed concentration of the mixture corresponding to an adiabatic temperature rise of 30 K and a flow rate ratio of $\gamma = 1.05$ were selected. Heat losses were omitted throughout the analysis.

Figure 7.1 left illustrates the kinetic selectivity of the experimental system. The temperature profile has the typical bell shape and complete conversion of both components is achieved. Concerning the second, less oxidizable component, the reaction front is slightly shifted to the reactor outlet. Ignition temperatures differing by 40 °C ($T_{ig,1} = 242$ °C $T_{ig,1} = 283$ °C at $\dot{m}_g = 1$ kg/m^{2}s) are highlighted by horizontal lines. Thus, with larger ignition temperatures, the maximum temperature increases and the reaction front velocities increase, as elucidated already in section 2.1.3.

However, if for the second reaction it is assumed a much smaller reaction rate ($\sigma = 1e4$), then both reaction fronts are shifted to the outlet and differ significantly in the spatial positions (fig. 7.1 right). In such cases the temperature profile shows a shoulder approximately at the ignition temperature of the second component. This is an important feature as it marks the temperature level at which different fronts can form in an SMBR.

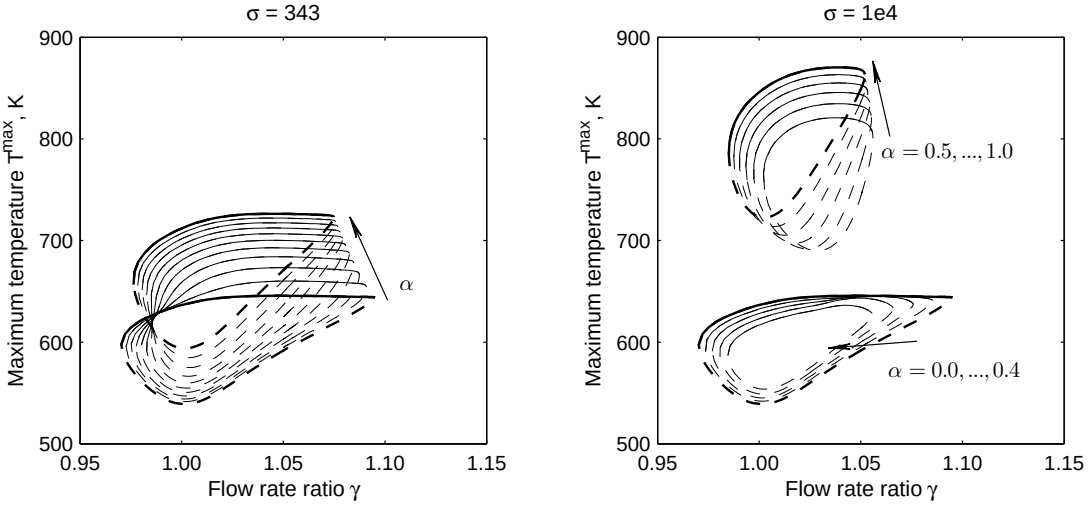

Figure 7.2.: Isola bifurcations for the maximum temperatures with respect to the flow rate ratio γ for the complete range of the binary mixture in terms of the fraction α. Left for the small kinetic selectivity ($\sigma = 343$), right for a very slow second oxidation reaction, $\sigma = 1e^4$. Thick lines indicate pure components. Model in sec. B.3, discussion in sec. 7.2.

Qualitative changes due to an increase in σ can be explained with the property of the reaction front already investigated in chapter 2.1.3 and with the transition into extinction as comprehensively discussed in section 4.4 devoted to the nonlinear analysis of the TMBR model. In case of a fixed flow rate ratio, the increased front velocity due to a decrease in the pre-exponential factor is responsible for the shift towards the reactor outlet. Thus, the second faster front could also leave the reactor in extreme cases. To prevent this situation, one can counteract by a decrease of the flow rate ratio, thus performing a faster switching. However, in the end, the front can break down even if switching and front velocity match. This was also shown to happen in the constant pattern solution: a minimum rate must be provided in order to form exothermic reaction fronts at reduced inlet temperatures. Here, the TMBR model describes both effects, regarding velocity and existence.

Below a nonlinear analysis of the TMBR model is performed in order to study the transitions of the reactor states for the parameters defined.

7.2. Introduction to Isola Splitting

Splitting due to Variations in the Composition α As a prelude to the analysis the two cases of different kinetic selectivities are considered again: the selectivity of the experimental system ($\sigma = 343$) and the case of larger differences in the pre-exponential factors ($\sigma = 1e4$). Figure 7.2 illustrates the bifurcation diagrams for the maximum reactor temperatures with respect to the flow rate ratio γ for the complete range of the binary composition ($\alpha = 0 \ldots 1$).

The isola of the pure components are highlighted by thick lines and the unstable solution branches are represented by intercepted lines. For the parameters of the simple mixture ($\sigma = 343$) the transition from the low temperature to the high temperature stable branch is smooth (fig. 7.2, left).

Figure 7.3 shows the corresponding conversions (eq. (2.42)) of the two components. Note that the conversions are shown only for feasible ranges, i.e. for the first component, $\alpha = 0,\ldots,0.9$, for the second, $\alpha = 0.1,\ldots,1.0$.

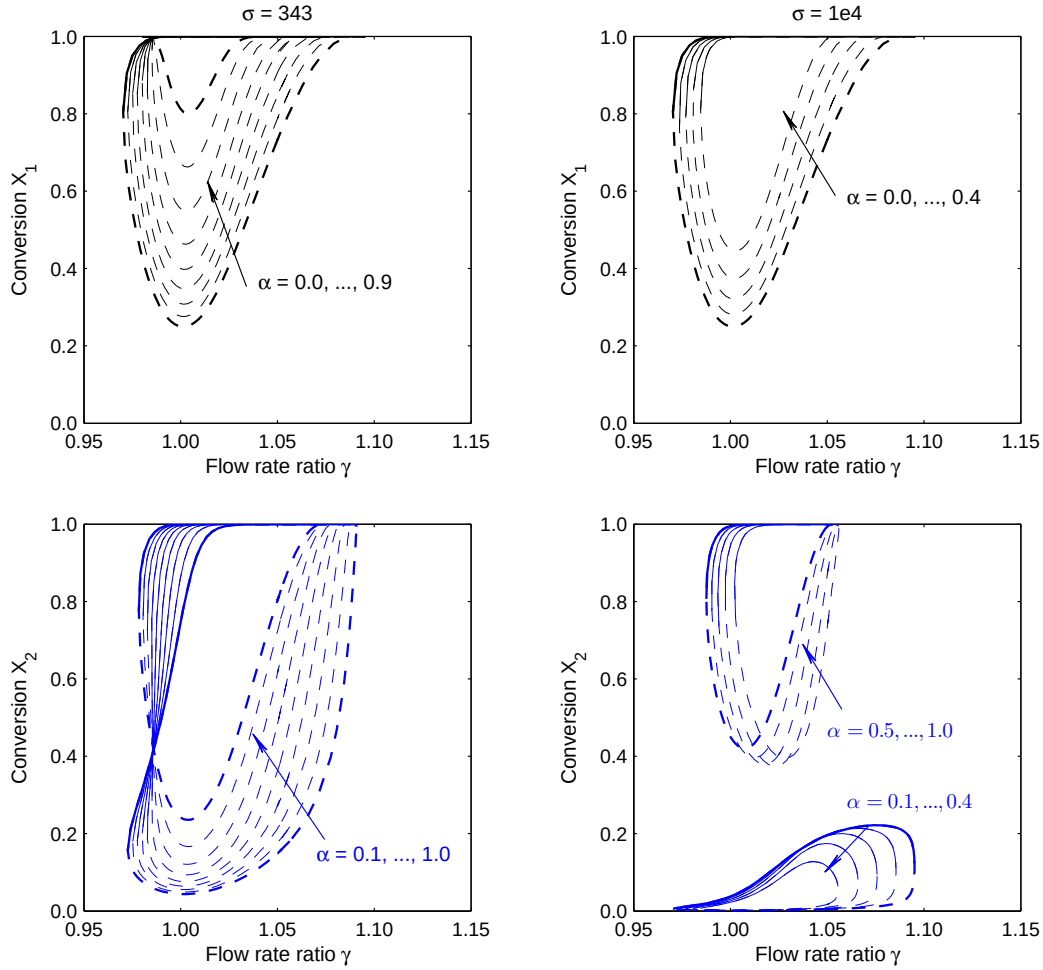

Figure 7.3.: Isola bifurcations for the conversion of the first, X_1, and the second, X_2, component with respect to the flow rate ratio γ for the complete range of the binary mixture in terms of the fraction α. Left for the small kinetic selectivity ($\sigma = 343$), right for a very slow second oxidation reaction, $\sigma = 1e^4$.

In case of $\sigma = 343$, it is important to observe that the conversions of both components, X_1 and X_2, are not identical throughout the flow rate ratio γ. A significantly lower conversion for the second X_2 is obtained for flow rate ratios below one (stable branches) and excess of the first component. Only if the fraction of the second is much larger, the picture changes and the complete conversion of both is achieved at similar flow rate ratios. The conversion of the first component is almost independent of the composition, which is due to the higher reactor temperature with larger fractions α (compare fig. 7.2, left).

The picture changes considerably in case of larger differences in reaction rates, $\sigma = 1e4$. Depending on the composition, two distinct isola in the temperature can be identified (fig 7.2 right). Starting from $\alpha = 0$, an isola at lower reactor temperatures exists, which shrinks as the fraction of the second is increased ($\alpha = 0.0,\ldots,0.4$). Beyond the fraction of $\alpha > 0.5$, a new

isola is obtained at significantly higher reactor temperatures.

The analysis of the conversion renders a clear picture of the underlying phenomena (fig. 7.3 right). At lower fractions, only an incomplete conversion of second component of about 0.2 can be achieved, while the first one is completely oxidized (Note that only branches corresponding to the low temperature isola are shown in the top right figure).

As the fraction is increased above 0.4 the high temperature isola appears. This time, the reactor shows also complete conversion of the second component. The attainable reactor states therefore strongly depend on the fraction of the second component, α, and the difference in the rates, σ.

Splitting due to Variations in the Kinetic Selectivities σ It is instructive to discuss the transition from a single isola into two distinct isola by changing σ, but for a fixed fraction α. Figure 7.4 shows three representative examples for the isola in terms of the reactor temperature and the conversion of the second component, X_2.

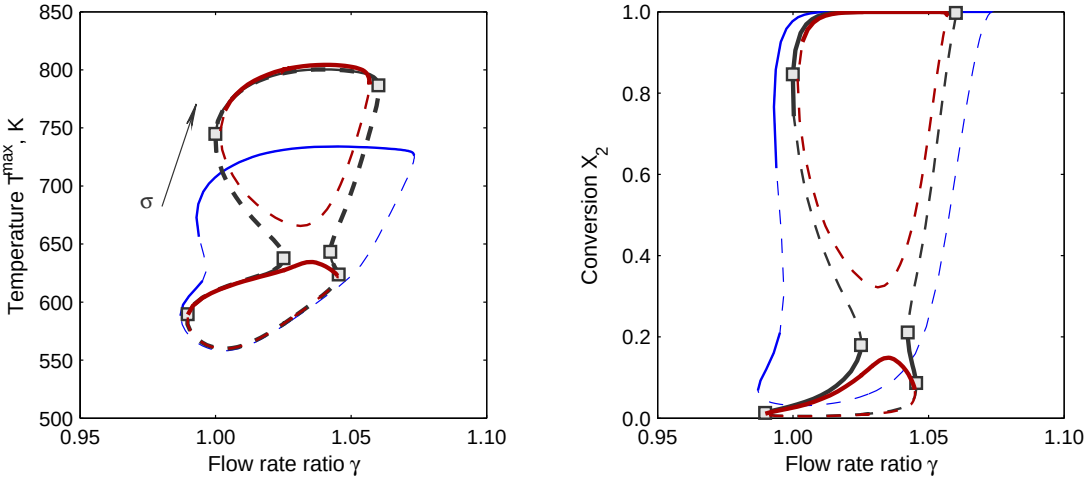

Figure 7.4.: Transition of a single isola into two distinct isola by increasing the kinetic selectivity for the example of σ 1000 (blue lines), 6000 (black lines) and 7000 (red lines) in case of an 1:1 mixture ($\alpha = 0.5$). Left, temperature and right, conversion of the second component. The symbols indicate the six limit points for $\sigma = 6000$.

Initially a single isola has two limit point. When σ increases up to e.g. 1000, the isola shows already four limit points, and in case of $\sigma = 6000$, six limit point are observed. Finally, the two distinct isola are characterized by two limit points each. The transition proceeds actually via the formation of double limits into a complete splitting in two distinct isola. This means, that selecting a specific bifurcation parameter γ, two limit points can exist simultaneously, though at different reactor temperatures (for a specific parameter σ). It will be explained later, under which conditions such double limits appear.

The conversion of the first component, X_1 (not shown), has a the unique solution allowing for complete oxidation, which is analogous to the previous results (fig 7.3). The conversion of the second component, X_2, shows the split into the distinct solutions branches (fig. 7.4, right), which analogously proceeds via six limit points.

It should be noted that the results in this chapter are given in terms of states of the process model. Alternatively it would also be instructive to consider the underlying reduced function

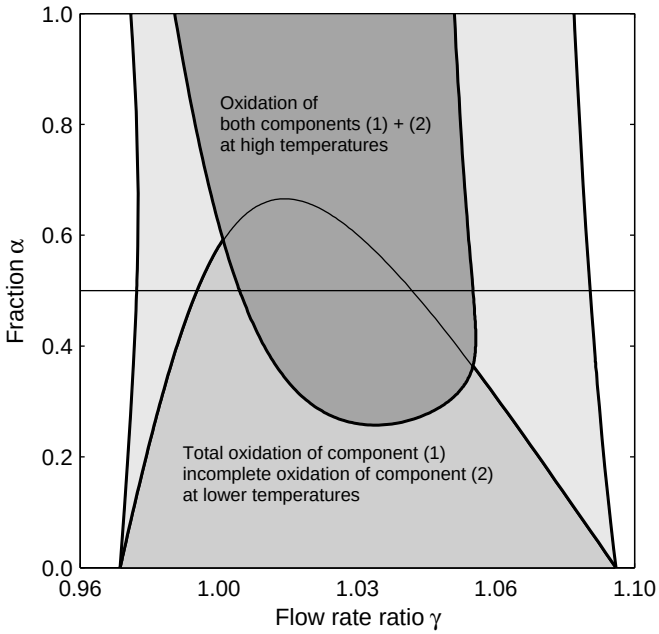

Figure 7.5.: Locus of limit points $LPC(\gamma, \alpha)$ for two specific kinetic selectivities, σ of 100 and $1.5e4$: Light gray area corresponds to $\sigma = 100$ and extends throughout complete range of α.
For $\sigma = 1.5e4$ two areas exist: Intermediate gray scaled area extends from 0 to $\alpha \approx 0.66$ with limited conversion of the second compound. Dark gray area ranges from $0.28 \lessapprox \alpha \lessapprox 1.0$ allowing for complete conversion of both reactants. Discussion in section 7.3.1 below.

discussed in section 4.1.2. In this respect it is recommended to see Golubitsky et al. [134] for a description of the transitions in distinct isola.

The results show that two distinct isola can form out of a single one and that the transition is triggered either by specific compositions or selectivities. As a next step an attempt was made to provide a better overview by studying the limit points in the respective parameter planes and to identify higher order singularities.

7.3. Characterization of the Transition Domain

7.3.1. Isola Splitting in Composition α and Kinetic Selectivity σ

The limit points of the isola have been solved for the fraction α in case of specific selectivities σ. As an introduction, figure 7.5 illustrates the results for two selected cases, $\sigma = 100$ and $\sigma = 1.5e4$. As previously shown, when the reaction rates do not differ much, $\sigma = 100$, complete oxidation of both components can always be assured. The corresponding region is the light gray area bounded by two continuous lines in the range of $\alpha = 0, \ldots, 1.0$ at almost constant flow rate ratios γ, left at 0.98 and right at 1.09. Obviously, this region represents the single isola solution which corresponds to bifurcation diagrams in figure 7.2 left.

In case of $\sigma = 1.5e4$, two areas appear which overlap. The intermediate gray scale area extends to $\alpha \approx 0.66$ starting from $\alpha = 0$. Enclosed are reactor states for complete conversion of the first, but incomplete oxidation of the second component.

The dark area in the range of $0.28 \lessapprox \alpha \lessapprox 1.0$ encloses the high temperate reactor states at full conversion of both components. In the region where the areas overlap, the start-up temperature decides about the final reactor state being attained, either the low temperature states for incomplete conversion or the high temperature states for complete oxidation of both reactants.

As a reminder, figure 7.3 shows the conversion and figure 7.2 (right) the temperature of bifurcation diagrams for $\sigma = 1e4$, which is quite similar regarding the case of $\sigma = 1.5e4$. In the example, it was shown the switch between a low temperature to a high temperature isola occurs at approximately $\alpha > 0.4$. However, this is a oversimplification of the real situation, as it neglects the presence of two isola existing simultaneously. This was due to the initial value used for the construction of the bifurcation diagrams. Instead of starting from a limit point curve in terms of (γ, α), it was used the $LPC\left(\gamma, T^{\text{in}}\right)$. As a consequence, not all isola bifurcations possible could be detected with this first approach (fig. 7.2 and 7.3).

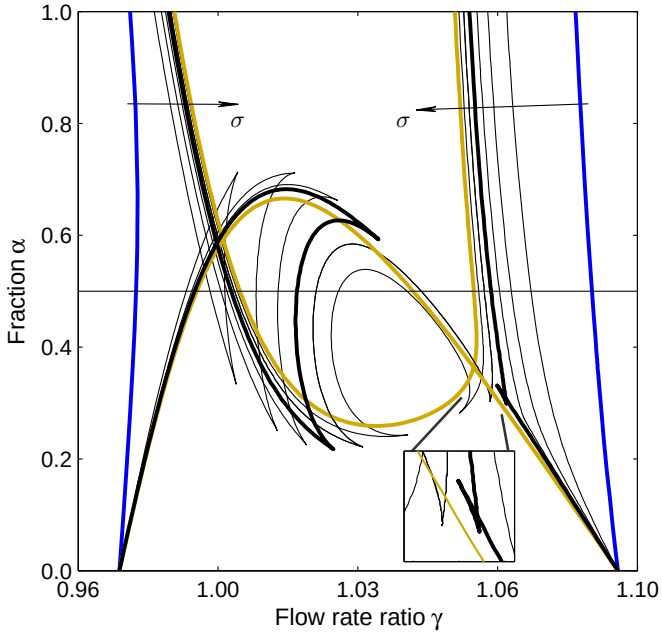

Figure 7.6.: Transition from a single in two distinct isola for the example of a family of limit point curves, $LPC\left(\gamma, \alpha\right)$, for various σ in the range $\sigma = 100$ (blue lines) and $\sigma = 1e4$ (yellow lines). The highlighted black line corresponds to $\sigma = 4000$. The inset indicates double limits appearing at larger flow rate ratios γ.

Therefore, it is more instructive to consider a comparison with figure 7.4, in which the kinetic selectivity σ was altered for a constant composition of $\alpha = 0.5$. The underlying transition agrees well with the parameter plane of figure 7.5. With increasing the kinetic selectivity, the number of limit point increases until the new second isola is born. Finally four limit points and two isola remain, i.e. similar to overlapping areas in figure 7.5 for $\alpha = 0.5$. The transition appears at a certain selectivity, beyond coexistence of two isola depends on the fraction α. E.g. if α is decreased, one switches back to the low temperature isola (incomplete oxidation), when α is increased, one can operate at high temperatures due to a single isola (complete conversion).

Up to this point, the transition was discussed for selected cases, the single isola at small

kinetic selectivities and the completely split operating regimes for a large selectivity in figure 7.5. The interesting details of the transition are studied with a family of limit point curves, $LPC = LPC(\gamma, \alpha)$, in figure 7.6.

In addition to figure 7.5 the black lines correspond to intermediate selectivities in the range from $\sigma = 100, 1000, \ldots, 7000$. The locus of the double limits can be identified by the crossings in the limit point curve, which appear for a certain parameter combination in terms of (γ, α, σ). Such a double limit explains the existence of two limit points above one another, which requires two stable and two unstable branches[1]. For example, the highlighted black line represents the limit points for $\sigma = 4000$. Two branches form, at a small and at a larger flow rate ratio, γ. Each of the branches is characterized by two cusps and a crossing in the LPC (note the inset to zoom in the region for the branch at $\gamma \approx 1.06$). E.g., in order to meet a double limit exactly, a fraction α of about 0.6 should be considered. The results also indicates, that the number of cusps differ as σ is increased and the transition into the distinct isola proceeds.

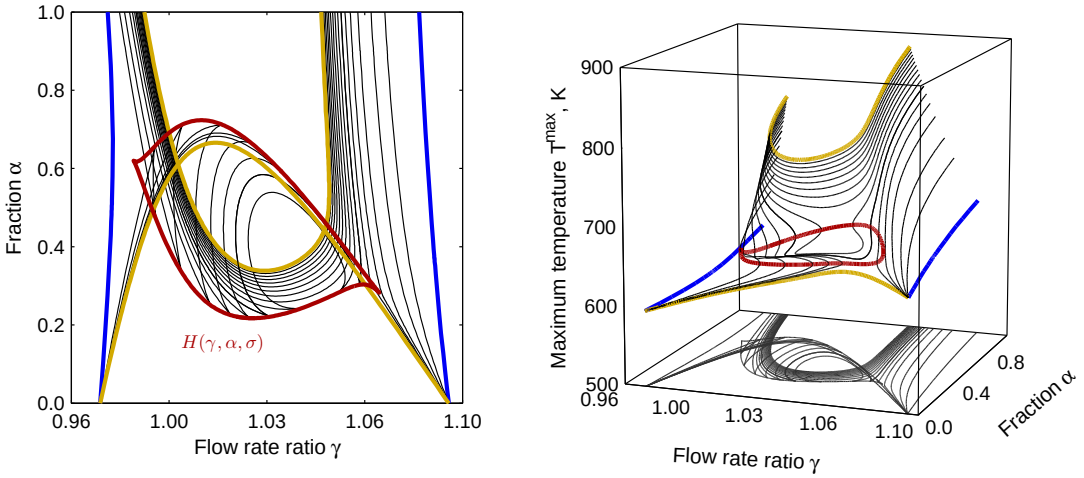

Figure 7.7.: Transition of the domain for a single isola in two distinct isola with increasing kinetic selectivity σ. Limit point curves, $LPC(\gamma, \alpha)$, are given as black lines for a range of σ $(100, 1.5e4)$, highlighting $\sigma = 100$ (blue) and $\sigma = 1.5e4$ (yellow). The hysteresis curve, $H(\gamma, \alpha, \sigma)$, (red line) connects the cusps (Note additional projections in figure 7.9). Calculation based on the TMBR model and parameters in B.3.

The locus of these cusps was determined by continuation of the hysteresis variety defined as $H = H(\gamma, \alpha, \sigma)$. Figure 7.7 illustrates the previous results adding the hysteresis curve as a red line and some additional limit point curves. In the right figure the results are shown in terms of the maximum reactor temperature as an indicator for the switching in the temperature regimes.

The shape of the hysteresis bifurcation resembles an onion with two spikes indicating the origin of double limits. This is an interesting result as it confirms the previous investigations regarding the transition in two isola. Depending on the fraction α, the double limit will emerge if approaching the region via continuation in γ. Parameterized functions connecting the double limits can not be calculated in the present work, but it is expected that they would be framed by the hysteresis bifurcations, though a one through connection between the ends

[1] See Golubitsky et al. [134] for definition, note that presently the software is unable to detect such points.

of the "onion" will probably not occur.

Figure 7.7 right illustrates the corresponding maximum temperatures of the singularities. Clearly, at larger selectivities, σ, also larger temperatures can be attained, however, this is restricted to certain fractions of the second component α. At small fractions, only the low temperature isola can form, and at larger fraction a single high temperature isola exists. In the transition domain at intermediate compositions, the attainable reactor states depend on initial temperature and flow rate ratio γ.

These results show that mixtures in which the components are converted with very different rates are more complex and demand further actions to control complete conversion in the SMBR. A further analysis details the bifurcation phenomena and options to be considered.

7.3.2. Transition Domain in the Parameters α and $\Delta T_{\mathrm{ad}}^{\mathrm{mix}}$

An intuitive approach to affect the range of isola multiplicities would be to control the inlet concentration. Hence, in this section is investigated the interaction of the singularities with respect to four parameters (γ, α, σ, $\Delta T_{\mathrm{ad}}^{\mathrm{mix}}$). First of all, the three-parameter set (γ, α, $\Delta T_{\mathrm{ad}}^{\mathrm{mix}}$) is examined, quite similar to the previous figure 7.7, and then the results are united to develop a more general view on the problem.

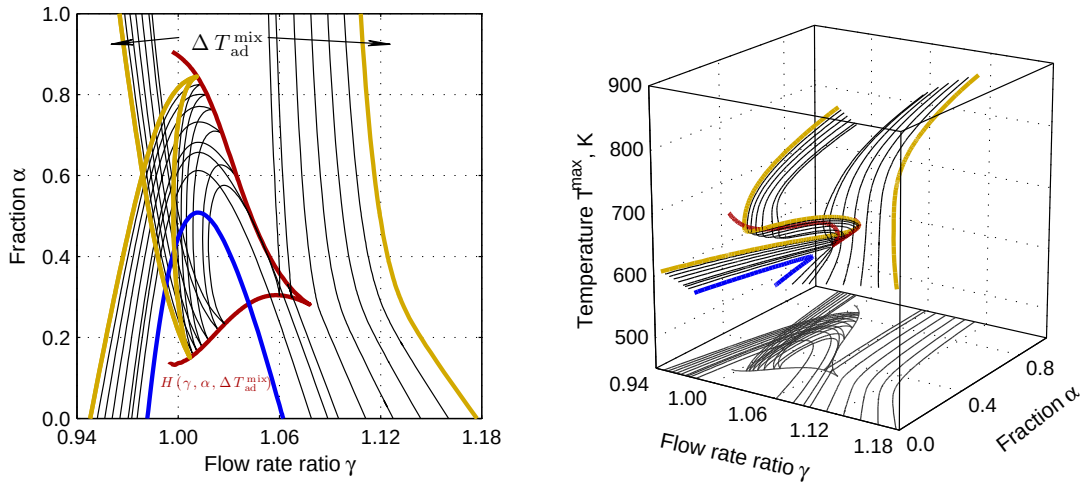

Figure 7.8.: Transition of the domain for a single isola in two distinct isola with increasing total feed concentration $\Delta T_{\mathrm{ad}}^{\mathrm{mix}}$. Limit point curves, $LPC(\gamma,\alpha)$, are given as black lines for a range of total feed concentrations according to $\Delta T_{\mathrm{ad}}^{\mathrm{mix}}$ (15,55 K), the hysteresis bifurcation (red line) connecting the cusp points. Limits for $\Delta T_{\mathrm{ad}}^{\mathrm{mix}} = 15$ K, blue, and $\Delta T_{\mathrm{ad}}^{\mathrm{mix}} = 55$ K, yellow lined (Note additional projections in figure 7.9). Calculation based on the TMBR model and parameters in B.3

The total feed concentration in terms of the adiabatic temperature rise $\Delta T_{\mathrm{ad}}^{\mathrm{mix}}$ (eq. (7.1)) was investigated in the limits between 15 and 55 K for a constant kinetic selectivity, σ, of $4e3$, which is right in the domain of the transition region of coexistence of isola bifurcations. Figure 7.8 illustrates the curves of limit point curves $LPC\left(\gamma,\alpha\right)$, it's range is highlighted by either yellow or blue lines. Hysteresis bifurcations defined by $H = H\left(\gamma,\alpha,\Delta T_{\mathrm{ad}}^{\mathrm{mix}}\right)$ connecting the cusps are indicated by the red line.

At the maximum value of $\Delta T_{\mathrm{ad}}^{\mathrm{mix}} = 55$ K (yellow lines), two cusp of the LPC are present for the branch at small γ values representing the curves of limit points at faster switching

operation. At the other side, the *LPC* limits the ignited states towards larger flow rate ratios or slow switching regimes, respectively. This is in accordance to the qualitative bifurcations diagrams in figure 7.4, where four limit points can exist at once (e.g. for $\alpha = 0.5$). The blue line represents the case for lean mixtures with and adiabatic temperature rise of 15 K framing the parameter set to maintain ignited reactor operation, however, at incomplete oxidation of the second component. An increase in the fraction α above 0.5 would lead to extinction, though.

If one considers an operation in the region of transition again, thus at a larger inlet concentration, several limitations can be discussed. Regarding conversion of the second component, the cusps located on the lower branch of the hysteresis bifurcation determines the limit of high temperature states, thus the domain for complete conversion of the second reactant. I.e., assuming 55 K, the limiting cusp is found at $\alpha = 0.16$. Only compositions above that value allow the second reaction can go to completion, thereby presuming $1.01 \lessapprox \gamma \lessapprox 1.1$. A generalization is available with the hysteresis bifurcation $H\left(\gamma, \alpha, \Delta T_{\mathrm{ad}}^{\mathrm{mix}}\right)$ (red line), specifically the branch at small α. This branch connecting the cusps consequently defines the minimum fraction α for complete oxidation, below only low temperature states are possible.

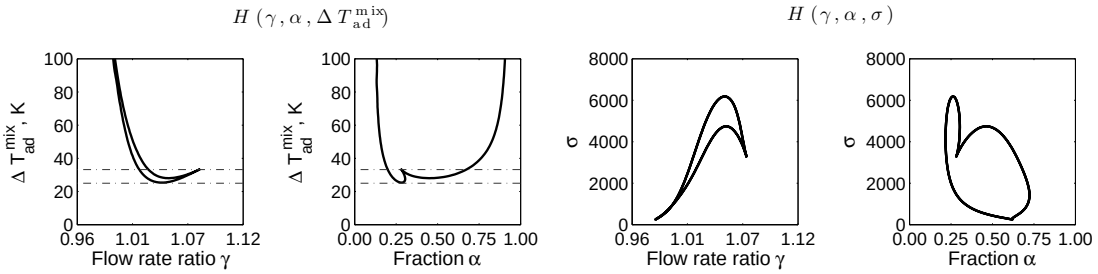

Figure 7.9.: Projections of hysteresis bifurcations H in the parameters γ and α with respect to the feed concentration in terms of $\Delta T_{\mathrm{ad}}^{\mathrm{mix}}$ (left) and the kinetic selectivity σ (right).

By decreasing the inlet concentration further, the isola would shrink and the limit point curves seem to move together. However, the cusp do not meet at the tip of hysteresis bifurcation as explained with the projections shown in figure 7.9. The tip of the hysteresis curve is found at larger inlet concentrations ($\Delta T_{\mathrm{ad}}^{\mathrm{mix}}$ =33.2 K), but the minimum is at a smaller inlet concentration ($\Delta T_{\mathrm{ad}}^{\mathrm{mix}}$ =25 K) (see dashed lines highlighting these limits).

This means that feed concentrations below 25 K generate curves of limit points which do not possess any cusps, which results in qualitatively similar curves as the example for $\Delta T_{\mathrm{ad}}^{\mathrm{mix}}$ =15 K (blue line in figure 7.8). For that reason, total feed concentrations below the hysteresis bifurcation allow only for complete oxidation of the first component.

What happens if the concentration is reduced even further. As it was shown for the single reaction system ($\alpha = 0$), an isola center in terms of $(\gamma, \Delta T_{\mathrm{ad}}^{\mathrm{mix}})$ represents the ignition limit at $\gamma \approx 0.99$ and ΔT_{ad} =5.7 K (see section 4.3.2). According to this, the limit point curve will finally shrink to a point solution identical to the isola center, which requires $\alpha = 0$, as found in the single component system.

Up to this point, the hysteresis bifurcation was discussed in detail. It turns out that both parameters, σ and $\Delta T_{\mathrm{ad}}^{\mathrm{mix}}$, generate cusps and double limits in the transitions region of the isola coexistence. So far, important limitations have been identified for a each single parameter set. It is rather interesting to unify the results. This offers an approach to generalize the reactor design problem.

7.3.3. Combinations of Hysteresis for σ and ΔT_{ad}^{mix}

In the next step of examination, families of the two different hysteresis bifurcations were calculated as illustrated in figure 7.10, left, $H\left(\gamma,\alpha,\Delta T_{ad}^{mix}\right)$ for different selectivities, σ, and in figure right, $H\left(\gamma,\alpha,\sigma\right)$ for several inlet concentrations, as ΔT_{ad}^{mix}. The domain of hysteresis bifurcations, which coincides with transition domain of the isola, increases with σ as well as with ΔT_{ad}^{mix}.

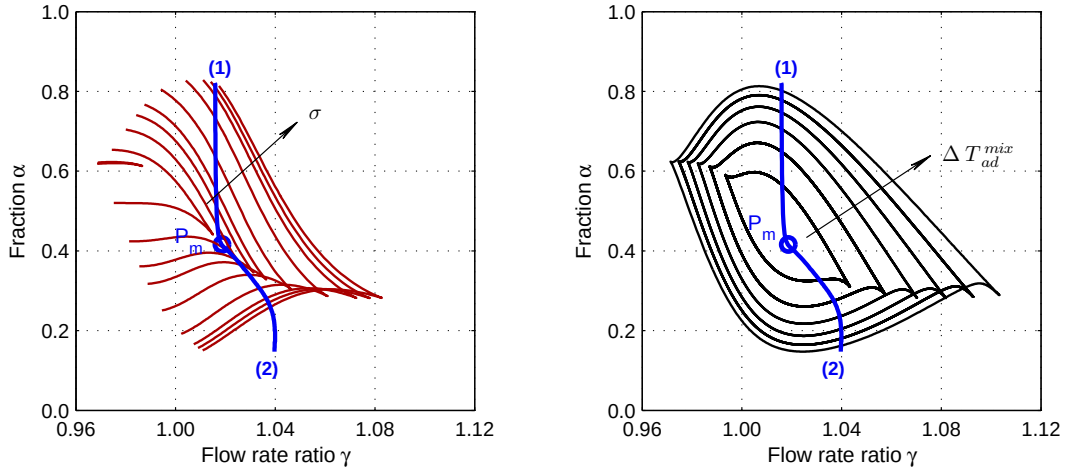

Figure 7.10.: Families of hysteresis curves, left $H\left(\gamma,\alpha,\Delta T_{ad}^{mix}\right)$ for a range of $\sigma = 250,\ldots,4500$, right for $H\left(\gamma,\alpha,\sigma\right)$ and a range of $\Delta T_{ad}^{mix} = 25,\ldots,45\,\mathrm{K}$. Blue lines represent loci of pitchfork bifurcations $P = P\left(\gamma,\alpha,\sigma,\Delta T_{ad}^{mix}\right)$, distinguished in two branches (1) and (2) originating from the point P_m (circle). Calculation based on the TMBR model and parameters in B.3.

In addition it was possible to identify the pitchfork bifurcation points located on the hysteresis bifurcation. Such a pitchfork can be generated e.g. by continuation in γ approaching a cusps, whereby the locus of the pitchfork bifurcation is defined by four parameter, $P = P\left(\gamma,\alpha,\sigma,\Delta T_{ad}^{mix}\right)$, with γ as the distinguished bifurcation parameter. The pitchfork bifurcation goes straight through the transition domain, defining the birth of the hysteresis bifurcations and therefore also the domain of isola splitting. The pitchfork in the center, denote as P_m, can be regarded as a minimal point with respect to ΔT_{ad}^{mix}, and is defined by $\sigma = 460$, $\Delta T_{ad}^{mix} = 14.57$, $\gamma = 1.0186$, and $\alpha = 0.416$. This center is marked with the circle in the figures, from which the two branches emerging are labeled as (1) and (2).

To explain the interrelation of hysteresis and pitchfork bifurcations it is instructive to consider two additional perspectives. Figure 7.11 gives an overview including the parameters α (left), and γ (right), as three dimensional illustrations; the corresponding projection in the parameter plane $(\Delta T_{ad}^{mix},\sigma)$ is finally given in figure 7.12.

Regarding the singularities in figure 7.11, the line colors correspond to the projections in figures 7.9 and 7.10. The combination of these families generate solution shells representing the domain of the isola transition. Regarding the fraction α, the solution shell encloses the transition domain in a cone like structure (fig. 7.11, left). The branches of the pitchfork are located on the shell emerging from P_m. The cone is actually formed by a combination of the hysteresis bifurcations as shown with the projections in figure 7.9 (second and fourth figure).

Figure 7.11 right illustrates another scenario, which is based on the flow rate ratio γ.

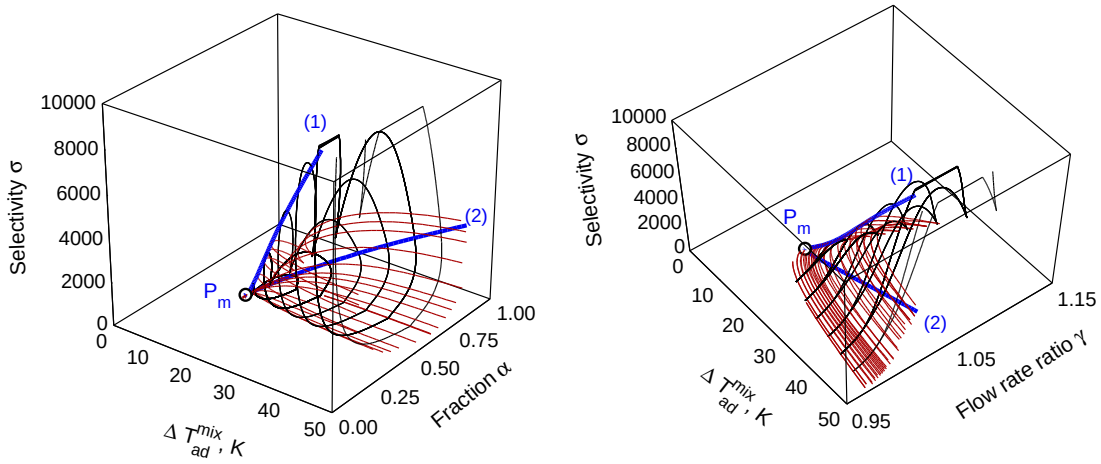

Figure 7.11.: Solution shells generated by hysteresis bifurcation curves $H\left(\gamma,\alpha,\Delta T_{\mathrm{ad}}^{\mathrm{mix}}\right)$ (red) and $H\left(\gamma,\alpha,\sigma\right)$ (black) in two parameter spaces, with respect to the fraction α, left, and w.r.t. γ, right. Blue lines represent pitchfork bifurcations distinguished in two branches, (1) and (2), emerging from the point P_m (circle). Calculation based on the TMBR Model and parameters in B.3.

Figuratively, the solution shell resembles a flat, leaf like structure (the leaf has a certain thickness of course). Such a structure is a combination of the projections shown in the first and third form illustrated in figure 7.9.

With this analysis, the hysteresis bifurcations identified reveal the expansion of the transition domain, and either the inlet concentration or the selectivity are responsible for its size. Even though the three dimensional figures do not allow an easy analysis, they offer a qualitative perspective which is quite useful for an interpretation of the projection in those two parameters of interest, as discussed in the next section.

7.4. Consolidation of Attainable Reactor States and Measures for Operation

In figure 7.12 are shown the results of the comprehensive study in the $\left(\Delta T_{\mathrm{ad}}^{\mathrm{mix}},\sigma\right)$ – plane, which is divided into four domains labeled (A) to (D) representing specific reactor operating regimes. It should be kept in mind, that the two other parameter, the fraction α and the flow rate ratio γ, have an influence on reactors states which can be attained as well. Therefor, projections previously discussed should be considered for interpretation.

These domains are characterized as follows:

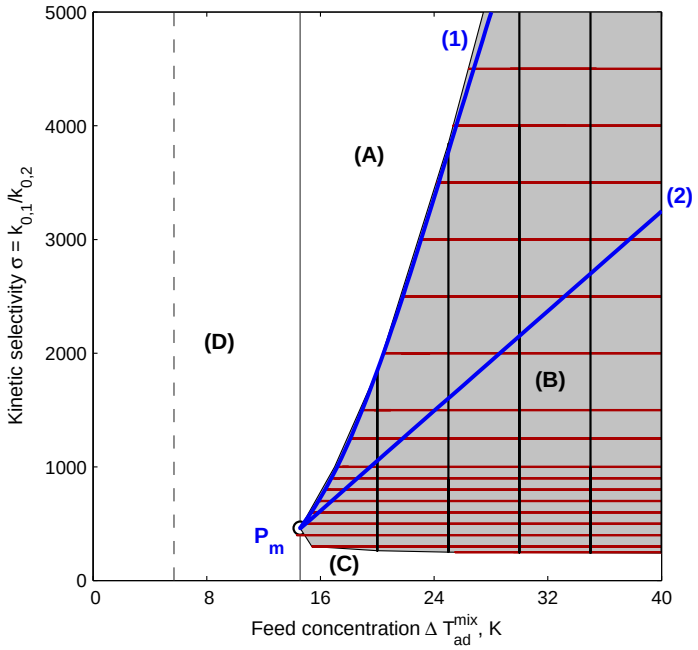

Figure 7.12.: Operating domains of the reactor for a binary mixture in the parameter plane $\left(\Delta T_{\mathrm{ad}}^{\mathrm{mix}}, \sigma\right)$. Transition domain (gray area), red lines represent hysteresis $H\left(\gamma, \alpha, \Delta T_{\mathrm{ad}}^{\mathrm{mix}}\right)$, black lines $H(\gamma, \alpha, \sigma)$ and blue lines the pitchfork bifurcation $P\left(\gamma, \alpha, \sigma, \Delta T_{\mathrm{ad}}^{\mathrm{mix}}\right)$. Letters explained below. Absolute ignition limit regarding ΔT_{ad} of the single component system, dashed vertical line (isola center, fig. 4.3 and section 4.3.4). Calculations based on the TMBR model and parameters in B.3.

Domain (A): Reactor operation at large selectivities σ is characterized by two distinguishable isola at intermediate compositions. Start-up temperatures decide, if high or lower temperature states will be attained. Moreover, for either very large or small fractions of the second component, α, one obtains respective single isola. Conversion of the second component is only ensured for the high temperature isola (fig. 7.5).

Domain (B): It marks the transition domain characterized by hysteresis bifurcations found specifically at the borders and double limit bifurcations may occur. Therefore, start-up temperatures can decide about conversion of the second component, as well as composition, α, and flow rate ratio, γ, (fig. 7.7 and 7.8).

Domain (C): The kinetic selectivity σ is small, such that there do not exist any hysteresis bifurcations. Only single isola solutions are found providing complete conversion of both components simultaneously (fig. 7.2 and 7.3).

Domain (D): Reducing the total inlet concentration ($\Delta T_{\mathrm{ad}}^{\mathrm{mix}}$) below the critical point P_m yields only single isola. Complete conversion may be achieved for the first component, however, not for the second component. Ignited states are limited regarding the total inlet concentration ($\Delta T_{\mathrm{ad}}^{\mathrm{mix}}$), which has been revealed for the single component system (dashed line indicated the locus of the isola center in terms of ΔT_{ad}, the ignition limit for $\alpha = 0$, fig. 4.11).

Four domains summarize qualitative different operation as condensed out of a four parameter space i.e. in $\left(\gamma, \alpha, \sigma, \Delta T_{\mathrm{ad}}^{\mathrm{mix}}\right)$. This is certainly the advantage of a systematic singularity analysis as it allows for identification of main features in a multiparametric context. Despite the complexity of the underlying operating domains regarding the bifurcation diagrams, a generalization of reaction engineering problems and appropriate solutions strategies can be extracted. In summary the analysis has shown that:

1. The reactor operation with a binary mixtures depends on the ignition of both reactions producing more complex multiplicities than in case of a single reaction.

2. Larger deviations in the reaction rates lead to the formation of two distinct isola. An isola at high temperatures assures complete conversion, the other only incomplete conversion of the mixture at lower temperatures.

3. Conversion of a component with a significantly smaller reaction rate is restricted to specific parameter combinations.

In contrast to oxidation of a single component investigated in the preceding chapters, the fraction of the second, more difficult to oxidize component, is a limiting factor. With respect to a complete conversion of both reactants, the following options should be considered for process design and control:

- If double isola exist because of large values in the reaction rate ratio σ (domain (A), fig. 7.12), a sufficient fraction of the less activated component should always be provided in the feed (fig. 7.7). In this way, operation at the high temperature branch is possible ensuring complete conversion of both components. In addition, a sufficiently large preheating temperature is required, providing activation of the second reaction to attain high temperature states.

- In the transition domain (domain B), a sufficient amount of the component difficult to be oxidized is also essential to provide high temperature states for complete oxidation of both components. Otherwise, in case of excess of the first component an increased total inlet concentration should be considered (lower hysteresis branch in figure 7.8)

- Co-feeding of a component with an intermediate reaction rate should be considered as an option to prevent isola splitting, thus providing single isola solutions throughout α.

In addition to these options which exploit concentration effects, an additional degree of freedom, the flow rate ratio γ or the respective switching time in a real SMBR, can be considered for control. Appendix C.4 addresses such control strategies for the SMBR.

Instead of complete oxidation of both components as sought in VOC applications, the opposite target could also be interesting, thus preventing ignition of an unwanted parallel reaction, for instance concerning safety issues. A thorough understanding of how mixtures affect the size and location of operating domains is also required, when exothermic synthesis reaction are investigated for SMBR application. The results obtained here, particularly the analysis how singularities evolve, can help to cope with such problems as well.

7.5. Summary

This chapter provides a theoretical description of the SMBR reactor operation with a binary mixtures based on the TMBR model. Two independent oxidation reaction were considered, for which local reactor temperature is responsible for the extent of the reactions and the existence of ignited states.

The reaction system was specified by the total amount of the two reactants, the fraction of the second component, the ratio between the pre-exponential factors (kinetic selectivity), and the flow rate ratio of the TMBR. The steady state solution revealed different, nonuniform, temperature profiles in case of large differences in the reaction rates, which can be explained with different reaction front velocities. For the second, less oxidizable component, the front is faster at increased temperatures.

The formation of two distinct isola was identified for large kinetic selectivities. Complete conversion can be achieve when operating in the high temperature isola, but incomplete conversion of the second component is observed when operating in the low temperature isola.

Singularity analysis was carried out in the set of four parameters to characterized the transition from a single isola in two distinct isola. Double limits, hysteresis and pitchfork bifurcations were encountered and used to organize a parameter map relating selectivity to total feed concentration. In this map, the reactor operation can be classified in four domains, one with two distinct isola, the transition domain, a domain with a single isola and complete oxidation, and finally one with a single isola and incomplete oxidation.

The measures to be considered for process control for larger kinetic selectivities are to provide excess of the less oxidizable component, a sufficiently high start-up temperature and a larger total feed concentration. In general, the reactor can handle a more complex feedstock provided appropriate control parameters are selected.

8. Summary and Conclusions

8.1. Summary

Periodic operation of chemical reactors offer additional degrees of freedom, which can be exploited to design new reactor concepts. First, the temporal variability allows for applying process cycles using the conventional reactor, thus alternating the boundary conditions. Secondly, and different to steady-state operation, nonlinear phenomena, such as traveling waves and associated accumulation effects occur, which can be exploited for process integration.

This work investigates the periodic operation of a cascade of catalytic fixed-bed reactors which offers a heat integrated reactor concept. As an example exothermic reactions were considered. Potential applications are the total oxidation of volatile organic compounds (VOC) in diluted off-gases and equilibrium limited reactions. The reactor principle aims at trapping exothermic reaction fronts in thermally coupled cascade of catalytic fixed-beds to accumulate the heat efficiently. In this way, an autothermal operation, in which the feed is introduced at ambient temperatures, can be achieved. Initially the cascade is heated up above the ignition temperature and cold feed is introduced. As a consequence, a traveling self-sustained exothermic front forms, which cools down the upstream fixed-bed section. To achieve a trapping effect, this cooled segment is switched to the end of the cascade, where it is heated up again. This principle can be regarded as a simulated moving bed reactor (SMBR).

This work intended to bring insight into the relevant aspects of the reactor concept based on theoretical and experimental investigations. Modeling, model reduction and nonlinear analysis were considered in the early design phases and helped to identify key parameters for process design and control. The experimental proof of the concept confirmed the theoretical predictions also carried out.

In a first chapter traveling fronts in fixed-beds were investigated. Basically two types of fronts had to be considered, a reaction front and a thermal front. The reaction front could be characterized by the constant pattern solution with respect to most relevant parameters. In a SMBR, both fronts occur simultaneously. The faster thermal front, which reheats the cold segments, precedes the slower exothermic reaction front. Reaching the ignition temperature was shown to be a necessary condition for the existence of traveling reaction fronts. Moreover, the switching times to maintain ignited reactor states at complete conversion are limited to a specific range. A comparison with the reverse-flow concept demonstrates the advantages to reduce slips of unconverted reactants, however, at the cost of a loss of heat integration efficiency.

Since the simulation of the periodic model is numerically expensive, a reduced reactor model was investigated. The approach considered is based on the limiting case of an infinite number of segments, in which the switching operation is transferred into a continuous solid phase countercurrent transport. In this so called true moving bed reactor (TMBR), discrete

switching times are transformed into a solid phase velocity, which allows a fast approximation of the periodic states of the SMBR. However, only with the quantification of numerical errors occurring during the solution of the discretized model equations it was possible to establish a sufficiently accurate agreement between the SMBR and TMBR models. Convergence for larger numbers of segments of the SMBR into the limiting case of the TMBR could be confirmed.

The heat integration gives rise to multiple reactor states. Therefore ignition-extinction phenomena were thoroughly investigated. It was shown that TMBR and SMBR models exhibit similar bifurcation phenomena, which motivated to consider the easier TMBR for a detailed analysis. Higher order singularities, such as hysteresis, isola and simple bifurcations were encountered, and finally an organizing center, a pitchfork bifurcation, could be identified. An important result is the isola center defining the process limit of the reactor at a certain low inlet temperature and a specific switching time. A detailed analysis revealed, in which way other process parameters, e.g. heat conduction, heat losses and the reaction rate affect this ignition limit with respect to the inlet concentration and the solid phase velocity. In addition, kinetic limitations were examined and organized in parametric maps, which allow a fast assessment of possible reaction applicable for the adiabatic SMBR.

The open-loop control, operating with predefined switching times, has a distinct disadvantage because of the narrow window of switching times available for stable ignited states. A permanent adjustment in closed-loop control using a feedback of temperatures was suggested. Three control concepts were investigated in chapter 5. They differ in the fronts to be observed, either the reaction front or the leading thermal front, and the window of observation. An efficient concepts is to monitor the reaction front passing the outlet of the active reactor segment to trigger the switch. The set-point to make this decision should be in the range between the inlet temperature and the ignition temperature. Disturbance rejection of the three concepts was investigated based on steps introduced in the flow rate and feed concentration.

The reactor operation was experimentally investigated using a two-bed SMBR. In the first part of chapter 6 the kinetics of the model reactions, oxidation of propene and ethene on a $CuCrO_x/Al_2O_3$ catalyst, have been determined for implementation in a reactor model. Systematic experiments of the SMBR in open-loop revealed the limits regarding applicable switching times. Although the parameterized SMBR model gave a good agreement regarding maximum temperature, it lacks to exactly describe the domain of ignited states. This is due to experimental uncertainties regarding the packing of the reactor and heat losses. It was also demonstrated, that closed-loop control can handle these conditions. Robust reactor control was further confirmed by experiments introducing step inputs in the total flow rate and in the feed concentration.

Also experiments with feed mixtures of propene and ethene of various composition were conducted. Increased temperatures and increased front velocities were observed in case of an excess of the less oxidizable ethene. In this case, the controller performs well. Nevertheless, when reaction rates of the two oxidation reactions would differ significantly, it was expected to encounter disappearance of available ignited states. In order to generalize the problem of processing a binary mixture, the ratio between the reaction rates, i.e. a kinetic selectivity, the total feed concentration, the composition and the flow rate ratio were considered as parameters for a detailed analysis. It turns out that two distinct isola at different temperatures

can form when the rates of oxidation increasingly differ. When operating in ignited states at lower temperatures, the less oxidizable component is only partially converted.

The transition from a single isola into the two distinct isola was found to proceed via double limit and hysteresis bifurcations. The results achieved were summarized in a two parameter map revealing four distinct operating domains. Sufficient preheating for the start-up of the reactor, an appropriate total feed concentration and excess of the less oxidizable reactant should be considered to achieve complete conversion of both reactants.

8.2. Conclusion and Suggestions for Further Activities

This thesis provides a comprehensive analysis of the SMBR concept, including front phenomena, nonlinear analysis and real experimental conditions. It was shown that model based analysis helps to explain experimental findings. Despite the complexity associated with a narrow operating window, it was demonstrated that even simple control concepts can be implemented for process control. In this regard, the periodic operation of catalytic fixed-bed reactors exploiting multiple segments is a promising reactor concept which should be subject of further research.

Several problems seen as objectives for the future are:

- Experimental studies with mixtures can help to verify the predictions of the nonlinear analysis presented in chapter 7. Experiments with gradient free isothermal reactors are highly recommended to collect a larger set of more precise kinetic data for model identification of feed mixtures.
- Catalyst dilution would be interesting to investigate as an option to modify heat capacities and activity profiles. Front velocity and maximum temperatures in the SMBR could be further adjusted in this way.
- Equilibrium limited reactions, e.g. the methanol synthesis, are interesting applications. A theoretical investigation can be based on the TMBR model. Comparison with an optimized conventional steady state reactor design employing interstage cooling should be considered.
- In synthesis reactions and also in case of liquid phase reactions a stronger non-ideal behavior can be expected, which may significantly affect the local fluid phase velocities. A systematic model development considering these effects can help to explore other potential applications.
- Several unsolved problems regarding control should be addressed. Feed mixtures may generate a more complex behavior, in which only certain states are attractive. Recovery of an almost extinguished state and discharge of excess heat are also interesting issues.

Bibliography

[1] K. Weissermel and H.-J. Arpe. *Industrial Organic Chemistry.* 3rd edition. VCH Weinheim, 1997.

[2] H. Vogel. *Ullmanns Encyclopedia of Industrial Chemistry: Process Development.* Wily-VCH, 2005.

[3] K. Sundmacher, A. Kienle, and A. Seidel-Morgenstern, editors. *Integrated Chemical Processes.* Wiley-V C H Verlag GmbH & Co. KGaA, Weinheim, 2005.

[4] A. I. Stankiewicz and J. A. Moulijn. "Process intensification: Transforming chemical engineering." In: *Chemical Engineering Progress* 96.1 (2000-01), pages 22–34.

[5] Y. S. Matros. "Unsteady processes in catalytic reactors." In: *Studies of Surface Science and Catalysis.* Volume 22. Elsevier Inc., 1985.

[6] D. W. Agar and W. Ruppel. "Multifunktionale Reaktoren für die heterogene Katalyse." In: *Chemie Ingenieur Technik* 60.10 (1988), pages 731–741.

[7] K. Westerterp. "Multifunctional reactors." In: *Chemical Engineering Science* 47.9-11 (1992-06), pages 2195–2206.

[8] U. Hoffmann and K. Sundmacher. "Multifunktionale Reaktoren." In: *Chemie Ingenieur Technik* 69.5 (1997), pages 613–622.

[9] Kulprathipanja. *Reactive Separation Processes.* 1st edition. Taylor & Francis, 2001.

[10] K. Hashimoto, S. Adachi, H. Noujima, and Y. Ueda. "A new process combining adsorption and enzyme reaction for producing higher-fructose syrup." In: *Biotechnology and Bioengineering* 25.10 (1983), pages 2371–2393.

[11] T. Aida and P. Silveston. *Cyclic Separating Reactors.* Blackwell Publishing Ltd, 2005.

[12] T. Falk and A. Seidel-Morgenstern. "Comparison between a fixed-bed reactor and a chromatographic reactor." In: *Chemical Engineering Science* 54.10 (1999-05), pages 1479–1485.

[13] J. G. Sanchez Marcano and T. Tsotsis, editors. *Catalytic Membranes and Membrane Reactors.* Wiley-VCH Verlag GmbH, Weinheim, 2002.

[14] A. Seidel-Morgenstern. "Analysis and experimental investigation of membrane reactors." In: *Integrated chemical processes.* Edited by K. Sundmacher, A. Kienle, and A. Seidel-Morgenstern. Wiley-VCH Verlag GmbH & Co. KGaA, Weinheim, 2005.

[15] A. Seidel-Morgenstern, editor. *Membrane Reactors: Distributing Reactants to Improve Selectivity and Yield.* Wiley-VCH Verlag GmbH & Co. KGaA, 2010.

[16] G. Kolios, A. Gritsch, B. Glöckler, and G. Eigenberger. "Enhancing Productivity and Thermal Efficiency of High-Temperature Endothermic Processes in Heat-Integrated Fixed-Bed Reactors." In: *Integrated chemical processes.* Edited by K. Sundmacher, A. Kienle, and A. Seidel-Morgenstern. 2005.

[17] G. Eigenberger, G. Kolios, and U. Nieken. "Thermal pattern formation and process intensification in chemical reaction engineering." In: *Chemical Engineering Science* 62.18-20 (2007), pages 4825–4841.

[18] G. Kolios, J. Frauhammer, and G. Eigenberger. "Autothermal fixed-bed reactor concepts." In: *Chemical Engineering Science* 55 (2000), pages 5945–5967.

[19] G. Eigenberger. "Fixed-Bed Reactors." In: *Ullmanns Encyclopedia of Industrial Chemistry* B4 (1992), pages 199–237.

[20] F. Cottrell. "Purifying gases and apparatus therefor." Patent 2,121,733. 1938.

[21] Y. S. Matros. *Catalytic Processes under Unsteady-State Conditions*. Volume 43. Studies of Surface Science and Catalysis. New York, NY ;Elsevier Science Pub. Co. Inc., 1989.

[22] J. D. Snyder and B. Subramaniam. "Numerical simulation of a periodic flow reversal reactor for sulfur dioxide oxidation." In: *Chemical Engineering Science* 48.24 (1993), pages 4051–4064.

[23] G. A. Bunimovich, N. V. Vernikovskaya, V. O. Strots, B. S. Balzhinimaev, and Y. S. Matros. "SO_2 Oxidation In A Reverse-Flow Reactor - Influence Of A Vanadium Catalyst Dynamic Properties." In: *Chemical Engineering Science* 50.4 (1995-02), pages 565–580.

[24] P. L. Silveston, R. R. Hudgins, S. Bogdashev, N. Vernijakovskaja, and Y. S. Matros. "Modelling of a periodically operating packed-bed SO_2 oxidation Reactor at high conversion." In: *Chemical Engineering Science* 49.3 (1994), pages 335–341.

[25] A. S. Noskov, L. N. Boborova, and Y. S. Matros. "Reverse-Process For Nox-Off Gases Decontamination." In: *Catalysis Today* 17.1-2 (1993-05), pages 293–300.

[26] Y. S. Matros. "Forced unsteady-state processes in heterogeneous catalytic reactors." In: *Canadian Journal Of Chemical Engineering* 74.5 (1996-10), pages 566–579.

[27] K. M. V. Bussche, S. N. Neophytides, I. A. Zolotarskii, and G. F. Froment. "Modelling and simulation of the reversed flow operation of a fixed-bed reactor for methanol synthesis." In: *Chemical Engineering Science* 48.19 (1993), pages 3335–3345.

[28] M. S. Kulkarni and M. P. Dudukovic. "A bidirectional fixed-bed reactor for coupling of exothermic and endothermic reactions." In: *AIChE Journal* 42.10 (1996), pages 2897–2910.

[29] M. Kulkarni and M. Dudukovic. "Periodic Operation of Asymmetric Bidirectional Fixed-Bed Reactors with Temperature Limitations." In: *Industrial & Engineering Chemistry Research* 37.3 (1998), pages 770–781.

[30] G. Kolios and G. Eigenberger. "Styrene synthesis in a reversed-flow reactor." In: *Chemical Engineering Science* 54 (1999), pages 2637–2646.

[31] M. van Sint Annaland. "A Novel Reverse flow Reactor Coupling Endothermic and Exothermic Reactions." PhD thesis. University Twente, 2000.

[32] B. Glöckler, G. Kolios, and G. Eigenberger. "Analysis of a novel reverse-flow reactor concept for autothermal methane steam reforming." In: *Chemical Engineering Science* 58 (2003), pages 593–601.

[33] G. Kolios, B. Glöckler, A. Gritsch, A. Morillo, and G. Eigenberger. "Heat-Integrated Reactor Concepts for Hydogen Production by Methane Steam Reforming." In: *Fuel Cells* 5.1 (2004), pages 52–64.

[34] B. Glöckler, G. Kolios, C. Tellaeche, and U. Nieken. "A Heat-Integrated Reverse-Flow Reactor Concept for Endothermic High-Temperature Syntheses. Part I: Fundamentals – Short-Cut Theory and Experimental Verification of a Traveling Endothermic Reaction Zone." In: *Chem. Eng. Technol.* 32.9 (2009), pages 1339–1347.

[35] H. Seiler and G. Emig. "Reduktions-Oxidations-Zyklen im Festbettreaktor mit periodischer Strömungsumkehr." In: *Chemie Ingenieur Technik* 70.11 (1998), pages 1397–1402.

[36] P. Heidebrecht, C. Hertel, and K. Sundmacher. "Conceptual analysis of a cyclic water gas shift reactor." In: *International Journal of Chemical Reactor Engineering* 6 (2008), A19.

[37] S. Noorman, M. van Sint Annaland, and J. Kuipers. "Experimental validation of packed bed chemical-looping combustion." In: *Chemical Engineering Science* 65.1 (2010), pages 92 –97.

[38] A. Zwijnenburg, A. Stankiewicz, and J. A. Moulijn. "Dynamic Operation of Chemical Reactors: Friend of Foe?" In: *Chemical Engineering Progress* (1998), pages 39–47.

[39] A. Renken. "Instationäre Prozessführung kontinuierlicher Reaktoren." In: *Chemie Ingenieur Technik* 54.6 (1982), pages 571–580.

[40] P. Silveston, R. R. Hudgins, and A. Renken. "Periodic operation of catalytic reactors – introduction and overview." In: *Catalysis Today* 25.2 (1995-08), pages 91–112.

[41] A. Markovic, A. Seidel-Morgenstern, and M. Petkovska. "Evaluation of the potential of periodically operated reactors based on the second order frequency response function." In: *Chemical Engineering Research and Design* 86.7 (2008-07), pages 682–691.

[42] W. Marquardt. "Wellenausbreitung in verfahrenstechnischen Prozessen." In: *Chemie Ingenieur Technik* 61.5 (1989), pages 362–377.

[43] C. Broughton and C. Gerhold. *US Patent 2985589*. Technical report. Universal Oil Products Company, Delaware, 1961.

[44] D. M. Ruthven. *Principles of adsorption and adsorption-processes*. John Wiley & Sohns, Inc., 1984.

[45] D. M. Ruthven and C. Ching. "Counter-current and simulated counter-current adsorption separation processes." In: *Chemical Engineering Science* 44.5 (1989), pages 1011–1038.

[46] G. Guiochon. "Preparative liquid chromatography." In: *Journal of Chromatography A* 965.1-2 (2002-08), pages 129–161.

[47] H.-K. Rhee, R. Aris, and N. R. Amundson. *First-Order Partial Differential Equations, Theory and Application of Single Equations*. Volume 1. Prentice-Hall, Englewood Cliffs, New Jersey, 1986.

[48] F. G. Helfferich and R. D. Whitley. "Non-linear waves in chromatography II. Wave interference and coherence in multicomponent systems." In: *Journal of Chromatography A* 734.1 (1996-05), pages 7–47.

[49] M. Mazzotti, G. Storti, and M. Morbidelli. "Optimal operation of simulated moving bed units for nonlinear chromatographic separations." In: *Journal of Chromatography A* 769.1 (1997-05), pages 3–24.

[50] S. Grüner, M. Mangold, and A. Kienle. "Dynamics of reaction separation processes in the limit of chemical equilibrium." In: *AIChE Journal* 52.3 (2006), pages 1010–1026.

[51] E. Wicke and D. Vortmeyer. "Zündzonen heterogener Reaktionen in gasdurchströmten Körnerschichten." In: *Bericht Bunsengesellschaft* 63 (1959), page 145.

[52] H.-K. Rhee, R. P. Lewis, and N. R. Amundson. "Creeping Profiles in Catalytic Fixed Bed Reactors. Continuous Models." In: *Ind. Eng. Chem. Fund.* 13.4 (1974), pages 317–323.

[53] O. V. Kiselev and Y. S. Matros. "Propagation of the combustion front of a gas mixture in a granular bed of catalyst." In: *Combustion, Explosion, and Shock Waves* 16.2 (1980-03), pages 152–157.

[54] V. Pinjala, Y. C. Chen, and D. Luss. "Wrong-way behavior of packed-bed reactors: II. Impact of thermal dispersion." In: *AIChE Journal* 34.10 (1988), pages 1663–1672.

[55] G. Lauschke and E. Dieter Gilles. “Circulating reaction zones in a packed-bed loop reactor.” In: *Chemical Engineering Science* 49.24, Part 2 (1994-12), pages 5359–5375.

[56] T. N. Haynes and H. S. Caram. “The simulated moving bed chemical reactor.” In: *Chemical Engineering Science* 49.24B (1994), pages 5465–5472.

[57] M. Brinkmann, A. A. Barresi, M. Vanni, and G. Baldi. “Unsteady state treatment of very lean waste gases in a network of catalytic burners.” In: *Catalysis Today* 47 (1999), pages 263–277.

[58] M. Sheintuch and O. Nekhamkina. “The Asymptotes of Loop Reactors.” In: *AIChE Journal* 51.1 (2005), pages 224–234.

[59] D. Fissore, A. A. Barresi, and D. Manca. “Modelling of methanol synthesis in a network of forced unsteady-state ring reactors by artificial neural networks for control purposes.” In: *Chemical Engineering Science* 59.19 (2004-10), pages 4033–4041.

[60] S. A. Velardi and A. A. Berresi. “Methanol synthesis in a forced unsteady-state reactor network.” In: *Chemical Engineering Science* 57 (2002), pages 2995–3004.

[61] S. Velardi, A. A. Barresi, D. Manca, and D. Fissore. “Complex dynamic behaviour of methanol synthesis in the ring reactor network.” In: *Chemical Engineering Journal* 99 (2004), pages 117–123.

[62] R. Sheinman and M. Sheintuch. “Loop Reactor Design and Control for Reversible Exothermic Reactions.” In: *Industrial & Engineering Chemistry Research* 48.11 (2009-06), pages 5185–5192.

[63] K. M. V. Bussche and G. Froment. “The STAR configuration for Methanol Synthesis in Reversed Flow Reactors.” In: *The Canadian Journal of Chemical Engineering* 74 (1996), pages 729–734.

[64] O. Levenspiel. *Chemical Reaction Engineering.* 3rd edition. John Wiley & Sohns, Inc., 1999.

[65] K. R. Westerterp, W. P. M. van Swaaij, and A. Beenackers. *Chemical Reactor Design and Operation.* 2nd edition. John Wiley & Sons, 1998.

[66] G. F. Froment and K. B. Bischoff. *Chemical reactor analysis and design.* John Wiley & Sohns, Inc., 1990.

[67] C. van Heerden. “Autothermic Processes.” In: *Industrial & Engineering Chemistry* 45.6 (1953-06), pages 1242–1247.

[68] J. Smoller. *Shock Waves and Reaction-Diffusion Equations.* Springer-Verlag New York, Inc., 1983.

[69] V. D. Sharma. *Quasilinear hyperbolic systems, compressible flows, and waves.* Taylor & Francis Group,LLC, 2010.

[70] D. A. Frank-Kamenetzki. *Stoff- und Wärmeübertragung in der chemischen Kinetik.* Übersetztung: J. Pawlowski. Springer-Verlag Berlin/Göttingen/Heidelberg, 1959.

[71] W. Kast. *Adsorption aus der Gasphase: ingenieurwissenschaftliche Grundlagen und technische Verfahren.* VCH Verlagsgesellschaft mbH, Weinheim, 1988.

[72] M. Mangold. “Nichtlineare Analyse und technische Nutzung zirkulierender Reaktionszonen.” PhD thesis. Universität Stuttgart, 2000.

[73] A. Burghardt, M. Berezowski, and E. W. Jacobsen. “Approximate characteristics of a moving temperature front in a fixed-bed catalytic reactor.” In: *Chemical Engineering and Processing* 38.1 (1999-01), pages 19–34.

[74] U. Nieken, G. Kolios, and G. Eigenberger. “Limiting Cases And Approximate Solutions For Fixed-Bed Reactors With Periodic-Flow Reversal.” In: *AIChE Journal* 41.8 (1995-08), pages 1915–1925.

[75] W. H. Press, S. A. Teukolsky, W. Vetterling, and B. Flannery. *Numerical Recipes in C: The Art of Scientific Computing*. Cambridge University Press, 1988.

[76] P. Deuflhard. *Newton Methods for nonlinear Problems*. Springer-Verlag Berlin Heidelberg, 2004.

[77] K. J. Beers. *Numerical Methods for Chemical Engineering Applications in MATLAB*. Cambridge University Press, 2007.

[78] N. Kubota. *Propellants and Explosives: Thermochemical Aspects of Combustion*. Wiley-VCH Verlag GmbH & Co. KGaA, Weinheim, 2002.

[79] J. Warnatz, U. Maas, and R. W. Dibble. *Combustion Physical and Chemical Fundamentals, Modeling and Simulation, Experiments, Pollutant Formation*. Springer-Verlag Berlin Heidelberg, 2006.

[80] S. McAllister, J.-Y. Chen, and A. C. Fernandez-Pello. *Fundamentals of Combustion Processes*. Springer Science + Business Media, LLC, 2011.

[81] F. Stoessel. *Thermal Safety of Chemical Processes Risk Assessment and Process Design*. Wiley-VCH Verlag GmbH & Co. KGaA, Weinheim, 2008.

[82] P. S. Mehta, W. N. Sams, and D. Luss. "Wrong-way behavior of packed-bed reactors: 1. The pseudo-homogeneous model." In: *AIChE Journal* 27.2 (1981), pages 234–246.

[83] Y. C. Chen and D. Luss. "Wrong-Way Behavior Of Packed-Bed Reactors - Influence Of Interphase Transport." In: *AIChE Journal* 35.7 (1989-07), pages 1148–1156.

[84] A. Ilin and D. Luss. "Wrong-Way Behavior Of Packed-Bed Reactors - Influence Of Reactant Adsorption On Support." In: *AIChE Journal* 38.10 (1992-10), pages 1609–1617.

[85] V. Yakhnin and M. Menzinger. "High-temperature transients in catalytic fixed-bed reactors." In: *Reviews of Chemical Engineering* 20.3-4 (2004), pages 175–224.

[86] M. Menzinger, V. Yakhnin, A. Jaree, P. L. Silveston, and R. R. Hudgins. "Dynamic responses of packed bed reactors." In: *Chemical Engineering Science* 59.19 (2004-10), pages 4011–4022.

[87] V. Z. Yakhnin and M. Menzinger. "Estimating spectral properties of the thermal instability in packed-bed reactors." In: *Chemical Engineering Science* 63.6 (2008-03), pages 1480–1489.

[88] J. Unger, G. Kolios, and G. Eigenberger. "On the efficient simulation and analysis of regenerative processes in cyclic operation." In: *Computers & Chemical Engineering* 21.Supplement 1 (1997-05), S167–S172.

[89] A. Gorbach, G. Eigenberger, and G. Kolios. "General Approach for the Reduction of Detailed Models for Fast Cycling Processes." In: *Industrial & Engineering Chemistry Research* 44.8 (2005-04), pages 2369–2381.

[90] S. Kolaczkowski. "Treatment of Volatile Organic Carbon (VOC) Emissions from Stationary Sources: Catalytic Oxidation of the Gaseous Phase." In: *Structured Catalysts and Reactors*. CRC Press Taylor & Francis Group, 2006.

[91] M. Petkovska. "Application of Nonlinear Frequency Response to Adsorption Systems with Complex Kinetic Mechanisms." In: *Adsorption* 11.0 (2005-07), pages 497–502.

[92] K. Kaczmarski and D. Antos. "Modified Rouchon and Rouchon-like algorithms for solving different models of multicomponent preparative chromatography." In: *Journal of Chromatography A* 756.1-2 (1996-12), pages 73–87.

[93] D. Beltscheva, P. Hugo, and A. Seidel-Morgenstern. "Linear two-step gradient counter-current chromatography: Analysis based on a recursive solution of an equilibrium stage model." In: *Journal of Chromatography A* 989.1 (2003-03), pages 31–45.

[94] M. Kaspereit, K. Gedicke, V. Zahn, A. W. Mahoney, and A. Seidel-Morgenstern. "Shortcut method for evaluation and design of a hybrid process for enantioseparations." In: *Journal of Chromatography A* 1092.1 (2005-10), pages 43–54.

[95] P. Sá Gomes, C. P. Leão, and A. E. Rodrigues. "Simulation of true moving bed adsorptive reactor: Detailed particle model and linear driving force approximations." In: *Chemical Engineering Science* 62.4 (2007-02), pages 1026–1041.

[96] M. Jakubith. *Grundoperationen und chemische Reaktionstechnik*. WILEY-VCH Verlag Weinheim, 1998.

[97] G. Guiochon, A. Felinger, D. G. Shirazi, and A. M. Katti. *Fundamentals of Preparative and Nonlinear Chromatography*. 2nd edition. Elsevier Inc., 2006.

[98] T. Arens, F. Hettlich, C. Karpfinger, U. Kockelkorn, K. Lichtenegger, and H. Stachel. *Mathematik*. Spektrum Akademischer Verlag Heidelberg, 2008.

[99] A. Seidel-Morgenstern. "Analysis of boundary conditions in the axial dispersion model by application of numerical laplace inversion." In: *Chemical Engineering Science* 46.10 (1991), pages 2567–2571.

[100] P. V. Danckwerts. "Continuous Flow Systems - Distribution Of Residence Times." In: *Chemical Engineering Science* 2.1 (1953), pages 1–13.

[101] J. F. Wehner and R. H. Wilhelm. "Boundary Conditions Of Flow Reactor." In: *Chemical Engineering Science* 6.2 (1956), pages 89–93.

[102] V. M. Zahn, M. Mangold, and A. Seidel-Morgenstern. "Autothermal operation of an adiabatic simulated counter current reactor." In: *Chemical Engineering Science* 65.1 (2010-01), pages 458–465.

[103] E. Dorfi and L. Drury. "Simple adaptive grids for 1 - D initial value problems." In: *Journal of Computational Physics* 69.1 (1987-03), pages 175–195.

[104] B. Koren. *A robust upwind discretisation method for advection, diffusion and source terms*. Technical report. Department of numerical Mathematics, CWI Amsterdam, The Netherlands, 1993.

[105] R. J. Leveque. *Finite Volume Methods for Hyperbolic Problems*. Cambridge University Press, 2004.

[106] I. R. Epstein and J. A. Pojman. *An Introduction to Nonlinear Chemical Dynamics, Oscillations, Waves, Patterns, and Chaos*. Edited by D. G. Truhlar. Oxford University Press, 1998.

[107] G. Ertl. "Non-Linear Dynamics: Oscillatory Kinetics and Spatio-Temporal Pattern Formation." In: *Handbook of Heterogeneous Catalysis*. Edited by G. Ertl, H. Knözinger, F. Schüth, and J. Weitkamp. Weinheim-VCH, 2008. Chapter 11.5, pages 2394–2411.

[108] M. Sheintuch and O. Nekhamkina. "Pattern formation in models of fixed-bed reactors." In: *Catalysis Today* 70.4 (2001-11), pages 369–382.

[109] D. Luss and M. Sheintuch. "Spatiotemporal patterns in catalytic systems." In: *Catalysis Today* 105.2 (2005-07), pages 254–274.

[110] O. Bilous and N. R. Amundson. "Chemical reactor stability and sensitivity." In: *AIChE Journal* 1.4 (1955), pages 513–521.

[111] G. Padberg and E. Wicke. "Stabiles und instabiles Verhalten eines adiabatischen Rohrreaktors am Beispiel der katalytischen CO-Oxidation." In: *Chemical Engineering Science* 22 (1967), pages 1035–1051.

[112] A. Uppal, W. H. Ray, and A. B. Poore. "Dynamic Behavior Of Continuous Stirred Tank Reactors." In: *Chemical Engineering Science* 29.4 (1974), pages 967–985.

[113] R. A. Schmitz. "Multiplicity, Stability, and Sensitivity of States in Chemically Reacting Systems – A Review." In: *Advances in Chemistry*. Volume 148. American Chemical Society, 1975-06, pages 156–211.

[114] E. D. Gilles, G. Eigenberger, and W. Ruppel. "Relaxation oscillations in chemical reactors." In: *AIChE Journal* 24.5 (1978), pages 912–920.

[115] S. Subramanian and V. Balakotaiah. "Classification of steady-state and dynamic behavior of distributed reactor models." In: *Chemical Engineering Science* 51.3 (1996-02), pages 401–421.

[116] M. Baldea and P. Daoutidis. "Dynamics and control of autothermal reactors for the production of hydrogen." In: *Chemical Engineering Science* 62.12 (2007-06), pages 3218–3230.

[117] V. Gehrke and W. Marquardt. "A singularity theory approach to the study of reactive distillation." In: *Computers & Chemical Engineering* 21.Supplement 1 (1997-05), S1001–S1006.

[118] W. Seider, D. Brengel, A. M. Provost, and S. Widagdo. "Nonlinear Analysis in Process Design. Why Overdesign To Avoid Complex Nonlinearities?" In: *Ind. Eng. Chem. Res.* 29 (1990), pages 805–818.

[119] W. Marquardt and M. Mönnigmann. "Constructive nonlinear dynamics in process systems engineering." In: *Computers & Chemical Engineering* 29.6 (2005-05), pages 1265–1275.

[120] J. Hahn, M. Mönnigmann, and W. Marquardt. "On the use of bifurcation analysis for robust controller tuning for nonlinear systems." In: *Journal of Process Control* 18.3-4 (2008-03), pages 408–420.

[121] D. D. Bruns and J. E. Bailey. "Nonlinear Feedback-Control For Operating A Nonisothermal CSTR Near An Unstable Steady-State." In: *Chemical Engineering Science* 32.3 (1977), pages 257–264.

[122] A. G. Salinger and G. Eigenberger. "The direct calculation of periodic states of the reverse flow reactor – II. Multiplicity and instability." In: *Chemical Engineering Science* 51.21 (1996-11), pages 4915–4922.

[123] J. Khinast and D. Luss. "Mapping Regions with different bifurcation diagrams of a reverse-flow reactor." In: *AIChE Journal* 43.8 (1997), pages 2034–2046.

[124] P. Altimari, P. Maffettone, S. Crecitelli, L. Russo, and E. Mancusi. "Nonlinear Dynamics of a VOC combustion loop reactor." In: *AIChE Journal* 52.8 (2006), pages 2812–2822.

[125] G. Continillo, A. Grabski, E. Mancusi, and L. Russo. "Bifurcation analysis of a periodically forced pair of tubular catalytic combustors." In: *Combustion Theory and Modelling* 10.6 (2006), pages 1023–1035.

[126] L. Russo, P. Altimari, E. Mancusi, P. L. Maffettone, and S. Crescitelli. "Complex dynamics and spatio-temporal patterns in a network of three distributed chemical reactors with periodical feed switching." In: *Chaos Solitons & Fractals* 28.3 (2006-05), pages 682–706.

[127] E. Mancusi, L. Russo, P. Altimari, P. Maffettone, and S. Crescitelli. "Effect of the Switch Strategy on the Stability of Reactor Networks." In: *Industrial & Engineering Chemistry Research* 46.20 (2007-09), pages 6510–6521.

[128] O. Nekhamkina and M. Sheintuch. "Structure of operating domains of loop reactors." In: *AIChE Journal* 54.5 (2008), pages 1292–1302.

[129] R. C. Hilborn. *Chaos and Nonlinear Dynamics: An Introduction for Scientists and Engineers*. Oxford University Press, USA, 2001.

[130] R. Aris. *Mathematical Modeling - A Chemical Engineer's Perspective*. Volume 1. Academic Press, 1999.

[131] E. N. Lorenz. *Predictability: Does the Flap of a Butterfly's Wings in Brazil Set Off a Tornado in Texas?* Talk presented Dec. 29, AAAS Section on Environmental Sciences, New Approaches to Global Weather: GARP. Sheraton Park Plaza Hotel, Boston, Mass. 1972.

[132] R. Thom. *Structural Stability and Morphogenesis: An Outline of a General Theory of Models*. W. A. Benjamin Advanced Bk Program, 1977.

[133] V. I. Arnold. *Geometrical methods in the theory of ordinary differential equations*. Springer-Verlag, New York, 1983.

[134] M. Golubitsky and D. G. Schaeffer. "Singularities and Groups in Bifurcation Theory." In: *Applied Mathematical Sciences 51*. Edited by F. John, J. E. Marsden, and L. Sirovich. Volume I. Springer-Verlag New York, 1985.

[135] Y. A. Kuznetsov. *Elements of applied bifurcation theory*. Edited by I. Karatzas and M. Yor. 2nd edition. Springer Verlag New-York, 1998.

[136] R. Seydel. "Practical Bifurcation and Stability Analysis." In: *Interdisciplinary Applied Mathematics*. Edited by S. S. Antman, J. E. Marsden, and L. Sirovich. Volume 5. Springer Science + Business Media, LLC, 2010.

[137] M. Marek and I. Schreiber. *Chaotic Behaviour of Deterministic Dissipative Systems*. Cambridge University Press, 1995.

[138] P. Plaschko and K. Brod. *Nichtlineare Dynamik, Bifurkation und Chaotische Systeme*. Vieweg, Braunschweig/Wiesbaden, 1995.

[139] B. Marx and W. Vogt. *Dynamische Systeme - Theorie und Numerik*. Spektrum Akademischer Verlag Heidelberg, 2011.

[140] X. Hua, M. Mangold, A. Kienle, and E. D. Gilles. "State profile estimation of an autothermal periodic fixed-bed reactor." In: *Chemical Engineering Science* 53.1 (1998-01), pages 47–58.

[141] M. Krasnyk, K. Bondareva, O. Milokhov, K. Teplinskiy, M. Ginkel, and A. Kienle. "The ProMoT/Diana simulation environment." In: *Proceedings of the 16th European symposium on computer aided process engineering and ninth international symposium on process systems engineering*. 2006, pages 445–450.

[142] M. Krasnyk. "DIANA – An object-oriented tool for nonlinear analysis of chemical processes." PhD thesis. Otto-von-Guericke Universität Magdeburg, 2008.

[143] V. I. Arnold. "On matrices depending on parameters." In: *Russian Mathematical Surveys* 26.2 (1971), page 29.

[144] R. Ball. "Understanding critical behaviour through visualization: A walk around the pitchfork." In: *Computer Physics Communications* 142.1-3 (2001-12), pages 71–75.

[145] R. Gilmore. *Catastrophe Theory for Scientists and Engineers*. Dover Publications, Inc. New York, 1981.

[146] V. M. Zahn, M. Mangold, M. Krasnyk, and A. Seidel-Morgenstern. "Theoretical Analysis of Heat Integration in a Periodically Operated Cascade of Catalytic Fixed-Bed Reactors." In: *Chemical Engineering & Technology* 32.9 (2009), pages 1326–1338.

[147] L. Russo, E. Mancusi, P. L. Maffettone, and S. Crescitelli. "Symmetry properties and bifurcation analysis of a class of periodically forced chemical reactors." In: *Chemical Engineering Science* 57.24 (2002-12), pages 5065–5082.

[148] J. Khinast, A. Gurumoorthy, and D. Luss. "Complex Dynamic features of a cooled reverse-flow reactor." In: *AIChE Journal* 44.5 (1998), pages 1128–1140.

[149] J. M. van de Graaf, M. Zwiep, F. Kapteijn, and J. A. Moulijn. "Application of a silicate-1 membrane reactor in metathesis reactions." In: *Applied Catalysis A-General* 178 (1999), pages 225–241.

[150] A. A. Barresi, M. Vanni, M. Brinkmann, and G. Baldi. "Control of an autothermal network of nonstationary catalytic reactors." In: *AIChE Journal* 45.7 (1999), pages 1597–1602.

[151] D. Fissore, R. Pisano, and A. A. Barresi. "Observer design for the Selective Catalytic Reduction of NOx in a loop reactor." In: *Chemical Engineering Journal* 128.2-3 (2007-04), pages 181–189.

[152] Y. Smagina and M. Sheintuch. "Control of rotating pulses in a loop reactor." In: *Journal Of Process Control* 19.6 (2009-06), pages 954–963.

[153] E. Mancusi, P. Altimari, S. Crescitelli, and L. Russo. "Temperature and conversion patterns in a network of catalytic reactors for methanol synthesis with different switch strategies." In: *Chemical Engineering Science* 65.16 (2010-08), pages 4579–4590.

[154] G. Ertl, H. Knözinger, and J. Weitkamp, editors. *Environmental Catalysis*. Wiley-VCH Verlag GmbH, Weinheim, 1999.

[155] *Council directive: On the limitation of emissions of volatile organic compounds due to the use of organic solvents in certain activities and installations*. European Comission. 1999-03.

[156] K. Everaert and J. Baeyens. "Catalytic combustion of volatile organic compounds." In: *Journal of Hazardous Materials* 109.1-3 (2004-06), pages 113–139.

[157] L. K. Wang, N. C. Pereira, and Y.-T. Hung, editors. *Air pollution control engineering*. Humana Press Inc. New Jersey, 2004.

[158] G. Ertl, H. Knözinger, F. Schüth, and J. Weitkamp, editors. *Handbook of Heterogeneous Catalysis*. Wiley-VCH, Weinheim, 2008.

[159] J. Berty. "Experiments in Catalystic Reaction Engineering." In: *Studies in surface science and catalysis*. Elsevier Science B.V., 1999.

[160] C. Hamel. "Experimentelle und modellbasierte Studien zur Herstellung kurzkettiger Alkene sowie von Synthesegas unter Verwendung poröser und dichter Membranen." PhD thesis. Otto-von-Guericke-Universität Magdeburg, 2008.

[161] C. Göcke. *Ermittlung der Reaktionskinetik der Totaloxidation von Propen und Ethen an einem CuCrO-Katalysator*. student research project. Otto-von-Guericke-Universität Magdeburg, 2011.

[162] J. J. Spivey. "Solid Catalyst for the Oxidation of Volatile Organic Compounds." In: *Handbook of Heterogeneous Catalysis*. Edited by G. Ertl, H. Knözinger, F. Schüth, and J. Weitkamp. Weinheim-VCH, 2008. Chapter 11.5, pages 2394–2411.

[163] P. Mars and D. V. Krevelen. "Oxidations carried out by means of vanadium oxide catalysts." In: *Chemical Engineering Science, Special Suppl.* 3 (1954).

[164] C. Doornkamp and V. Ponec. "The universal character of the Mars and Van Krevelen mechanism." In: *Journal of Molecular Catalysis A: Chemical* 162.1-2 (2000-11), pages 19–32.

[165] J. Hagen. *Industrial Catalysis*. WILEY-VCH Weinheim, 2006.

[166] S. H. Taylor, C. S. Heneghan, G. J. Hutchings, and I. D. Hudson. "The activity and mechanism of uranium oxide catalysts for the oxidative destruction of volatile organic compounds." In: *Catalysis Today* 59.3-4 (2000-06), pages 249–259.

[167] S. Ordonez, L. Bello, H. Sastre, R. Rosal, and F. V. Diez. "Kinetics of the deep oxidation of benzene, toluene, n-hexane and their binary mixtures over a platinum on gamma-alumina catalyst." In: *Applied Catalysis B-Environmental* 38.2 (2002-08), pages 139–149.

[168] W. Li, J. Wang, and H. Gong. "Catalytic combustion of VOCs on non-noble metal catalysts." In: *Catalysis Today* 148.1-2 (2009-10), pages 81–87.

[169] S. Utsumi, F. E. Vallejos-Burgos, C. M. Campos, X. García, A. L. Gordon, G. Pecchi, and L. R. Radovic. "Preparation and characterization of inexpensive heterogeneous catalysts for air pollution control: Two case studies." In: *Catalysis Today* 123.1-4 (2007-05), pages 208–217.

[170] D. Delimaris and T. Ioannides. "VOC oxidation over CuO-CeO2 catalysts prepared by a combustion method." In: *Applied Catalysis B: Environmental* 89.1-2 (2009-07), pages 295–302.

[171] J. I. Gutiérrez-Ortiz, B. de Rivas, R. López-Fonseca, and J. R. González-Velasco. "Catalytic purification of waste gases containing VOC mixtures with Ce/Zr solid solutions." In: *Applied Catalysis B: Environmental* 65.3-4 (2006-06), pages 191–200.

[172] S. C. Kim and W. G. Shim. "Catalytic combustion of VOCs over a series of manganese oxide catalysts." In: *Applied Catalysis B: Environmental* 98.3-4 (2010-08), pages 180–185.

[173] C. Cellier, V. Ruaux, C. Lahousse, P. Grange, and E. M. Gaigneaux. "Extent of the participation of lattice oxygen from gamma-MnO2 in VOCs total oxidation: Influence of the VOCs nature." In: *Catalysis Today* 117.1-3 (2006-09), pages 350–355.

[174] V. Santos, M. Pereira, J. Órfão, and J. Figueiredo. "The role of lattice oxygen on the activity of manganese oxides towards the oxidation of volatile organic compounds." In: *Applied Catalysis B: Environmental* 99.1-2 (2010-08), pages 353–363.

[175] A. A. Barresi and G. Baldi. "Deep Catalytic Oxidation of Aromatic Hydrocarbon Mixtures: Reciprocal Inhibition Effects and Kinetics." In: *Industrial & Engineering Chemistry Research* 33.12 (1994-12), pages 2964–2974.

[176] L. van de Beld, M. van der Ven, and K. Westerterp. "A kinetic study of the complete oxidation of ethene, propane and their mixtures on a Pd/Al2O3 catalyst." In: *Chemical Engineering and Processing* 34.5 (1995-10), pages 469–478.

[177] R. H. Harris, V. J. Boyd, G. J. Hutchings, and S. H. Taylor. "Water as a Promoter of the Complete Oxidation of Volatile Organic Compounds over Uranium Oxide Catalysts." In: *Catalysis Letters* 78 (1 2002). 10.1023/A:1014916920128, pages 369–372.

[178] S. H. Taylor. "Heterogeneous Catalysis by Uranium Oxides." In: *Metal Oxide Catalysis*. Edited by S. Jackson and J. S. J. Hargreaves. Wiley-VCH Verlag Gmbh & Co. KGaA, Weinheim, 2009.

[179] J. B. Butt. *Reaction Kinetics and Reactor Design*. Marcel Dekker, Inc., 2000.

[180] N. Emberger. "Zur Reaktionskinetik der Selektivoxidation von n-Butan an einem technischen $(VO)_2P_2O_7$-Katalysator." PhD thesis. Otto-von-Guericke-Universität Magdeburg, 2005.

[181] VDI. *VDI Wärmeatlas*. Springer-Verlag Berlin Heidelberg, 2006.

[182] R. Mezaki and J. R. Kittrell. "Parametric Sensitivity In Fitting Nonlinear Kinetic Models." In: *Industrial And Engineering Chemistry* 59.5 (1967), pages 63–&.

[183] M. Joshi. "Statistical Analysis of Models and Parameters in Chemical and Biochemical Reaction Networks." PhD thesis. Otto-von-Guericke-Universität Magdeburg, 2007.

[184] T. F. Edgar, D. M. Himmelblau, and L. S. Ladson. *Optimization of chemical processes, second edition*. Mc Graw Hill, 2001.

[185] J. Nocedal and S. J. Wright. *Numerical Optimization, second edition*. Springer, 2006.

[186] M. Papageorgiou. *Optimierung, Statische, dynamische, stochastische Verfahren für die Anwendung.* Oldenbourg Verlag GmbH, München, 1996.

[187] J. R. R. A. Martins, P. Sturdza, and J. Alonso. "The Complex-Step Derivative Approximation." In: *ACM Transactions on Mathematical Software* 29.3 (2003), pages 245–262.

[188] M. S. Ridout. "Statistical Applications of the Complex-Step Method of Numerical Differentiation." In: *The American Statistician* 63.1 (2009-02), pages 66–74.

[189] L. Shampine. "Accurate Numerical Derivatives in MATLAB." In: *ACM Transactions on Mathematical Software* 33.4 (2007), pages 1–17.

[190] S. Körkel. "Numerische Methoden für Optimale Versuchsplanungprobleme bei nichtlinearen DAE-Modellen." PhD thesis. Ruprecht-Karls Universität Heidelberg, 2002.

[191] A. de Klerk. "Adiabatic Laboratory Reactor Design and Verification." In: *Industrial & Engineering Chemistry Research* 44.25 (2005), pages 9440–9445.

[192] D. Fissore, A. A. Barresi, G. Baldi, M. A. G. Hevia, S. Ordóñez, and F. V. Díez. "Design and testing of small-scale unsteady-state afterburners and reactors." In: *AIChE Journal* 51.6 (2005), pages 1654–1664.

[193] M. A. G. Hevia, S. Ordóñez, and F. V. Díez. "Effect of wall properties on the behavior of bench-scale reverse flow reactors." In: *AIChE Journal* 52.9 (2006), pages 3203–3209.

[194] M. Winterberg and E. Tsotsas. "Impact of tube-to-particle-diameter ratio on pressure drop in packed beds." In: *AIChE Journal* 46.5 (2000), pages 1084–1088.

[195] T. Grewer. "Thermische Stabilität von Reaktionsgemischen." In: *Chemie Ingenieur Technik* 47.6 (1975), pages 230–236.

[196] J. Steinbach. *Safety Assessment for Chemical Processes.* Wiley-VCH Verlag GmbH & Co. KGaA, Weinheim, 1999.

[197] B. A. Finlayson. *Numerical Methods for Problems with Moving Fronts.* Ravenna Park Publishing, 1992.

[198] J. W. Thomas. "Numerical Partial Differential Equations: Finite Difference Methods." In: *Texts in Applied Mathematics.* Edited by J. E. Marsden, L. Sirovich, M. Golubitsky, and W. Jäger. 22. Springer-Verlag New York, 1995.

[199] J. H. Ferzinger and M. Perić. *Numerische Strömungsmechanik.* Springer-Verlag Berlin Heidelberg, 2008.

[200] S. Larsson and V. Thomée. "Partial Differential Equations with Numerical Methods." In: *Texts in Applied Mathematics.* Edited by J. E. Marsden, L. sirovich, and S. Antman. 45. Springer-Verlag Berlin Heidelberg, 2009.

[201] A. Vande Wouwer, P. Saucez, and W. E. Schiesser, editors. *Adaptive Methods of Lines.* Chapman & Hall/CRC, 2001.

[202] U. Nowak. *Adaptive Linienmethoden für nichtlineare parabolische Systeme in einer Raumdimension.* Technical report. Konrad Zuse Institut Berlin, 1993.

[203] J. Frauhammer, H. Klein, G. Eigenberger, and U. Nowak. "Solving moving boundary problems with an adaptive moving grid method: Rotary heat exchangers with condensation and evaporation." In: *Chemical Engineering Science* 53.19 (1998-10), pages 3393–3411.

[204] A. Salden. "Adsorption/Incineration Processes for Waste Gas Purification." Logos Verlag Berlin 2002 ISBN 3-89722-841-6. Institut für Chemische Verfahrenstechnik, Universität Stuttgart, 2001.

[205] K. E. Brenan, S. L. Campbell, and L. R. Petzold. *Numerical Solution of Initial-Value Problems in Differential-Algebraic Equations.* Society for Industrial and Applied Mathematics (SIAM), 1996.

[206] M. Caracotsios and W. E. Stewart. "Sensitivity analysis of initial-value problems with mixed ODEs and algebraic equations." In: *Comput. Chem. Eng.* 9.4 (1985), pages 359–365.

[207] D. T. Croft and M. D. LeVan. "Periodic states of adsorption cycles–I. Direct determination and stability." In: *Chemical Engineering Science* 49.11 (1994-06), pages 1821–1829.

[208] T. L. van Noorden, S. M. V. Lunel, and A. Bliek. "Acceleration of the determination of periodic states of cyclically operated reactors and separators." In: *Chemical Engineering Science* 57 (2002), pages 1041–1055.

[209] Y. Ding and M. D. LeVan. "Periodic states of adsorption cycles III. Convergence acceleration for direct determination." In: *Chemical Engineering Science* 56.17 (2001-09), pages 5217–5230.

[210] B. A. van de Rotten, S. M. Verduyn Lunel, and A. Bliek. "Efficient simulation of periodically forced reactors with radial gradients." In: *Chemical Engineering Science* 61.21 (2006-11), pages 6981–6994.

[211] K. Lust, D. Roose, A. Spence, and A. R. Champneys. "An Adaptive Newton-Picard Algorithm with Subspace Iteration for Computing Periodic Solutions." In: *SIAM Journal on Scientific Computing* 19.4 (1998), pages 1188–.

[212] T. L. van Noorden, S. M. V. Lunel, and A. Bliek. "The efficient computation of periodic states of cyclically operated chemical prozesses [noorden 2003]." In: *IMA Journal of Applied Mathematics* 68 (2003), pages 149–166.

[213] A. G. Salinger and G. Eigenberger. "The direct calculation of periodic states of the reverse flow reactor – I: methodology and propane combustion results." In: *Chemical Engineering Science* 51.21 (1996), pages 4903–4913.

[214] Y. Kawajiri and L. T. Biegler. "Optimization strategies for simulated moving bed and PowerFeed processes." In: *AIChE J.* 52.4 (2006), pages 1343–1350.

[215] R. David and H. Alla. "On hybrid Petri nets." In: *Discrete Event Dynamic Systems-Theory And Applications* 11.1-2 (2001-01), pages 9–40.

[216] J. Lunze and F. Lamnabhi-Lagarrigue, editors. *Handbook of Hybrid System Control – Theory, Tools, Applications.* Cambridge University Press, 2009.

[217] R. Köhler. *Beschreibung Code-Generator 2.0 zur Erzeugung von DIVA-Grundelementen.* Institut für Systemdynamik und Regelungstechnik. Stuttgart, 2000.

[218] D. Vortmeyer and E. Haidegger. "Discrimination of 3 approaches to evaluate heat fluxes for wall-cooled fixed-bed chemical reactors." In: *Chemical Engineering Science* 46.10 (1991), pages 2651–2660.

[219] F. Tränkle, M. Zeitz, M. Ginkel, and E. D. Gilles. "PROMOT: A Modeling Tool for Chemical Processes." In: *Mathematical and Computer Modelling of Dynamical Systems* 6 (2000), pages 283–307.

[220] VDI-GVC. *VDI-Wärmeatlas.* Springer Berlin-Heidelberg, 2006.

[221] F. Pascal and F. W. Jones. "Numerical calculations of the thermal conductivities of composites: a 2-D model." In: *Geophysical Journal International* 118.3 (1994), pages 623–635.

[222] D Vortmeyer and R. J. Schaeffer. "Equivalence of One-phase and 2-phase Models For Heat-transfer Processes In Packed-beds - One-dimensional Theory." In: *Chemical Engineering Science* 29.2 (1974), pages 485–491.

[223] E.-U. Schlünder and E. Tsotsas. *Wärmeübertragung in Festbetten, durchmischten Schüttgütern und Wirbelschichten.* Georg Thieme Verlag, 1988.

[224] R. Taylor and R. Krishna. *Multicomponent mass transfer.* John Wiley & Sohns, Inc., 1993.

[225] M. Winterberg, E. Tsotsas, A. Krischke, and D. Vortmeyer. "A simple and coherent set of coefficients for modelling of heat and mass transport with and without chemical reaction in tubes filled with spheres." In: *Chemical Engineering Science* 55.5 (2000-03), pages 967–979.

[226] H. Martin and M. Nilles. "Radiale Wärmeleitung in durchströmten Schüttungsrohren - eine vergleichende Übersicht neuer experimenteller Befunde." In: *Chemie Ingenieur Technik* 64.9 (1992), page 813.

[227] S. Yagi and D. Kunii. "Studies on heat transfer near wall surface in packed beds." In: *AIChE Journal* 6.1 (1960), pages 97–104.

[228] C.-H. Li and B. Finlayson. "Heat transfer in packed beds–a reevaluation." In: *Chemical Engineering Science* 32.9 (1977), pages 1055–1066.

[229] O. Bey and G. Eigenberger. "Gas flow and heat transfer through catalyst filled tubes." In: *International Journal of Thermal Sciences* 40.2 (2001-02), pages 152–164.

[230] D. Wen and Y. Ding. "Heat transfer of gas flow through a packed bed." In: *Chemical Engineering Science* 61.11 (2006-06), pages 3532–3542.

[231] A. P. De Wasch and G. F. Froment. "Heat-transfer In Packed-beds." In: *Chemical Engineering Science* 27.3 (1972), pages 567–576.

Nomenclature

Latin Symbols

A_q	cross section	m^2
a_V	specific surface	m^2/m^3
B_0	thermal reaction number	
c	concentration	mol/m^3
c_p	constant pressure heat capacity	J/kg K
D	diameter	m^2/s
D	mass dispersion	m^2/s
d_f	degrees of freedom	
ΔH_R	reaction enthalpy	J/mol
ΔT_{ad}	adiabatic temperature rise	K
E_a	activation energy	J/mol
$\boldsymbol{f}$	function vector	
F	phase ratio	
f	function or observed model variable	
f_D	differential equation	
f_n	difference equation	
$\boldsymbol{g}$	vector of algebraic functions	
G	function (family)	
g	reduced function	
H	hysteresis variety	
h_w	wall heat transfer coefficient	W/m^2K
I_c	isola center	
k	reaction rate constant	
k_0	pre-exponential factor	
L	length	m
Le_1	Lewis-number	
Le_2	Lewis-number	
LP	limit point	
LPC	limit point curve	
$\dot{M}$	mass flow rate	g/s
$\dot{m}$	mass flow density	g/sm^2
m	mass	kg
m	position index of the SMBR	
$\widetilde{M}$	molar mass	g/mol
N	number of stages	

n	mole number	mol
n	reaction order	
N_c	number of components	
N_m	minimum number of nodes	
N_p	number of nodes	
N_{par}	number of parameters	
N_R	number of reactions	
$\boldsymbol{p}$	vector of parameters	
P	pitchfork bifurcation	
P	poincaré map	
p	parameter of Petri net	
p	perturbation term	
p	pressure	N/m^2
p_e	parameter Petri net	
Pe_h	peclet number for heat transport	
Pe_hs	peclet number with respect to the solid phase	
Pe_n	numerical Peclet number	
Pe_ns	numerical Peclet number with respect to the solid phase	
Q	heat	J
$\dot{Q}$	heat flow	J/s
$\dot{q}$	heat flux	W/m^2
R	radius	m
r	reaction rate	
R^2	regression coefficient	
R_c^2	corrected regression coefficient	
R_g	universal gas constant	J/molK
s_i	place of a Petri net	
S_b	simple bifurcation	
T	temperature	°C, K
t	time	s
t_i	transition of a Petri net	
x_e	state of Petri net	
t_sw	switching time of SMBR	s
$\boldsymbol{u}$	vector of inputs	
U	perimeter	m
u	velocity	m/s
u_R	velocity of reaction front	m/s
u_T	velocity of thermal front	m/s
$\dot{V}$	flow rate	m^3/s
V	volume	m^3
w	mass fraction	
$\boldsymbol{x}$	state vector	
X	conversion	
y	variable	

z	spatial coordinate	m

Greek Symbols

α	fraction	
α	bifurcation parameter	
β	mass transfer coefficient	m^2/s
∇	gradient operator	
Δ	difference operator	
Δz	space increment	
Δz_m	maximum space increment	
ε	void fraction	
ε_m	machine precision	
γ	reduced switching time or flow rate ratio	
κ	condition number	
λ	heat conduction	W/mK
λ	characteristic bifurcation parameter	
λ	eigenvalue	
λ^{mod}	modified heat conduction	W/mK
λ_n	numerical heat conduction	W/mK
λ_s	simulated heat conduction	W/mK
ν	stoichiometric matrix/ scalar	
ω	parameter sensitivity	
φ	temperature difference	K
φ	transfer function	
ρ	density	kg/m^3
Σ	poincaré section	
σ^2	variance	
σ	kinetic selectivity	
τ	residence time	s
$\hat{\boldsymbol{\theta}}$	vector of estimated parameters	
Θ_n	truncation error of the dispersive model	
Θ_{ns}	truncation error of the countercurrent model	
$\boldsymbol{\theta}$	parameter vector	
ξ	extent of reaction	mol
ζ	transformed axial coordinate	

Subscripts

acc	accumulated
ax	axial
b	bulk property
bed	bed property
cyc	cycle
eff	effective
g	gas phase

h	valve	
i	index	
ig	ignition	
j	index	
K	catalyst	
L	air	
M	jacket	
m	index	
m	mean value	
m	molecular	
n	index	
obs	observation	
p	particle	
r	radial	
R	reaction, reactor	
ref	reference	
s	solid or catalyst phase	
Seg	segment	
sp	set-point	
tot	total	
u	ambient	
w	reactor wall	

Superscripts

0	zeroth order	
A	area	
abs	absolute value	
i	interstitial	
init	initial value	
in	input	
k	index	
out	output	
rel	relative value	
V	volume	

Abbreviations

AF	amplification factor	
BC	boundary condition	
DMR	distance to maximum rate	m
DNR	distance of no return	m
$\boldsymbol{FIM}$	fisher information matrix	
IC	initial condition	
SMBR	simulated moving bed reactor	
SSR	sum of squares of residuals	

SST	total sum of squares	
TMBR	true moving bed reactor	
TMR	time to maximum rate	s
TNR	time of no return	s

A. Explosion Theory Revisited for the Estimation of Ignition Temperatures in Fixed-Bed Reactors

A.1. The conventional explosion theory

The conventional explosion theory was developed by Semenov in 1928 and it is predominately used to assess safe process conditions of cooled batch reactors [79–81, 195] suggesting the well known Semenov-diagram. The idea assumes a uniform temperature in the reactor vessel and a heat flow across the jacket. Critical conditions can be identified for the cooling capacity to maintain a stable reactor temperature. Violation can lead to unrecoverable reactor runaway due to an unstable solution of the energy balance of the reactor.

The theory of Frank-Kamenetskii added further important ideas, which deals with spatially distributed systems and provides critical conditions used e.g. for the assessment of save storage conditions for chemicals. In his work he also introduced a convenient linearization of the Arrhenius equation [70, 81] considered also below.

Today, the so called time to maximum rate and the time of no return are numbers for a safety assessment [81]. In this work, analogies of these number to fixed-bed reactors are investigated, which lead to a new approach for the estimation of ignition temperatures. In contrast to the isothermal approach based on a zeroth order reaction discussed in section 2.2.1), this new non-isothermal approach also accounts for the inlet concentration.

A.1.1. Non-Isothermal Reactor Balance

As a starting point the energy balance of a batch reactor for a zeroth order reaction is considered, which reads:

$$V_R \rho c_p \frac{\mathrm{d}T}{\mathrm{d}t} = V_R(-\Delta H_R) k_0^{(0)} \exp\left(-\frac{E_a}{RT}\right) \qquad IC: T(t=0) = T^{\text{init}} \tag{A.1}$$

In equation (A.1), again $k_0^{(0)}$ is the rate constant of a zeros order reaction and V_R a constant reactor volume. After introducing the initial concentration, c^{init}, as an adiabatic temperature rise, a first order pre-exponential factor, k_0, equation (A.1) becomes (recall eq. 2.37):

$$\frac{\mathrm{d}T}{\mathrm{d}t} = \Delta T_{\text{ad}} k_0 \exp\left(-\frac{E_a}{RT}\right) \tag{A.2}$$

The product $\Delta T_{\mathrm{ad}} k_0$ can also be regarded as a heat release rate. Separation of variables and rearrangement of (A.2) gives:

$$\mathrm{d}t = \frac{1}{\Delta T_{\mathrm{ad}} k_0 \exp\left(-\frac{E_a}{\mathrm{R_g} T}\right)} \mathrm{d}T = \frac{1}{\Delta T_{\mathrm{ad}} k_0} \exp\left(\frac{E_a}{\mathrm{R_g} T}\right) \mathrm{d}T \tag{A.3}$$

The analysis of critical time intervals, t^*, is thus concerned with the solution of the following integral equation:

$$t^* = \frac{1}{\Delta T_{\mathrm{ad}} k_0} \int_{T_0}^{T^*} \exp\left(\frac{E_a}{\mathrm{R_g} T}\right) \mathrm{d}T \tag{A.4}$$

In this form two problems need to be considered. First, the integral of the exponential term and second, the specification of an upper integration limit, T^*. Note that in equation (A.4) the lower integration limit is regarded as a reference temperature T_0, which is either the initial temperature of a batch reactor or later the inlet temperature of a fixed-bed reactor.

A.1.2. Transformation of the Arrhenius Exponential

A common approach for a transformation of the Arrhenius equation is based on the expansion of exponential term according to:

$$k_0 \exp\left(-\frac{E_a}{\mathrm{R_g} T}\right) = k_0(T_0) \exp\left(-\frac{E_a}{\mathrm{R_g} T_0}\right) \exp\left(-\frac{E_a}{\mathrm{R_g} T}\right) \exp\left(\frac{E_a}{\mathrm{R_g} T_0}\right) \tag{A.5}$$

$$= k_0(T_0) \exp\left(-\frac{E_a}{\mathrm{R_g}} \left(\frac{1}{T} - \frac{1}{T_0}\right)\right) \qquad \text{with } k(T_0) = k_0 \exp\left(-\frac{E_a}{\mathrm{R_g} T_0}\right) \tag{A.6}$$

This transformation is often used for estimation of kinetic parameters as it is well known to reduce the parameter correlation between the pre-exponential factor and the activation energy [182]. Since the analysis of safe conditions is restricted to the neighborhood of the reference temperature T_0, it holds $T - T_0 \ll T_0$. As a further simplification it can be assumed that $T \cdot T_0 \approx T_0^2$ [81], which leads to the argument in the exponential term:

$$-\frac{E_a}{\mathrm{R_g}} \left(\frac{1}{T} - \frac{1}{T_0}\right) = \frac{E_a}{\mathrm{R_g}} \left(\frac{T - T_0}{T T_0}\right) \approx \frac{E_a}{\mathrm{R_g}} \left(\frac{T - T_0}{T_0^2}\right) \tag{A.7}$$

The original approach by Frank-Kamenetskii is based directly on a linearization of the exponential term [70]. He suggested to expand the term $\exp\left(-\frac{E}{\mathrm{R_g} T}\right)$ in a Taylor series at the reference temperature T_0 and truncate after the linear term.

$$-\frac{E_a}{\mathrm{R_g} T} \approx -\frac{E_a}{\mathrm{R_g} T_0} + \frac{E_a}{\mathrm{R_g} T_0^2} (T - T_0) \tag{A.8}$$

The linearized form of an exponential term reads accordingly:

$$\exp\left(-\frac{E_a}{\mathrm{R_g}T}\right) \approx \exp\left(-\frac{E_a}{\mathrm{R_g}T_0}\right)\exp\left(\frac{E_a}{\mathrm{R_g}T_0^2}\,(T-T_0)\right) \tag{A.9}$$

In the following it is straight forward to implement the transformed Arrhenius exponential eq. (A.9) in the reactor energy balance:

$$\frac{\mathrm{d}T}{\mathrm{d}t} = \Delta T_{\mathrm{ad}} k_0 \exp\left(-\frac{E_a}{\mathrm{R_g}T_0}\right)\exp\left(\frac{E_a}{\mathrm{R_g}T_0^2}\,(T-T_0)\right) \tag{A.10}$$

Typically a variable transformation from T in φ with φ being the difference to the reference temperature ($\varphi = T - T_0$) is performed:

$$\frac{\mathrm{d}\varphi}{\mathrm{d}t} = \Delta T_{\mathrm{ad}} k_0 \exp\left(-\frac{E_a}{\mathrm{R_g}T_0}\right)\exp\left(\frac{E_a}{\mathrm{R_g}T_0^2}\varphi\right) \tag{A.11}$$

Equation (A.11) needs to be solved with appropriate integration limits.

A.1.3. Integration Limits

Two specific integration limits are considered.

The time to maximum rate (TMR) For a single reaction the maximum reaction rate is achieved at a temperature, such that $T \geq T_0 + \Delta T_{\mathrm{ad}}$. According to the explosion theory the timespan is required to consume the initial amount of reactant, which actually takes place in the moment of an explosion.

This induction time, the time to reach the maximum rate (TMR) can be obtained by integration from $\varphi = 0$ to the maximum temperature. This is achieved in the limit of an infinitely large temperature, thus $\varphi \to \infty$. See Steinbach [196] for an alternative treatment, which however results in a similar time to maximum rate, TMR:

$$\int_0^t \mathrm{d}t = \frac{1}{\Delta T_{\mathrm{ad}} k_0}\exp\left(\frac{E_a}{\mathrm{R_g}T_0}\right)\int_0^\infty \exp\left(-\frac{E_a}{\mathrm{R_g}T_0^2}\varphi\right)\mathrm{d}\varphi \tag{A.12}$$

$$\mathrm{TMR} = \frac{1}{\Delta T_{\mathrm{ad}} k_0}\exp\left(\frac{E_a}{\mathrm{R_g}T_0}\right)\frac{\mathrm{R_g}T_0^2}{E_a} \tag{A.13}$$

The time to maximum rate is given as:

$$\mathrm{TMR} = \frac{1}{k_0 \exp\left(\frac{E}{\mathrm{R_g}T_0}\right)}\frac{1}{B_0} \tag{A.14}$$

The characteristic time interval depends on the reciprocal of the rate and the temperature sensitivity given in terms of the reaction number B_0 defined for a specific reference tempera-

ture T_0 [196]:

$$B_0 = \frac{\Delta T_{\mathrm{ad}} E_a}{\mathrm{R_g} T_0^2} \tag{A.15}$$

The time of no return (TNR) The TNR corresponds to the timespan to reach the critical temperature of the reactor. The critical temperature is obtained from the Semenov's explosion theory, $T_c = \frac{E_a}{\mathrm{R_g} T^2}$. Beyond this time interval, even recovery of the cooling system after a malfunction will not help to restore a stable reactor operation [81].

The upper integration limit for the TNR is $\varphi = T_c = \frac{\mathrm{R_g} T_0^2}{E_a}$ and the characteristic time interval can be derived:

$$\int_0^t \mathrm{d}t = \frac{1}{\Delta T_{\mathrm{ad}} k_0} \exp\left(\frac{E_a}{\mathrm{R_g} T_0}\right) \int_0^{T_c} \exp\left(-\frac{E_a}{\mathrm{R_g} T_0^2}\varphi\right) \mathrm{d}\varphi \tag{A.16}$$

$$\mathrm{TNR} = \frac{1}{\Delta T_{\mathrm{ad}} k_0} \exp\left(\frac{E_a}{\mathrm{R_g} T_0}\right) \frac{\mathrm{R_g} T_0^2}{E_a} \frac{\exp - 1}{\exp} \tag{A.17}$$

Obviously the relation between the TNR and the TMR is:

$$\mathrm{TNR} = \frac{\exp - 1}{\exp} \mathrm{TMR} = e^* \mathrm{TMR} = 0.6321 \mathrm{TMR} \tag{A.18}$$

Similar to equation (2.43) for the minimal conversion at the ignition temperature, the exponential factor e^* appears. Here, equation (A.18) relates two characteristic times of the non-isothermal batch process, which is extended to fixed-bed reactors below.

A.2. Fixed-Bed Reactor

A.2.1. Characteristic Distances

Although the explosion theory is basically meant to identify critical situation in a batch process, in this work the idea is exploited for the analysis of ignition temperatures in fixed-bed reactors. This is possible because the of similarity between the corresponding models of the ideal reactors, batch and plug flow, respectively. It is straight forward to analyze the following balance describing the temperature profile of the reactor:

$$u_g \rho c_p \frac{\mathrm{d}T}{\mathrm{d}z} = (-\Delta H_R) k_0^{(0)} \exp\left(-\frac{E_a}{\mathrm{R_g} T}\right) \tag{A.19}$$

$$\text{or:} \qquad u_g \frac{\mathrm{d}T}{\mathrm{d}z} = \Delta T_{\mathrm{ad}} k_0 \exp\left(-\frac{E_a}{\mathrm{R_g} T}\right) \tag{A.20}$$

Equation (A.20) is analogous to equation (A.2), only the independent variables changed and the gas velocity, u_g, is introduced.

In this work the approach requires two new figures; instead of the time to maximum rate (TMR), a "distance to maximum rate" (DNR) is defined, and correspondingly it can be given a

"distance of no return" (DNR). Thus, after transformation in the temperature difference φ, the first number, the distance to maximum rate, can be defined:

$$\frac{1}{u_g}\int_0^{L_R} \mathrm{d}z = \frac{1}{\Delta T_{\mathrm{ad}} k_0} \exp\left(\frac{E_a}{\mathrm{R_g} T_0}\right) \int_0^{\infty} \exp\left(-\frac{E_a}{\mathrm{R_g} T_0^2}\varphi\right) \mathrm{d}\varphi \tag{A.21}$$

$$\frac{L_R}{u_g} = \frac{1}{\Delta T_{\mathrm{ad}} k_0} \exp\left(\frac{E_a}{\mathrm{R_g} T_0}\right) \frac{\mathrm{R_g} T_0^2}{E_a} \tag{A.22}$$

$$\mathrm{DMR} = \frac{u_g}{\Delta T_{\mathrm{ad}} k_0} \exp\left(\frac{E_a}{\mathrm{R_g} T_0}\right) \frac{\mathrm{R_g} T_0^2}{E_a} \tag{A.23}$$

The DMR is the distance in the reactor, at which complete conversion should be achieved. And the "distance of no return" is defined for the critical temperature T_c according to:

$$\mathrm{DNR} = \frac{\exp - 1}{\exp} \frac{u_g}{\Delta T_{\mathrm{ad}} k_0} \exp\left(\frac{E_a}{\mathrm{R_g} T_0}\right) \frac{\mathrm{R_g} T_0^2}{E_a} \tag{A.24}$$

Again, the relation between the numbers is the exponential factor e^*:

$$\mathrm{DNR} = \frac{\exp - 1}{\exp} \mathrm{DMR} = e^* \ \mathrm{DMR} = 0.6321 \ \mathrm{DNR} \tag{A.25}$$

The relationship is similar to equation (A.18) derived for batch reactors.

A.2.2. Limiting Cases

It is instructive to restate the DMR according to:

$$\frac{L_R}{u_g} = \frac{1}{k_0 \exp\left(-\frac{E_a}{\mathrm{R_g} T_0}\right)} \frac{1}{\Delta T_{\mathrm{ad}}} \frac{\mathrm{R_g} T_0^2}{E_a} \tag{A.26}$$

The result corresponds to the isothermal balance used to derive the ignition temperature (eq. (2.39)), though augmented by the reciprocal of the thermal reaction number B_0 (eq. (A.15)).

$$\tau_g = \tau_R \cdot \frac{1}{B_0} \tag{A.27}$$

$$\tau_g = \tau_R \cdot \frac{1}{\Delta T_{\mathrm{ad}}} \frac{\mathrm{R_g} T_0^2}{E_a} \tag{A.28}$$

In equation (A.27) the characteristic numbers are evaluated for a certain constant temperature T_0. This temperature corresponds to the lower integration limit, the inlet temperature T^{in} of the adiabatic fixed-bed reactor. When it is required to reach the maximum rate (DMR), it consequently holds that $T^{\mathrm{max}} = T^{\mathrm{in}} + \Delta T_{\mathrm{ad}}$.

In contrast to the isothermal approach used for an estimate of the ignition temperature in section 2.2.1, the non-isothermal approach accounts for the inlet concentration (ΔT_{ad}). This time, however, an explicit solution of the ignition temperature is not available, but the

equation (A.27) can be solved iteratively. Before doing so, at first it is instructive to discuss specific limiting cases of equation (A.27) in the following form:

$$\frac{\tau_g}{\tau_R} = \frac{1}{B_0} = \frac{1}{\Delta T_{\mathrm{ad}}} \frac{\mathrm{R_g} T_0^2}{E_a} \tag{A.29}$$

The limits of (A.29) regarding concentration effects are:

- In the limit of small inlet concentrations, $\Delta T_{\mathrm{ad}} \to 0$, the residence time should increase, $\frac{\tau_g}{\tau_R} \to \infty$, to maintain complete conversion.
- In the limit of large inlet concentrations, $\Delta T_{\mathrm{ad}} \to \infty$, the residence time can be reduced, $\frac{\tau_g}{\tau_R} \to 0$, still maintaining complete conversion.
- For the special case that $B_0 = 1$, the inlet concentration corresponds to an adiabatic temperature rise of:

  $$\Delta T_{\mathrm{ad}} = \frac{\mathrm{R_g} T_0^2}{E_a} \tag{A.30}$$

  and the ignition temperature takes the already known explicit form:

  $$T_{\mathrm{ig}} = \frac{E_a}{\mathrm{R_g} \ln\left(\frac{L k_0}{u_g}\right)} \tag{A.31}$$

  which is in accord to the analysis of isothermal case (equation (2.40)). The difference is the influence of the inlet concentration by statement (A.30) in case of the non-isothermal approach, by contrast $\Delta T_{\mathrm{ad}} \to 0$ was assumed for the isothermal approach. Thus, although the expressions for the ignition temperatures are similar, the presumptions are not.

A.2.3. Evaluation of Limiting Cases

The limiting cases can be validated by the solution of the steady-state fixed-bed model for the example of a first order reaction according to the following mass and energy balances:

$$u_g \frac{\mathrm{d}c}{\mathrm{d}z} = -k_0 \exp\left(-\frac{E_a}{\mathrm{R_g} T}\right) c \tag{A.32}$$

$$u_g \rho c_p \frac{\mathrm{d}T}{\mathrm{d}z} = (-\Delta H_R) k_0 \exp\left(-\frac{E_a}{\mathrm{R_g} T}\right) c \tag{A.33}$$

Figure A.1 illustrates the temperature amplification for the two different feed concentration, $\Delta T_{\mathrm{ad}} = 0.001$ representing the isothermal case and $\Delta T_{\mathrm{ad}} = \frac{\mathrm{R_g} T_0^2}{E_a}$ for the third limiting case (eq. (A.30)) of the non-isothermal theory, and the corresponding ignition temperature valid for both. Due to the higher inlet concentration of the non-isothermal approach (eq. (A.30)), a higher conversion is obtained along with the increasing inlet temperature. Although the explosion theory required complete conversion as introduced with an upper integration limit

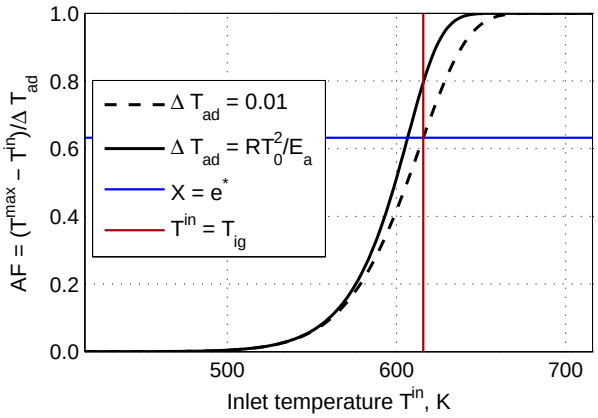

Figure A.1.: Influence of the inlet temperature on the temperature amplification AF in a steady state fixed-bed reactor for the example of a first order reaction (eq. (A.32) and (A.33)) compared with estimates for the ignition temperature. The special case in the limit $\frac{\Delta T_{\mathrm{ad}}}{\mathrm{R_g} T^{\mathrm{in}}/E_a} = 1$ obtained from the non-isothermal theory (eq. (A.29)) gives the same ignition temperature of the isothermal theory (eq. (2.40)) (red line). The amplification AF (eq. (1.1)) corresponds to the conversion of the steady-state fixed-bed reactor and the minimal conversion for the isothermal ignition temperature is e^* (eq. (2.43)).

of infinity, only about 80 % of conversion are achieved. In contrast, the isothermal approach was shown to give a conversion of exactly $X = e^* \approx 0.632$ for a first order reaction.

Figure A.2 (left) illustrates the influence of the inlet concentration for a series of five amplification curves corresponding to reduced adiabatic temperature rises of: $\frac{\Delta T_{\mathrm{ad}}}{\mathrm{R_g} T^{\mathrm{in}}/E_a} = 0.01, 1, 2, 3$ and 4 (black lines). The gray symbols indicate the inlet temperatures for complete conversion when reaching AF = 1. These curves are compared with ignition temperature based on the non-isothermal theory solving eq. (A.27). The blue line corresponds to the second y-axis for the reduced concentration. The symbols on this lines indicate the estimated ignition temperatures for the five concentrations selected. The red vertical line indicates the isothermal ignition temperature, which is identical to the non-isothermal ignition temperature, when condition (A.30) is considered.

The ignition temperatures do not meet the inlet temperatures of the fixed-bed model, at which complete conversion is achieved. The inlet temperatures are found either at larger values for the small concentrations or conversely, underestimate the ignition temperatures at higher inlet concentrations. In case of $\frac{\Delta T_{\mathrm{ad}}}{\mathrm{R_g} T^{\mathrm{in}}/E_a} = 1$, about 80 % conversion is achieved (second concentration, as already shown in A.1).

In order to make this result more transparent, the right figure of A.2 shows the inlet temperatures at which complete conversion was achieved (steady-state fixed-bed model) over the non-isothermal ignition temperatures (eq. (A.27)). This parity plot indicates, that for a very diluted mixture the non-isothermal approach gives higher ignition temperatures. On the other hand, in case of higher inlet concentrations, the ignition temperatures are lower than actually required to reach complete conversion. The deviations, however, become systematically smaller with increased inlet concentrations.

An explanation for the differences is the linearization of the Arrhenius exponential (eq. A.1.2) which offers only local validity in the close neighborhood of the inlet temperature. This is cer-

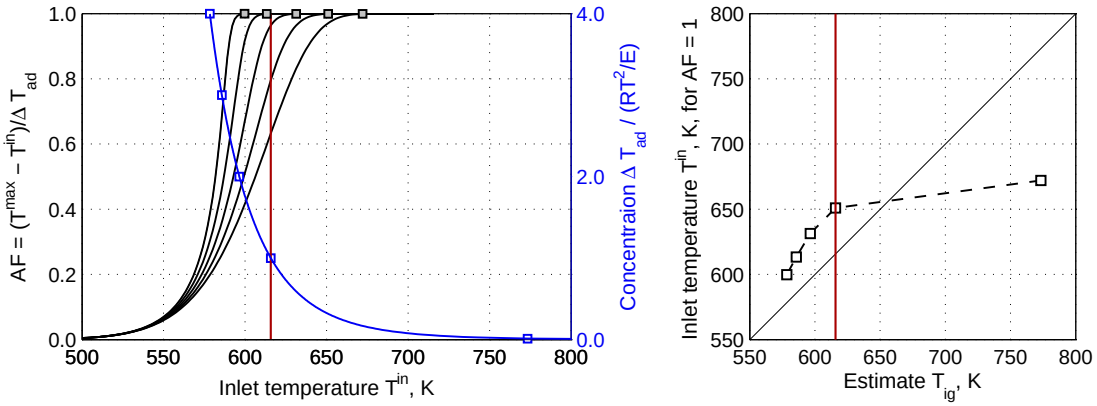

Figure A.2.: Left, temperature amplification with respect to the inlet temperature (black lines) for five different inlet concentrations, gray symbols for $AF = 1$. Right axis shows the non-isothermal ignition temperature (A.27) (continuous blue line). Concentrations are given as multitudes of $\Delta T_{\mathrm{ad}}/(\mathrm{R_g}T^2/E_a) = 0.01, 1, 2, 3, 4$. Right fig. compares the model with the estimate. The red line is the case for the concentration defined by (A.30), which matches the isothermal T_{ig}.

tainly violated for the cases of larger feed concentrations, as they lead to substantial nonlinear temperature profiles in the fixed-beds. Moreover, the non-isothermal approach is also based on a zeroth-order reaction, which is an oversimplification for the first order rate considered above. Despite these discrepancies, the sensitivity with respect to the inlet concentration is well reflected by the non-isothermal approach, thus offering a useful approximation to discuss the impact of concentrations on the ignition temperatures.

A.3. Summary and Conclusions

Whereas the isothermal approach for the ignition temperature was based on the mass balance for a zeroth order reaction, for the non-isothermal a linearization of the energy balance originated from explosion theory was exploited. It turns out that in addition to characteristic residence and reaction times, this approach accounts for the effects of the inlet concentration, which is introduced via the thermal reaction number. Three limiting cases were briefly discussed and it was shown for a specific example of a first order reaction, how the non-isothermal approach can be related to the temperature amplification in a steady state fixed-bed model. Although the theory lacks of high precision for this example, the impact of the concentration on the ignition temperature is qualitatively described.

B. Modeling and Numerical Solution Methods

B.1. Pseudo-Homogeneous One-Dimensional SMBR Reactor Model

For the simulation of the SMBR the one-dimensional pseudo-homogeneous model was used with the underlying assumptions:

- Pressure drop, radial concentration and temperature gradients are neglected.
- Incompressible flow and a constant mass flow density.
- The ideal gas law applies with properties of air.

The model reads:

$$\varepsilon \rho_g \frac{\partial w_i^j}{\partial t} = -\dot{m}_g \frac{\partial w_i^j}{\partial z} + D \frac{\partial^2 w_i^j}{\partial z^2} + \nu_i \tilde{M}_i^j r(c_i^j, T^j) \tag{B.1}$$

$$\left(\varepsilon(\rho c_p)_g + (1-\varepsilon)(\rho c_p)_s\right) \frac{\partial T^j}{\partial t} = -\dot{m}_g c_{p,g} \frac{\partial T^j}{\partial z} + \lambda \frac{\partial^2 T^j}{\partial z^2} + (-\Delta H_R) r(c_i^j, T^j) \tag{B.2}$$

$$w_i^j(t=0,z) = w_i^{j,\text{init}}(z)$$

$$T^j(t=0,z) = T^{j,\text{init}}(z)$$

$$i = 1, N_c \qquad j = 1, N_{\text{Seg}}$$

It this model a density change of the gas phase is considered:

$$\rho(z,t) = \frac{p_g \widetilde{M}_{\text{air}}}{\text{R}_\text{g} T(z,t)} \tag{B.3}$$

The boundary condition account for the switching in an SMBR are of third kind according to Danckwerts [100].

$$\dot{m}_g w_i^{j,\text{in}} = \dot{m}_g w_i^{j,0} - D\frac{\partial w_i^{j,0}}{\partial z} \tag{B.4}$$

$$\dot{m}_g c_{p,g} T^{j,\text{in}} = \dot{m}_g c_{p,g} T^{j,0} - \lambda\frac{\partial T^{j,0}}{\partial z} \tag{B.5}$$

$$w_i^{j,\text{in}} = \begin{cases} w_i^{N_{\text{Seg}},L} & \text{, if} \quad j = 1 \\ w_i^{j-1,L} & \text{, if} \quad j = 2,\ldots,N_{\text{Seg}} \end{cases} \tag{B.6}$$

$$T^{j,\text{in}} = \begin{cases} T^{N_{\text{Seg}},L} & \text{, if} \quad j = 1 \\ T^{j-1,L} & \text{, if} \quad j = 2,\ldots,N_{\text{Seg}} \end{cases} \tag{B.7}$$

The inner boundary at the entrance is denoted by "0" and the outlet boundary with "L". The BC corresponds to the case for which the feed is in front of the first segment and are modified according to the switching policy for subsequent switches. This topic is detailed in section C.

For the investigation of the reactor concept a single exothermic reaction is assumed with parameters according to [74], see table B.1.

Table B.1.: Parameters used for the 1D pseudo-homogeneous reactor model according to [74]

k_0	9.52e6 1/s	ε	0.69
E_a	69247 J/mol	D	1e^{-4} kg/ms
$c_{p,g}$	1.1 kJ/kgK	$(\rho c_p)_m$	428.2 kJ/kgK
ΔH_R	-2040 kJ/mol		

B.2. Reverse-Rlow Reactor Model

For flow reversal the convective flux need to be switched in the model, which is implemented by sign change of the convective term, whereby h is a parameter alternating between -1 and 1.

$$\varepsilon\rho_g\frac{\partial w_i}{\partial t} = -h\,\dot{m}_g\frac{\partial w_i}{\partial z} + D\frac{\partial^2 w_i}{\partial z^2} + \nu_i\tilde{M}_i r(c_i,T) \tag{B.8}$$

$$\left(\varepsilon(\rho c_p)_g + (1-\varepsilon)(\rho c_p)_s\right)\frac{\partial T}{\partial t} = -h\,\dot{m}_g c_{p,g}\frac{\partial T}{\partial z} + \lambda\frac{\partial^2 T}{\partial z^2} + (-\Delta H_R) r(c_i,T) \tag{B.9}$$

$$w_i(t=0,z) = w_i^{\text{init}}(z)$$

$$T(t=0,z) = T^{\text{init}}(z)$$

$$i = 1, N_c \qquad j = 1$$

The BCs are similar to the SMBR and switching was implemented by conditional expressions. In addition the discretization scheme needs to be corrected accordingly.

B.3. The TMBR model

The TMBR model is described in section 3.1.2 and summarized below:

$$\varepsilon\rho\frac{\partial w_i}{\partial t} = -u_g\rho_g\frac{\partial w_i}{\partial z} + D\frac{\partial^2 w_i}{\partial z^2} + \sum_j \nu_i r_j(c_i,T) \tag{B.10}$$

$$\begin{aligned}\left(\rho c_p\right)_m\frac{\partial T}{\partial t} = &-u_g(\rho c_p)_g\frac{\partial T}{\partial z} + u_s(\rho c_p)_s\frac{\partial T}{\partial z}\\ &+\lambda\frac{\partial^2 T}{\partial z^2} + \sum_j(-\Delta H_R)r_j(c_i,T) - 2h_w/R_w(T-T_u)\end{aligned} \tag{B.11}$$

$$\text{IC:}\quad w_i(t=0,z) = w_i^{\text{init}}(z) \qquad T(t=0,z) = T^{\text{init}}(z) \tag{B.12}$$

Appropriate boundary conditions were investigated in section 3.1.3. Usually the following form was used:

$$z=0: \qquad \lambda\frac{\partial T}{\partial z}\Big|_{0^+} = u_g(\rho c_p)_g\left(T|_{0^+} - T_g^{\text{in}}\right) \tag{B.13}$$

$$z=L: \qquad 0 = u_g(\rho c_p)_g\left(T|_{L^-} - T_g^{\text{out}}\right) - u_s(\rho c_p)_s\left(T|_{L^-} - T|_{0^+}\right) \tag{B.14}$$

Note that in most cases the trivial form, identical temperatures at the boundaries, works as well. For the mass balances the BC are:

$$z=0: \qquad u_g\rho_g w_i^{\text{in}} = u_g\rho_g w_i|_{0^+} - D\frac{\partial w_i}{\partial z}\Big|_{0^+} \tag{B.15}$$

$$z=L: \qquad 0 = \frac{\partial w_i}{\partial z}\Big|_{L^-} \tag{B.16}$$

Parameters used for the investigation of the single reaction system are listed in B.1. The conversion from solid phase velocity to switching times of an SMBR is given in section 3.1.4.

In case of a feed mixture, the parameters listed below in table B.2 were used. The simplified the first order reaction rates (tab. 6.1) and parameters according to the experimental reactor were considered.

Table B.2.: Parameters used in chapter 7. Heat transfer through the jacket was omitted ($h_W = 0$) and the inlet temperature assumed constant at $T^{\text{in}} = 300\,\text{K}$.

$\dot{m}_g$	$1.0\,\text{kg/sm}^2$	ε	0.43
E_{a1}	128.4 kJ/mol	E_{a2}	111.4 kJ/mol
k_0	$1.012\cdot10^{13}$ J/mol	D	1e^{-4} kg/ms
$c_{p,g}$	1.116 kJ/kgK	λ	$4.46\cdot10^{\cdot4}$ W/mK
$\Delta H_{R,1}$	−1926 kJ/mol	$\Delta H_{R,2}$	−1322 kJ/mol

B.4. Numerical Solution Method and Description of the Hybrid System

B.4.1. Solution Method of the Dynamic Model

The reactor balances represent systems of nonlinear partial differential equations, which have a hyperbolic character and are considered as convection dominant systems. Generally, the balances are often discretized in order to reduce the problem for which know numerical solvers, such as integrators and solvers for nonlinear systems of equations, are available [197–200]. A wide spread method for the solution of partial differential equations (PDE) is the method of lines, in which the spatial domain is discretized and the resulting system of ODE solved using a standard integrator. The resulting stiff system of equations can be solved with implicit or semi-implicit solvers which can unfortunately lead to a very small time stepping. Another aspect is the increased stiffness introduced through the switching events. This is due to the interruption of fronts and the large gradients at the boundaries occurring immediately after the switch. Several solutions to this problems have been developed. Moving grids can be applied which adapt the spatial resolution to the moving front position [103, 201]. Specific tools have been developed for the simulation of traveling fronts, though, demanding a sufficient parabolic nature of the PDEs (PDEXPACK [202]); with application in [203, 204]. Also high resolution schemes based on finite volume discretization are alternatives [104, 105]. After all, selection for a specific solver is always a trade-off between required precision and an acceptable calculation time.

Regarding appropriate calculation times for the simulation of cyclic steady states, the choice was made for a robust difference scheme for the spatial coordinate and an efficient integrator for stiff problems. The first order spatial gradients were approximated by an upwind scheme and for the second order a central difference approximation was used. Inner grid nodes were employed for the gradient approximation of the boundary condition. The uniform grid can is defined by:

$$j = 1, \dots N_p \quad \text{with} \qquad \Delta z = \frac{L}{N_p - 2} \tag{B.17}$$

with j being the index of the grid nodes and the approximations have the from:

$$\frac{\partial x}{\partial z} \approx \frac{x_j - x_{j-1}}{\Delta z} \qquad \frac{\partial^2 x}{\partial z^2} \approx \frac{2x_{j-1} - x_j + x_{j+1}}{\Delta z^2} \tag{B.18}$$

Thereby the boundaries are treated as algebraic equations, e.g.

$$0 = (x^{\text{in}} - x_1) + \frac{x_2 - x_1}{\Delta z} \qquad 0 = x_{N_p} - x_{N_p - 1} \tag{B.19}$$

Here, just the coefficients are omitted for the sake of clarity. Note that this approach need to be considered in the space increment (eq. B.17). After discretization, the system of PDEs is reduced to a system of differential algebraic equation. Several efficient solver are available [205, 206].

B.4.2. On the Solution of the Cyclic Reactor Model

In periodic systems a time dependence of the solution is introduced either autonomously or by explicit functions. For that reason, a constant steady state cannot be attained and an analogous cyclic steady state is usually considered. Concerning the SMBR, the period of the system can be defined e.g. as the timespan to complete a cycle.

Typically, the periodic system will be determined by its inherent periodicity and a relaxation on the cyclic steady state. This idea is sketched in figure B.1. The initial state is given by a state vector $\boldsymbol{x}_0$ and in subsequent cycles the states of the system ($\boldsymbol{x} \in \Re^n$) pierce a hyperplane, the *Poincaré*-section, which is an object with one less the dimension of the system ($\Sigma \in \Re^{(n-1)}$). The points piercing this section are described by the *Poincaré* map P, with k being the index of the subsequent periods.

$$\boldsymbol{x}_{k+1} = P(\boldsymbol{x}_k) \qquad k = 1,2,\ldots \tag{B.20}$$

A cyclic steady state is reached in case the initial and the final states within a period coincide in a single point of the section:

$$\boldsymbol{x}_k^* = P(\boldsymbol{x}_k^*) \tag{B.21}$$

With $\boldsymbol{x}^*$ the fixed point of the map P. Alternatively this settled state can be regarded as a cyclic periodic orbit which is characterized by a period time. Selecting any state on this orbit as an initial value, this initial state will be met again exactly after the characteristic period time [135].

Often a certain tolerance is used for the determination of the cyclic steady state. For example, the deviations between subsequent periods can be calculated based on the norm of the state vector according to following expression.

$$e_k = \frac{||P(\boldsymbol{x}_k) - \boldsymbol{x}_{k+1}||_1}{||\boldsymbol{x}_{k+1}||_1} \tag{B.22}$$

If e_k, the error of the k-th cycle, falls below a specific small tolerance, a sufficiently accurate approximation of cyclic steady state is achieved.

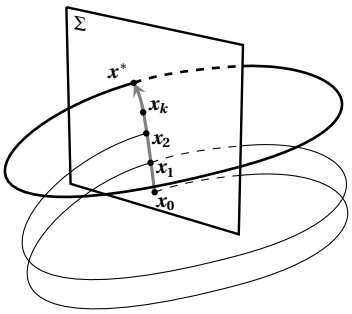

Figure B.1.: Poincaré section Σ and periodic orbit.

Several concepts were suggested for the solution to this problem. First of all, the simulation of the complete dynamics of the process is very common. This approach is denoted as *successive substitution* [207], *Picard iteration* [208] or simply *direct dynamic simulation* [88]. The initial conditions for a new period correspond the final conditions of the previous period ($\boldsymbol{x}_{k+1}^0 = \boldsymbol{x}_{k+1}$). In many cases the convergence is very slow and a large number of cycles is usually needed. This becomes even more severe for processes with very small accumulation effects as illustrate by Gorbach et al. [89] for an adsorption process.

Another approach is based on shooting and solving the following equation:

$$\boldsymbol{e}_k = P(\boldsymbol{x}_k^0) - \boldsymbol{x}_{k+1} = 0 \tag{B.23}$$

with the initial profiles $\boldsymbol{x}_k^0$ treated as depending variables. Applying Taylor series approximation a Newton-type solver could take on the following problem.

$$\boldsymbol{x}_{k+1}^0 = \boldsymbol{x}_k^0 - \left(\frac{\partial \boldsymbol{e}_k}{\partial \boldsymbol{x}_k^0}\right)^{-1} \boldsymbol{e}_k \tag{B.24}$$

In contrast to the direct dynamic simulation, the final and initial states between two subsequent cycles differ and a faster convergence to the cyclic steady state can be achieved. Pictorially, the Poincaré section is not simply pierced any longer, but the emersion points are shifted already more to the final state within the course of iteration.

In equation B.24 the Jacobian consist of the gradients of the $\boldsymbol{e}_k$ with respect to the initial states $\boldsymbol{x}_k^0$. This Jacobian is the bottleneck of the approach. Special algorithms have been developed to cope with the requirements of the typically large system of equation. For example the *Broyden*-method [209, 210] or methods exploiting only relevant dynamic variables of the system (*RPM - recursive projection method* [211, 212]).

A global discretization, meaning a space and time discretization including a periodic boundary condition, was also investigated and applied successfully [122, 213]. This approach is especially useful within scope of parameter continuations. Disadvantages are seen in the computationally expensive Jacobian matrix and a proper initialization. Recently, this method was used for the optimization in chromatographic SMB exploiting modern optimization algorithms [214].

This work intends to investigate the SMBR by parameter studies and dynamic simulations. For that reason the simulation environments DIVA and DIANA were selected as they offer a appropriate numerical framework. Specifically the parameter continuation of the forced periodic SMBR and an efficient event handling required for the SMBR simulation are well implemented in these tools.

C. Controller Implementation and Specifications

C.1. Interpretation of the Periodic Discrete-Event Dynamic Model

This section focuses upon the features of the switched SMBR model containing a discrete-time part for the switching events and a continuous part for the continuous front dynamics. Such models are regarded as hybrid models and are an field of active research specifically in control theory [215, 216].

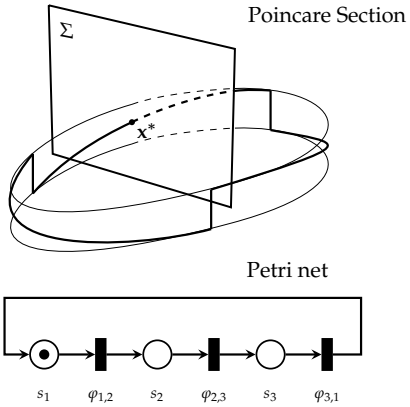

Figure C.1.: The switched periodic reactor can be regarded as periodic orbit piercing the Poincaré section after a cycle completed, while jumps indicate switching events. Below the corresponding Petri net used for a structured modeling of the controller is shown for the example of three transitions and three places representing controller 3.

In the dynamic models the switching time corresponds to an event time at which a discontinuity in the state is introduced, here due to the boundary condition. Figure C.1 shows a sketch of a possible periodic orbit being disrupted after specific period times or switching times, respectively. Those jumps in the system state represent the action of the on-off valves. With this figure it is intuitively clear, that within a complete cycle arbitrary complex switching events may be implemented. This also means, that the underlying switching times or the number of switches are not restricted, as long as the periodic orbit comes back to its initial state. Although this figure is not meant to provide a very strict definition in the mathematical sense, it provides an illustrative view on the underlying dynamics.

In the lower part of figure is shown a Petri net as a corresponding modeling entity for the hybrid model. The Petri net consist of places, transitions and directed arcs, in which the arcs determine the pre/post connections. In this work, the places are used to assign the active feed and product ports, and the transitions define the conditions for triggering the discrete

switches according to a prescribed policy.

The initial place is marked with a single token. Starting from such an initial state, the reactor is switched according to the specified control law until the same initial state of the reactor has been reached again (in cyclic steady state). Hence, the Petri net describes a loop of places and transitions representing the valve positions of the cyclic reactor.

Note that in the present work open-loop denotes the operation with predefined switching times and closed-loop control is based on a feedback of temperature signals. Therefore the transition are either parameter dependent functions in the first case or the transitions are state dependent. Additional information about the elements and the numerical methods available in DIVA are documented in [217].

C.2. Open-Loop Control

The Petri net for an open-loop control is based on two places, s_1 and s_2, as well as two transitions, t_1 and t_2. With a given constant switching time, one option is a representation as an explicit event. Nevertheless an implicit transitions was used in this work which allowed parameter continuation of the switched periodic system. The transition is triggered when the corresponding φ-function (φ_1 and φ_2) becomes zero. Then the token activates the next prescribed place.

Below, this will be explained based on a three segmented reactor. At first a position index m is defined as

$$m \in \mathbb{Z}^+ : 1, \ldots, N_{\mathrm{Seg}} \tag{C.1}$$

This index is implemented in conditional statements in the boundary condition of the respective reactor balances. In case m is 2, the feed position is in front of the second and the product port at the end of the first segment, and so forth. An additional dynamic state x_e is implemented as a function depending on the switching time t_{sw} and an parameter p_e:

$$\frac{\mathrm{d}x_e}{\mathrm{d}t} = \frac{p_e}{0{,}5 \cdot t_{\mathrm{sw}}} \tag{C.2}$$

The state x_e alternates in the range between 0 and 1 describing a zig-zag path. This can be achieved, if the initial state and the sign of the gradient (via p_e) are periodically switched. At the first place s_1 it holds that.

$$s_1 : p_e := 1 \qquad x_e := 0 \tag{C.3}$$

And for the second place s_2 following definition apply.

$$s_2 : p_e := -1 \qquad m := \mod(m, N_{\mathrm{Seg}}) + 1 \tag{C.4}$$

The modulus operator ensures that m is switched from one to N_{Seg} and then starting from one again. In this way, counting indexes are avoided. Finally, the two transitions are defined

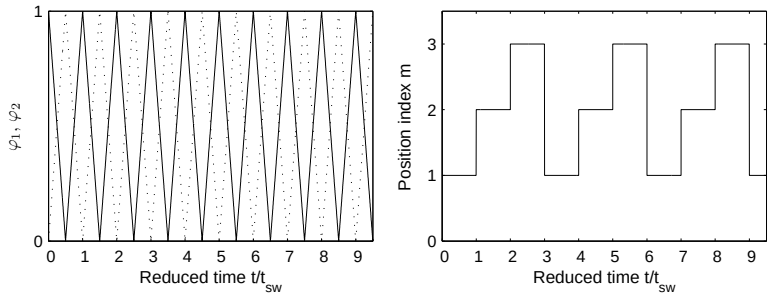

Figure C.2.: Transitions φ_1 and φ_2 (left) and the position index m (right) for the Petri net for open-loop control.

as:

$$t_1 : \varphi_1 = 1 - x_e \tag{C.5}$$

$$t_2 : \varphi_2 = x_e \tag{C.6}$$

Figure C.2 shows the φ-functions and the index m. For this example, the index is switched between 1 and 3 according to the three segments considered. This procedure allows a description in which all model parts, including that of the Petri net, are independent of time. This is an option to transfer a non-autonomous switched model in an quasi autonomous model, allowing numerical parameter continuations in DIVA. The continuation method is described in [72].

C.3. Closed-Loop Control

Figure C.3 shows the corresponding Petri nets used for the implementation of the three concepts investigated. From top, *controller 1*, *controller 2* and *controller 3*. These nets should be considered as a possible solution, albeit simpler alternatives can be implemented as well.

C.3.1. Control Based on a Single Sensor (*controller 1*)

The first Petri net is an example to model *controller 1*, the control concept based on a single thermocouple monitoring the reaction front. Five places and five transitions are employed, though only the first transition t_1 is used to monitor the reactor state. The time of the front to pass a distance of a segment is measured only in the first one, and subsequent switching functions are triggered according to this measured switching time until the update in the subsequent cycle. The net contains some additional variables defined by:

$$\frac{\mathrm{d}t_{\mathrm{res}}}{\mathrm{d}t} = 1 \tag{C.7}$$

$$\frac{\mathrm{d}t_{h,\mathrm{sw}}}{\mathrm{d}t} = \frac{p_a}{0.5\,t_{\mathrm{sw}}} \tag{C.8}$$

Table C.1 summarizes the relations used.

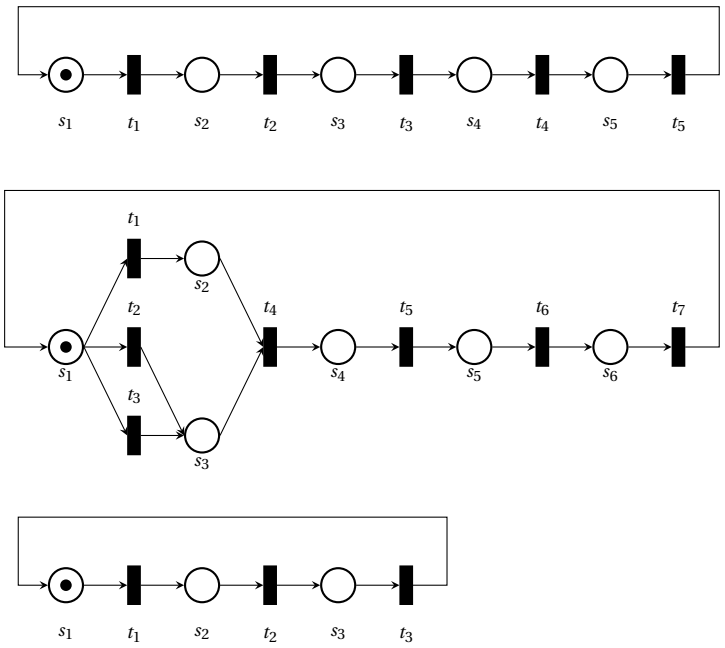

Figure C.3.: Structured Petri nets for modeling of controller, the first net represents the controller 1, the second net to the controller consisting of two thermocouples, *controller 2* and the last one represents controller 3.

Table C.1.: Parameterization of the Petri net for *controller 1*.

Places	Transitions
$s_1 := \begin{cases} t_{\text{res}} = 0 \\ p_a = 0 \\ m = \mod(m, N_{\text{Seg}}) + 1 \end{cases}$	$t_{1,2} : \varphi(t) = T_A(t) - T_{A,th}$
$s_2 := \begin{cases} t_{\text{sw}} = t_{\text{res}} \\ p_a = 1 \\ t_{h,\text{sw}} = 0 \\ m = \mod(m, N_{\text{Seg}}) + 1 \end{cases}$	$t_{2,3} : \varphi(t) = 1 - t_{h,\text{sw}}$
$s_3 := \begin{cases} p_a = -1 \end{cases}$	$t_{3,4} : \varphi(t) = t_{h,\text{sw}}$
$s_4 := \begin{cases} p_a = 1 \\ t_{h,\text{sw}} = 0 \\ m = \mod(m, N_{\text{Seg}}) + 1 \end{cases}$	$t_{4,5} : \varphi(t) = 1 - t_{h,\text{sw}}$
$s_5 := \begin{cases} p_a = -11 \\ t_{h,\text{sw}} = 0 \\ m = \mod(m, N_{\text{Seg}}) + 1 \end{cases}$	$t_{5,1} : \varphi(t) = t_{h,\text{sw}}$

C.3.2. Control Based on the Leading Thermal Front (*controller 2*)

The second concept triggers the events by monitoring the leading thermal front. Though for the start up phase it is required to observe the reaction front because of the absence of a sufficiently steep thermal front. Subsequent events are triggered according to the switching time estimated in the first period. When the initial phase is reached, depending on the threshold for the two sensors a decision is made, which front is used for measuring of the switching times.

Table C.2.: Parameterization of the Petri net for the control of the dispersive front, *controller 2*.

Places	Transitions
$s_1 := \begin{cases} t_{\mathrm{res}} = 0 \\ p_a = 0 \\ m = \mod(m, N_{\mathrm{Seg}}) + 1 \end{cases}$	
$s_2 := \begin{cases} t_{\mathrm{sw}} = t_{\mathrm{res}} \\ p_a = 1 \\ t_{h,\mathrm{sw}} = 0 \\ m = \mod(m, N_{\mathrm{Seg}}) + 1 \end{cases}$	$t_{2,3} : \varphi(t) = 1 - t_{h,\mathrm{sw}}$
$s_3 := \begin{cases} t_{\mathrm{sw}} = t_{\mathrm{res}} \\ p_a = 1 \\ t_{h,\mathrm{sw}} = 0 \\ m = \mod(m, N_{\mathrm{Seg}}) + 1 \end{cases}$	$t_{2,3} : \varphi(t) = 1 - t_{h,\mathrm{sw}}$
$s_4 := \begin{cases} p_a = -1 \end{cases}$	$t_{3,4} : \varphi(t) = t_{h,\mathrm{sw}}$
$s_5 := \begin{cases} p_a = 1 \\ t_{h,\mathrm{sw}} = 0 \\ m = \mod(m, N_{\mathrm{Seg}}) + 1 \end{cases}$	$t_{4,5} : \varphi(t) = 1 - t_{h,\mathrm{sw}}$
$s_6 := \begin{cases} p_a = -1 \end{cases}$	$t_{5,1} : \varphi(t) = t_{h,\mathrm{sw}}$

Additional help variables are defined as:

$$\frac{\mathrm{d}t_{\mathrm{res}}}{\mathrm{d}t} = 1 \tag{C.9}$$

$$\frac{\mathrm{d}t_{h,\mathrm{sw}}}{\mathrm{d}t} = \frac{p_a}{0.5\,t_{\mathrm{sw}}} \tag{C.10}$$

And the transition functions, which did not fit in the table are given below:

$$\varphi_{1,2}(t) = \begin{cases} T_A(t) - T_{A,\mathrm{sp}} & \text{if} \quad (R = 1) \cap (T_B - T_{B,\mathrm{sp}}) > 0 \\ 0 & \text{else} \end{cases} \tag{C.11}$$

$$\varphi_{1,3}(t) = \begin{cases} -(T_B(t) - T_{B,\mathrm{sp}} + 1) & \text{if} \quad (R = 1) \cap (T_B - T_{B,\mathrm{sp}} \leq 0) \cap (T_A - T_{A,\mathrm{sp}} \leq 0) \\ 0 \quad \text{else} \end{cases} \tag{C.12}$$

$$\varphi_{1,4}(t) = \begin{cases} -(T_B(t) - T_{B,\mathrm{sp}}) & \text{if} \quad (R = 2) \cap (T_B - T_{B,\mathrm{sp}}) \leq 0 \\ 0 \quad \text{else} \end{cases} \tag{C.13}$$

C.3.3. Control Based on the Reaction Front in each Segment (*controller 3*)

A third version proposed in this work controls the switching events using a sensor at the end of each reactor segment. The three segmented reactor is modeled by three places and three transitions. Throughout this work the set-point in each segment is the same. As an alternative

Table C.3.: Parameterization of the Petri net for *controller 3*

Places	Transitions
$s_1 := \{ m = \mod(m, N_{\mathrm{Seg}}) + 1$	$\varphi_{1,2}(t) = T_A - T_{A,\mathrm{sp}}$
$s_2 := \{ m = \mod(m, N_{\mathrm{Seg}}) + 1$	$\varphi_{2,3}(t) = T_B - T_{B,\mathrm{sp}}$
$s_3 := \{ m = \mod(m, N_{\mathrm{Seg}}) + 1$	$\varphi_{3,1}(t) = T_C - T_{C,\mathrm{sp}}$

only two places according to the Petri net below can be used.

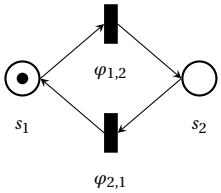

Figure C.4.: Alternative Petri net for *controller 3*

This net is set up using the following expressions:

$$s_1 = s_2 := \{ m = \mod(m, N_{\mathrm{Seg}}) + 1 \tag{C.14}$$

$$\varphi_{1,2} = \varphi_{2,1} := \begin{cases} m = 1 & T_A - T_{A,\mathrm{sp}} \\ m = 2 & T_B - T_{B,\mathrm{sp}} \\ m = 3 & T_C - T_{C,\mathrm{sp}} \end{cases} \tag{C.15}$$

The Petri net approach fosters a systematical development of reactor control concepts. Extension to incorporate additional control loops, i.e. combined with PI control, is possible.

C.4. Reactor Control for Mixtures

C.4.1. Open-Loop Reactor Control

The analysis of the TMBR model in chapter 7 has revealed the existence of two different reaction fronts in the binary mixture. As long as there exists a single isola, the quality of the temperature front does not change compared to the single component system. However, in case of a solution branch consisting of more than two limit points, also inflection points in the TMBR temperature profiles can emerge. This applies for the case of distinct isola, as shown with the profiles in figure 7.1 corresponding to the isola in 7.2.

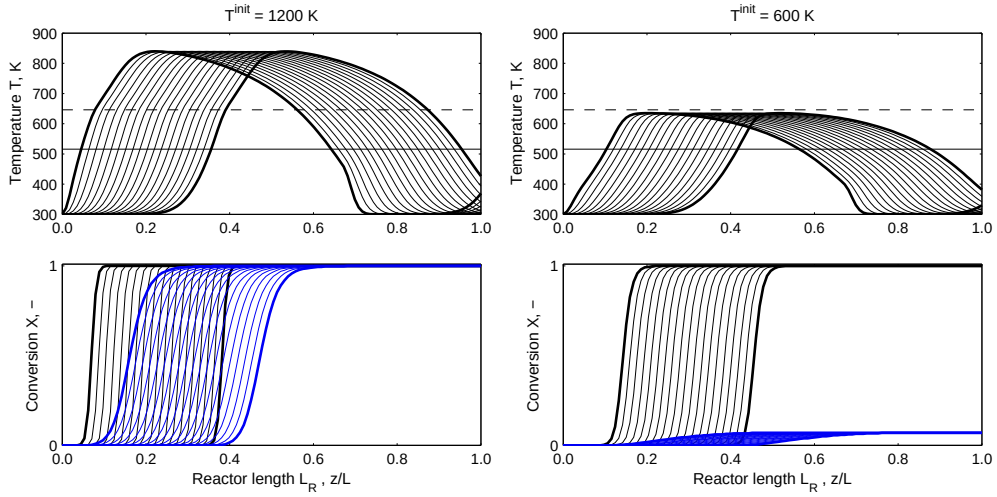

Figure C.5.: Open-loop SMBR profiles in case the feed is in front of the first segment. Black lines for conversion of the first, and blue for the second component. ($\Delta T_{ad}^{mix} = 30$ K, $\gamma = 1.0$, $\alpha = 0.5$, $\sigma = 1e4$, left $T^{init} = 1200K$, right $T^{init} = 600K$).

In case of the SMBR, different temperature fronts appear as the kinetic selectivity σ becomes very large. This is shown for $\sigma = 1e4$ in figure C.5. Two cases are considered, an initial temperature of T^{init} 1200 K and of 600 K (the calculations have been performed with a reduced accuracy for an efficient assessment of possible options for SMBR control).

The reaction fronts correspond the steady state approximation with the TMBR model (figure 7.1). The front with the smaller reaction rate is faster. At approximately the ignition temperature of second reaction, the temperature front shows a kink. At this temperature the second, faster reaction front proceeds with a faster temperature front as well. Thus, two reaction fronts can occur.

In case a too small initial temperature has been selected, for instance 600 K below the ignition temperature of the second reaction, only the first reaction goes to completion. Thereby only a single temperature front, but two reaction fronts appear. The single temperature front is faster than in the mixture. The reaction front of the second reaction attains values up to only 3 % conversion. This means, that in case of distinct isola, it mainly depends on the initial temperature whether the high or low temperature isola is attained. This qualitative picture was already discussed in scope of the formation of distinct isola as the fraction α is changed (section 7.2, 7.3). There it was already shown that the low temperature isola is accompanied by reduced conversion of the second component similar to the SMBR.

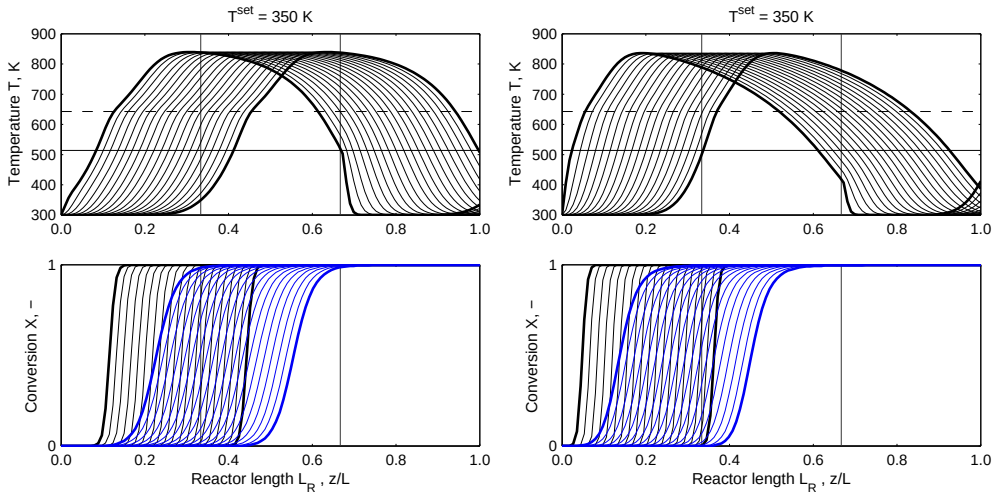

Figure C.6.: Closed-loop control of the SMBR based on *controller 3*. Black lines for conversion of the first, and blue for the second component. ($\Delta T_{\mathrm{ad}}^{\mathrm{mix}} = 30$ K, $\alpha = 0.5$, $\sigma = 1e4$, left $T^{\mathrm{set}} = 310K$, right $T^{\mathrm{set}} = 450K$).

C.4.2. Closed-Loop Reactor Control

C.4.2.1. Control Based on Reaction Front

The controller based on the reaction front, *controller 3* in this work, was investigated for the mixture. At first, a large preheating temperature of 1200 K was selected and the applicable set-points determined.

Examples for two different set-points are illustrated in figure C.6. As a guide for the eyes the temperature front at 1/3 of the reactor length is monitored for the switch. For the set-point of 350 K both reaction fronts exhibit complete conversion and the maximum temperature correspond approximately to solution branch of the high temperature isola. If the set-point is at 450 K, the conversion of the second component is still maintained. Though beyond, the set-point would violate the limit set by the ignition temperature of the first reaction as shown for the single component system. This also applies for the mixture studied. An explanation is, analogous to the single reaction (see figure 5.7), that the set-point selected is responsible for the switching time of the controller being associated with a value of the stable isola branch. In case of smaller set-points, a solution at larger flow rate ratios and vice versa, are obtained. Since in the mixture were identified single or distinct isola, which do not increase in γ compared to single component, but rather in the maximum temperature, it is not expected to find larger domains of the set-points for stable ignited states. This means, that unless the total feed concentration is increased and the domain in γ enlarged, the domain of set-points will not be favorable for processing mixtures.

Similar to the open-loop control the initial temperature decides about the conversion of the second component and the maximum reactor temperature attained. Disturbances in the feed composition can therefore not always be handled, because the transition regime of the isola split may be traversed. As a consequence, only complete conversion of the first, but not always conversion of the second component can be guaranteed with *controller 3*. Advanced control concepts should be investigated for these cases.

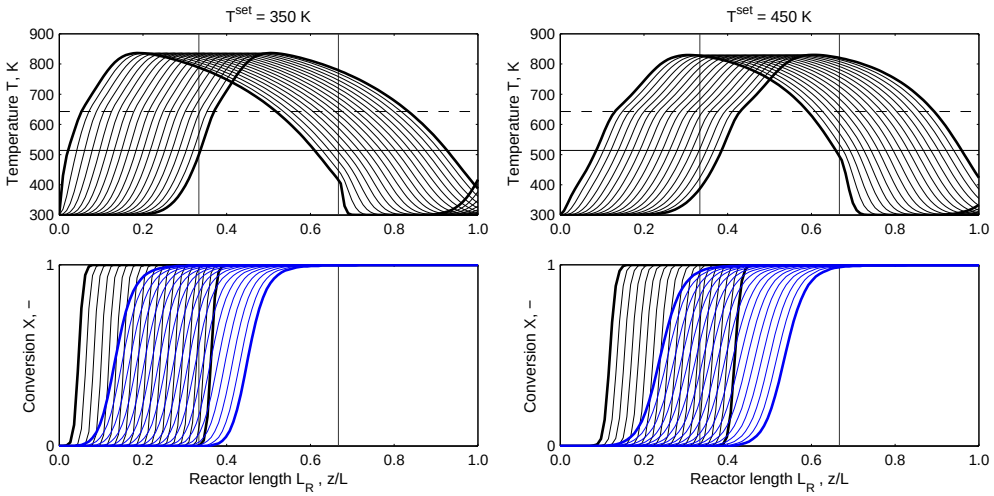

Figure C.7.: Closed-loop control of the SMBR based on *controller 3*. Black lines for conversion of the first, and blue for the second component. ($\Delta T_{\mathrm{ad}}^{\mathrm{mix}} = 30$ K, $\alpha = 0.5$, $\sigma = 1e4$, left $T^{\mathrm{set}} = 350$ K, right $T^{\mathrm{set}} = 450K$).

C.4.2.2. Observation of the Leading Thermal Front

An alternative is the observation of the leading thermal front using *controller 2* as suggested in chapter 5. The concept was modified to a window of observation of only a single switching period to speed up the relaxation onto the cyclic steady state.

Within the start-up phase the sensor for the reaction front is ruling. After several switches, the second sensor becomes active and determines the adjusted switching times. Therefore it is the set-point for the leading thermal front determining dynamics and front positions at switching events.

Figure C.7 illustrates two selected set-points for the leading thermal front. This time, the point of observation is at the end of the reactor cascade.

The influence of the set-points is seen in the front positions. A smaller set-point shifts the reaction fronts to the reactor inlet. Thereby the smallest possible set-point was found to be 350 K, below extinctions occurs. Increasing the set-point yields larger switching times and thus greater time spans for the fronts to travel. The largest set-point is limited by approximately the ignition temperature of the first component. The set-point for the reaction front is limited between the second set-point and approximately the maximum temperature or the preheating temperature. With proper set-points selected the controller can handle mixtures and ensures complete conversion similar to the *controller 3*. Again, fluctuations in the fraction may lead to an operation at the low temperature isola with corresponding reduced conversion of the second component.

C.4.3. Discussion of Concepts and Summary

Open and closed-loop control for SMBR was investigated for the case of feed mixtures with significantly different reaction rates. It turns out, that distinct reaction fronts can occur which can become challenging regarding control concepts. A faster reaction front can form at high temperatures.

Control based on the reaction front (*controller 3*) may fail to capture both fronts due to the temperature set-points below the base point of the fast reaction front. In such cases the controller is unable to notice the presence of the fast front and conversion of the second, less oxidizable component cannot be achieved.

As an alternative, the control based on the leading thermal front (*controller 2*) was examined. For the faster reaction fronts, the single thermal front will still be leading and thus appropriate for observation. However, the domain of feasible set-points is narrow and should be identified carefully.

Further research is needed, in particular for control of fluctuations in the mixture. This is due to the existence of single isola of low temperature in case the feed is deficient of the less oxidizable component. This requires to restore high temperature ignited states from intermediate ignited states, which seems to be a problem in case of distinct isola. Such extreme cases requires a priori knowledge about the reaction system and the number of available isola. Then, either actions to affect the distinct isola, e.g. unify them by co-feeding of a component with intermediate reactivity, or by higher inlet concentrations to at least reach the transition domain. This can help to recover a high temperature reactor state.

D. Reactor Model used for Comparison with Experiments

Fixed-bed reactor models differ much in the degree of complexity of the physics involved, and correspondingly in the efforts for parameterization. A well established classification for continuum models is the one by Froment et al. [66] providing an instructive picture of the implemented phases and dimensions. Typically the models are distinguished whether they consider a single pseudo-homogeneous phase or heterogeneous phases and with respect to the spatial resolution in only a single axial or additionally in the radial direction. Furthermore, velocity profiles and intra particle resistances can be considered.

The choice was made for the one dimensional pseudo-homogeneous model, similar to the model used in the theoretical parts. In addition, a wall balance was considered to represent better the heat conduction observed in the experiments. In this section, the model is derived and the parameters listed as used for the simulations presented in the experimental chapter.

D.1. Reactor Model

The following derivations are based on the control volume of a fixed-bed and a reactor wall as illustrated in figure D.1.

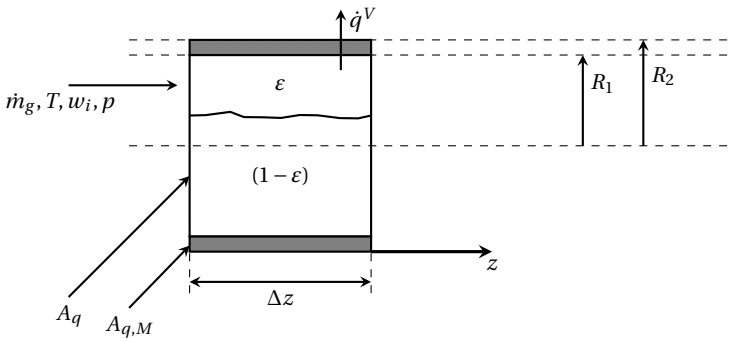

Figure D.1.: Control volume of the one dimensional reactor model.

Assumptions:

- The fixed-bed is represented by a pseudo-homogeneous phase neglecting interphase transport limitations and radial gradients. Such a model can be regarded as an effective reactor model typically used for dynamic simulations [66].
- The superficial velocity is a reduced interstitial velocity according to $u_g = \varepsilon u_g^*$ with a constant void fraction ε.

- The model accounts for a heat flux $\dot{q}^V$ across the jacket. The reactor jacket is modeled to represent heat conduction, accumulation and heat transfer to the surrounding.

- The pressure drop is omitted in the model, but was considered for the identification of the void fraction based on experiments.

- Due to the large temperature fluctuation, changes in the density affect the local gas phase velocities. The gas is assumed to be incompressible and volume changes due to reaction are omitted.

- Ideal gas law applies due to the pressure close to ambient conditions and the dilution of the reactants.

The density of the gas and the concentration of the chemical species can be expressed as

$$\rho_g = \frac{p\widetilde{M}_L}{\mathrm{R_g}T} \qquad c_i = w_i \frac{\rho_g}{\widetilde{M}_i} \tag{D.1}$$

The density is based on air and varies locally according to the temperature fronts. The local concentrations, as implemented in the rate law, thus, depend on the mass fractions and the local density.

D.1.1. Continuity Equation

Continuity of the gas phase in the control volume $\Delta V = \varepsilon A_q \Delta z$ is considered [96]. Expansion in a Taylor series leads to the following balances:

$$\frac{\partial}{\partial t}(\varepsilon A_q \Delta z \rho_g) = (\varepsilon A_q \rho_g u_g^*)_z - (\varepsilon A_q \rho_g u_g^*)_{z+\Delta z} = -\frac{\partial(\varepsilon \rho_g u_g^*)}{\partial z} A_q \Delta z \tag{D.2}$$

$$\varepsilon \frac{\partial(\rho_g)}{\partial t} = -\varepsilon \frac{\partial(\rho_g u_g^*)}{\partial z} \tag{D.3}$$

$$\varepsilon \frac{\partial(\rho_g)}{\partial t} = -\frac{\partial(\rho_g u_g)}{\partial z} \tag{D.4}$$

Assuming incompressibility yields:

$$\frac{\partial(\varepsilon \rho_g)}{\partial t} = -\frac{\partial(\varepsilon \rho u^*)_g}{\partial z} = 0 \tag{D.5}$$

$$u_g^i(z) = \frac{\dot{m}_g}{\varepsilon \rho_g(z)} \qquad \text{Interstitial velocity} \tag{D.6}$$

$$u_g(z) = \frac{\dot{m}_g}{\rho_g(z)} \qquad \text{Superficial velocity} \tag{D.7}$$

D.1.2. Material Balance

The material balance for a species i is defined by:

$$\varepsilon\rho_g\frac{\partial w_i}{\partial t} = -\dot{m}_g\frac{\partial w_i}{\partial z} + \frac{\partial}{\partial z}\left(\rho_g D_i\frac{\partial w_i}{\partial z}\right) + \widetilde{M}_i\rho_b\sum_j \nu_{ij} r_j(c_i,T) \qquad i = 1,\dots N_c \tag{D.8}$$

and corresponding initial and boundary conditions according to [100] read:

$$w_i(z,t=0) = w_i^{\text{init}} \qquad i = 1,\dots N_c \tag{D.9}$$

$$\dot{m}_g w_i^{\text{in}} = \dot{m}_g w_i|_{z=0} - \rho_g D_i\frac{\partial w_i}{\partial z}\Big|_{z=0} \tag{D.10}$$

$$\frac{\partial w_i}{\partial z}\Big|_{z=L} = 0 \qquad i = 1,\dots N_c \tag{D.11}$$

The species diffusion is replaced by an effective diffusion coefficient valid for all species [66].

D.1.3. Thermal Energy Balance

The differential balance of the control volume has a general form:

$$\left(\varepsilon(\rho c_p)_g + (1-\varepsilon)(\rho c_p)_s\right)\frac{\partial T}{\partial t} = -c_{p,g}\dot{m}_g\frac{\partial T}{\partial z} + \frac{\partial}{\partial z}\left(\lambda\frac{\partial T}{\partial z}\right) + \dot{q}^V + \rho_b\sum_j(\Delta H_R)_j r_j(c_i,T) \tag{D.12}$$

incorporating the heat flux related to the control volume $\dot{q}^V$ as defined by a specific heat transfer area a^V:

$$\dot{q}^V = \dot{q}^A a^V \tag{D.13}$$

The area can be derived from the control volume:

$$a_1^V = \frac{\Delta A}{\Delta V} = \frac{U_1\Delta z}{A_q\Delta z} = \frac{2\pi R_1}{\pi(R_1^2)} = \frac{2}{R_1} \tag{D.14}$$

Assuming a linear driving force for the heat flux between the reactor temperature T and its surrounding T_U yields the balance:

$$\left(\varepsilon(\rho c_p)_g + (1-\varepsilon)(\rho c_p)_s\right)\frac{\partial T}{\partial t} = -c_{p,g}\dot{m}_g\frac{\partial T}{\partial z} + \frac{\partial}{\partial z}\left(\lambda\frac{\partial T}{\partial z}\right) + \frac{2h_w}{R_1}(T_U - T) + \rho_b\sum_j(\Delta H_R)_j r_j(c_i,T) \tag{D.15}$$

With corresponding initial and boundary conditions:

$$T(z, t=0) = T^{\text{init}} \tag{D.16}$$

$$\dot{m}_g c_{p,g} T^{\text{in}} = \dot{m}_g c_{p,g} T|_{z=0} - \lambda \frac{\partial T}{\partial z}\Big|_{z=0} \qquad \frac{\partial T}{\partial z}\Big|_{z=L} = 0 \tag{D.17}$$

h_W is the heat transfer coefficient accounting for heat transfer resistances due to the two boundary layers and due to heat conduction through the jacket. An effective axial heat conductivity, λ depends on the properties of the system and on the superficial gas phase velocity. In addition the wall balance is included, which is sometimes recommended in the case of wall cooled reactors [218].

D.1.4. Reactor Jacket

The balance for the differential volume $\Delta V_M = A_{q,M}\Delta z$ of the reactor jacket is:

$$A_{q,M}\Delta z(\rho c_p)_M \frac{\partial T_M}{\partial t} = A_{q,M}\Delta z\left(\frac{\partial}{\partial z}\left(\lambda_M \frac{\partial T}{\partial z}\right)\right) + A_{q,M}\Delta z\left(\dot{q}_1^V - \dot{q}_2^V\right) \tag{D.18}$$

Heat transfer takes place via heat conduction in the axial direction and transport from inside the fixed-bed, q_1^V, to the surrounding, q_2^V, with the heat transfer areas:

$$a_1^V = \frac{\Delta A_1}{\Delta V_M} = \frac{U_1 \Delta z}{A_{q,M}\Delta z} = \frac{2\pi R_1}{\pi(R_2^2 - R_1^2)} = \frac{2R_1}{(R_2^2 - R_1^2)} \tag{D.19}$$

$$a_2^V = \frac{U_2 \Delta z}{A_{q,M}\Delta z} = \frac{2R_2}{(R_2^2 - R_1^2)} \tag{D.20}$$

The energy balance of the jacket reads:

$$(\rho c_p)_M \frac{\partial T_M}{\partial t} = \frac{\partial}{\partial z}\left(\lambda_M \frac{\partial T_M}{\partial z}\right) + \dot{q}_i^V - \dot{q}_a^V \tag{D.21}$$

The reactor balance is modified to account for the heat flux to the jacket with the heat transfer coefficient α_1 according to:

$$\begin{aligned}\left(\varepsilon(\rho c_p)_g + (1-\varepsilon)(\rho c_p)_s\right)\frac{\partial T}{\partial t} = &- c_{p,g}\dot{m}_g \frac{\partial T}{\partial z} + \frac{\partial}{\partial z}\left(\lambda \frac{\partial T}{\partial z}\right) \\ &+ \frac{2\alpha_1}{R_1}(T_M - T) + \rho_b \sum_j (\Delta H_R)_j r_j(c_i, T)\end{aligned} \tag{D.22}$$

Boundary conditions of equation D.17 apply here as well. The energy balance of the jacked finally reads:

$$(\rho c_p)_M \frac{\partial T_M}{\partial t} = \frac{\partial}{\partial z}\left(\lambda_M \frac{\partial T_M}{\partial z}\right) + \alpha_1 \frac{2R_1}{(R_2^2 - R_1^2)}(T - T_M) + \alpha_2 \frac{2R_2}{(R_2^2 - R_1^2)}(T_U - T_M) \tag{D.23}$$

With boundary conditions:

$$\left.\frac{\partial T_M}{\partial z}\right|_{z=0} = \left.\frac{\partial T_M}{\partial z}\right|_{z=L} = 0 \tag{D.24}$$

D.1.5. Valves

The valves are included in the model to account for local heat sinks. In this respect, the first approach considered is to lump all effects resulting from the reactor connections, valves and pipings, in a single energy balance:

$$V_h(\rho c_p)_h \frac{\mathrm{d}T_h}{\mathrm{d}t} = \dot{V}_g(\rho c_p)_g(T^{\mathrm{in}} - T_h) + \dot{Q}_U \tag{D.25}$$

The energy transport through the valve (index h) is determined by the heat capacity of the gas, a lumped capacitance and a heat flow to the surroundings, $\dot{Q}_U$. Pressure-volume work and pressure drop are neglected. For a volume specific form and a linear driving force for the heat flux, the energy balance is represented by:

$$(\rho c_p)_h \frac{\mathrm{d}T_h}{\mathrm{d}t} = \frac{\dot{V}_g}{V_h}(\rho c_p)_g(T^{\mathrm{in}} - T_h) + \dot{q}^V \tag{D.26}$$

$$= \frac{\dot{m}_{h,g}}{L_h} c_{p,g}(T^{\mathrm{in}} - T_h) + \alpha_h a_h^v (T_u - T_h) \qquad \text{IC:} \quad T_h(t=0) = T_h^{\mathrm{init}} \tag{D.27}$$

The mass flow density is assumed to be constant, $\dot{m}_{h,g} = \frac{\dot{M}_g}{A_{q,h}}$. For the case that no reaction takes place the mass fractions remain unchanged, $0 = w_i^{\mathrm{in}} - w_i$. The parameters for the apparent valve properties are estimates based on steel and the geometries of the setup.

D.1.6. Structured Modeling of Periodic Reactor

The model parts are organized in the modeling framework PROMOT [219] and structured as illustrated in figure D.2. As a central element, the controller unit is connected with the two fixed-beds, the incoming feed and a product sink, as well as to the valves. The material and energy fluxes are connecting feed with the product via the fixed-beds, while the switching is organized by a Petri-net implemented in the controller (see appendix C for specifications). Temperature feedback for the closed-loop control is realized by temperature signals connected from each reactor unit to the controller unit.

D.2. TMBR Model

The TMBR model used for the comparison with experiments 6.13 also accounts for the heat losses through the reactor jacket.

$$\varepsilon \rho_g \frac{\partial w_i}{\partial t} = -\dot{m}_g \frac{\partial w_i}{\partial z} + D\frac{\partial^2 w_i}{\partial z^2} + \widetilde{M}_i \rho_b \sum_j \nu_{i,j} r_j(c_i, T) \tag{D.28}$$

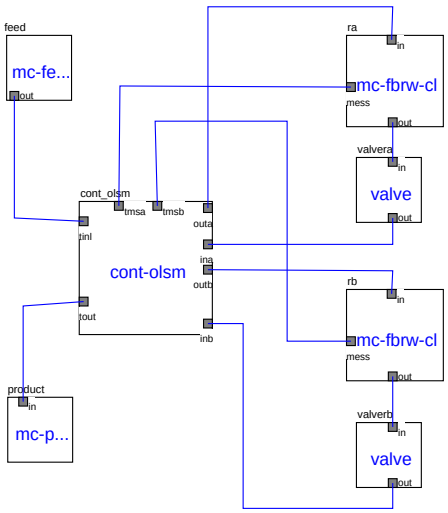

Figure D.2.: Structured reactor model consisting of fixed-bed reactors, switching valves and a controller.

$$\dot{m}_g w_i^{\text{in}} = \dot{m}_g w_i|_{z=0} - D\frac{\partial w_i}{\partial z}\Big|_{z=0}, \qquad \frac{\partial w_i}{\partial z}\Big|_{z=L} = 0, \qquad i = 1,\dots N_c \tag{D.29}$$

For the reactor jacket:

$$(\rho c_p)_M \frac{\partial T_M}{\partial t} = \lambda_M \frac{\partial^2 T_M}{\partial z^2} + \alpha_1 \frac{2R_1}{(R_2^2 - R_1^2)}(T - T_M) + \alpha_2 \frac{2R_2}{(R_2^2 - R_1^2)}(T_u - T_M) \tag{D.30}$$

$$\frac{\partial T_M}{\partial z}\Big|_{z=0} = 0 \qquad \frac{\partial T_M}{\partial z}\Big|_{z=L} = 0 \tag{D.31}$$

The fixed-bed energy balance:

$$\begin{aligned}\left(\varepsilon(\rho c_p)_g + (1-\varepsilon)(\rho c_p)_s\right)\frac{\partial T}{\partial t} = &\left(-c_{p,g}\dot{m}_g + (\rho c_p)_s u_s\right)\frac{\partial T}{\partial z} + \lambda\frac{\partial^2 T}{\partial z^2} \\ &+ \frac{2\alpha_1}{R_1}(T_M - T) + \rho_b \sum_j (\Delta H_R)_j r_j(c_i, T)\end{aligned} \tag{D.32}$$

$$T(z=0) = T(z=L_R) = T^{\text{in}} \tag{D.33}$$

D.3. Parameterization

The transport parameters are obtained from known correlations. Measurements of the heat capacities have been performed for the catalyst and the steel.

D.3.1. Physical Properties

The physical values presented here are required for the correlations of heat and mass transport properties.

D.3.1.1. Gas Phase

The gas phase is composed of air (L), ethylene (1), and propene (2) with a constant oxygen content corresponding to that of air. The molar masses are:

$$\widetilde{M}_L = 28.9644\,\text{g/mol} \quad \widetilde{M}_1 = 28.05\,\text{g/mol} \quad \widetilde{M}_2 = 42.08\,\text{g/mol} \tag{D.34}$$

The molecular diffusion coefficients calculated according the Fuller with diffusion volumes of 19.7 for air , 41.04 ethene and 61.56 propene [220].

Viscosity The dynamic viscosity for air is calculated based on mixing rules suggested by *Wilke* [220] and substituted by a polynomial valid for the temperature range $0-800\,^{\circ}\text{C}$:

$$\eta = -1.43\cdot 10^{-5}T^2 + 5.51296\cdot 10^{-2}T + 4.123144 \tag{D.35}$$

in µPas with temperature T in Kelvin.

Heat Capacity The following polynomial based on air mixture was used to represent the heat capacity of air in the range of $0-800\,^{\circ}\text{C}$ (alternatively [221])

$$c_{p,g} = 8.331059\cdot 10^{-8}T^2 + 8.551957988\cdot 10^{-5}T + 9.800184093\cdot 10^{-1} \tag{D.36}$$

in kJ/kg K with temperature T in unit Kelvin.

Heat Conduction The following polynomial based on air mixture valid for the range $0-800\,^{\circ}\text{C}$ was used.

$$\lambda_g = -1.3377\cdot 10^{-9}T^2 + 6.3662\cdot 10^{-5}T + 8.12\cdot 10^{-3} \tag{D.37}$$

in W/mK with temperature T in unit Kelvin.

D.3.1.2. Physical Properties of Solids

Heat Capacities A thermal DSC analyzer (*TG-DSC 111, Setaram*) used to determine the temperature dependent heat capacity of steel and the calorimeter (*C80 Evolution, Setaram*) for the catalyst $CuCrO_x/Al_2O_3$ as well as α-Al_2O_3. The results are illustrated in figure D.3.

The $CuCrO_x/Al_2O_3$ catalyst heat capacity increases with the temperature. Repeated measurements confirmed this trend and for modeling, to account for the larger operating temperature, a value of 1.3 kJ/kgK has been selected. The heat capacity for $\alpha - Al_2O_3$ is documented as well. The results shown slightly smaller values compared to the $CuCrO_x/Al_2O_3$.

Table D.1.: Densities and heat capacities of solids

	Density ρ kg/m^3	Heat capacity c_p kJ/kgK
$CuCrO_x/Al_2O_3$ Catalyst	1155	≈ 1.5
$\alpha - Al_2O_3$	3980	≈ 1.0
Steel 1.428	7900	0.5

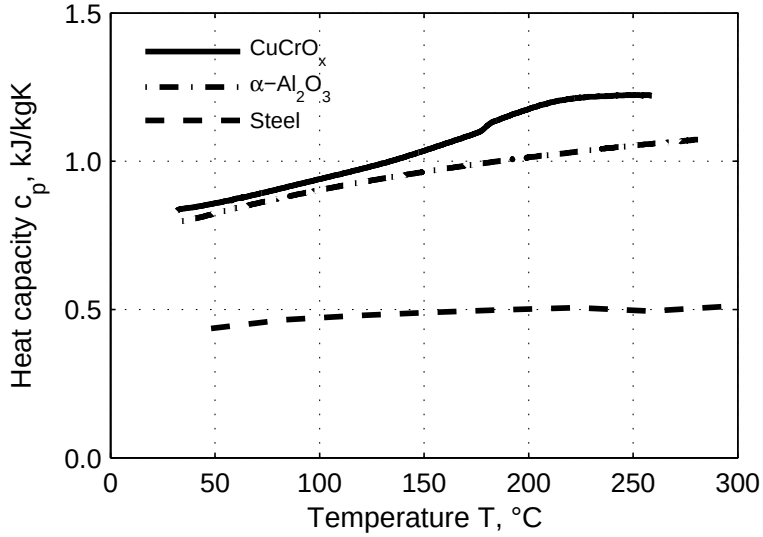

Figure D.3.: Heat capacities of solids.

For steel (1.4128) a well known heat capacities were determined for the temperature range with approximately 0.5 kJ/kgK, a result which is in good agreement with the literature [220]. The selected values are listed with the corresponding densities in table D.1.

Heat Conductivity For the steel *1.4828* the heat conductivity is in the range of 12 to 22 W/mK and can be represented by the following linear equation (based on data in [220]):

$$\lambda_M = 0.0154T + 8,5 \qquad \text{W/mK} \tag{D.38}$$

with temperature T in Kelvin.

The heat conductivity of the catalyst λ_K was assumed to be $5,4$ W/mK. However, this assumption is not very precise and can vary by approximate 10 % due to active species and uncertainties in the quality of the bulk material.

D.3.2. Axial Transport

The problem with the one-dimensional model is, that it is not representative for larger experimental data sets recorded for the purpose of parameterization of the heat transfer problem, which are valid for steady-state problems often in absence of chemical reactions. In this respect, the one-dimensional model is typically used for basic design and evaluation of control concepts. The parameterization suggested here therefore applies only to the experimental findings in this work.

D.3.2.1. Heat Conductivity

The axial conductivity is an effective value which accounts for an axial and an radial portion [66]. Despite a fair number of publications dealing with the standard model (pseudo-

homogeneous, axial and radial resolution) only little systematic studies are known for effective models. Vortmeyer et al. [222] suggested an effective heat conductivity explained with the derived equivalence condition for the heterogeneous model and the pseudo-homogeneous model.

$$\lambda_{\text{eff}} = (1-\varepsilon)\lambda_s + \frac{(\dot{m}_g c_{p,g})^2}{a_p \alpha_p} \tag{D.39}$$

With α_p the interface heat transfer coefficient and a_p the specific interface area between the two phases considered in the heterogeneous model.

The axial heat conductivity for the corresponding standard model can be calculated according to *Zehner, Bauer, Schlünder* as documented in VDI-GVC [220, Mh 1-15]:

$$\frac{\lambda_{\text{ax}}}{\lambda_g} = k_{\text{bed}} + \frac{Pe_0}{K_{\text{ax}}}, \quad Pe_0 = \frac{u_0 (\rho c_p)_g d_p}{\lambda_g}, \quad K_{\text{ax}} = 2 \tag{D.40}$$

The axial heat conductivity depends linearly on the Peclet number with the corresponding heat conductivity k_{bed} of the specific heat conduction at stagnant flow conditions [220]. This value accounts for several factors, such as heat radiation, geometry and properties of the gas and the solid.

D.3.2.2. Radial Heat Conductivity

The radial heat conductivity is required for the estimation of the wall heat transfer [220]:

$$\frac{\lambda_r}{\lambda_g} = k_{\text{bed}} + \frac{Pe_0}{K_r}, \qquad Pe_0 = \frac{u_0 (\rho c_p)_g d_p}{\lambda_g}, \qquad K_r = 8 \tag{D.41}$$

Again, a linear dependence on the Peclet number is assumed, but the slope is somewhat smaller compared to the axial heat conduction.

D.3.2.3. Effective Axial Mass Dispersion

Effective axial dispersion can be described by the following relation assuming averaged and space independent values of the molecular dispersion of the species present in the gas phase and of the gas velocity [220, 223]:

$$\frac{D_{\text{ax}}}{D_m} = \frac{D_{\text{bed}}}{D_m} + \frac{Pe_0}{K_{\text{ax}}} \tag{D.42}$$

In equation (D.42) the first term on the RHS accounts for the situation stagnant conditions, which can be obtain from the porosity of the fixed-bed and the molecular diffusion [220]:

$$\frac{D_{\text{bed}}}{D_m} = 1 - \sqrt{1-\varepsilon} \tag{D.43}$$

In the second term of equation (D.42), Pe_o is the mass Peclet number defined by:

$$Pe_0 = \frac{u_0 d_p}{D_m} \tag{D.44}$$

Axial mass dispersion in fixed-beds is determined by several factors. Under stagnant conditions the dispersion takes place in the gas phase by molecular diffusion of the individual species [224]. Under flow the molecular dispersion is superimposed by local velocity distribution consisting of eddy dispersion, transversal mixing and flow through bypasses.

Moreover, the correlations are actually valid only for the steady state simulations and being applied in within the standard model. For industrial applications, however, the axial mass dispersion is often neglected in one dimensional models [66].

D.3.3. Heat Transfer Through the Reactor Jacket

Heat transfer to the wall has always been considered within the scope of axial and radial heat transport problems in fixed-beds. The heat flux involved has a radial direction to the wall and is inherently connected with the radial heat conduction with inside the fixed-bed [66, 225]. Using the standard model, two different approaches are well known: In the first case, the so call α_W-model, a boundary condition of the third kind is employed inducing temperature jump similar to contact resistances between two solid phases [226]. The alternative approach, the λ_r-model avoids jump conditions [225].

Despite of the well developed standard model, in the effective model the wall heat transfer is represented by a linear driving force and an overall wall heat transfer coefficient α_1. Typically this effective coefficient is the sum of the transfer resistance to the wall and the resistance in the bed. For special cases based on the analysis of the standard model, analytical expressions are available, for instance for a constant heat flux at the boundary [66, 226].

$$\frac{1}{\alpha_1} = \frac{1}{\alpha_W} + \frac{R_1}{4\lambda_r} \tag{D.45}$$

In equation (D.45) the first term on the RHS is the wall resistance and the second the inner resistance accounting for the radial heat conduction and the reactor radius.

The heat transfer to the wall is a local property described by α_w, which should be distinguished from the overall heat transfer coefficient h_w [223] used for the parameterization of the correlation. The corresponding Nusselt number for the heat transfer problem is defined by:

$$Nu_W = \frac{\alpha_w d_p}{\lambda_g} \tag{D.46}$$

At the beginning the correlations were only depending on the particle Reynolds number, for instance Yagi et al. [227], Li et al. [228]. Recently, a correlation was published accounting for radial heat conduction [229]. A comparison is given by [230]. The correlation by De Wasch et al. [231] was applied in this work since it is closest to the experimental system. However, significant differences in the correlations are found. Moreover, the uncertainties of this

approach are seen in the simplified analytical equation (D.45), which is restricted to steady state balances and a constant wall heat flux. Another cause of error is the presence of chemical reactions which cause inhomogeneous heat fluxes.

This work attempts to include the reactor wall balance to represent better the heat conduction in the fixed-bed. For that reason, the radial heat flux to the surrounding is determined by the second heat transfer coefficient α_2 in equation (D.23). Several correlations exist for the defined geometries and materials and would also apply for the complex geometry [220], nevertheless, this parameter was finally treated as an unknown and fitted in order to describe all experiments.

D.3.4. Correlation for Pressure Drop

The *Ergun*-equation was used to relate pressure drop and gas phase velocity, which was used to determine the void fractions of the fixed-beds reactors [220]:

$$\frac{\partial p}{\partial z} = 150\frac{(1-\varepsilon)^2}{\varepsilon^3}\frac{\eta}{d_p^2}u_g + 1.75\frac{(1-\varepsilon)}{\varepsilon^2}\frac{\rho_g}{d_p}u_g^2 \tag{D.47}$$

D.3.5. Listing of Parameters

Table D.2.: Parameters of power law kinetics of ethene and propene on $CuCrO_x/Al_2O_3$ catalyst

	k_0 $mol^{1-\alpha}/(kg\ s\ l^{1-\alpha})$	E_a kJ/mol	α
Ethene	$5.131 \cdot 10^9$	116.5	0.689
Propene	$8.672 \cdot 10^{10}$	135.3	0.292

	k_0 $l/(kg\ s)$	E_a kJ/mol
Ethene	$2.947 \cdot 10^{10}$	111.4
Propene	$1.012 \cdot 10^{13}$	128.4

Table D.3.: Parameters of the experimental system

ε	0.450	mean void fraction
c_K	1.5 kJ/kgK	heat capacity catalyst
ρ_K	1190 kg/m^3	density catalyst
ρ_w	7900 kg/m^3	density steel
λ_{ax}	0.7 W/mK	axial heat conductivity of fixed-bed
λ_w	15 W/mK	heat conductivity of reactor wall
α_2	0.006 kW/m^{2}K	heat transfer
α_h	0.0101 kW/m^{2}K	heat transfer valve
$(\rho c_p)_h$	4500 kJ/kgK	heat capacity
T_u	298 K	ambient temperature
L_{Seg}	0.45 m	reactor length
$D_{1,\text{Seg}}$	0.0212 m	inner diameter
$D_{2,\text{Seg}}$	0.0254 m	outer diameter
d_p	0.001 m	particle diameter
$\widetilde{M}_L$	0.02896 kg/mol	molar mass air
$\widetilde{M}_1$	0.02805 kg/mol	molar mass ethene
$\widetilde{M}_2$	0.04208 kg/mol	molar mass propene
$\Delta H_{R,1}$	−1926 kJ/mol	reaction enthalpy propene oxidation
$\Delta H_{R,2}$	−1322 kJ/mol	reaction enthalpy ethene oxidation